UNIVERSITÀ DEGLI STUDI DI PADOVA

DIPARTIMENTO DI FISICA E ASTRONOMIA "G. GALILEI"

CORSO DI DOTTORATO DI RICERCA IN ASTRONOMIA

CICLO XXXII

UNIVERSIDAD DE LA LAGUNA

DEPARTAMENTO DE ASTROFÍSICA

PROGRAMA DE DOCTORADO EN ASTROFÍSICA

DIRECT MEASUREMENT OF THE BAR PATTERN SPEED IN STRONGLY AND WEAKLY BARRED GALAXIES

Ph.D. School Coordinator: Ch.mo Prof. Giampaolo Piotto
Supervisor: Prof. Enrico Maria Corsini
Co-supervisor: Dr. José Alfonso López Aguerri

Ph.D. Candidate: Virginia Cuomo

External referees:
Prof. Martin Bureau
Prof. Françoise Combes

Al bimbo maliano
morto attraversando il Mediterraneo,
custodendo nella tasca
la sua pagella e i suoi sogni.

Contents

List of Figures

List of Tables

Riassunto

Le barre sono strutture che si trovano comunemente nelle galassie dell'Universo locale, indipendentemente dalla loro morfologia, luminosità e dall'ambiente in cui sono immerse. Le proprietà fotometriche, cinematiche e dinamiche delle barre dipendono dai meccanismi della loro formazione e dai processi evolutivi, che includono lo scambio di momento angolare con le altre componenti galattiche. La loro formazione può essere indotta da instabilità interne, che danno luogo barre che ruotano velocemente e che possono rallentare durante la loro successiva evoluzione, o da interazioni mareali, che portano alla formazione di barre che ruotano più lentamente. Un'accurata misura della velocità angolare della barra consente quindi di dedurre informazioni cruciali sulla distribuzione di massa e sul processo di formazione delle galassie barrate. In questa tesi ci proponiamo di ampliare il campione di galassie fortemente e debolmente barrate con misure dirette di velocità angolare della barra applicando il metodo di Tremaine e Weinberg a dati spettroscopici a campo integrale di grande qualità e di esplorare le relazioni tra le proprietà delle barre e delle loro galassie ospiti.

Presentiamo l'analisi di Tremaine e Weinberg di NGC 4264, una galassia lenticolare barrata che si trova nella regione dell'Ammasso della Vergine ed è in fase di interazione con la sua galassia vicina, NGC 4261. Analizzando la fotometria superficiale ottenuta dalle immagini nelle bande i e g della Sloan Digital Sky Survey e la cinematica stellare dalla spettroscopia a campo integrale eseguita con lo strumento Multi Unit Spectroscopic Explorer montato sul Very Large Telescope, caratterizziamo la barra di NGC 4264 misurandone la lunghezza, la forza e la velocità angolare. Ricaviamo la velocità circolare della galassia dalla velocità di rotazione delle stelle attraverso le equazioni dell'idrodinamica stellare e deriviamo il tasso di rotazione della barra. Troviamo che NGC 4264 ospita una barra forte ed estesa, che sta ruotando il più velocemente possibile, come tutte le altre barre analizzate finora. L'accurata misura del tasso di rotazione della barra ci consente di dedurre che la formazione della barra di NGC 4264 è imputabile a processi interni e non all'interazione in corso con NGC 4261 o da interazioni avvenute in passato con altre galassie nella regione dell'Ammasso della Vergine.

Investighiamo il processo di formazione delle barre deboli, che finora sono stato relativamente trascurate. A questo scopo, selezioniamo un campione di 29 galassie vicine e debolmente barrate, con un'ampia varietà di morfologie e luminosità e con caratteristiche adatte all'applicazione del metodo di Tremaine e Weinberg. Combinando la nostra analisi con studi precedenti, confrontiamo le proprietà delle barre deboli con quelle delle barre forti. Ricaviamo la lunghezza e la forza delle barre dalle immagini in banda r della Sloan Digital Sky Survey e la velocità angolare dalla cinematica stellare ottenuta dalla Calar Alto Integral Field Area

Survey. In primo luogo, troviamo che il 45 per cento delle galassie nel campione che sono state classificate come debolmente barrate attraverso un'ispezione visuale, risultano o non ospitare realmente una barra oppure la componente allungata, che si osserva nelle loro regioni centrali, non sta ruotando rigidamente. La velocità angolare della barra è ottenuta per 16 oggetti del campione. Due galassie ospitano una barra che ruota troppo rapidamente, in un regime di velocità non fisico. Adottando un criterio quantitativo basato sulla forza della barra per distinguere tra barre forti e deboli, troviamo che le galassie debolmente barrate ospitano barre meno estese e con raggi di corotazione inferiori rispetto alle loro controparti forti. Barre deboli e forti hanno velocità angolari e tassi di rotazione simili, che sono constistenti con il regime di una rapida rotazione. Non osserviamo differenze tra la prominenza dello sferoide centrale in galassie debolmente e fortemente barrate, mentre quasi tutte le barre deboli risiedono nelle regioni interne dei dischi, contrariamente a quanto accade alle barre forti. Escludiamo quindi che il processo di indebolimento delle barre sia dovuto solo alla prominenza dello sferoide e che la formazione delle barre deboli sia imputabile all'interazione con un oggetto compagno. I nostri risultati osservativi suggeriscono che le barre deboli possano trovarsi in sistemi galattici evoluti, in cui avviene un minore scambio di momento angolare tra la barra e le altre componenti galattiche rispetto a quanto succede in presenza di barre forti.

Rivisitiamo le relazioni tra le proprietà delle barre e delle loro galassie ospiti. Collezioniamo tutte le 100 galassie, di cui attualmente è disponibile una misura diretta di velocità angolare della barra. Per ogni oggetto consideriamo la lunghezza, la forza, la velocità angolare, il raggio di corotazione e il tasso di rotazione, così come il tipo morfologico e la magnitudine assoluta in banda r ottenuta dalla Sloan Digital Sky Survey della galassia ospite. Deriviamo anche il rapporto tra la luminosità totale della galassia e quella dello sferoide da una decomposizione fotometrica disponibile per un sottocampione di oggetti. Limitiamo la nostra analisi alle 75 galassie che abbiano piccoli errori relativi sulla velocità angolare della barra e che non ospitino barre ultraveloci. Confermiamo i risultati osservativi precedenti secondo cui le barre più estese ruotano più lentamente e hanno raggi di corotazione maggiori e che le galassie dominate dal disco ospitano le barre più deboli. Inoltre, troviamo che le barre più forti ruotano più lentamente, come previsto dallo scambio di momento angolare che avviene durante l'evoluzione della galassia e che dipende dalle proprietà di quest'ultima. Questo risultato, insieme al fatto che osserviamo le barre forti in galassie dominate dal contributo dello sferoide è in accordo con uno scenario di coevoluzione tra barra e sferoide che si inserisce in uno scenario più ampio in cui galassie più massicce si sono formate più rapidamente nel passato e hanno avuto più tempo per rallentare le loro barre, aumentarne l'estensione e spostare il raggio di corotazione nelle regioni più esterne.

Infine, discutiamo alcune questioni ancora aperte relative all'applicazione e ai risultati del metodo di Tremaine e Weinberg, che riguardano le barre ultraveloci e le barre lente e suggeriamo alcune linee di ricerca per possibili indagini future.

Abstract

Bars are a common feature in the local Universe across a wide range of galaxy morphologies, luminosities, and environments. The photometric, kinematic, and dynamical properties of bars depend on their formation mechanism and evolution process including the interchange of angular momentum with the other galaxy components. Their formation can be either induced by internal instabilities giving rise to fast rotating bars possibly slowing down during their evolution, or by tidal interactions triggering slowly rotating bars. Thus, the accurate measurement of the angular frequency of a bar, its pattern speed, allows to infer information about the mass distribution and formation process of barred galaxies. In this thesis we aim at increasing the sample of direct measurements of the bar pattern speed in strongly and weakly barred galaxies by applying the Tremaine-Weinberg method to high-quality integral-field spectroscopic data and at exploring the relations between the properties of bars and their host galaxies.

We present a Tremaine-Weinberg analysis of NGC 4264, a barred lenticular galaxy in the region of the Virgo Cluster undergoing a tidal interaction with one of its neighbours, NGC 4261. Analysing the surface photometry from the Sloan Digital Sky Survey i- and g-band images and the stellar kinematics from the integral-field spectroscopy performed with the Multi Unit Spectroscopic Explorer at the Very Large Telescope, we characterise the bar of NGC 4264 by measuring the radius, strength and pattern speed. We derive the circular velocity of the galaxy in the disc region by correcting the stellar streaming velocity for asymmetric drift and calculate the corresponding bar rotation rate. We find that NGC 4264 hosts a strong and large bar which is rotating as fast as it can like nearly all the other bars measured so far. The accurate measurement of the bar rotation rate allows us to infer that the formation of the bar of NGC 4264 is due to self-generated internal processes and not triggered by the ongoing interaction nor by a previous interaction with an other galaxy in the region of the Virgo Cluster.

In addition, we investigate the formation process of weak bars, which have been generally neglected to date. To this aim, we select a sample of 29 nearby weakly barred galaxies, spanning a wide range of morphological types and luminosities, and with characteristics suitable for the application of the Tremaine-Weinberg method. Combining our analysis with previous studies, we compare the properties of weak and strong bars. We measure the bar radius and strength from the r-band images available in the Sloan Digital Sky Survey and bar pattern speed from the stellar kinematics obtained by the Calar Alto Integral Field Area survey. As a first result, 45 per cent of the galaxies in the sample, which are morphologically classified

as weakly barred galaxies from a visual inspection, turn out not to host an actual bar component, or their central elongated component is not in rigid rotation. The bar pattern speed is successfully derived for 16 objects. Two of them host a bar rotating unphysically too fast. Using a quantitative criterion based on the bar strength to differentiate weak and strong bars, we find that the weakly barred galaxies host shorter bars and shorter corotation radii than their strongly barred counterparts. Weak and strong bars have similar bar pattern speeds and rotation rates, which are all consistent with being fast. We do not observe any difference between the bulge prominence in weakly and strongly barred galaxies, whereas nearly all the weak bars reside in the disc inner parts, contrary to strong bars. We exclude that the bar weakening is only related to the bulge prominence and that the formation of weak bars is triggered by the tidal interaction with a companion. Our observational results suggest that weak bars may be evolved systems exchanging less angular momentum with other galactic components than strong bars.

We revisit the relations between the properties of bars and their host galaxies. We collect all the 100 galaxies known to have a direct measurement of bar pattern speed. For each object we consider the length, strength, pattern speed, corotation radius, and rotation rate of the bar as well as the Hubble type and absolute Sloan Digital Sky Survey r-band magnitude of the host galaxy. We also derive the bulge-to-total luminosity ratio for a subsample of galaxies with an available photometric decomposition. We limit our analysis to the 75 galaxies with a relatively small relative error on the bar pattern speed and not hosting an ultrafast bar. We confirm earlier observational findings that longer bars rotate with a slower bar pattern speed, shorter bars are weaker, fast bars rotate with higher bar pattern speed and have shorter corotation radii, and disc-dominated galaxies host weaker bars. In addition, we find that stronger bars rotate slower as predicted for the interchange of angular momentum during bar evolution depending on galaxy properties. This result together with the fact that we observe stronger bars in bulge-dominated galaxies is in agreement with a scenario of downsizing in bar formation and co-evolution of bars and bulges if more massive galaxies formed earlier their bars and had sufficient time to slow down, grow in length, and push outwards corotation.

Finally, we discuss some open issues related to the application and results of the Tremaine-Weinberg method about ultrafast bars and slow bars and outline a few ideas for future investigations.

Chapter 1

Introduction

Galaxies are the basic constituents of the Universe and can be defined as complex systems made of stars, gas, and dust with a wide range of shapes (Binney & Tremaine, 2008). This is suggestive of many different physical processes taking place within each galaxy and/or with other galaxies. In the observable Universe there are about 10^{11} galaxies, hosting $10^7 - 10^{11}$ stars, with typical total masses of $10^8 - 10^{12}\ M_\odot$.

Since the early morphological classifications, bars in galaxies have played an important role. Hubble (1926) noticed that some spiral galaxies have a bright line, corresponding to a bar, running through them. He defined this class of objects as "barred spiral galaxies" and located them along one of the tuning-fork diagram arms, parallel to the sequence of the "normal spiral galaxies". A prominent role was given to barred galaxies by de Vaucouleurs (1959) and van den Bergh (1976) as well. In fact, de Vaucouleurs (1959) divided disc galaxies into different "families" according to the prominence of the bar, which can be present or not. Even an intermediate stage of weakly-barred galaxies is possible (Fig. 1.1). Generally, the spiral pattern of barred spirals originates either tangent to a ring encompassing the bar or at the ends of the bar.

Nowadays, it is known that many disc galaxies, including the Milky Way, host a central bar which contains up to ~ 30 per cent of the total light (Aguerri et al., 2001). These structures form from a dynamical instability in differentially rotating stellar discs and are not static, since they tumble around the galaxy centre.

1.1 General properties of galaxy bars

1.1.1 Bar incidence

Bars are observed in ~ 50 per cent of galaxy discs in the optical bands, and this fraction rises to ~ 70 per cent in the near-infrared (Knapen et al., 2000; Aguerri et al., 2009; Nair & Abraham, 2010). Indeed, a large number of galaxies which appeared unbarred in the blue photographic plates used in the early classifications turned out to be barred or to host a weaker non-axisymmetric feature of a similar kind when imaged by digital detectors in red

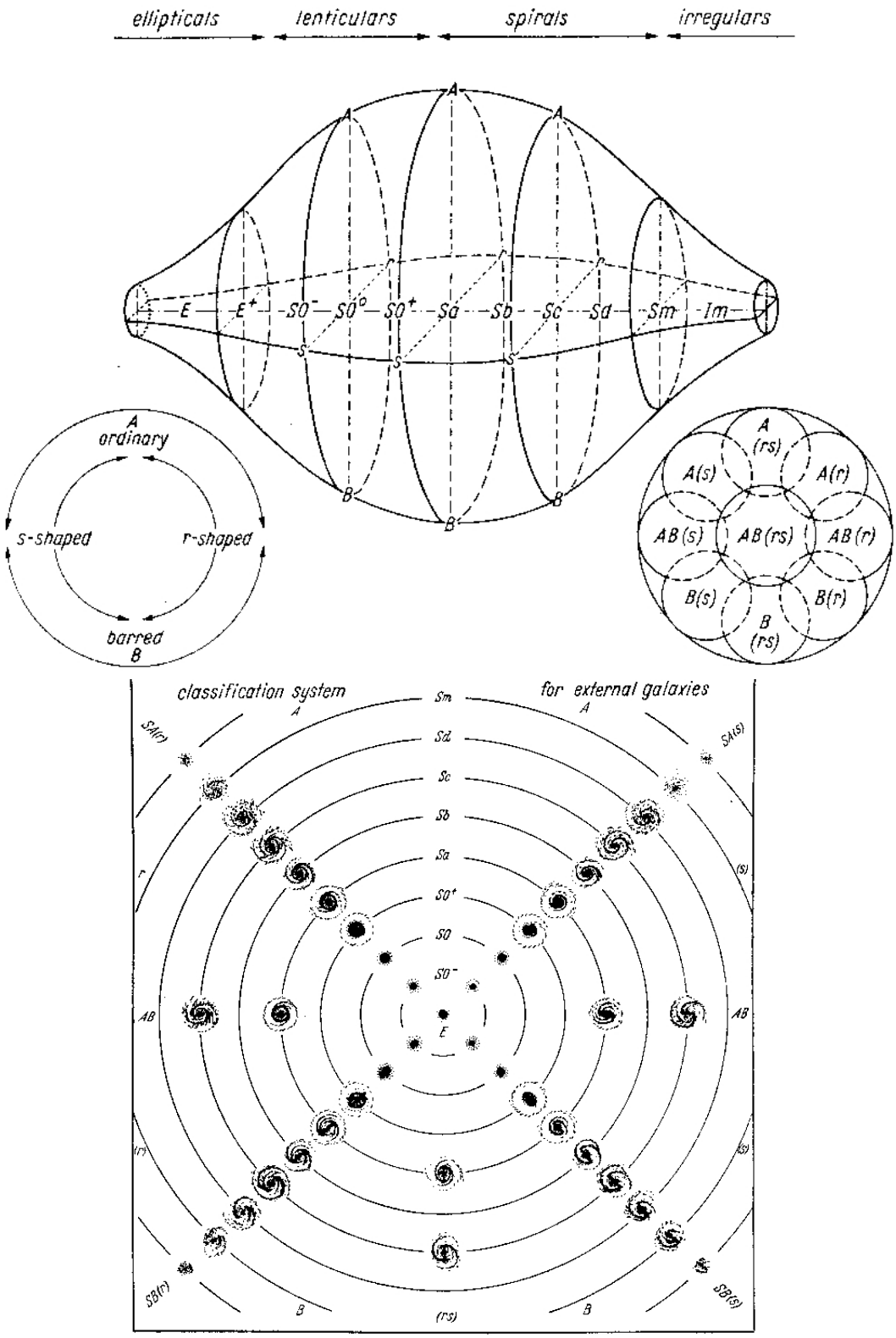

Figure 1.1: *Top panel*: A three-dimensional representation of the revised morphological classification scheme by de Vaucouleurs (1959). *Bottom panel*: a plane projection of the classification.

and near-infrared bands. Recently, Buta et al. (2015) analysed $\sim$ 2300 galaxies with the mid-infrared Spitzer bands and found strong and weak bars in $\sim$ 60 per cent of the sample spanning a wide range in morphologies, from S0 to Im, in agreement with previous results from Marinova & Jogee (2007).

While observations show that bars are ubiquitous in low-redshift galaxies, tracing the bar fraction as a function of redshift is still an open issue. Answering this question may help to understand the reason why bars form. Many studies about the bar fraction at $z \lesssim 1$ found some evolution, even if this is not unanimous (Abraham et al., 1999; Jogee et al., 2004; Sheth et al., 2008). Both Cameron et al. (2010) and Melvin et al. (2014) observed a decrease of visually-identified strong bars from $\sim$ 35 per cent at $z = 0.2$ to $\sim$ 15 per cent at $z = 1$. Simmons et al. (2014) provided the bar fraction out to $z \sim 2$ based on near-infrared Hubble Space Telescope (HST) images for $\sim$ 900 luminosity-selected galaxies. They found a fraction of $\sim$ 10 per cent of barred galaxies at $0.5 < z < 2.0$. Up to $z \sim 1$, the result is consistent with previous studies based on similar analysis and with the predictions of zoom-in cosmological simulations, which locate the main epoch of disc setting and bar formation at $z < 1$. At $z \sim 1.5$ bars are expected to disappear because more frequent mergers make discs dynamically hotter, preventing bar formation. However, Simmons et al. (2014) found bars even at $z \sim 2$, with no evolution between $1 < z < 2$.

The bar fraction in nearby galaxies depends on morphological type, being lower in lenticulars than in spirals (Marinova & Jogee, 2007; Aguerri et al., 2009; Li et al., 2017). Dividing their sample in morphological classes, Buta et al. (2015) found that bars reside more in Scd–Sm galaxies ($\sim$ 80 per cent) than in S0/a-Sc galaxies ($\sim$ 55 per cent). The significant difference between the early- and late-type samples diminishes when galaxies with large inclinations are included, but is not completely ruled out, except for the most face-on subsample, in agreement with Barazza et al. (2008). Bars are observed in nearly all the Magellanic type galaxies (Odewahn, 1996).

The bar fraction is a strong function of the galaxy luminosity (or equivalently stellar mass), since it peaks for giant galaxies and decreases in both the low and high-mass regimes (Méndez-Abreu et al., 2010; Nair & Abraham, 2010; Sánchez-Janssen et al., 2010). In his analysis of $\sim$ 1200 galaxies with Spitzer images, Erwin (2018) found a maximum in bar frequency for galaxy stellar masses $\sim 10^{9.7} M_{\odot}$ and confirms the decline at both lower and higher masses.

The bar fraction distribution as a function of galaxy luminosity varies significantly also from cluster to field environment. Méndez-Abreu et al. (2012) studied the bar fraction in three different environments ranging from the field to the Virgo and Coma clusters. They observed a large difference between the bar fraction distributions as a function of galaxy luminosity in the field and Coma Cluster, with Virgo being an intermediate case. Barred galaxies peak at $M_r \simeq -20.5$ mag in clusters and at $M_r \simeq -19.0$ mag in the field. This was interpreted as a variation of the effect of environment on bar formation depending on galaxy luminosity: brighter disc galaxies are stable enough against close interactions to maintain cold their discs, so the bar formation is triggered by interactions when the galaxies are probably in a pre-cluster stage. For fainter galaxies, the interactions become strong enough to heat

up the discs inhibiting bar formation. Similar conclusions were drawn by Lin et al. (2014), who analysed ~ 30000 barred galaxies in the local Universe and their environment with Sloan Digital Sky Survey (SDSS) data. After removing any dependence on stellar mass, color, and stellar surface mass density, they found that the clustering of barred and unbarred galaxies is different when splitting the sample in early- and late-type galaxies. In fact, early-type barred galaxies seem to be more strongly clustered on scales from a few 100 kpc to 1 Mpc when compared to early-type unbarred galaxies. At these intermediate scales, the correlation function is dominated by the one-halo term, which would indicate that barred early-type galaxies are more frequently satellite systems. This is similar to what Barway et al. (2011) found in S0 galaxies: a higher bar fraction in clusters rather than in the field. Moreover, barred late-type galaxies have few neighbors within ~ 50 kpc, since tidal forces from close companions suppress the formation/growth of bars.

Bars principally consist of an old stellar population (de Vaucouleurs, 1959; Elmegreen & Elmegreen, 1985), however near-infrared images are the most suitable to reveal the presence of a bar because the extinction in near-infrared bands is only $0.1 - 0.2$ times that in visual light, so the dust has only a minimal effect in galaxy images making easier the bar identification.

Consolandi (2016) analysed the radial profiles of a pure sample of late-type barred galaxies among thousands of optical images from the SDSS, finding that bars are redder than their surrounding discs, because they host an older stellar population with no star formation. Moreover, the redness appeared to increase with the galaxy mass.

Barazza et al. (2008) found a weak trend between colour and bar fraction, which is slowly declining for redder colours. Erwin (2018) confirmed the previous results finding an overall roughly flat behaviour of bar frequency over a wide range of colours ($g - r \approx 0.1 - 0.8$), with a weak trend of declining bar fraction to redder colours. Other authors, however, found conflicting results based on SDSS images (Masters et al., 2012; Lee et al., 2012), which can be explained as due to a selection bias.

1.1.2 Bar surface brightness profile

The galaxy surface brightness is given by the various contributions of the different galaxy components. Describing the contribution of bars is not straightforward because these components show a wide range of light fractions, shapes, and sizes.

Elmegreen & Elmegreen (1985) and Elmegreen et al. (1996) studied the light profiles of bars in a sample of 32 barred galaxies with blue and near-infrared surface photometry. They found and confirmed that the surface brightness radial profile of a barred galaxy can be either uniform along the bar length, having a flat profile, or characterised by an exponential-like profile (Fig. 1.2).

The flat profile is observed preferentially for the bars of early-type galaxies (SB0-SBc), while the exponential profile is more common in late-type ones (SBc-SBm). Bars with a flat profile are large with respect to the galaxy size. Probably, they originate from an excess of old and young stars at the bar ends, because the orbits crowd near the inner 4:1 resonance. They are usually associated with an excess of light at the ends of the structure. Contrary to flat profiles, the exponential ones do not host the crowding of bar orbits arising from an

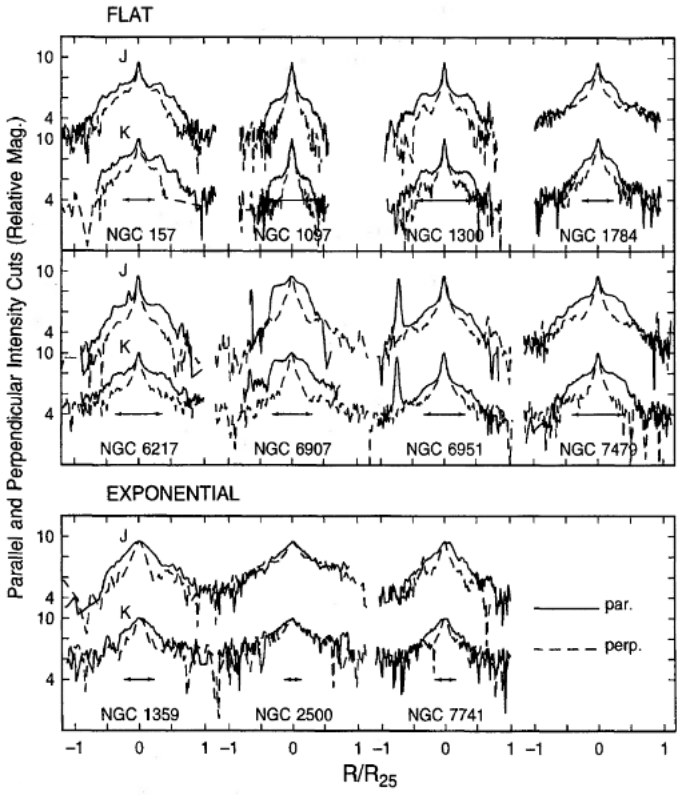

Figure 1.2: *Top panels*: surface brightness radial profiles of flat bars. *Bottom panels*: surface brightness radial profiles of exponential bars. In each panel, the radial profiles are measured along the major (*solid line*) and minor axis (*dashed line*) of the bar observed in J (*top profiles*) and K (*bottom profiles*) bandbands. The horizontal arrows mark the extension of the bars. From Elmegreen et al. (1996).

excess old and young stars at the ends of the bar, or the offset leading dust lanes, usually associated with an inner Lindblad resonance (ILR) inside the bar (Elmegreen et al., 1996; Quillen, 1996).

End-of-bar star formation regions, spiral arms, and rings are commonly observed along the bar, but only the latter two are observed perpendicular to the bar. When azimuthally averaged, the radial profiles of both flat and exponential bars are nearly exponential. Similar results were confirmed by other studies (Ohta et al., 1990; Combes & Elmegreen, 1993), even if there are also conflicting conclusions (Seigar & James, 1998).

In order to describe the bar contribution to a galaxy surface brightness, several parametric laws were proposed in the literature.

Athanassoula et al. (1990) showed how the bar isophotes can be successfully described using generalized ellipses, which cover also boxy or discy shapes as a function of an extra parameter c (Fig. 1.3). Assuming a Cartesian coordinate system (x, y, z) with the origin in the galaxy centre, the x-axis parallel to the direction of right ascension and pointing westward, the y-axis parallel to the direction of declination and pointing northward, and the z-axis along the line-of-sight (LOS) and pointing toward the observer, the plane of the sky is the (x, y)

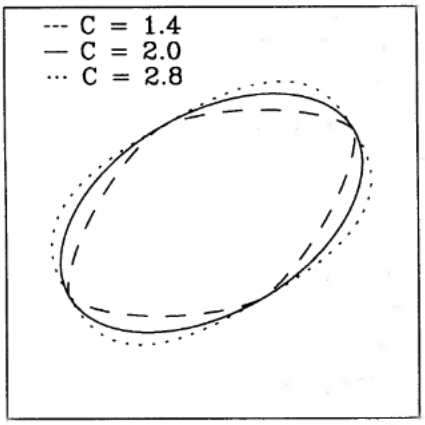

Figure 1.3: Three examples of generalized ellipses according to the value of the shape parameter c. From Athanassoula et al. (1990).

plane. In this frame, when the principal axes of the ellipse are aligned with the coordinate axes, the radial coordinate is defined as

$$r = \left(|x|^c + \left| \frac{y}{(1-\epsilon)} \right|^c \right)^{1/c}, \tag{1.1}$$

where ϵ is the ellipticity and c is the shape parameter of the isophotes, and they are constant as a function of radius. It is equivalent to the $\cos 4\theta$ Fourier coefficient usually adopted to describe the boxiness/discyness of the isophotes (Jedrzejewski, 1987), but applied to all the isophotes of the bar. A perfect ellipse is obtained for $c = 2$, a diamond discy shape is visible for $c < 2$ and a rectangle boxy shape for $c > 2$.

The surface brightness radial profile of a Ferrers ellipsoid (Ferrers, 1877; Laurikainen et al., 2005, Fig. 1.4) is given by

$$I_{\rm bar}^{\rm Ferrers}(r) = \begin{cases} I_{0,\rm bar} \left[1 - (r/R_{\rm bar})^2\right]^{n_{\rm bar}+0.5} & \text{if } r \leq R_{\rm bar} \\ 0 & \text{if } r > R_{\rm bar} \end{cases}, \tag{1.2}$$

where $I_{0,\rm bar}$ is the central surface brightness, $R_{\rm bar}$ is the bar radius, and $n_{\rm bar}$ is a shape parameter of the bar, commonly adopted to be equal to 2 (Laurikainen et al., 2005). In this case the distance r of each image pixel (x, y) from the galaxy centre (x_0, y_0) is

$$\begin{aligned} r(x,y) &= [(-\Delta x \sin {\rm PA}_{\rm bar} + \Delta y \cos {\rm PA}_{\rm bar})^c + \\ &\quad (\Delta x \cos {\rm PA}_{\rm bar} - \Delta y \sin {\rm PA}_{\rm bar})^c / q_{\rm bar}^c]^{1/c} \end{aligned} \tag{1.3}$$

where $\Delta x = x - x_0$, $\Delta y = y - y_0$, $q_{\rm bar} = 1 - \epsilon_{\rm bar}$ is the bar axial ratio deriving from the constant ellipticity $\epsilon_{\rm bar}$ of the bar, and ${\rm PA}_{\rm bar}$ is the PA of the bar, giving its orientation.

and the total luminosity of the bar associated with this profile is

$$L_{\rm T,bar}^{\rm Ferrers} = \int_0^{2\pi} \int_0^{\infty} I(\theta, r) r dr d\theta = \pi I_{0,\rm bar} \frac{q_{\rm bar}}{R(c)} R_{\rm bar}^2 \frac{\Gamma(7/2)}{\Gamma(9/2)}, \tag{1.4}$$

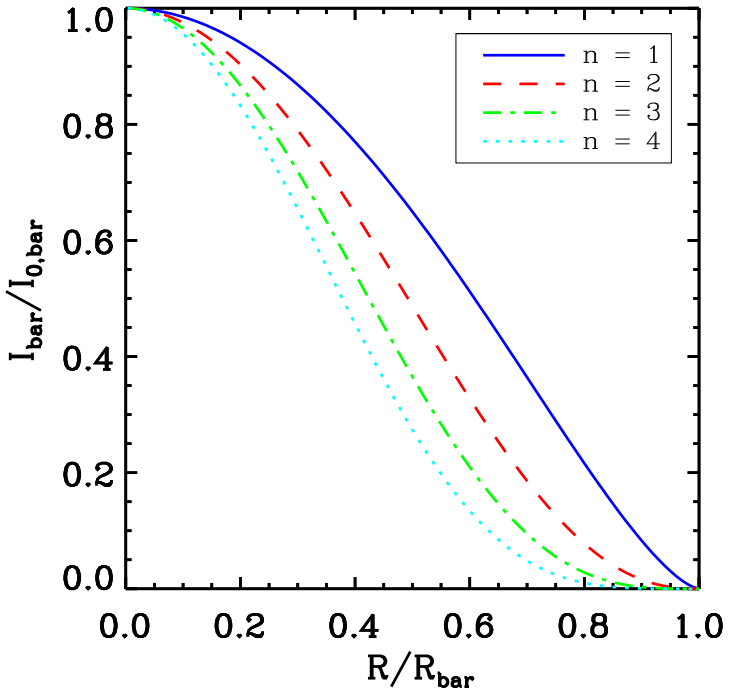

Figure 1.4: Surface brightness profiles of a Ferrers bar according to different values of the shape parameter $n_{\rm bar}$. The profiles have the same central surface brightness $I_{0,\rm bar}$ and the same bar length $R_{\rm bar}$.

where $R(c)$ is a function taking into account the different areal ratio between a perfect ellipse and a generalized ellipse described by the parameter c, and it is defined as

$$R(c) = \frac{\pi(c-2)}{4\beta\left(\frac{1}{c-2}, 1+\frac{1}{c-2}\right)}. \tag{1.5}$$

The surface brightness radial profile of a flat bar (Prieto et al., 1997; Aguerri et al., 2005) is given by

$$I_{\rm bar}^{\rm flat}(r) = I_{0,\rm bar}\left(\frac{1}{1+e^{\frac{r-R_{\rm bar}}{r_{\rm s}}}}\right) \tag{1.6}$$

and it is expected to fall off with a scalelength $r_{\rm s}$ for radii larger than $R_{\rm bar}$. In this case, the total luminosity of the bar is

$$L_{\rm T,bar}^{\rm flat} = -2\pi I_{0,\rm bar} r_{\rm s}^2 Li_2(-e^{R_{\rm bar}/r_{\rm s}})\frac{q_{\rm bar}}{R(c)}, \tag{1.7}$$

where Li_2 is the dilogarithm function (Abramowitz & Stengun, 1964).

Finally, the surface brightness radial profile of a Freeman bar (Freeman, 1966; Aguerri et al., 2005) is

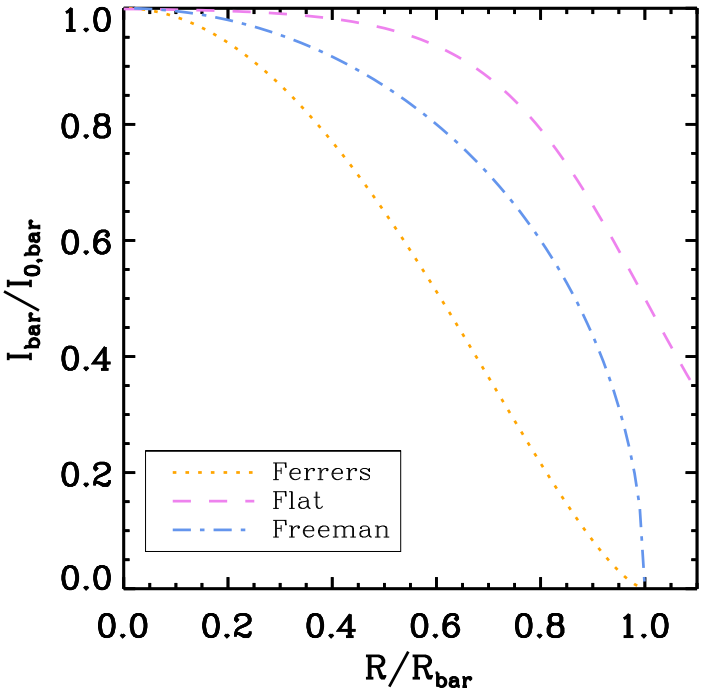

Figure 1.5: Surface brightness radial profile of a Ferrers bar (*dotted orange line*), a flat bar (*violet dashed line*), and a Freeman bar (*light blue dot-dashed line*). All the profiles have the same central surface brightness $I_{0,\mathrm{bar}}$ and the same bar length R_{bar}.

$$I_{\mathrm{bar}}^{\mathrm{Freeman}}(r) = I_{0,\mathrm{bar}}\sqrt{1-\left(\frac{r}{R_{\mathrm{bar}}}\right)^2} \tag{1.8}$$

and the associated total luminosity is

$$L_{\mathrm{T,bar}}^{\mathrm{Freeman}} = \frac{2}{3}\pi I_{0,\mathrm{bar}} R_{\mathrm{bar}}^2 \frac{q_{\mathrm{bar}}}{R(c)}. \tag{1.9}$$

Figure 1.5 shows the comparison between Ferrers, flat, and Freeman profiles.

When an iterative profile-fitting routine for the decomposition of galaxy surface brightnesses including a bar component was proposed by Prieto et al. (2001), they found that within their 11 sample galaxies half were better modelled by a Freeman profile, and the other half with a flat profile.

1.1.3 Bar intrinsic shape

Méndez-Abreu et al. (2018b) presented the first statistical study concerning the intrinsic three-dimensional (3D) shapes of bars and how they are related to the different galaxy properties, using 83 galaxies from the Calar Alto Legacy Integral Field Area Survey (CALIFA) survey. They used a statistical approach based on the knowledge of the projected geometric parameters (ellipticity and major axis position angle) of both bars and discs obtained

from a multi-component photometric decomposition. At first order, bars are considered to be single triaxial ellipsoids sharing the same equatorial plane and centre as the disc, which is considered to be an oblate ellipsoid with a given intrinsic thickness. With this methodology, they derived the intrinsic axial ratios (B/A and C/A) of the 3D triaxial ellipsoids describing the bars, which are divided into four different cases: oblate-triaxial (or axisymmetric) in-plane ellipsoids (when they are flattened with respect to the disc equatorial plane) if $C/B < B/A$; oblate-triaxial off-plane ellipsoids (when they are elongated along the polar axis) if $C/A > B/C$ and $C/A < 1$; prolate-triaxial (or axisymmetric) in-plane ellipsoids if $C/A < B/C$ and $C/B > B/A$; or elongated along the polar axis off-plane ellipsoids if $C/A > 1$. They found most of the bars in the nearby Universe are, to first order, prolate-triaxial ellipsoids (68 per cent) with different degrees of flattening, plus a small fraction of oblate-triaxial ellipsoids (14 per cent), as shown in Fig. 1.6. Bars appear to span a wide range in both B/A ($0.1 < B/A < 1.0$) and C/A ($0.1 < C/A < 0.8$), with median values of $B/A \sim 0.31$ and $C/A \sim 0.34$, in agreement with the results of other photometric decomposition approaches (Compère et al., 2014), 3D N-body simulations (Pfenniger & Friedli, 1991; Debattista et al., 2006), or hydrodynamical simulations (England, 1989). The intrinsic flattening of the bars matches well the typical intrinsic flattening of stellar discs at the corresponding galaxy mass, confirming bars originate from discs. Moreover, Méndez-Abreu et al. (2018b) observed a relation between the intrinsic shape of bars and both the galaxy Hubble type and stellar mass. In fact, bars in massive S0 galaxies are thicker and more circular, (i.e. oblate-triaxial ellipsoids), than those in less massive spirals, (i.e. prolate-triaxial ellipsoids). This is again suggestive that bars reflect the flattening of discs, since early- and late-type galaxies discs are known to have statistically different intrinsic thickening (Ryden, 2006). The recovered intrinsic axial ratios correlate with other properties of the host galaxies. Concerning the bulge properties, both B/A and C/A turned out to correlate with the Sérsic index n and bulge-to-total luminosity ratio B/T. More prominent and more concentrated (corresponding to larger B/T and n) bulges are related with thicker and more circular bars (corresponding to larger C/A and B/A). Concerning the disc properties, the bar intrinsic shape correlates with the disc $(g-r)$ colour, since redder discs have thicker and more circular bars. Regarding the bar properties, the bar intrinsic flattening correlates with all the explored bar parameters, pointing towards more prominent (with larger bar-to-total luminosity ratio Bar/T), brighter (with larger central surface brightness of the bar), and shorter (with smaller bar radius) bars being thicker (with larger C/A). All these findings confirm the tight link between bars and their host galaxies. Finally, comparing the results of Costantin et al. (2018), who performed a similar analysis on the bulges of 31 objects in common with their sample, Méndez-Abreu et al. (2018b) found that 52 per cent and 16 per cent of bulges are either more or less vertically extended than their surrounding bar, respectively. Those bulges with a nearly spherical shape are surrounded by a prolate thinner bar. This suggests that these percentages might be representative of the fraction of classical and disc-like bulges in the sample.

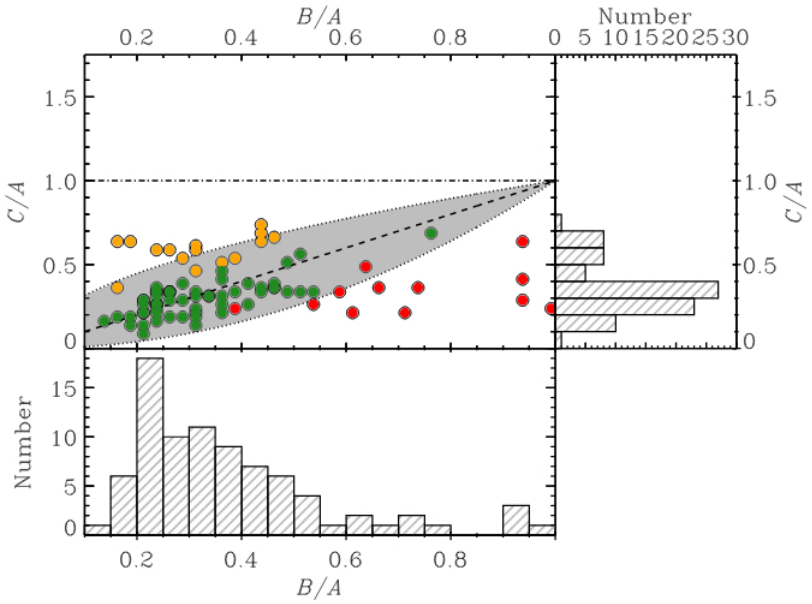

Figure 1.6: Distributions of the intrinsic axial ratios of bars in the CALIFA survey. From Méndez-Abreu et al. (2018b).

1.2 Strong and weak bars

For the first time, de Vaucouleurs (1959) recognized bar morphologies intermediate between those of ordinary and barred spirals, such as in M83. He introduced the notation SA for unbarred spirals and SB for the barred ones, so that he could use the combined notation SAB for transitional cases. His classification was based on a visual quantification of the prominence of the bar in the optical images, which is generally defined as the strength of the bar (see Sec. 1.3.2 for a discussion). To date there is no unique separation between SB and SAB objects, and many classifications based on different properties of the bars have been proposed. Weak bars are the most difficult to be visually identified and classified (Lee et al., 2019).

Buta & Block (2001a) proposed an extension of de Vaucouleurs classification, using a quantitative definition where a bar is strong if the tangential forces it induces are large. In this way, they defined seven bar strength classes: class 0 for unbarred galaxies, class 1 and 2 for weak bars, mainly defined as SAB from de Vaucouleurs, and class 2 to 6 for strong bars in SB galaxies.

An alternative possibility to define strong and weak bars is to use the ellipticity of the bar $\epsilon_{\rm bar}$ measured from the isophote at the ends of the bar. The strongest bars present $\epsilon_{\rm bar} \approx 0.8$ and they are long and massive (Aguerri, 1999; Whyte et al., 2002). The strength can be estimated also from the peak of the $m = 2$ component of a radial Fourier analysis (Athanassoula, 2003; Athanassoula et al., 2013) and it ranges from ~ 0.75 for strong bars to ~ 0.25 for weak bars. Marinova & Jogee (2007) related the strength of the bar with the ellipticity of the component, from the analysis of almost 200 bright nearby galaxies with low to intermediate inclinations. Only 7 per cent of the images in B band and 10 per cent of

those in H band present low values of bar strength ($0.25 < \epsilon_{\rm bar} < 0.40$), while 70 per cent of the images in B band and 71 per cent of those in H band have high values of bar strength ($0.50 < \epsilon_{\rm bar} < 0.75$).

Another possibility consists in using different properties of the bars. Vera et al. (2016) classified a large sample of galaxies by visual inspection of their SDSS $g + r + i$ combined images. If the size of the bar is at least 30 per cent of that of the host galaxy, the structure is defined as strong and this is found in less than ~ 10 per cent of the cases. If the size of the bar is less than 30 per cent of that of the host galaxy, it is defined as weak and found in ~ 13 per cent of galaxies. Objects for which it is difficult to decide are defined as ambiguous-barred galaxies and they correspond to ~ 12 per cent of the cases, while the remaining ~ 65 per cent of objects are unbarred. The resulting low fraction of barred galaxies disagrees with previous studies, but it can be due to limitations of the visual classification based on SDSS data.

Kruk et al. (2018) identified a sample of weakly barred galaxies from 3500 nearby galaxies from the Galaxy Zoo (Lintott et al., 2008), which are on average 1.5 times shorter than strong bars in both relative and absolute sizes. The classification into weak, intermediate, and strong bars is based on visual inspection and considering both the relative size of the bars compared to their disc and the prominence of bars. This classification however is affected by the low angular resolution of SDSS data.

More recently, Lee et al. (2019) have studied the fraction of barred galaxies in a sample of ~ 900 galaxies from the SDSS applying a visual inspection. They have found a bar fraction encompassing $\sim$ 30 per cent of strong bars and $\sim$ 33 per cent of weak bars. Moreover, they have compared the presence of strong or weak bars to other galaxy properties: strong bars are located more frequently in early-type, red, bulge-dominated and more-concentrated galaxies, while the fraction of weak bars increases toward late-type, blue, disc-dominant, and less-concentrated galaxies.

With similar methods, weak bars were observed in half of the barred galaxies analysed in near-infrared bands (Buta et al., 2007).

1.3 Characterising bars

A bar can be fully described through three properties: its radius $R_{\rm bar}$, strength $S_{\rm bar}$, and pattern speed $\Omega_{\rm bar}$. The bar radius and strength are photometric properties and can be derived analysing optical and/or near-infrared images. The bar pattern speed is a dynamical parameter, which requires kinematic measurements.

1.3.1 Bar radius

The bar radius $R_{\rm bar}$ can be defined as the length of the bar semi-major axis and represents the extension of the stellar orbits supporting the bar (Contopoulos & Papayannopoulos, 1980; Contopoulos, 1981).

Bars do not usually present sharp edges and are often associated with other components (such as rings and/or spiral arms) which may affect the proper identification of the bar boundaries. When the spiral structure with its visible star formation beyond the bar is not

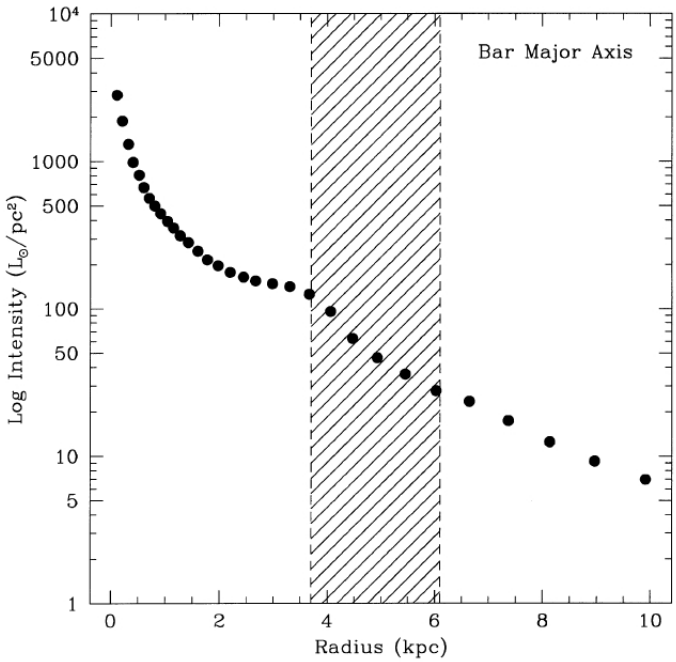

Figure 1.7: Surface brightness profile along the bar major axis of NGC 4596. The flat plateau is in correspondence of the bar. The end of the bar is located at the 'shoulder' of the plateau, on the shorter side of the hatched region. From Gerssen et al. (1999).

present, such as in SB0 galaxies, it is difficult to recover the bar ends. Moreover, the presence of a large bulge further complicates the analysis (Aguerri et al., 2005). This is why the determination of $R_{\rm bar}$ is not an easy task (Aguerri et al., 2009).

Several methods have been developed to derive $R_{\rm bar}$, but each of them suffers from some limitations (Corsini, 2011). In order to overcome the problems related to the choice of a single method, usually $R_{\rm bar}$ is estimated combining the results of different independent methods (see e.g., Corsini et al., 2003; Aguerri et al., 2015; Guo et al., 2019). Here we present a summary of the most widely used methods which are adopted to recover $R_{\rm bar}$.

- A visual estimation of the bar radius from the inspection of galaxy images (Kormendy, 1979; Martin, 1995) or from the slope change of the surface brightness profile along the bar major axis (Gerssen et al., 1999) should be only adopted to give a first guess of the bar size or to validate other measurements. The visual inspection consists in measuring the extension of the bar directly from the images. This procedure is not reliable for images with a low spatial resolution and/or poor signal-to-noise ratio S/N and it becomes even less credible for high-redshift galaxies. Moreover, it is difficult to apply it to large samples and it is very subjective, especially when images with different qualities are used. The luminosity profiles along the bar major axis commonly present a flat plateau, especially in early-type galaxies. The bar radius can be roughly obtained in correspondence of the end of the plateau. Figure 1.7 shows an example of the method based on the slope change of the surface brightness profile along the bar major axis.

- The study of the radial profile of ellipticity ϵ and position angle PA of the ellipses which best fit the galaxy isophotes (Menéndez-Delmestre et al., 2007; Aguerri et al., 2009; Guo et al., 2019) or of the phase angle ϕ_2 of the deprojected ellipses (Debattista et al., 2002; Corsini et al., 2007; Rautiainen et al., 2008) requires calibration on mock galaxy images in order to set the maximum variation of each isophotal parameter which constrains the bar radius.

  For an unbarred galaxy, the isophotal profile of ϵ usually shows a global increase from low values in the centre to a constant value at large radii, while the PA profile presents as well a typical constant behaviour in the outer parts of the galaxy. Both these observed constant values in the outer parts of the galaxy are related to the inclination i and orientation of the line-of-nodes (LON) of the galaxy disc. Undisturbed barred galaxies usually show a similar behaviour at large radii, while in the inner parts the profile of ϵ presents a local peak and a sudden decrease towards a minimum value ($\Delta\epsilon \geq 0.08$), which corresponds to the region of the disc where the isophotes become circular in the face-on case. On the other hand, the radial profile of PA is constant in the bar region (ΔPA $\leq 20°$) (Wozniak & Pierce, 1991; Wozniak et al., 1995; Aguerri et al., 2000). These peculiarities are due to the shape and orientation of the stellar orbits of the bar (Contopoulos & Grosbol, 1989; Athanassoula, 1992). Due to these characteristics visible in the radial profiles of ϵ and PA, the extension of the bar can be identified from the location of the maximum and minimum values of ϵ, which represent a lower and upper limit for $R_{\rm bar}$, respectively (Fig. 1.8).

  Operatively, the galaxy isophotes are described with ellipse fitting (Jedrzejewski, 1987). Each isophotal contour of a given semi-major axis length is described as

$$I(\theta) = c_0 + \sum_{n=1}^{\infty}[c_n \cos(n\theta) + s_n \sin(n\theta)]. \tag{1.10}$$

  If the isophotal contour is perfectly described by an ellipse, the only term that survives is the c_0, which represents the mean intensity along the contour. The departure from perfect ellipses is quantified by the Fourier components: errors in the position of the centre of the ellipse leads to non zero values for c_1 and s_1, while errors in ϵ and PA are given by the c_2 and s_2 terms, respectively. From this, it is possible to build the radial profile of ϵ and PA. The radius of the bar is given by the length of the semi-major axis at which ϵ reaches its maximum in the bar region. This peak is usually well defined and easy to be recognised, even for the case of weak bars, but not for too inclined galaxies. However, this method seems to underestimate the real $R_{\rm bar}$ because it corresponds typically to half of the extension of the bar (Wozniak et al., 1995). An example of the analysis of the ϵ profile is shown in Fig. 1.9, b.

- A complementary method is based on the analysis of the PA radial profile. In this case, $R_{\rm bar}$ is defined as the position where the PA changes by a typical value of 5° with respect to the value corresponding to the maximum in ϵ (Wozniak et al., 1995; Michel-Dansac & Wozniak, 2006). This criterion gives higher values than expected and can be considered

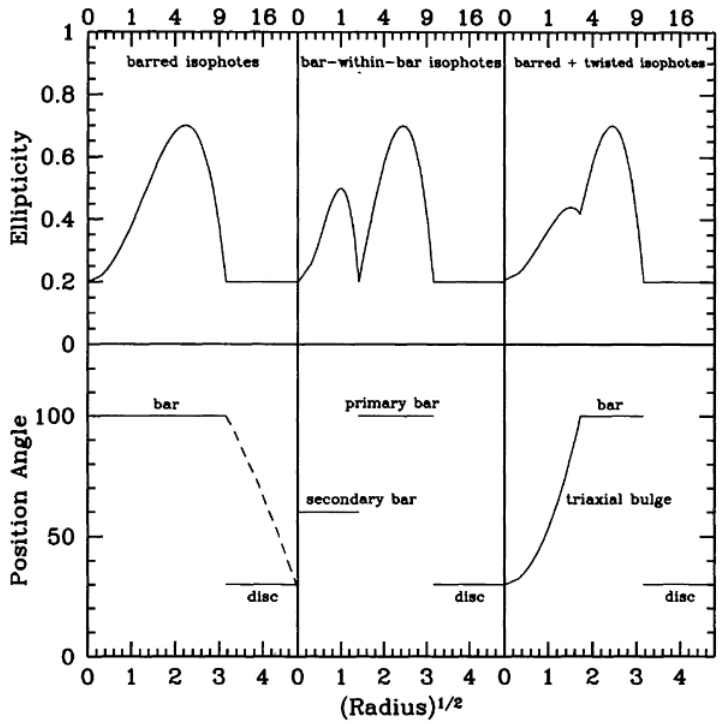

Figure 1.8: *Top panels*: schematic behaviour of the ellipticity profile of a barred galaxy. *Bottom panels*: schematic behaviour of the position angle profile. Different cases are shown: the bar case (*left panels*); primary and secondary bars case (*middle panels*); triaxial bulge and bar case (*right panels*). From Wozniak et al. (1995).

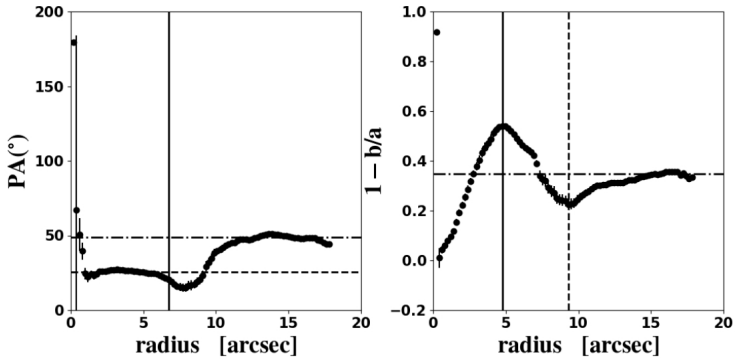

Figure 1.9: Ellipse fitting of the r-band isophotes of the galaxy `manga-8439-6102`. *Left panel*: position angle profile, (a). The bar radius inferred from the PA radial profile is marked (*solid line*). *Right panel*: ellipticity profile (b). The radii of the local maximum (*solid line*) and minimum (*dashed line*) of the ellipticity profile are marked. From Guo et al. (2019).

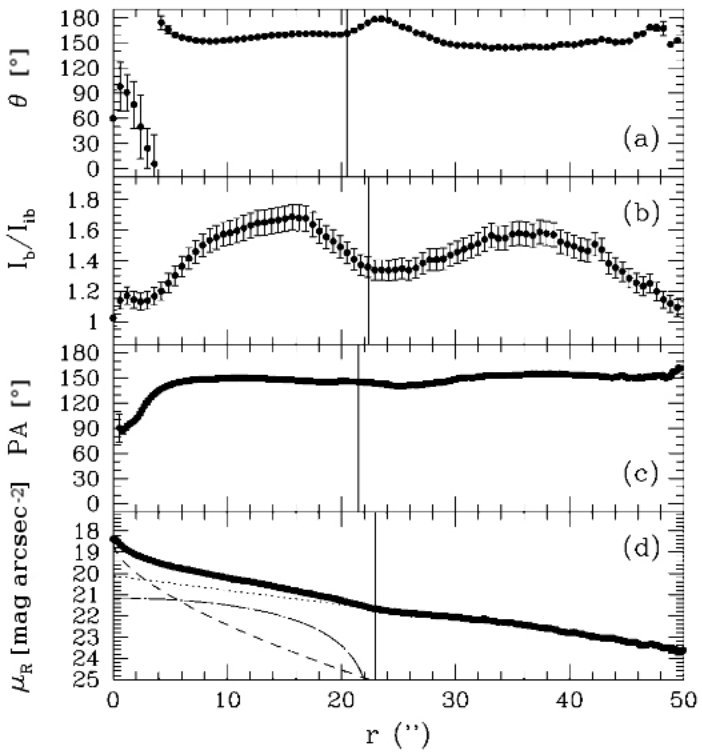

Figure 1.10: Bar radius of NGC 4431 measured from the phase angle of the $m = 2$ Fourier component (a), bar/interbar intensity ratio (b), position angle of the deprojected isophotal ellipses (c) and surface brightness decomposition (d). The values of bar radius obtained with the different methods are marked (*vertical lines*). From Corsini et al. (2007).

an upper limit for the actual value of $R_{\rm bar}$. An example of the analysis of the PA profile is shown in Fig. 1.9, a.

- A similar approach based on ellipse fitting consists in the analysis of the PA of the deprojected isophotal profiles (Aguerri et al., 2003). The deprojected image is obtained performing a stretching of the original image along the disc minor axis by a factor equal to $1/\cos i$, where the flux is conserved. The values of PA and i of the disc can be estimated from the isophotal fitting of the disc region. In this case, $R_{\rm bar}$ is defined as the position where the PA changes by a value of 10° from the PA of the ellipse with the maximum value of ϵ (Fig.1.10, c). A difference of 10° is a reasonable choice because changing this value between 5° and 15° results in $R_{\rm bar}$ estimates compatible within 1σ error.

  Analogously, the ϵ profile obtained from the deprojected image can be used to determine $R_{\rm bar}$, because a sharp break in the profile highlights the end of this component (Debattista et al., 2002).

- Fourier decomposition of the galaxy light to analyse the bar/interbar intensity ratio (Ohta et al., 1990; Aguerri et al., 2000, 2003) or the phase angle ϕ_2 of the Fourier mode

$m = 2$ has been widely used to recover $R_{\rm bar}$ (Quillen et al., 1994; Aguerri et al., 2003; Rautiainen et al., 2005). However, this method can be hampered by the presence of a non-axisymmetric disc and strong spiral arms.

Given a coordinate system (r, ϕ), where the origin is coincident with the centre of the galaxy, the x coordinate traces the LON and the y coordinate is chosen in order to define a Cartesian reference frame (x, y), the deprojected azimuthal radial profile of the luminosity of the galaxy $I(r, \phi)$ can be described with a Fourier series

$$I(r,\phi) = \frac{A_0(r)}{2} + \sum_{m=1}^{\infty} [A_m(r)\cos(m\phi) + B_m(r)\sin(m\phi)] \tag{1.11}$$

where the Fourier components are defined by

$$A_m(r) = \frac{1}{\pi}\int_0^{2\pi} I(r,\phi)\cos(m\phi)\mathrm{d}\phi \tag{1.12}$$

$$B_m(r) = \frac{1}{\pi}\int_0^{2\pi} I(r,\phi)\sin(m\phi)\mathrm{d}\phi, \tag{1.13}$$

the Fourier amplitude of the m-th component is defined as

$$I_m(r) = \begin{cases} A_0(r)/2 & \text{if } m = 0 \\ \sqrt{A_m^2(r) + B_m^2(r)} & \text{if } m \neq 0. \end{cases} \tag{1.14}$$

In the bar region, the relative amplitudes I_m/I_0 of the even Fourier components ($m = 2, 4, 6, ...$) are larger than the odd ones ($m = 1, 3, 5, ...$), and the dominant one is the $m = 2$. Moreover, the azimuthal luminosity profiles in the bar region are characterised by narrow peaks followed by flat profiles, rather than sinusoidal curves. The departure from a sinusoidal behaviour is due to the contribution of the relative even Fourier components larger than $m = 2$ (Ohta et al., 1990, Fig. 1.11).

Through this analysis $R_{\rm bar}$ can be recovered from the luminosity contrast between the bar and interbar intensity as a function of radial distance (Aguerri et al., 2000). The intensity of the bar is defined as $I_{\rm bar} = I_0 + I_2 + I_4 + I_6$, while that of the interbar is defined as $I_{\rm ibar} = I_0 - I_2 + I_4 - I_6$. The bar region is where the bar/interbar intensity ratio $I_{\rm bar}/I_{\rm ibar} > 0.5 \times [\max(I_{\rm bar}/I_{\rm ibar}) - \min(I_{\rm bar}/I_{\rm ibar})] + \min(I_{\rm bar}/I_{\rm ibar})$ and $R_{\rm bar}$ corresponds to the full width at half maximum (FWHM) of the curve given by $I_{\rm bar}/I_{\rm ibar}$ as a function of radius (Fig. 1.10, b). This method was tested with N-body simulations resulting to provide an error of 4 per cent on $R_{\rm bar}$ (Athanassoula & Misiriotis, 2002).

The phase angle $\phi_2 = \arctan[A_2(R)/B_2(R)]$ of the $m = 2$ Fourier component is roughly constant within the bar region, but outside the bulge ($\Delta\phi \leq 20^\circ$). So, $R_{\rm bar}$ can be defined through this range (Debattista & Sellwood, 2000, Fig. 1.10, a). However, this

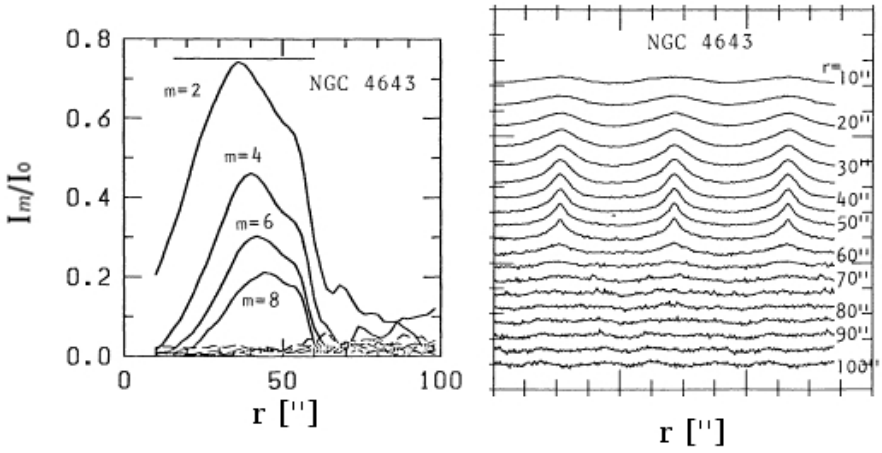

Figure 1.11: Fourier analysis of NGC 4643. *Left panel*: relative amplitudes I_m/I_0 of the first four even Fourier components $m = 2, 4, 6, 8$. *Right panel*: azimuthal profiles along concentric circumferences traced in the galactic plane. From Ohta et al. (1990).

method is not always applicable because the constant behaviour of the ϕ_2 can be masked by the presence of a strong bulge component (Debattista et al., 2002).

- Finally, another method often used to recover $R_{\rm bar}$ consists in the photometric decomposition of the galaxy image (Prieto et al., 2001; Aguerri et al., 2005; Laurikainen et al., 2009; Méndez-Abreu et al., 2018b). The surface brightness profile can be described through the contribution of multiple galaxy components, including the bar (see Sec. 1.1 for a discussion). This method depends on the adopted parametric laws for the different galaxy components (Fig. 1.10, d).

Aguerri et al. (2009) measured $R_{\rm bar}$ in a sample of ~ 2000 galaxies, using the radial profile of ϵ and PA. Their results show that the mean value of the bar radii is different according to the method. In lenticular galaxies, $\langle R_{\rm bar}\rangle = 5.6$ kpc when using the PA, and 3.5 kpc when using ϵ. In spiral galaxies of types S0/a-Sb, $\langle R_{\rm bar}\rangle = 5.4$ kpc when using the PA, and 4.0 kpc when using ϵ. Finally, in spiral galaxies of types Sc-Sm, $\langle R_{\rm bar}\rangle = 4.9$ kpc when using the PA, and 3.8 kpc when using ϵ. Bar radii obtained with the ϵ profile are systematically shorter that the PA ones. For the latter method, lenticular galaxies host the shortest bars, while for the former methods they host the largest bars. It is not possible to draw a clear conclusion, since $R_{\rm bar}$ measurements appear to be strongly affected by the method used. The only evident conclusion is that the longest bars seem to be hosted in bigger galaxies, in terms of Petrosian radius. In their sample of ~ 150 galaxies observed in infrared, Menéndez-Delmestre et al. (2007) found $\langle R_{\rm bar}\rangle = 5.4 \pm 3.3$ kpc for Sa-Sb galaxies and $\langle R_{\rm bar}\rangle = 2.2 \pm 1.7$ kpc for Sc-Sd galaxies obtained using the ϵ profiles. Bars seem to be larger in early-type spirals, also when $R_{\rm bar}$ is normalised with the optical half-light radius or with the disc scalelengths and the size of the bar does not depends on its strength (Erwin, 2005).

1.3.2 Bar strength

Several methods have been used to measure the bar strength $S_{\rm bar}$. This parameter describes the contribution to the galaxy potential of the non-axisymmetric density of the bar (Buta et al., 2001) and it can be used to distinguish between strong and weak bars. Here we present the most widely used methods to recover $S_{\rm bar}$.

- A first method to describe $S_{\rm bar}$ is based on the value of the bar ellipticity $\epsilon_{\rm bar}$ (Abraham & Merrifield, 2000; Aguerri et al., 2009). In this case $S_{\rm bar}$ is given by

$$S_{\rm bar} = \frac{2}{\pi}[\arctan(1-\epsilon_{\rm bar})^{-1/2} - \arctan(1-\epsilon_{\rm bar})^{1/2}], \tag{1.15}$$

  where $\epsilon_{\rm bar}$ can be obtained modelling the shape of the bar with a photometric decomposition or analysing the ϵ radial profile, where the value of $\epsilon_{\rm bar}$ is identified in correspondence of the bar boundary. In this case, $S_{\rm bar}$ can vary from zero for an unbarred galaxy to one for a strong bar. For an elliptical bar with uniform surface brightness, this quantity represents the minimum fraction of bar stars that one would have to rearrange to transform the structure into an axisymmetric distribution.

- This definition of $S_{\rm bar}$ correlates with an other very famous formulation, the so-called $Q_{\rm t}$ parameter, which quantifies the maximum value of the ratio of the tangential force to the mean axisymmetric radial force in a barred galaxy (Combes & Sanders, 1981; Buta & Block, 2001b). It is defined as

$$Q_{\rm t}(R) = \frac{F_{\rm t}^{\rm max}(R)}{\langle F_{\rm r}(R)\rangle} \tag{1.16}$$

  where $F_{\rm t}^{\rm max}(R) = [\partial\Phi(R,\theta)/\partial\theta]_{\rm max}$ represents the maximum amplitude of the tangential force at radius R given the gravitational potential $\Phi(R,\theta)$ and $\langle F_{\rm r}(R)\rangle = R(d\Phi_0/dR)$ is the mean axisymmetric radial force at the same radius, derived from the $m=0$ component of the gravitational potential Φ_0. Although $Q_{\rm t}$ depends on radius, its maximum value can provide a single measurement of the strength of the bar for a whole galaxy, if the gravitational potential is known. So, Eq. 1.16 can be used to measure directly $S_{\rm bar}$ from the force field of the bar derived from an image (Buta & Block, 2001b).

- The strength of a bar can be also recovered using Fourier analysis. A first definition was used by Aguerri et al. (2000),

$$S_{\rm bar} = \frac{1}{R_{\rm bar}}\int_0^{R_{\rm bar}} \frac{I_2(r)}{I_0(r)}{\rm d}r, \tag{1.17}$$

  while a second definition is based on the peak of the $m=2$ relative component of the radial Fourier series, (Athanassoula & Misiriotis, 2002; Guo et al., 2019)

$$S_{\rm bar} = \max\Big(\frac{I_2(r)}{I_0(r)}\Big). \tag{1.18}$$

Aguerri et al. (2009) measured the mean values of $S_{\rm bar}$ using the $\epsilon_{\rm bar}$ method and found $\langle S_{\rm bar}\rangle = 0.16$ for SB0 galaxies, $\langle S_{\rm bar}\rangle = 0.19$ for SB0/a-SBb galaxies, and $\langle S_{\rm bar}\rangle = 0.20$ for SBc-SBm galaxies. The smaller value found in SB0 galaxies may be due to the presence of a large bulge influencing the correct evaluation of $\epsilon_{\rm bar}$. On the contrary, Menéndez-Delmestre et al. (2007) found larger values for the mean bar ellipticity: $\langle \epsilon_{\rm bar}\rangle = 0.54 \pm 0.13$ for SBa-SBb galaxies and $\langle \epsilon_{\rm bar}\rangle = 0.48 \pm 0.12$ for SBc-SBd galaxies, which are consistent within the uncertainties.

Since the different methodologies are connected to different properties of the bar, they can give considerably different results for the same object.

1.3.3 Bar pattern speed

The bar pattern speed $\Omega_{\rm bar}$ is the angular speed of the bar tumbling around the galaxy centre. $\Omega_{\rm bar}$ is usually parametrised by the bar rotation rate $\mathcal{R} = R_{\rm cr}/R_{\rm bar}$, where $R_{\rm cr}$ is the corotation radius, the galactocentric distance at which the stars and gas rotates at the same speed as quasi-static propagating density waves they belong to, in this case the bar. This is the place where the gravitational and centrifugal forces cancel out in the rest frame of the bar and it can be defined through the bar pattern speed as $\Omega_{\rm bar} R_{\rm cr} = V_{\rm circ}$, where $V_{\rm circ}$ is the circular velocity of the galaxy. When the rotation curve is flat, the corotation radius is derived as $R_{\rm cr} = V_{\rm circ}/\Omega_{\rm bar}$.

There are several methods developed to recover this important dynamical parameter, most of them require some modelling.

Indirect methods

- Rings are good indicators of galaxy resonances (Kormendy, 1979; Buta, 1995). Dynamical simulations show that nuclear rings are located near the ILR, the inner rings near corotation or near the ultra-harmonic resonance (UHR) while outer rings trace well the outer Lindblad resonance (OLR): these are the best candidates to derive $\Omega_{\rm bar}$. They can be analysed in barred galaxies through ultraviolet photometry (Jeong et al., 2007), even at intermediate redshift (Pérez et al., 2012). Building an extended galaxy mass model, it is possible to recover the circular velocity $V_{\rm circ}$ curve (and epicyclic frequency κ) and some other relevant frequencies (such as the ILR, OLR and UHR frequencies $\Omega_{\rm bar} \pm \kappa/2, \Omega_{\rm bar} - \kappa/4$). If a ring traces a Lindblad resonance, $\Omega_{\rm bar}$ can be found from the frequency diagram in correspondence of the radius of the ring (Fig. 1.12). Despite the simplicity of the method, it is not straightforward to correctly identify the nature and location of rings in galaxies.

- Font et al. (2011) developed a method to first recover $R_{\rm cr}$ of the galaxy, and hence derive $\Omega_{\rm bar}$. It is based on the phase change of the non-circular radial velocity vector observed across corotation. Using a bi-dimensional (2D) map of the LOS velocity obtained from gas, a mean rotation curve can be derived and used to build a 2D rotation velocity model. This is subtracted from the observed velocity field leaving the residuals of a projected non-circular velocity field. First of all, the residual field has to be cleaned

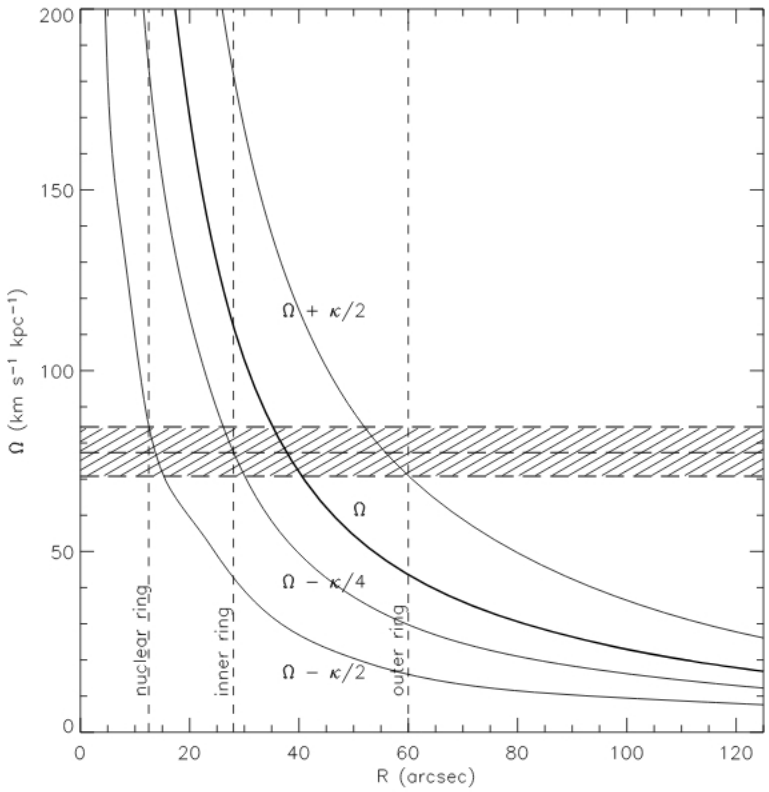

Figure 1.12: Frequency diagram of NGC 2974. The location of the nuclear, inner, and outer rings are shown (*dashed lines*). All three locations are used to define the range of possible bar pattern speeds and corresponding error (*dashed region*). From Jeong et al. (2007).

from null residual velocities, then an histogram is built, considering the points which contain a substantial change in LOS velocity, from inflow to outflow and viceversa, with respect to the galactocentric radius. The histogram allows to identify one or more peaks, corresponding to one or multiple corotation radii, respectively. Then comparing the resulting radii with the galaxy image, it is possible to assign a corotation radius to the bar feature (Fig. 1.13). The frequency curve obtained from the measured rotation curve of the galaxy allows to derive $\Omega_{\rm bar}$ from the corresponding $R_{\rm cr}$.

- An alternative method to directly recover $R_{\rm cr}$ is based on the analysis of the location of shock-induced star formation regions with respect to the spiral arms (Puerari & Dottori, 1997; Seigar et al., 2018). In fact, star formation produces an azimuthal gradient of stellar age across the spiral arms that has opposite signs on either side of $R_{\rm cr}$. A comoving observer will see a switch in the azimuthal order of young and old stars across the arm. A Fourier analysis of both blue and infrared images (corresponding to young and older disk stellar population) highlights the behaviour of the phase angles of the spiral density wave and shock front, respectively. The two phase angles intersect at $R_{\rm cr}$. The actual $R_{\rm cr}$ value corresponding to the bar has to be identified by inspecting the galaxy morphology (Fig. 1.14).

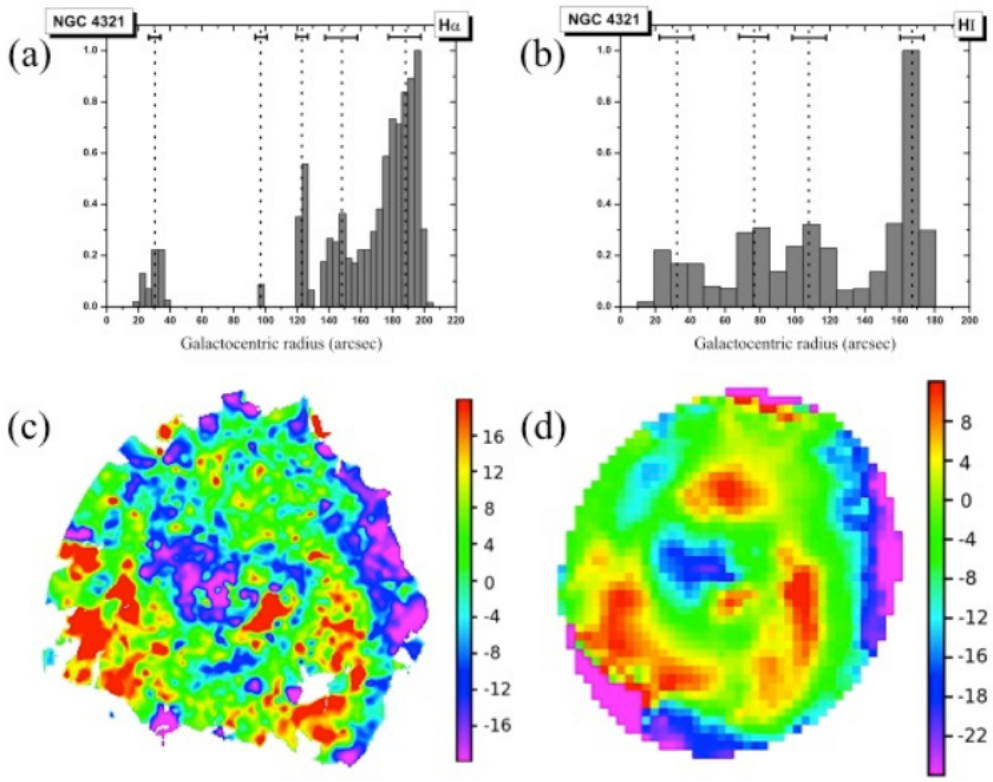

Figure 1.13: *Top panels*: normalised histograms of the density of sign changes in the residual velocity maps of NGC 4321 as a function of the radius in the galactic plane. *Bottom panels*: residual velocity maps. The normalised histograms and residual velocity maps are based on both the $H\alpha$ velocity field (*left panels*), and on HI velocity field (*right panels*). From Font et al. (2011).

- The comparison of the gas velocity and density field with dynamical models of gas flows can be applied to inclined galaxies (Fig. 1.15). To build the galaxy potential through the hydrodynamical model, it is necessary to add an axysimmetric component mainly derived from the observed rotation curve and a perturbing component derived from the surface brightness of the bar and spiral structure. In this way, many features of the gas morphology and kinematics can be reproduced. However, the results strongly depend on the modelled photometric and kinematic features and it is not always possible to find a unique solution for the best-fitting parameters, including $\Omega_{\rm bar}$ (Lindblad & Kristen, 1996; Lin et al., 2013).

- Athanassoula (1992) proposed to analyse the offset and shape of dust lanes to measure $R_{\rm cr}$, because they are indicative of the presence of a ILR. The author performed a hydrodynamical simulation of gas flow and observed, in the standard case, a low density of the gas in the bar region except for the centremost part and two narrow lanes offset from the bar major axis towards the leading side of the bar, where the gas accumulates. These high concentrations of gas are associated in real galaxies with dust lanes where

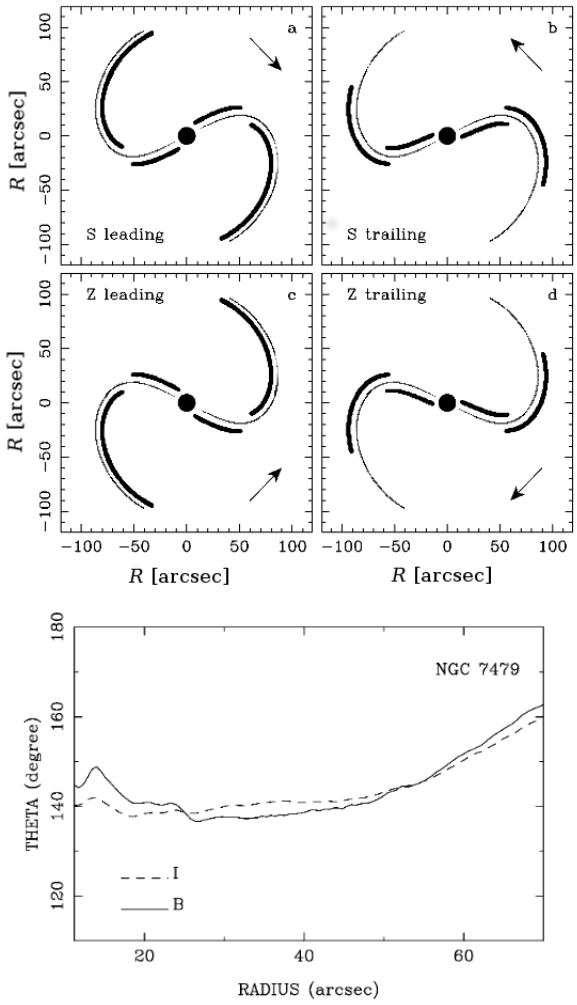

Figure 1.14: *Top panels*: the position of the shock front (*heavy line*) with respect to the density wave (*light line*) in different cases: leading, S-type (a); trailing, S-type (b); leading, Z-type (c); trailing, Z-type wave (d). The arrow in each panel indicates the sense of the disc rotation. *Bottom panel*: relative behavior of the two-armed phase in B- and I-bands. From Puerari & Dottori (1997).

shocks happen. These shocks are linked to the properties of the periodic orbits, since they form if the x_1 orbits have either loops or large curvature values at their apocentres. The shape of the shock loci depends on a number of parameters characterizing the bar and disc potentials, including $R_{\rm cr}$. In particular, an offset and leading dust lane on each side of the bar indicates the presence of an ILR near the centre of the bar, while a single, relatively straight, and continuous dust lane along the bar excludes the presence of an ILR. When this resonance is present, $\mathcal{R} < 1.2$, and $R_{\rm cr}$ is recovered. Moreover, straight offset dust lanes are associated to strong long bars and with no star formation, while inward curved offset dust lanes arise in weak fat bars, together with star formation. This method requires a careful study and a correct interpretation of the dust lanes

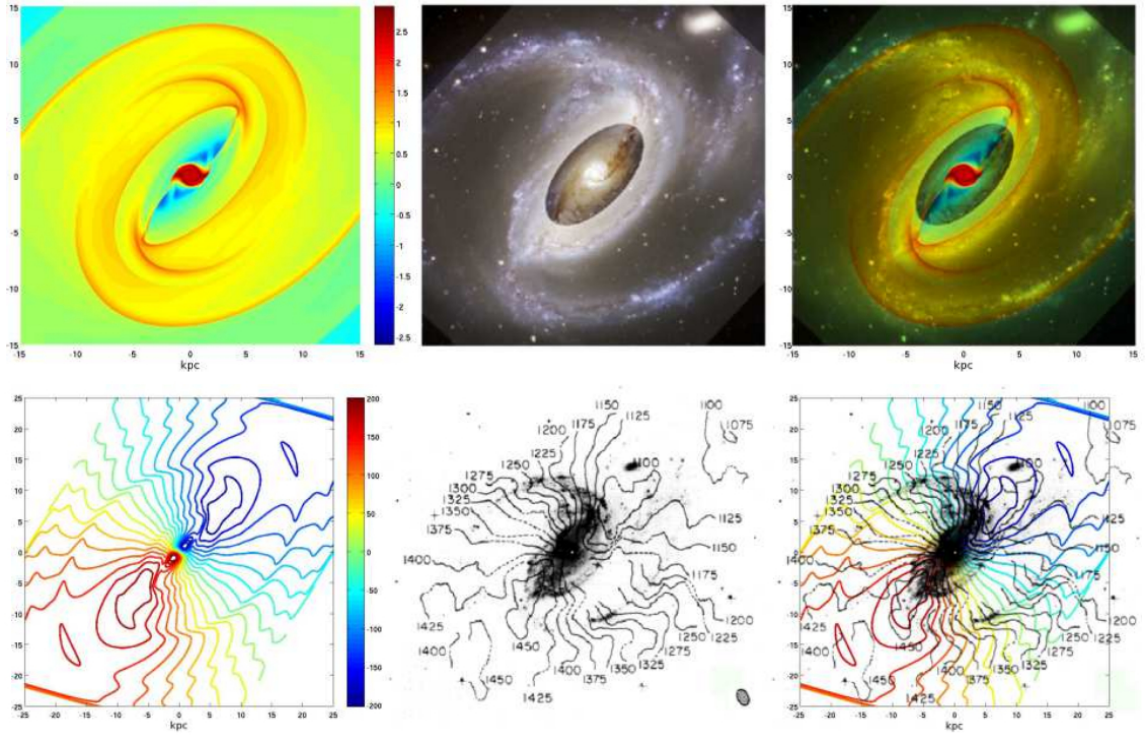

Figure 1.15: *Top panels*: simulated projected density distribution of NGC 1097 convolved with the synthesized beam of the HI column densities (*left panel*), optical image of the galaxy (*middle panel*), and the superposition of the two (*right panel*). *Bottom panels*: comparisons of simulated and observed velocity fields with isovelocity curves from the simulated velocity field (*left panel*) convolved with the synthetised beams of the HI observation, superimposed with the optical image (*middle panel*), and the superimposition of the two (*right panel*). From Lin et al. (2013).

(Fig. 1.16).

- A way to recover $R_{\rm cr}$ based on the phase shift between the density perturbation and potential in the presence of a bar was developed by Zhang & Buta (2007) using infrared images. When a bar perturbation is present, the phase shift changes from positive (density spirals lead potential spirals) inside corotation to negative (density spirals lag potential spirals) outside corotation. Given a surface mass-density map of a disc galaxy, one can convert the densities into a potential and directly measure the phase shift radial profile. This provides the location of the corotation resonance without kinematic data (Fig. 1.17). The method can lead to the identification of many $R_{\rm cr}$ so again the main difficulty is to identify the one corresponding to the bar perturbation.

- Finally, it is also possible to model the observed morphology of barred galaxies with N-body simulations (England et al., 1990; Aguerri et al., 2001; Weiner et al., 2001; Rautiainen et al., 2008). The gravitational potential of the galaxy can be derived from photometry, with a chosen value of mass-to-light ratio. In this case, $\Omega_{\rm bar}$ is derived

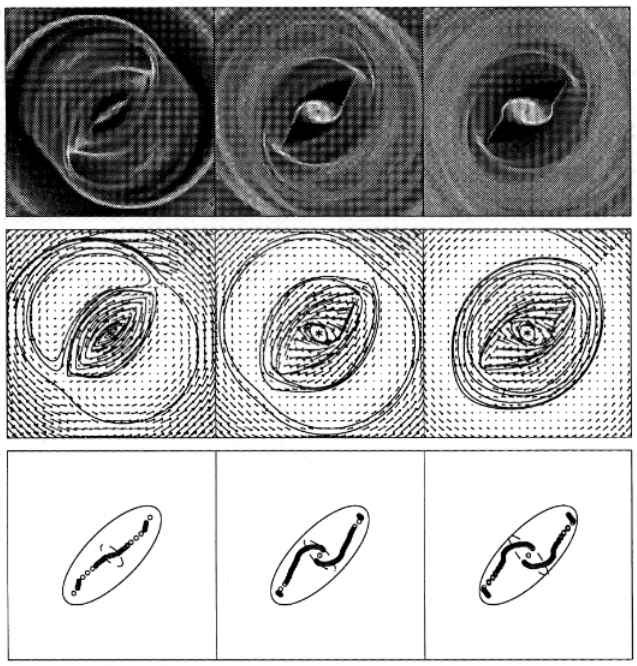

Figure 1.16: Gas responses for three models of a inhomogeneous bar with different bar radii and pattern speeds. Gas density (*top panels*), gas flow lines and velocity vectors (*middle panels*), and loci of the maximum values of the density (*bottom panels*) with the largest extension of the x_2 family orbits along the minor axis (*dashed lines*) are shown. From Athanassoula (1992).

from the response of gaseous and stellar disc particles to a rigidly rotating potential (Fig. 1.18).

The Tremaine-Weinberg method

Tremaine & Weinberg (1984, hereafter TW) developed a technique to recover $\Omega_{\rm bar}$ in a barred galaxy without using any dynamical model. With their approach, $\Omega_{\rm bar}$ is directly determined from observable quantities measured for a tracer population of stars or gas, which only has to satisfy the continuity equation. The simple idea is to observe the surface brightness and radial velocity of the tracer along apertures located parallel to the LON. When both position and velocity are measured with respect to the galaxy centre, then the luminosity-weighted mean velocity divided by the luminosity-weighted mean position, is equal to $\Omega_{\rm bar} \sin i$, where i is the disc inclination.

In its first application, the method was tested on a numerically simulated galaxy resulting in a reliable measurement of $\Omega_{\rm bar}$ with 15 per cent accuracy. Tremaine & Weinberg (1984) firstly tried to apply their method to HI gas data, but they were not able to obtain conclusive results, because the continuity equation required by the method was not respected by the gaseous tracer.

The TW method is based on three simple assumptions:

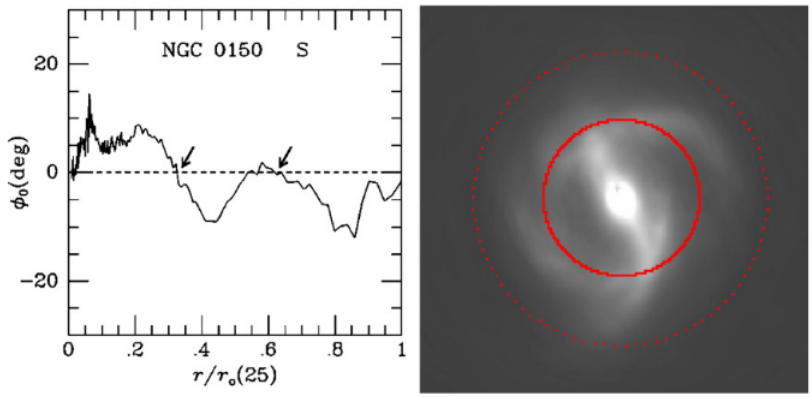

Figure 1.17: *Left panel*: phase-shift radial profile of NGC 150. The arrows represent the location of the corotation radii. *Right panel*: H-band image of the galaxy and the location of the corotation radii (*red circles*). From Buta & Zhang (2009).

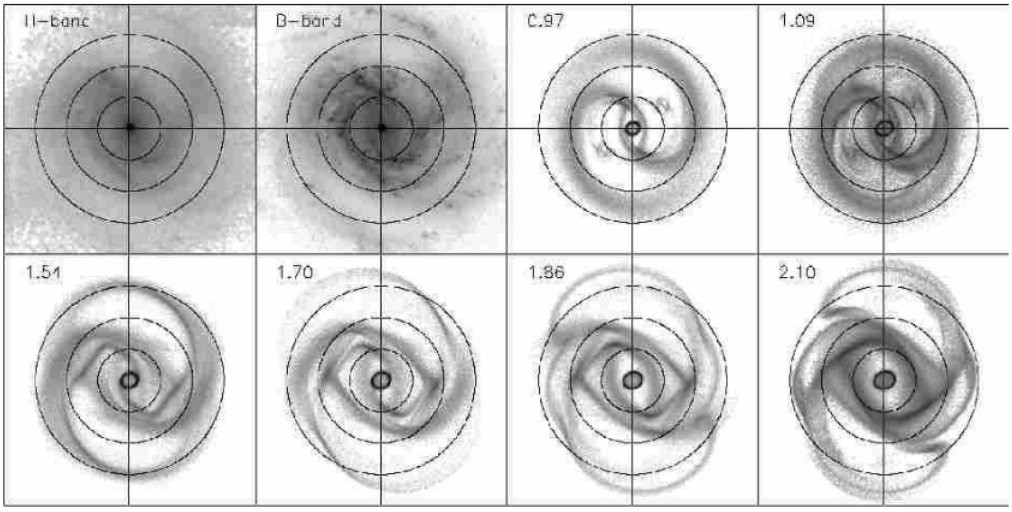

Figure 1.18: Different models corresponding to different bar pattern speed for NGC 4303. The first two frames show the deprojected images of the galaxy in H- and B-bands, while all the other show different simulations, consisting in a disc of collisionless stellar particles and inelastically colliding gas particles in a given potentials. The numbers indicate the corresponding ratio between corotation and bar radii. From Rautiainen et al. (2008).

- the disc of the galaxy is flat. For an infinitely thin disc, we assume (x, y) and (X, Y) to be the Cartesian coordinates in the galaxy and sky plane, respectively, with the origin in the galaxy centre and the abscissa axes located along the LON. A point (x, y) is projected onto the sky plane in $(X, Y) = (x, y \cos i)$, where i is the disc inclination. The same analysis can be repeated for a thick disc;

- the bar is characterised by a well-defined $\Omega_{\rm bar}$. The surface brightness profile of the tracer $\Sigma(x, y, t)$ is constant in a frame rotating with angular speed $\Omega_{\rm bar}$. Using the polar coordinates (r, ϕ), where $x = r \cos\phi$ and $y = r \sin\phi$, at any time t the surface brightness depends on (r, ϕ, t) only through r and $\phi - \Omega_{\rm bar} t$, because $\Sigma(x, y, t) = \hat{\Sigma}(r, \phi - \Omega_{\rm bar} t)$, where $\hat{\Sigma}$ is the time-dependent surface brightness in polar coordinates;

- the surface brightness of the tracer must obey the continuity equation. Moreover, the surface brightness must be proportional to the surface mass density of the tracer. The ideal tracer is a stellar component in absence of significant star formation and patchy dust obscuration, such as the old stellar population of SB0 galaxies. For spiral galaxies, it is possible to use HI observations, but it is necessary to exclude that it is transformed into molecular gas or stars as it rotates around the galaxy centre and that its surface brightness is reduced by large optical depth. When the continuity equation holds,

$$\frac{\partial \Sigma(x, y, t)}{\partial t} + \frac{\partial}{\partial x}[\Sigma(x, y, t) v_x(x, y, t)] + \frac{\partial}{\partial y}[\Sigma(x, y, t) v_y(x, y, t)] = 0, \tag{1.19}$$

where (v_x, v_y) is the mean velocity of the tracer at (x, y, t) measured relative to the rest frame of the disc. Even if the pattern speed is allowed to vary with radius within a galaxy, at a given radius it simply rotates around with time (Merrifield et al., 2006). The temporal derivative can be rewritten as

$$\frac{\partial \Sigma}{\partial t} = -\Omega_{\rm bar} \frac{\hat{\Sigma}}{\partial \phi} = \Omega_{\rm bar} \left(y \frac{\partial \Sigma}{\partial x} - x \frac{\partial \Sigma}{\partial y} \right), \tag{1.20}$$

and it can be substituted in Eq. 1.19 and integrated in x to eliminate the unobservable v_x component of velocity, leading to

$$\Omega_{\rm bar} y \int_{-\infty}^{+\infty} \frac{\partial \Sigma}{\partial x} dx - \Omega_{\rm bar} \int_{-\infty}^{+\infty} x \frac{\partial \Sigma}{\partial y} dx + \int_{-\infty}^{+\infty} \frac{\partial (\Sigma v_x)}{\partial x} dx + \int_{-\infty}^{+\infty} \frac{\partial (\Sigma v_y)}{\partial y} dx = 0. \tag{1.21}$$

The first and third terms vanish because $\Sigma(x, y, t) \to 0$ as $|x| \to \infty$. Integrating with respect to y from y to $+\infty$, we obtain

$$\Omega_{\rm bar} \int_{-\infty}^{\infty} \Sigma(x, y, t) x dx = \int_{-\infty}^{\infty} \Sigma(x, y, t) v_y(x, y, t) dx, \tag{1.22}$$

where the constant of integration is null because $\Sigma(x, y, t) \to 0$ as $|y| \to \infty$. In the sky

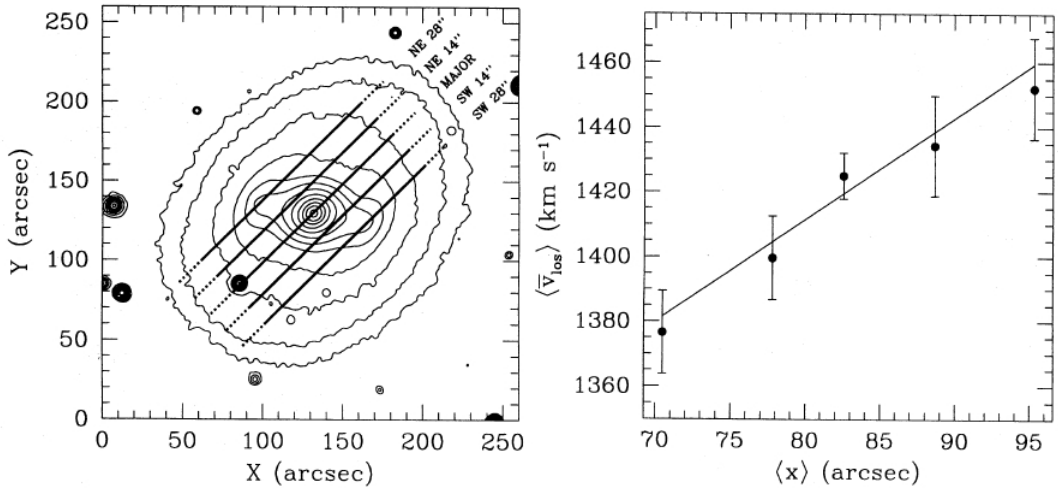

Figure 1.19: *Left panel*: contour plot of the I-band image of NGC 936, overlaid with the position of the slits defined *a priori* to performing the spectral observations. *Right panel*: kinematic and photometric integrals measured along the different slits, overlaid with the best-fitting line, which corresponds to the bar pattern speed. From Merrifield & Kuijken (1995).

plane, the radial velocity $V_{||} = v_y \sin i$ and so we get

$$\Omega_{\rm bar} \sin i \int_{-\infty}^{\infty} \Sigma(X,Y) X dX = \int_{-\infty}^{\infty} \Sigma(X,Y) V_{||}(X,Y) dX. \tag{1.23}$$

Multiplying both sides by an arbitrary odd weight function and integrating over Y

$$\Omega_{\rm bar} \sin i = \frac{\int_{-\infty}^{\infty} h(Y) dY \int_{-\infty}^{\infty} \Sigma(X,Y) V_{||}(X,Y) dX}{\int_{-\infty}^{\infty} h(Y) dY \int_{-\infty}^{\infty} \Sigma(X,Y) X dX}. \tag{1.24}$$

At this point, $\Omega_{\rm bar}$ is obtained in terms of observable quantities: i can be evaluated from an isophotal analysis in the disc region, the surface brightness distribution is known from optical photometry, and the velocity field is derived from long-slit spectroscopy (after have defined *a-priori* a reasonable number of slits) or from integral-field (IFU) spectroscopy (where the pseudo-slits can be defined *a posteriori*). Regardless of the observing techniques, the apertures (slits or pseudo-slits) have to be located parallel to the LON of the galaxy, one centred on the galaxy centre and the others offset by a distance Y_0. Figures 1.19 and 1.20 shows examples of the application of the TW method to long-slit and IFU spectroscopy, respectively.

The integration in X ranges over $-\infty \leq X \leq +\infty$, but it is sufficient to integrate over $-X_0 \leq X \leq X_0$ if the disc is axisymmetric at $|X| \geq X_0$. For a weight function $h(Y) = \delta(Y - Y_0)$, the integration in Y is performed over an arbitrary interval, even if it theoretically ranges over $-\infty \leq Y \leq +\infty$. Such a weight function corresponds to an aperture parallel to the disc major axis and offset by a distance Y_0. With these

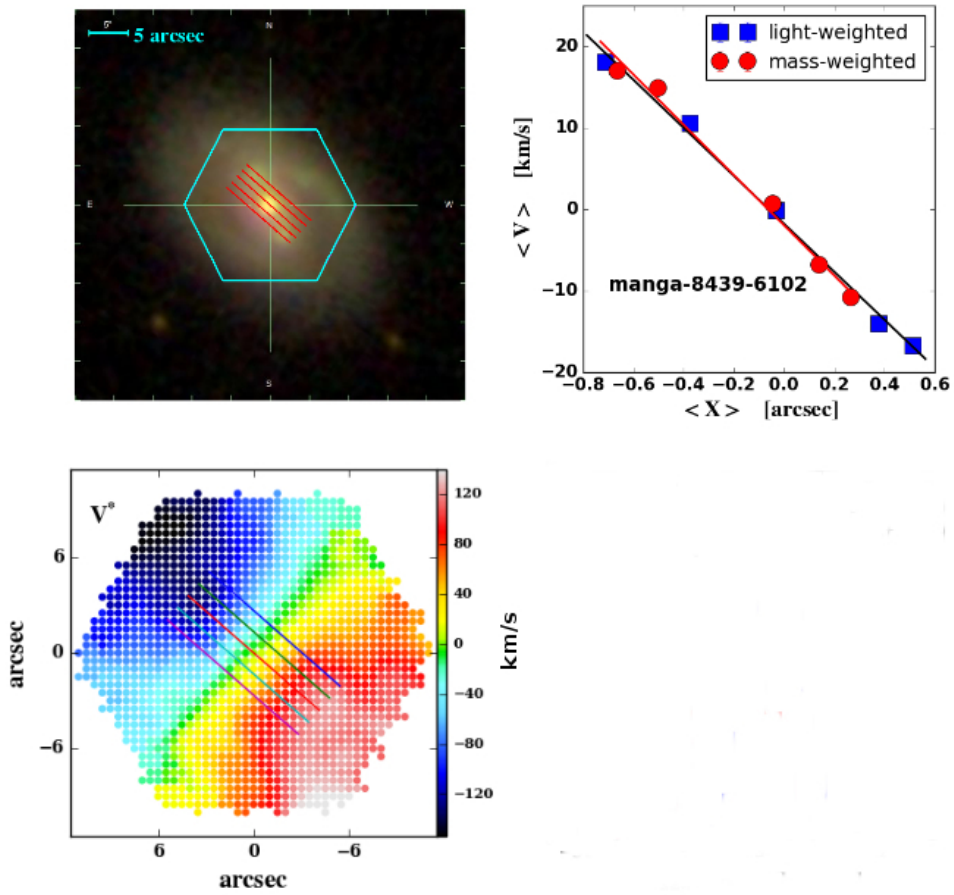

Figure 1.20: *Top-left panel*: SDSS $g + r + i$ combined image of the galaxy m̂anga-8439-6102. The MaNGA fibre bundle (*hexagon*), and the pseudo-slits defined *a posteriori* (*red lines*) are indicated. *Top-right panel*: light-weighted (*blue*) and mass-weighted (*red*) kinematic and photometric integrals measured along the different pseudo-slits. Superimposed is the best-fitting line, giving the bar pattern speed. *Bottom panel*: velocity map obtained from the MaNGA datacube with superimposed the location of the pseudo-slits. From Guo et al. (2019).

assumptions, it is possible to obtain an independent measurement of $\Omega_{\rm bar}$ for each aperture.

To build an odd weight function we use two slits offset by $\pm Y_0$, so $h(Y) = \delta(Y - Y_0) - \delta(Y + Y_0)$. The perturbations from axisymmetry are small in many galaxies. In this case,

$$\Sigma = \Sigma_{\rm a}(r) + \epsilon \sum_{m=-\infty}^{+\infty} \Sigma_m(r) e^{im(\phi - \Omega_{\rm bar} t)} \tag{1.25}$$

$$v = \Omega(r) r \hat{\phi} + \epsilon \sum_{m=-\infty}^{+\infty} (v_{rm} \hat{r} + v_{\phi m} \hat{\phi}) e^{im(\phi - \Omega_{\rm bar} t)}, \tag{1.26}$$

where $\Omega(r)$ is the circular angular speed at radius r, $\hat{r}$ and $\hat{\phi}$ are the radial and azimuthal unit vectors, the integer m is the azimuthal wavenumber, and $0 < \epsilon \ll 1$. If we substitute Eq. 1.26 in Eq. 1.24 while neglecting all factors of order ϵ^2, and with an odd weight function in Y, then the perturbations with odd values of m do not contribute to the integrals on the right-hand side of Eq. 1.24. Since the bar is characterised by an even m value, an odd weighting function eliminates any contamination from independent perturbations with odd m and possibly different pattern speeds.

Merrifield & Kuijken (1995) refined the TW method, normalising both the numerator and denominator of the right-hand side of Eq. 1.24 with the total luminosity in the aperture. The TW method then simply reduces to

$$\Omega_{\rm bar} \sin i = \frac{\langle V \rangle - V_{\rm sys}}{\langle X \rangle - X_{\rm C}}, \tag{1.27}$$

where

$$\langle X \rangle = \frac{\int_{-\infty}^{\infty} h(Y) dY \int_{-\infty}^{\infty} \Sigma(X,Y) X dX}{\int_{-\infty}^{\infty} h(Y) dY \int_{-\infty}^{\infty} \Sigma(X,Y) dX} \tag{1.28}$$

is the luminosity-weighted mean of the position of the tracer, while

$$\langle V \rangle = \frac{\int_{-\infty}^{\infty} h(Y) dY \int_{-\infty}^{\infty} \Sigma(X,Y) V_{||}(X,Y) dX}{\int_{-\infty}^{\infty} h(Y) dY \int_{-\infty}^{\infty} \Sigma(X,Y) dX} \tag{1.29}$$

is the luminosity-weighted LOS velocity of the tracer, $(X_{\rm C}, Y_{\rm C})$ is the position of the galaxy centre, and $V_{\rm sys}$ is the systemic velocity. When the centre and $V_{\rm sys}$ are known, Eq. 1.27 further simplifies and becomes

$$\Omega_{\rm bar} \sin i = \frac{\langle V \rangle}{\langle X \rangle}. \tag{1.30}$$

In particular, $\langle V \rangle$ can be obtained collapsing the data along the spatial direction in each aperture and measuring the LOS velocity from the single high S/N one-dimensional (1D) spectrum. Since the resulting spectral line profiles are significantly asymmetric, reflecting the distribution of $V_{||}(X,Y)$ along the aperture, it is necessary to measure also the broadening function of the spectral lines.

Even if optical observations are limited by seeing effects, $\Omega_{\rm bar}$ obtained with the TW method is not biased by low resolution (Zou et al., 2019). In fact, the observed surface brightness $\Sigma_0(X,Y)$ and velocity fields $V_0(X,Y)$ are related to the real surface brightness and velocity by a convolution with the point spread function $W(X,Y)$:

$$\Sigma_0(X,Y) = \int W(X-X',Y-Y')\Sigma_0(X',Y')dX'dY' \qquad (1.31)$$

$$\Sigma_0(X,Y)V_0(X,Y) = \int W(X-X',Y-Y')\Sigma_0(X',Y') \times V_{||}(X',Y')dX'dY'. \qquad (1.32)$$

As long as $W(X,Y)$ is an even function of X, Eq. 1.24 is still valid when Σ and $V_{||}$ are replaced by $\Sigma_0(X,Y)$ and $V_0(X,Y)$. Moreover, Eq. 1.24 is valid also in the thick disc case, as long as the net streaming velocity perpendicular to the disc plane is zero.

Sources of errors in the TW method

Despite its simple formulation and lack of modelling dependence, the TW method suffers from different sources of errors. The main problems can be related to the identification of the galaxy centre and measure of the galaxy systemic velocity, low S/N ratios of the spectra, limited number of apertures and their misalignment with respect to the disc major axis, and the presence of spurious elements (such as stars, strong spiral arms and/or asymmetric structure within the apertures) in the galaxy discs.

First of all, to successfully apply the TW method, the galaxies should satisfy some requirements. They should have an intermediate inclination and their bars should be elongated at an intermediate PA between the disc major and minor axes. Low-inclination galaxies are characterised by small stellar velocities, large relative velocity errors, and a large uncertainty on the disc PA, while highly-inclined galaxies makes it difficult to identify the bar and locate the apertures. A bar aligned with the disc major axis gives $\langle X \rangle = 0$ arcsec, while a bar aligned with the disc minor axis is characterised by $\langle V \rangle = 0$ km s^{-1}, according to Eqs. 1.28 and 1.29.

The determination of the galaxy centre (X_C, Y_C) and systemic velocity V_{sys} is required for the determination of Ω_{bar} (Eq. 1.27). This issue can be solved by a smart choice of the weighting function. Since barred galaxies are nearly point-symmetric around their centres, it is convenient to choose a weighting function which is odd in Y. In fact, the application of the TW method is insensitive to centring errors if the weighted total luminosity $L = \int_{-\infty}^{\infty} h(Y)dY \int_{-\infty}^{\infty} \Sigma(X,Y)dX$ is null. In long-slit spectroscopy this problem reduces to identify a reference position and velocity frame common to all the slits, which however is not always straightforward. In IFU spectroscopy the centring errors are minimized by the unambiguous determination of the common reference frame, which allows to know the exact position at which the velocity and surface brightness of the tracer are measured.

The values of $\langle X \rangle$ and $\langle V \rangle$ represent differences of luminosity and velocity across $X = 0$, respectively, and their estimation is affected by the noise of the data. The S/N ratio of the spectral data can be increased by collapsing a long-slit spectrum along its spatial direction (Merrifield & Kuijken, 1995), or by co-adding all the spectra within a pseudo-slit (Debattista & Williams, 2004; Aguerri et al., 2015). This produces a single 1D spectrum with a high S/N ratio. Broad-band luminosity profiles have higher S/N ratios than luminosity profiles derived from spectra, particularly at large radii (Aguerri et al., 2003). In this case, the

luminosity profiles have to be extracted exactly at the same location, sampling and resolution as the spectra. The advent of IFU spectroscopy allows to increase the S/N of the spectra by rebinning adjacent spaxels.

The most critical point of the TW application consists in the determination of the PA of the disc major axis (corresponding to the LON), parallel to which the apertures have to be located (Debattista, 2003; Zou et al., 2019). Debattista (2003) investigated the maximum permitted misalignment between the PA of the apertures and the real PA of the galaxy disc. The result depends on the galaxy inclination and bar orientation with respect to the LON. A misalignment of 1° to 4° leads to $\Delta\Omega_{\rm bar}/\Omega_{\rm bar} = 0.3$. Galaxies with an inclination of about 60° and the bar oriented at about 20° from the LON are less sensitive to misalignment (Fig. 1.21).

Gerssen & Debattista (2007) studied the effects of dust obscuration and star formation on the stellar-based TW measurements with numerical simulations. They found that $\Delta\Omega_{\rm bar}/\Omega_{\rm bar} = 0.05$ for a diffuse disc of dust with a typically observed value of extinction $A_{\rm V} = 3$. Adopting an unrealistically large $A_{\rm V} = 8$ leads to $\Delta\Omega_{\rm bar}/\Omega_{\rm bar} = 0.15$. Moreover, prominent dust lanes are typically observed in barred galaxies, and they tend to enlarge the measured value of $\Omega_{\rm bar}$ if the position angle difference of the bar with respect to the disc major axis is $\Delta{\rm PA} > 0°$ and decrease it when $\Delta{\rm PA} < 0°$. For a dust lane with $A_{\rm V} = 3$ $0.08 < \Delta\Omega_{\rm bar}/\Omega_{\rm bar} < 0.25$ (Fig. 1.22). Performing near-infrared spectroscopy may help to minimise the effects of dust obscuration. Moreover, the effect of star formation does not change this conclusion, so it is possible to extend the application of the TW method to the stellar component of late-type barred galaxies, after carefully avoiding and/or masking the region affected by these spurious elements (Aguerri et al., 2015).

Extra structures in the discs, such as outer rings, spiral arms, and/or non-axisymmetric discs, may affect the results of the TW method. For example, a warp in the disc represents a non-axisymmetric disturbance with null pattern speed. Since the warp is located in the outer parts of the disc, while the bar lives in the inner region, it is possible to take into account its effect by excluding the outer region of the disc from the analysis. A preliminary analysis of high-quality imaging is mandatory, in order to identify and discard target galaxies with extra structures.

The accuracy of $\Omega_{\rm bar}$ depends on the number of the observed apertures, since its value can be derived from the slope of the linear relation between the integrals. The number of slits is fixed and usually small (up to 5) in long-slit spectroscopy. The situation is improved by IFU spectroscopy, which allows to optimise *a posteriori* the number and orientation of the pseudo-slits extraction.

An assessment of the impact of disc ellipticity (Ryden, 2004; Rodríguez & Padilla, 2013) on TW measurements is still missing.

Due to the increasing importance of IFU data, Zou et al. (2019) explored potential limitations, biases, and uncertainties associated with TW measurements based on these data with an N-body simulation of a barred disc galaxy. The authors created a series of mock datasets varying the properties of the galaxy (PA of the disc, PA of the bar with respect to the disc axes, disc i), and of the pseudo-slits (width, spatial resolution and binning, PA misalignment). They claimed the importance of testing the convergence of the integrals to

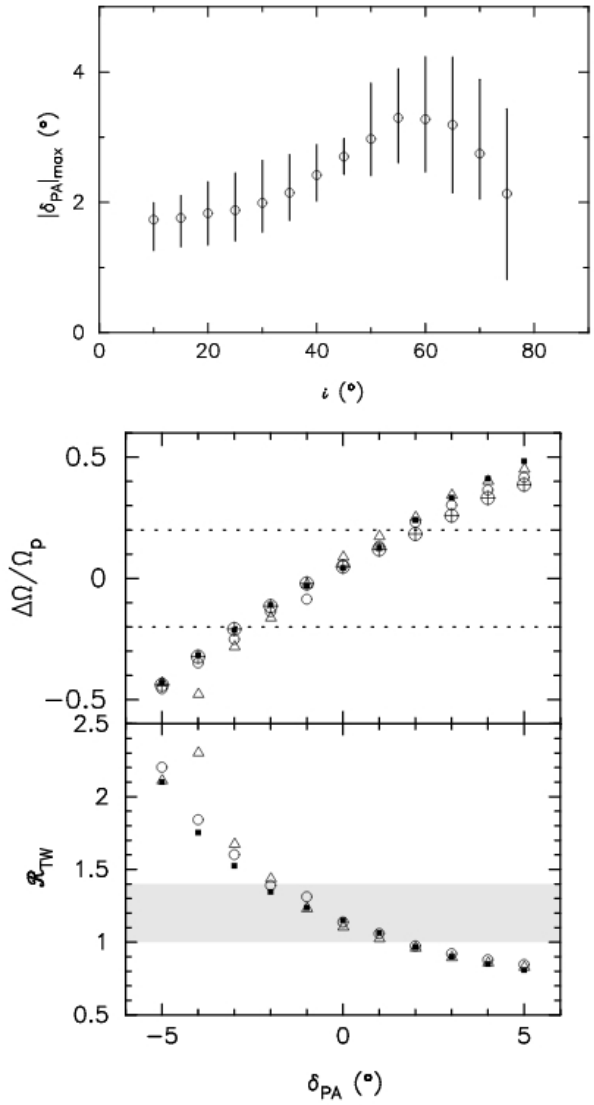

Figure 1.21: *Top panel*: maximum permitted error in the disc PA as a function of disc i, required to have $\Omega_{\rm bar}$ accurate to 30 per cent. The bar PA with respect to the disc major axis is allowed to vary in the range between 15° and 75°. The circles represents the mean values of error in PA and the error bars indicate the extreme cases. *Bottom panels*: $\Delta\Omega_{\rm bar}/\Omega_{\rm bar}$ and ratio between $R_{\rm cr}$ and $R_{\rm bar}$ as a function of the errors in the disc PA, for a given $i = 45°$. Different values of the bar PA (30° - *circles*, 45° - *triangles*, and 60° - *filled squares*) are presented. Errors of 20 per cent are shown (*dotted lines*). From Debattista (2003).

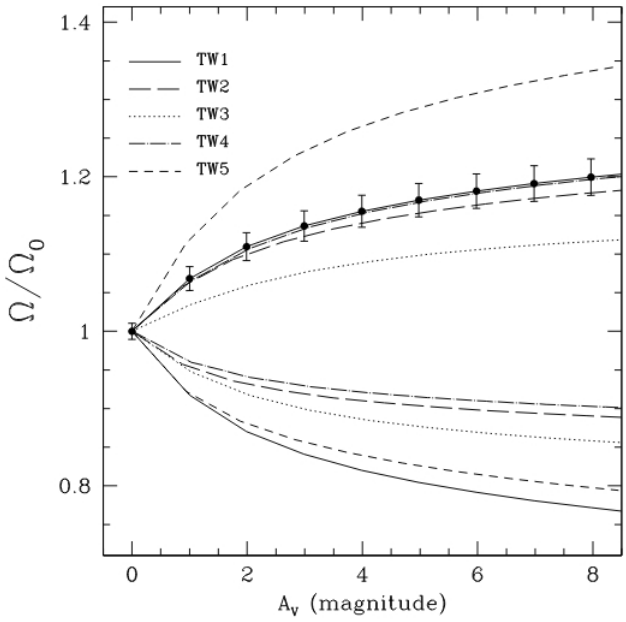

Figure 1.22: Ratio between the observed bar pattern speed and the intrinsic one, as a function of dust face-on extinction A_V for different N-body models. For each model, two curves are shown: a ratio greater than one corresponds to a bar PA $= +45°$, while a ratio lower than one corresponds to a bar PA $= -45°$. The different line types correspond to models with various morphologies and pattern speeds but with the same dust lane geometry and dust distribution. From Gerssen & Debattista (2007).

a constant value which help to identify the minimum length to be adopted to define the pseudo-slits and to exclude PA misalignment and/or presence of spurious elements affecting the accuracy of the TW measurements. Moreover, only pseudo-slits located within the bar region yield accurate $\Omega_{\rm bar}$ measurements, so it is better to exclude apertures near the ends of the bar. Irregularly-shaped apertures have to be avoided, rather it is better to recast the data and define perfectly rectangular pseudo-slits. Finally, the pseudo-slit width does not affect TW measurements significantly, unless it is smaller than the seeing, neither the spatial resolution of the observations itself.

The TW method was first applied with long-slit spectroscopy (see Corsini, 2011, for a review). More than ten $\Omega_{\rm bar}$ estimates were obtained with typical uncertainties of ~ 30 per cent and mainly on early-type disc galaxies.

The advent of IFU spectroscopy allowed to reduce the uncertainties and enlarge the sample of TW measured $\Omega_{\rm bar}$ (Aguerri et al., 2015; Guo et al., 2019). The method was applied to late-type galaxies too. This required to address the effects of dust and spurious elements, such as star-forming regions and/or other galaxy components.

Gaseous tracers

The application of the TW method to gas tracers rather than stars requires more caution. Different gas phases are usually present in galaxies (molecular, atomic, and ionized gas), and each phase may not obey the continuity equation. However, the gas in the dominant phase may approximately satisfy it. So far, examples of successful $\Omega_{\rm bar}$ measurements have been carried out using observations of CO (Rand & Wallin, 2004; Zimmer et al., 2004), HI (Bureau et al., 1999; Banerjee et al., 2013), and HII (Chemin & Hernandez, 2009; Beckman et al., 2011).

Beckman et al. (2011) applied the TW method using a Fabry-Perot spectrometer to get both the maps of surface brightness and velocity of the gas with Hα emission in 10 objects. The advantage to use this kind of instrument is to be able to map an extended source in a single emission line and to obtain a well-suited velocity map from which it is possible to extract tens of pseudo-slits. However, it is still necessary to use a surface brightness map from a component which obeys the continuity equation and to carefully deal with a complicated velocity field, which is on one hand globally dominated by the large-scale gravitational potential, but on the other hand locally dominated by specific effects of the flows around massive star-forming regions, and large-scale shocks. To solve the continuity problem, Beckman et al. (2011) used the stellar continuum information associated with each pixel of the Hα image. Nevertheless, it is not possible to avoid gas motions which do not correspond to the density wave pattern: the gas motions are globally associated with the bar, together with streaming motions associated with the arms, which are symmetric and cancel out in the TW integration, but locally they are due to the expanding features given by winds and supernovae around OB associations. Since these motions are close to isotropic in the plane of the galaxy, they do not cause major perturbations to the TW integrals. A similar analysis was performed by Chemin & Hernandez (2009) on the low surface brightness spiral galaxy UGC 628 (Fig. 1.23).

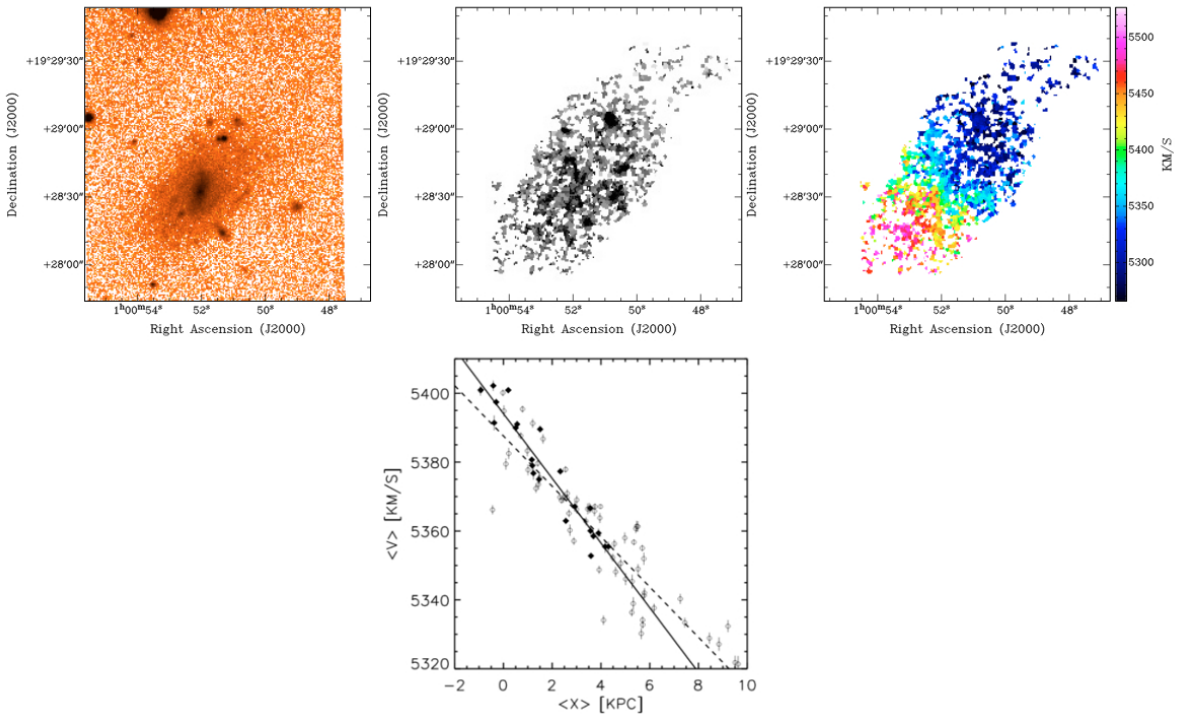

Figure 1.23: *Top panels*: R-band image of UGC 628, Hα integrated emission map, and LOS velocity map. *Bottom panel*: photometric and kinematic integrals and best-fitting lines corresponding to the pattern speed of the bar (*filled symbols* and *line*) and of the arms (*open symbols* and *line*). From Chemin & Hernandez (2009).

1.3.4 Corotation radius and bar rotation rate

The pattern speed $\Omega_{\rm bar}$ is the fundamental dynamical property of a bar because it controls the orbit distribution, gas infall rate, locations of resonances, and constrains the bar formation and dark matter (DM) content.

Given a star rotating on an almost circular orbit, with an angular frequency Ω and a radial frequency κ, for small oscillations Ω and κ are related by

$$\kappa^2 = 4\Omega^2 + R\frac{d\Omega^2}{dR}. \tag{1.33}$$

When a perturbation with pattern speed $\Omega_{\rm p}$ is introduced, the tangential frequency of the star in the rest-frame of the perturbation becomes $\Omega - \Omega_{\rm p}$ while the radial frequency is κ. For a bar perturbation ($\Omega_{\rm p} = \Omega_{\rm bar}$), the star overtakes the bar (i.e., it rotates in the same sense as the bar in the bar rest-frame) if $\Omega - \Omega_{\rm p} > 0$, while the bar overtakes the star (i.e., the star rotates in the opposite sense to the bar) if $\Omega - \Omega_{\rm p} < 0$.

In the rest-frame of the bar, a resonance occurs when the star completes an integer number of radial oscillations for each time it goes once around the perturbation. The simple case is when both the star and the bar have the same angular frequency, in this case $\Omega - \Omega_{\rm p} = 0$ and the resonance is called corotation. A bar-like perturbation has a symmetry given by $m = 2$.

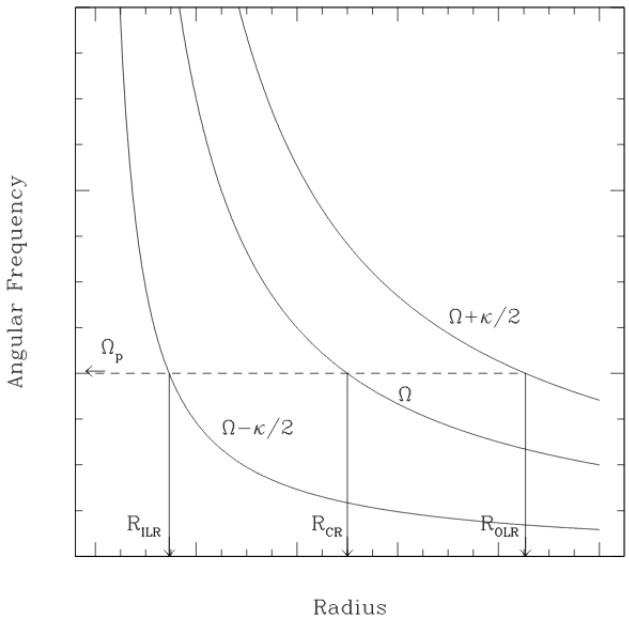

Figure 1.24: Angular frequencies in arbitrary units for a flat rotation curve. The corotation resonance, ILR and OLR are marked. From Canzian (1998).

The interesting case is when the star completes two radial oscillations for each time it goes around the bar (Fig. 1.24). When the star overtakes the bar,

$$\Omega_{\rm p} = \Omega - \frac{1}{2}\kappa. \tag{1.34}$$

This corresponds to the ILR. When the bar overtakes the star,

$$\Omega_{\rm p} = \Omega + \frac{1}{2}\kappa, \tag{1.35}$$

and this is the outer Lindblad resonance (OLR).

The distance-independent ratio between $R_{\rm cr}$ and $R_{\rm bar}$, which is the bar rotation rate $\mathcal{R} \equiv R_{\rm cr}/R_{\rm bar}$, is used to parametrise $\Omega_{\rm bar}$ and requires the knowledge of the circular velocity of the galaxy $V_{\rm circ}$, since $R_{\rm cr}$ is the ratio between $V_{\rm circ}$ and $\Omega_{\rm bar}$ and can be recovered with several methods presented in Sec. 1.3.3.

The asymmetric drift equation (Binney & Tremaine, 2008) allows to derive $V_{\rm circ}$ from the measured stellar kinematics in the disc region (Debattista et al., 2002; Aguerri et al., 2003, 2015). The measured LOS stellar velocity and velocity dispersion can be described as

$$v_{\rm stars} = \sqrt{V_{\rm circ}^2 + \sigma_R^2 \left[1 - \frac{\sigma_\theta^2}{\sigma_R^2} - R\left(\frac{1}{h} + \frac{2}{a}\right)\right]} \cos\theta \sin i \tag{1.36}$$

$$\sigma_{\rm stars} = \sigma_R \sqrt{\sin^2 i \left[\sin^2\theta + \frac{\sigma_\theta^2}{\sigma_R^2}\cos^2\theta\right] + \frac{\sigma_{0,z}^2}{\sigma_{0,R}^2}\cos^2 i}, \tag{1.37}$$

where (r, ϕ) and (R, θ) are the polar coordinates defined on the sky and galactic plane with respect to the LON, respectively. The coordinates are related through the equations

$$R = r\frac{\cos\phi}{\cos\theta} \tag{1.38}$$

$$\theta = \arctan\frac{\tan\phi}{\cos i}, \tag{1.39}$$

while h and i are the scalelength and inclination of the disc, respectively, and can be estimated for example with a photometric decomposition including the disc component (see Sec. 1.3.1), while the three components of the velocity dispersion are assumed to have exponential radial profiles with the same scalelength a but different central values $\sigma_{0,R}$, $\sigma_{0,\theta}$, and $\sigma_{0,z}$, respectively

$$\sigma_R = \sigma_{0,R}e^{-\frac{R}{a}} \tag{1.40}$$

$$\sigma_\theta = \sigma_{0,\theta}e^{-\frac{R}{a}} \tag{1.41}$$

$$\sigma_z = \sigma_{0,z}e^{-\frac{R}{a}} \tag{1.42}$$

where the axial ratios of the velocity ellipsoid are $(\sigma_\theta/\sigma_R, \sigma_z/\sigma_R) = (\sigma_{0,\theta}/\sigma_{0,R}, \sigma_{0,z}/\sigma_{0,R})$, implying its shape does not change with radius.

Adopting some reasonable assumptions, it is possible to describe the measured LOS stellar kinematics using Eq. 1.36 and 1.37 and to recover $V_{\rm circ}$ as free parameter of the problem. In fact, the circular velocity can be parametrised with a power law

$$V_{\rm circ} = V_0 R^\alpha. \tag{1.43}$$

Finally, it is possible to assume the epicyclic approximation ($\sigma_\theta/\sigma_R = \sqrt{0.5(1+\alpha)}$) and a value of σ_z/σ_R between 0.86 and 0.27 depending on the morphological type (Gerssen & Shapiro Griffin, 2012; Aguerri et al., 2015).

The asymmetric drift correction is not needed to recover $V_{\rm circ}$, when gas kinematics is available, for example in late-type galaxies. In fact, gas is generally a dynamically cold tracer and in such case its rotation curve can be directly modelled, for example with Eq. 1.43 (Leung et al., 2018).

A different approach to recover $V_{\rm circ}$ is based on complete dynamical modelling. Leung et al. (2018) and Guo et al. (2019) built Jeans axisymmetric dynamical (JAM) models, following the prescription of Cappellari et al. (2013a).

As far as the value of $\mathcal{R}$ is concerned, dynamical arguments show that if $\mathcal{R} < 1.0$, the stellar orbits are elongated perpendicular to the major axis of the bar and it dissolves (Contopoulos & Papayannopoulos, 1980; Contopoulos, 1981). Bars with $1.0 \leq \mathcal{R} \leq 1.4$ end close to corotation and rotate as fast as they can, whereas bars with $\mathcal{R} > 1.4$ fall short of corotation and are termed slow (Fig. 1.25). The dividing value at 1.4 between long/fast and short/slow bars is given by consensus (Athanassoula, 1992; Debattista & Sellwood, 2000) and it does not imply a specific value of the pattern speed. The definition of $\mathcal{R}$ was introduced by Elmegreen (1996),

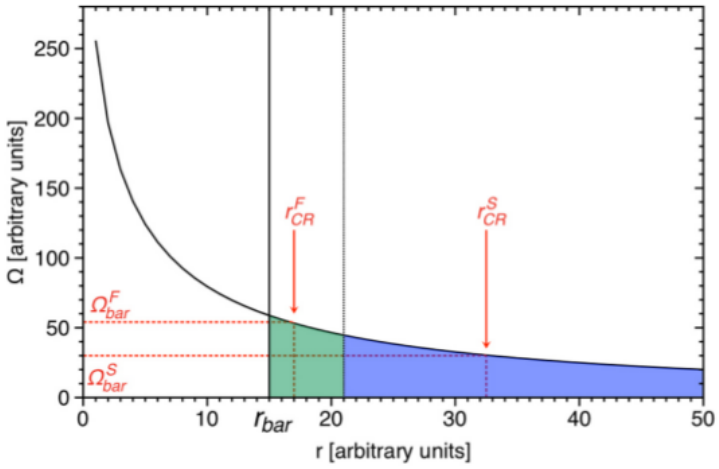

Figure 1.25: Schematic representation of fast versus slow bars: frequency curve for a given flat circular velocity curve. The bar length (*solid vertical line*), and the critical radius defined as 1.4 times the bar length are indicated (*dotted vertical line*). It separates the fast rotator range (*green*) from the slow rotator range (*blue*). Two possible corotation radii and their corresponding pattern speeds are marked as well (*red*). From Font et al. (2017).

to show how bars commonly end inside corotation, possibly between the 4:1 resonance and corotation. The bar-spiral transition does not occur at corotation, so the spiral arms extend for a significant distance inside corotation.

Both analytical work (Weinberg, 1985) and numerical simulations (e.g., Little & Carlberg, 1991; Debattista & Sellwood, 1998; O'Neill & Dubinski, 2003; Villa-Vargas et al., 2010; Athanassoula et al., 2013) show that $\Omega_{\rm bar}$ decreases with time as a consequence of the angular momentum exchange within the galaxy and the dynamical friction exerted on the bar by the DM halo. In both cases, a massive and centrally-concentrated DM halo causes a slow down of the bars because there is more mass ready to absorb angular momentum near the resonances and the dynamical friction is more efficient (see also Athanassoula 2014 and Sellwood 2014 for further discussion). This allowed Debattista & Sellwood (2000) to put tight constraints on the DM distribution of barred galaxies and argue that galaxies hosting fast bars should be embedded in DM halos with a low central density, such as those required for maximum discs. Moreover, other galaxy parameters, such as the halo triaxiality, the presence of gas, and the disc velocity dispersion influence the angular momentum exchange within the galaxy (Athanassoula, 2003; Athanassoula et al., 2013). These make the measurement of the rotation rates of bars highly desirable, not only to investigate the secular evolution of barred galaxies, but also to test whether the measured DM distribution matches that predicted by cosmological simulations in the cold DM framework (Navarro et al., 1996; Moore et al., 1998; Zasov et al., 2017).

Around 80 galaxies have been analysed so far with the TW method, each providing an estimate for $\mathcal{R}$. Neglecting measurements with large uncertainties, ~ 90 per cent of the bars are consistent with the fast regime at 95 per cent confident level. These galaxies have little DM in their central regions, confirming the hypothesis of maximum disc, derived from the

study of rotation curves in unbarred galaxies (Debattista & Sellwood, 2000; Starkman et al., 2018). The remaining 10 per cent have $\mathcal{R} < 1.0$ at 95 per cent confident level. Collecting both literature data (Corsini, 2011) and adding 15 galaxies from the CALIFA survey (Walcher et al., 2014), Aguerri et al. (2015) analysed a sample of 32 galaxies with a large range of galaxy morphology with the TW method. They found a mean value of $\langle\mathcal{R}\rangle \sim 1.0$, and no trend with the Hubble type, concluding that both early- and late-type barred galaxies host fast bars. More recently, Guo et al. (2019) analysed 51 objects from the Mapping Nearby Galaxies at Apache Point Observatory survey (MaNGA, Bundy et al., 2015). The authors did not find any correlation between $\mathcal{R}$ and the analysed galaxy properties, such as the DM fraction inside the effective radius, stellar age and metallicity, and $S_{\rm bar}$. They claimed to be prevented to find any correlation since the bar slowdown process and angular momentum exchange involve many factors.

Bars with $\mathcal{R} < 1.0$ are termed 'ultrafast' and are theoretically unexpected. Buta & Zhang (2009) first observed a non-negligible fraction of ultrafast bars, when applying an alternative indirect method to measure $\Omega_{\rm bar}$. Concerning the TW results, ultrafast bars appear to be mainly in late-type galaxies, which are more difficult to study with this method because of dust, spiral arms and gas. Using N-body simulations, Zou et al. (2019) suggested ultrafast bars can result in TW analysis when the angle between the bar and the assumed disc PA is overestimated, when the bar is too close to the disc minor axis, and/or if the FOV is too small to reach the convergence of the integrals.

Guo et al. (2019) identified one bar with high probability to be ultrafast, but they thought it could result from errors introduced by a number of approximations and hypotheses in measuring $\Omega_{\rm bar}$ and $R_{\rm bar}$.

Rautiainen et al. (2008) collected $\mathcal{R}$ measurements from the literature based on indirect methods. In contrast to the TW method, these results showed that while early-type barred galaxies always host fast bars, late-type barred galaxies can have both slow and fast bars. However, $\mathcal{R}$ based on indirect methods are face values, often lacking solid error estimates (Rautiainen et al., 2008, Fig. 1.26).

1.4 Life cycle of bars

Galactic stellar bars are evolving systems which play an active role in their own evolution. As bars are born, they also die. Indeed unbarred galaxies either did not have time yet to develop a bar, or they hosted one in the past which is now dissolved (Friedli, 1999).

1.4.1 Bar formation

The formation of a bar in an isolated galaxy is generally attributed to internal processes and typically includes three main phases: the initial growth, subsequent buckling, and final secular evolution (e.g. Hohl, 1971; Noguchi, 1987; Sellwood, 1981; Toomre, 1981; Raha et al., 1991; Debattista et al., 2006; Combes, 2008; Athanassoula et al., 2013; Martinez-Valpuesta et al., 2017). The bar growth takes ~ 2 Gyr, at the end of which a clear non-axysimmetric stellar structure stands out in the disc. Then the bar can experience the buckling phase,

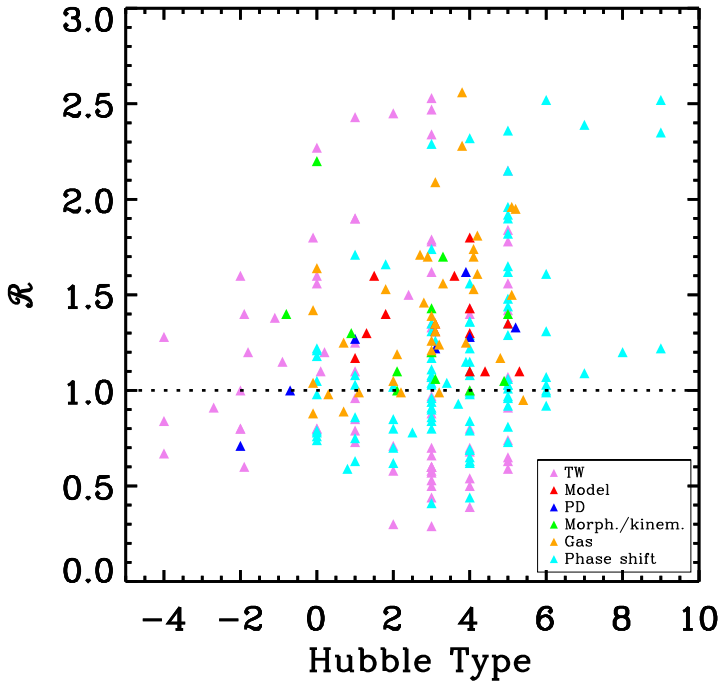

Figure 1.26: Bar rotation rate as a function of galaxy morphological type, obtained with different methods in the literature and presented in Sec. 1.3.3. The morphological types are described through the Hubble stage, ranging from E^+ ($T = -4$) to Sm ($T = 9$); the symbols are colour-coded according to the method used to recover $\mathcal{R}$: the TW method (*violet*), the method based on a comparison of the gas velocity and density field with dynamical models of gas flows (*red*), the method developed by Puerari & Dottori (1997) based on the location of shock-induced star-formation regions with respect to the spiral arm (*blue*), methods based on morphological or kinematical arguments, such as the Fourier analysis (*green*), the method used by Rautiainen et al. (2008) based on N-body simulations to reproduce the galaxy morphology (*orange*), and the method proposed by Zhang & Buta (2007) based on the phase shift between the density perturbation and potential (*cyan*). The $\mathcal{R} < 1.0$ regime is marked (*dotted line*). Adapted from Rautiainen et al. (2008).

which is an unstable period of ~ 1 Gyr, when the bar weakens. During this time, the bar increases the radial velocity dispersion of stars in the disc, creating a strong anisotropy in the velocity dispersions, destabilising the bar in the vertical direction (Martinez-Valpuesta et al., 2006; Athanassoula, 2008; Erwin & Debattista, 2016). The following secular evolution takes place during several Gyrs and the bar slowly increases its length and strength. The bar pattern speed decreases at a rate depending on the amount of angular momentum exchanged between the disc and other galactic components and on the dynamical friction exerted on the bar by the DM halo. Other external events, such as interactions with companions and satellites (Athanassoula et al., 2013; Martinez-Valpuesta et al., 2016; Łokas, 2018), and internal properties, such the gas fraction, the shape of the DM halo, and the presence of a central mass concentration (CMC) (Athanassoula, 2003; Debattista et al., 2006; Athanassoula et al.,

2013), further influence the formation and evolution of a bar.

Bars can form through two different mechanisms: they either form spontaneously in unstable and nearly isolated stellar discs (Hohl, 1971; Sellwood, 1981) or they are induced by close interactions (Noguchi, 1988; Martinez-Valpuesta et al., 2017).

In the internal formation scenario, disc instability occurs for low values of the Toomre stability parameter $Q_\star$. The stability condition is $Q_\star > 2.0$ at all radii, when the surface mass density gradient towards the galactic centre is not too steep (Athanassoula & Sellwood, 1986), but it is even lower if the centre is very dense. A supermassive black hole (SBH) completely prevents the bar formation if it reaches a few percent of the stellar disc mass (Friedli et al., 1994). In this scenario, bars should appear ~ 6 Gyr after the beginning of the disc build-up, i.e. around $z \approx 0.5$ (Noguchi, 1996).

In the external formation scenario, induced bars can appear in both cold and hot discs, since the instability condition is less severe with $Q_\star < 3.0$. During an encounter, large-scale perturbations are observed. Depending on the stabilizing factor, either a fast or a slow bar can form (Noguchi, 1987; Martinez-Valpuesta et al., 2017). In particular, interactions are responsible for bar formation in dwarf galaxies, where the tidal forces are particularly strong (Łokas et al., 2014).

On the other hand, there are conditions preventing bar formation. For example, when the DM halo mass increases, the rotational kinetic energy to potential ratio increases producing a stabilising effect (Ostriker & Peebles, 1973), while baryon-dominated system can be bar stable when they have a rapidly rising $V_{\rm circ}$, given by a dense centre (Sellwood & Evans, 2001).

1.4.2 Bar evolution

The bar does not remain unchanged and suffers many evolutionary processes (Martinet, 1995). These events can be quick or slow, occurring on dynamical (~ 0.1 Gyr) and cosmological (~ 10 Gyr) timescales, and they may affect or not the whole galaxy, acting on large (> 10 kpc) and small (< 1 kpc) scales. As an example, $\Omega_{\rm bar}$ evolves affecting the orbital structure of the galaxy. A low value of $\Omega_{\rm bar}$ corresponds to the onset of ILRs and of the anti-bar x_2 and x_3 families of periodic orbits. When the bar forms with a high value of $\Omega_{\rm bar}$, which then decreases with a typical timescale ~ 5 Gyr (Combes & Sanders, 1981; Little & Carlberg, 1991), the bar slowdown is fast during the first few rotations and then stabilizes at a lower value. This is due to the fact that many chaotic particles are escaping from $R_{\rm cr}$, where they originate, carrying away a significant amount of angular momentum. While $\Omega_{\rm bar}$ decreases, $R_{\rm cr}$ moves outwards and $\mathcal{R}$ tends to grow although $R_{\rm bar}$ is increasing as well.

When a massive live DM halo is present, the slowdown can be even more pronounced due to the dynamical friction exerted by the DM halo on the bar and/or because the exchange of angular momentum is more efficient if a huge amount of mass lies in the centre of the galaxy (Weinberg, 1985; Debattista & Sellwood, 1998; Athanassoula et al., 2013). The timescale of this effect is inversely proportional to the mass of the DM halo and could be as small as a few hundreds of millions years.

However, most of $\Omega_{\rm bar}$ measurements (including all the ones obtained with the TW method) show that bars are likely to be fast-rotating structures. This led Debattista &

Sellwood (1998) to conclude that barred galaxies have only a weak contribution of DM in their central regions.

When a dissipative component is present or if the galaxy suffers from a significant interaction, other mechanisms may occur. For instance, the central bar-driven gas fueling suppresses the decrease of $\Omega_{\rm bar}$, which then remains nearly constant or can even be accelerated (Berentzen et al., 1998; Villa-Vargas et al., 2010), as gas loses angular momentum in favor of the bar which can be renewed (Bournaud & Combes, 2002; Combes, 2011). Close and nearly co-planar interactions may also induce $\Omega_{\rm bar}$ fluctuations (Miwa & Noguchi, 1998). Nevertheless, all these effects are modest and have only a temporary effect, whereas the long-term scenario in their presence is the decrease of $\Omega_{\rm bar}$ and possibly the final dissolution of the bar (Bournaud et al., 2005). Many other factors contribute to the slowdown of $\Omega_{\rm bar}$, such as the velocity dispersion of the halo and disc material and the triaxiality of the halo (Athanassoula, 2003).

A bar-like morphology for the gas is present within some stellar bars, generally leading the stellar bar by a few degrees. Their evolution is regulated by star formation and in general they are not long-lived features (Friedli, 1999; Laine et al., 1999). Three examples of HI gaseous bars have been analysed so far with the TW method based on gas kinematics: all these bars turned out to be slow (Bureau et al., 1999; Banerjee et al., 2013; Patra & Jog, 2019).

1.4.3 Primary and secondary bars

About 30 per cent of disc galaxies host a misaligned secondary (small-scale) bar embedded inside the primary large-scale one (Erwin, 2004, 2011; Moiseev, 2011; Buta et al., 2015). The two bars are expected to be dynamical decoupled (Friedli & Martinet, 1993) since they are randomly oriented with respect to each other. The only effort to apply the TW to recover the pattern speeds in a double barred galaxy was performed by Corsini et al. (2003) on NGC 2950. The authors concluded the primary and secondary bars embedded in the galaxy are rotating with different angular frequencies, the secondary bar having a higher pattern speed. Font et al. (2014) used the phase reversals in the non-circular motion to recover $R_{\rm cr}$ in a sample of eight double-barred galaxies and concluded the secondary bars rotate more rapidly than the primary bars by a factor between 3.3 and 3.6. Secondary bars might play a key role in fueling the active galactic nucleus (Shlosman et al., 1989) and they may affect the formation of new stellar structures, such as kinematically decoupled inner discs, counter-rotating gas, or disc-like bulges (de Lorenzo-Cáceres et al., 2013). The origin of bars within bars is still under debate. Proposed scenarios include gas inflow through the primary bar, which induces the formation of an inner gaseous bar that then forms stars (Friedli & Martinet, 1993; Englmaier & Shlosman, 2004), and gas inflow through the primary bar creating an inner stellar disc, which then becomes dynamically cold and forms a secondary stellar bar (Du et al., 2015; Wozniak, 2015). In the first case, gaseous bars are expected to be short-lived, lasting only a few galaxy rotations, whereas in the second case, secondary bars can be both long-lived or short-lived and destroyed by the CMC. Recent observations of a secondary bar with a boxy/peanut (B/P) shape undergoing buckling in NGC 1291 (Méndez-Abreu et al., 2019) strongly suggest that

secondary and primary bars are governed by the same physical processes, and that secondary bars might not be short-lived structures as they mimic the evolution of primary bars with one or more buckling phases, not yet reproduced by numerical simulations.

1.4.4 Bar buckling instability

Bars are thin ($c/a \simeq 0.1$) only in the early stages of their evolution. After a few bar rotations (~ 1 Gyr), their central regions (up to a few kpc) grow in the vertical direction and become much thicker ($c/a \simeq 0.3$). During this phase, generally occurring after the bar is completely formed and lasting ~ 2 Gyr, the bar creates a B/P bulge (Combes & Sanders, 1981; Combes et al., 1990; Raha et al., 1991; Martinez-Valpuesta et al., 2006; Méndez-Abreu et al., 2018b), easily visible in ~ 45 per cent of edge-on external galaxies (Bureau & Freeman, 1997; Lütticke et al., 2000), but recently caught in the Milky Way as well (see Sec. 1.5). This implies a connection between bars and B/P bulges, confirmed by the signatures of gas kinematics either on direct (Kuijken & Merrifield, 1995), or on retrograde orbits (Emsellem & Arsenault, 1997).

This phase leading to the formation of a B/P structure is called in literature with different names: bending, boxy-peanut, buckling, or fire-hose instability (Fig. 1.27). The nature of this instability is still controversial. It could be a resonant bending fed by vertical diffusion of orbits, due to the space part of the distribution function (Combes et al., 1990; Pfenniger & Friedli, 1991) or a collective instability resulting from the velocity part of the distribution function (Raha et al., 1991; Merritt & Sellwood, 1994), possibly occurring in cold young stellar discs (Griv & Chiueh, 1998). The observed B/P structures probably result from a 2:1:1 resonant bending (ratio of radial κ, circular Ω, and vertical v_z frequencies in a 3D perturbation). Before the bending, the orbital structure is dominated by the 2D x_1 (direct) and x_4 (retrograde) periodic orbit families. After the bending, fully 3D families appear, mainly the 2:1:1 banana and anti-banana ones (bifurcating from the x_1) and the 1:1:1 anomalous ones (bifurcating from the x_4). B/P structures end near the vertical ILR, i.e. typically at around half of $R_{\rm cr}$, and do not require any macroscopic vertical asymmetry to form. These structures extend ~ 0.5 times the bar size (Bureau et al., 1999). Their incidence depends mainly on galaxy mass, while colour, bar size, and gas fraction seem to be irrelevant (Erwin & Debattista, 2017).

The high incidence of B/P structures provides observational evidence that bars generally survive for at least several galaxy rotations, implying they are long-lived structures with a minimum age of ~ 4 Gyr since their assembly lasts ~ 2 Gyr (Méndez-Abreu et al., 2019; de Lorenzo-Cáceres et al., 2019b). The buckling instability may also cause bar annihilation (Raha et al., 1991) and/or occur many times, accompanied by a remarkable decrease of $\Omega_{\rm bar}$ (Martinez-Valpuesta et al., 2006).

1.4.5 Bar metallicity

A bar is also characterized by irregular (chaotic) orbits and gravitational torques, which lead to large-scale ($\gtrsim 1$ kpc) diffusion and mixing of stars, and produce transfer of angular

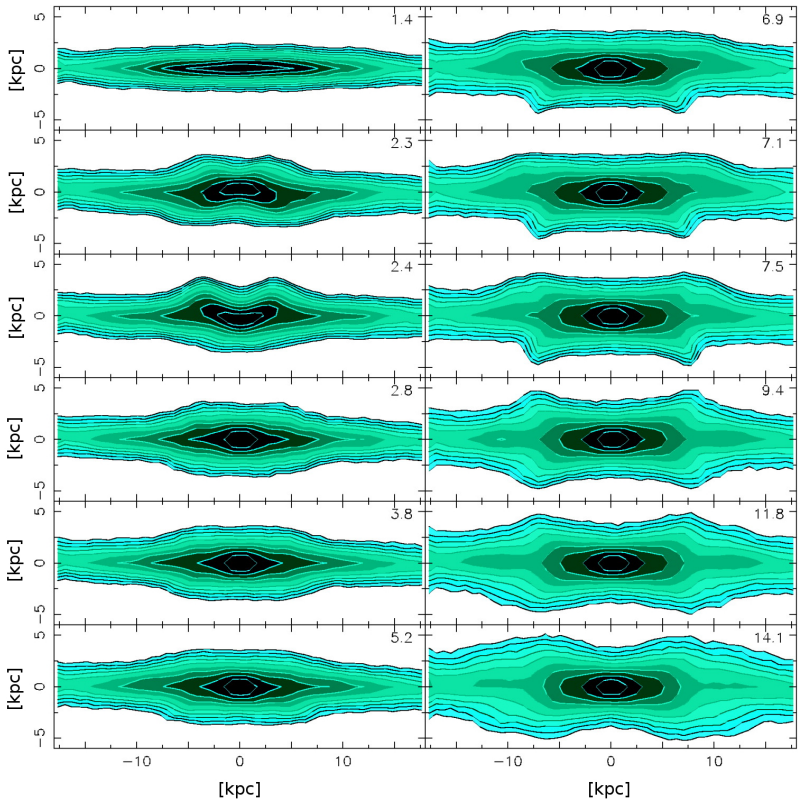

Figure 1.27: Time evolution of the vertical structure in the bar as seen from an edge-on view along the minor axis of the bar. The length is given in kpc and time in Gyr. The maximal vertical asymmetries correspond to two recurrent bucklings. From Martinez-Valpuesta et al. (2006).

momentum and matter, especially gas (Athanassoula, 1992; Bureau et al., 2007). This affects the stellar and gaseous abundance profiles. Chaos is expected to increase together with $S_{\rm bar}$, CMC, or asymmetries. Strong 3D N-body bars typically host ~ 35 per cent of hot chaotic orbits, ~ 45 per cent of bar orbits, and ~ 20 per cent of disc populations. At some critical value of $S_{\rm bar}$, there is significant diffusion in both radial and vertical directions (Olle & Pfenniger, 1998), and bar-generated features are visible in stellar and gaseous abundance profiles (Friedli, 1998). In fact, when a strong bar appears, any smooth and steep initial abundance gradient $d\log A/dR < 0$ is distorted by a plateau near $R_{\rm cr}$ and a pronounced flattening in the disc region. Models with $d\log A/dz < 0$ quickly develop B/P isoabundance contours, whereas models with $d\log A/dz = 0$ become X-shaped and present positive gradients in the disc region. Concerning the gas, a severe flattening occurs in the disc region (Friedli et al., 1994) and a break near $R_{\rm cr}$ in young bars (Martinet & Friedli, 1997). During the early phase of bar evolution, gas dilution by significant gas inflow is compensating the heavy-element production by star formation, so the gradients are maintained. In late-type galaxies the oxygen abundances from HII regions have weaker gradients (Vila-Costas & Edmunds, 1992) and the gradients are shallower when the bar is stronger (Martin & Roy, 1994). Observed

breaks in abundance profiles are related to ~ 1 Gyr old bars (Roy & Walsh, 1997).

An early-type barred galaxies sample was studied by Pérez & Sánchez-Blázquez (2011), focusing on stellar properties of bars and bulges. The authors found more metal rich bulges in barred galaxies, for a given stellar central velocity dispersion, and defined three types of bars according to the metallicity and age distributions along the radius: 1) Bars with negative metallicity gradients, with mean young/intermediate populations (< 2 Gyr), and the lowest velocity dispersions; 2) Bars with null metallicity gradients along the bar and negative age gradients (i.e younger populations at the bar's ends); 3) Bars with positive metallicity gradients, i.e. more metal rich at the bar's ends, higher velocity dispersions, and older mean populations.

To summarize, young stellar bars ($\lesssim 2$ Gyr) are expected to be thin, with a large $\Omega_{\rm bar}$, and intense star formation towards the centre. The gaseous radial abundance profile presents a break near $R_{\rm cr}$, and decoupled secondary bars are unlikely. Old bars ($\gtrsim 2$ Gyr) are thick (possibly associated with B/P features), with small $\Omega_{\rm bar}$ and a moderate star-formation, mainly located in a circumnuclear ring. The gaseous radial abundance profile is flat, and the presence of secondary bars is more common.

1.4.6 Bar dissolution

Bars are subject to dissolution, which can be due to internal or external processes and can be sudden or progressive. The main reason is the growth of a significant CMC. This feature generates ILRs which strongly modify the orbital structure. In fact, x_1 bar-supporting orbits are depopulated in favor of chaotic and x_2 anti-bar orbits (Pfenniger & Norman, 1990). Several mechanisms were advocated to explain how a CMC can accumulate. They include bar-driven gas accretion (Friedli & Martinet, 1993; Bournaud et al., 2005), growth of SBHs (Friedli et al., 1994), accretion of satellites (Pfenniger & Friedli, 1991), or an extreme merging (Barnes & Hernquist, 1991). Massive nuclear rings also act to weaken or dissolve the bar, mainly outside the ring (Heller & Shlosman, 1996).

The role of the bulge and of the shape of the DM halo on the evolution of bars was investigated by Athanassoula (2003), who studied the effect of a CMC and considered different types of haloes. If the CMC is not present, the bar undergoes the standard secular evolution and it steadily becomes slower and stronger. On the contrary, the bar weakens and its $\Omega_{\rm bar}$ increases in galaxies with a CMC. Since the bar evolution is also driven by the shape of the DM halo, the presence of a CMC could finally result in the destruction of the bar if it formed in a disc-dominated rather than in a halo-dominated galaxy. The CMC may be built from gas flowing toward the galaxy centre driven by the barred potential (Athanassoula, 2005). More specifically, Bournaud & Combes (2002) and Bournaud et al. (2005) found that significant gas accretion in the presence of a massive bulge produces different episodes of bar destruction and rebuilding. At each step, the newly formed bar is shorter and weaker while its $\Omega_{\rm bar}$ is faster than the previous one. At the same time, the galaxy expands and the bulge mass increases. Debattista et al. (2006) claimed the effect of the gas on the bar amplitude depends on its physics. If the gas can cool, it rapidly becomes centrally concentrated.

The criterion for the annihilation of the bar depends both on the mass and concentration

of the CMC and can be defined as $\gamma_{\rm ann} \equiv M_{\rm centre}/M_{\rm total}$. The time to reach $\gamma_{\rm ann}$ is equivalent to the bar annihilation timescale and depends on the accretion rate, probably spanning a wide interval, something like $0.2 - 20$ Gyr.

In summary, the formation and evolution of a bar are responsible for various major changes of the host galaxy. These modifications affect the morphology, orbital structure, dynamics, star formation, central fueling rates, and the abundance profiles. As a consequence, a remarkable galaxy metamorphosis within the Hubble sequence can be observed.

1.5 The Milky Way bar

The Milky Way is a luminous barred spiral galaxy hosting a diffuse stellar halo, a dominant disc, and a central B/P bulge, which appears to be in a relatively late stage of evolution based on its low specific star formation rate (see e.g., Bland-Hawthorn & Gerhard, 2016, for a review).

The observed B/P bulge forms the inner part of the Galactic bar. The boxy nature of the bulge was observed through the Cosmic Background Satellite (COBE) near-infrared photometry and the Two Micron All Sky Survey (2MASS) count map (Binney et al., 1997; Skrutskie et al., 2006) and is consistent with the observed cylindrical rotation commonly observed in barred bulges (Ness et al., 2013) and with the non-circular motions seen in HI and CO longitude-velocity diagrams, suggestive of a barred potential (Englmaier & Gerhard, 1999). The very central part of the Milky Way hosts a dense nuclear stellar disc, possibly containing a separate 200 pc-scale secondary bar (Rodriguez-Fernandez & Combes, 2008).

The dominant bulge population of red clump giant (RCG) stars shows a B/P-shaped with an exponential density distribution, similar to the inner 3D part of an evolved N-body bar (Wegg & Gerhard, 2013). In fact, the RCG bulge appears strongly barred, with a face-on projected axis ratio $\sim (1 : 2.1)$ for isophotes reaching ~ 2 kpc along the major axis; it has a strong B/P shape viewed side-on and a boxy shape as seen from the Sun (Portail et al., 2015).

The inner part of the Galactic disc, between the region of the nuclear stellar disc and ~ 2 kpc, is poorly studied because of strong extinction and crowding. The Apache Point Observatory Galaxy Evolution Experiment (APOGEE) LOS velocity histograms, however, show cold kinematics typical of a young bar's stars (Aumer & Schönrich, 2015). The bulge presents a small vertical scaleheight ($h_z = 180$ pc), which may suggest the existence of a central disc-like, high-density pseudo-bulge structure, as observed in many galaxies hosting a B/P bulge (Bureau et al., 2006) and interpreted in terms of a rounder and more nearly axisymmetric central part of the B/P bulge by means of an N-body model (Gerhard & Martinez-Valpuesta, 2012). Moreover, the innermost 300 pc of the Milky Way are characterized by a strongly asymmetric distribution of molecular gas, a region called the Central Molecular Zone (CMZ). Indeed, ~ 75 per cent of molecular emission comes from positive longitudes and only ~ 25 per cent from negative longitudes (Ridley et al., 2017). The observed asymmetry can be explained as an unsteady flow of gas in a barred potential, which develops spontaneously due to the combination of a hydrodynamical wiggle instability and a thermal instability (Wada & Koda,

2004; Sormani et al., 2017).

The CMZ can be identified as a mildly-elliptical gaseous disc/ring like structure transiting in a barred potential between the x_1 and x_2 orbits (Binney et al., 1991). The x_1 orbits are elongated parallel to the bar major axis and become self-intersecting below a critical energy in the presence of an ILR. In the outer regions of the bar, the gas follows the x_1 orbits, while dissipative processes make it slowly drift inwards along a sequence of such orbits. When it reaches the intersecting orbit, it transits within a dynamical time from the x_1 to the x_2 orbits, which are mainly elongated perpendicular to the bar major axis. The transition happens through the formation of large-scale shocks, which are unstable due to the hydrodynamical wiggle instability and correspond to the dust lanes observed in external barred galaxies (Athanassoula & Misiriotis, 2002). Then the shocked gas moves towards the centre until at some smaller radius it piles up and organises into a visible disc/ring-like structure, following x_2 orbits. This is a transient phenomenon, which is expected to present the opposite geometry in tens of Myr (Sormani et al., 2018).

The central region of the Milky Way within ~ 200 pc is dominated by the nuclear stellar disc. Longitudinal asymmetries in a map of projected 2MASS star counts suggest the presence of a 200 pc scale secondary bar which is distinct from the B/P bulge, although the projection of the primary Galactic bar itself leads to similar inverted asymmetries in the centre (Gerhard & Martinez-Valpuesta, 2012).

It is still debated if the Milky Way contains a classical bulge. In fact, there are many structural and kinematic properties suggesting that most of the Galactic bulge was built from the disc through secular evolution (Sellwood, 2014).

In N-body models, B/P bulges are the inner part of longer and planar bars formed through buckling out of the galaxy plane during disc evolution and/or from orbits in vertical resonance (Raha et al., 1991; Athanassoula, 2005). Thus also the Milky Way is expected to have a thin bar component extending well outside the B/P bulge. However, locating and studying the Galactic bar is difficult because of dust extinction and superposition with the star-forming disc at low-latitudes towards the centre.

An overdensity of stars in the Milky Way disc plane out to $l \simeq 28^\circ$ was found (Hammersley et al., 2000; Cabrera-Lavers et al., 2008), and confirmed as a strong bar-like structures at positive longitudes with Spitzer mid-infrared star counts (Benjamin et al., 2005). This structure presents a vertical scalelength of less than 100 pc, characteristic of a disc feature and because of its wide longitude extent and narrow LOS extent it was termed the "long bar".

Analysing RCG stars from the combined 2MASS, UKIRT Infrared Deep Sky (UKIDSS), Vista Variables in the Via Lactea (VVV) and Galactic Legacy Infrared Mid-Plane Survey Extraordinaire (GLIMPSE) surveys, Wegg et al. (2015) investigated the long bar in a wide latitude and longitude area and found it extends to $l \sim 25^\circ$ at $|b| \sim 5^\circ$ from the Galactic plane and to $l \sim 30^\circ$ at lower latitudes with an angle to the LOS of $28^\circ - 33^\circ$. The vertical scaleheight appeared to decrease continuously from the B/P bulge to the long bar, suggesting the former to be the vertical extension of a longer, flatter bar, similar to the structures observed in external galaxies and N-body models, with a half semi-major axis length $R_{\rm bar} = 5.0 \pm 0.2$

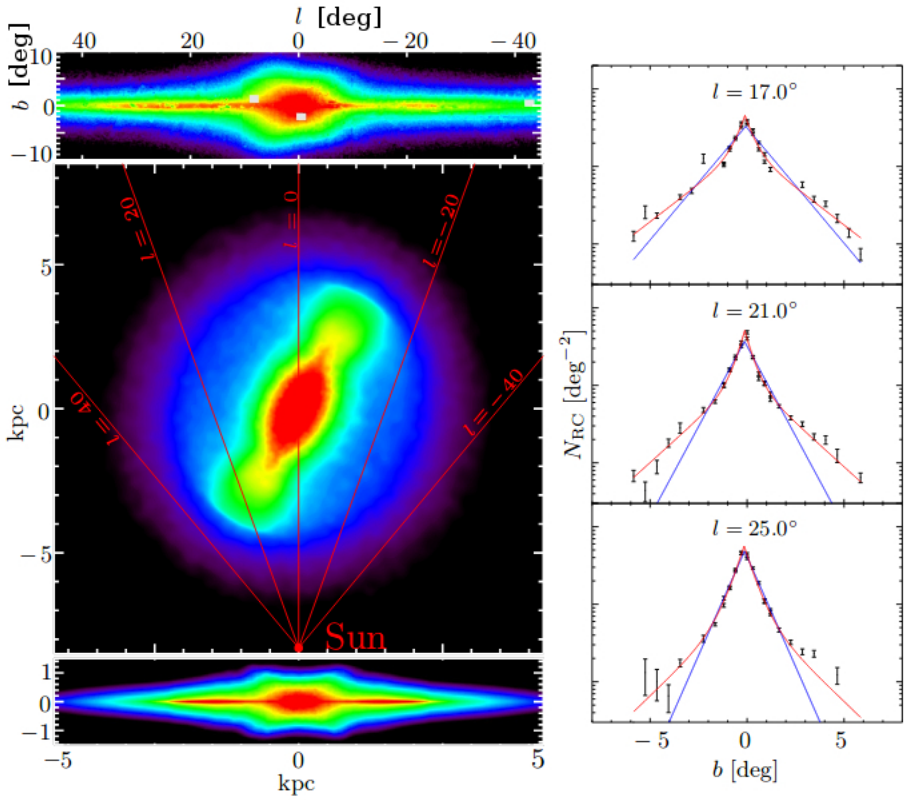

Figure 1.28: *Left panels*: projections of the Galactic B/P bulge and long bar reconstructed from near-infrared star counts. *Top panel*: inner Galaxy as seen from the Sun; *middle panel*: projection of best-fitting RCG star count model as seen from the North Galactic Pole; *bottom left*: side-on view showing the transition from the B/P bulge to the long bar and disk. *Right panels*: vertical surface density profiles of RCG stars for several longitude slices in the long bar region. The double exponential model is shown (*red line*). The fraction of stars in the superthin component increases with longitude. From Bland-Hawthorn & Gerhard (2016).

kpc. The authors also found two different vertical scaleheights in the long bar: a first one ($h_{z,\mathrm{th}} = 180$ pc) corresponds to the thin bar, reminiscent of the old thin disc near the Sun with a density decreasing outwards roughly exponentially, and a second superthin component ($h_{z,\mathrm{th}} = 45$ pc) with a density increasing outwards towards the bar ends. Stars in this component have an estimated vertical velocity dispersion $\sigma \simeq 20$ km s^{-1} and should be younger than the thin component, arising from star formation towards the bar ends or from disc stars captured by the bar. Figure 1.28 shows the projections of the best model for the combined bulge and long bar from Bland-Hawthorn & Gerhard (2016), together with their double exponential vertical profile.

Studing the intrinsic shape of the Milky Way bulge with radial velocities allowed Vásquez et al. (2013) to observe from a sample of 454 bulge giants evidence of streaming motions within the bar in the same sense as the bar rotates. Clarke et al. (2019) derived LOS integrated and distance-resolved maps of mean proper motions and dispersions from the VVV Infrared Astrometric Catalogue (VIRAC) and Gaia data, and used a dynamical model to aid in their

interpretation. The derived mean longitudinal proper motion $\langle \mu_l^* \rangle$ isocontours are tilted, due to the streaming motions in the bar. The mean latitudinal proper motion $\langle \mu_b \rangle$ map shows a quadrupole signature, caused by the composite effect of the bar pattern rotation and longitudinal streaming motions in the bar.

From the RCG star density using isochrones and a Kroupa initial mass function, Wegg et al. (2015) estimated the stellar mass of the bar. They found $M_{\rm th} \simeq 7 \times 10^9 M_\odot$ for the thin bar component, assuming a 10 Gyr old and α-enhanced population, and $M_{\rm th} \simeq 3.3 \times 10^9 M_\odot$ for the superthin component, assuming a constant past star formation rate. Because of its size and mass, the long bar is suspected to have some impact on the dynamics of the Galactic disc inside the Solar circle, particularly on the gas flows and the spiral arms, but perhaps also on its surface density and scalelength.

There was a large debate whether the Milky Way hosts a long or a short bar. The observations of kinematic groups, such as the Hercules stream, induced by the non-axisymmetries in the Galactic potential, contribute to the discussion (D'Onghia & Aguerri, 2019). When the Galactic bar is short ($\sim$ 3 kpc) and fast rotating ($\Omega_{\rm bar}$ = 55 km s^{-1} kpc^{-1}), models locating the OLR of the Galactic bar near the Sun explain well the bimodal distribution of the velocity between a moving group of low-velocity stars centered on the Local Standard of Rest and an association of stars moving outward and rotating more slowly than the Sun, such as the Hercules stream (Monari et al., 2017; Fragkoudi et al., 2019). However, several measurement of the Galactic bar pattern speed are recently converging around a typical value of $\Omega_{\rm bar} = 40$ km s^{-1} kpc^{-1}. Portail et al. (2017) found $\Omega_{\rm bar} = 39.0 \pm 3.5$ km s^{-1} kpc^{-1} using bulge stellar-dynamical models, Bovy et al. (2019) found $\Omega_{\rm bar} = 41 \pm 3$ km s^{-1} kpc^{-1} applying the continuity equation locally on the long bar, while Sormani & Magorrian (2015) found $\Omega_{\rm bar}$ between 40 and 42 km s^{-1} kpc^{-1} from gas dynamical models of the (l, v) plot. These results place the OLR at $\sim$ 10.5 kpc from the Galactic centre, so the Hercules stream consists of stars trapped at $R_{\rm cr}$, which is consistent to be located at $R \sim 5.8$ kpc. In this case the Galactic bar has a rotation rate $\mathcal{R} = 1.16$, implying that the Milky Way hosts a dynamically fast and long bar.

1.6 Aim and outline of the thesis

The aim of this thesis is to enlarge the sample of direct measurements of the bar pattern speed in strongly and weakly barred galaxies, by applying the TW method to IFU spectroscopic data, and to explore possible relations with the properties of the host galaxy. The Chapters are organised as follow.

Chapter 2 We present surface photometry and stellar kinematics of NGC 4264, a barred lenticular galaxy in the region of the Virgo Cluster undergoing a tidal interaction with one of its neighbours, NGC 4261. We measured the bar radius ($R_{\rm bar} = 3.2 \pm 0.5$ kpc) and strength ($S_{\rm bar} = 0.31 \pm 0.04$) of NGC 4264 from SDSS imaging, and its bar pattern speed ($\Omega_{\rm bar} = 71 \pm 4$ km s^{-1} kpc^{-1}) using the TW method with stellar-absorption IFU spectroscopy performed with the Multi Unit Spectroscopic Explorer (MUSE) at the Very Large Telescope

(VLT). We derived the circular velocity in the disc region ($V_{\rm circ} = 189 \pm 10$ km s^{-1}) by correcting the stellar streaming velocity for asymmetric drift and calculated the corotation radius ($R_{\rm cr} = 2.8 \pm 0.2$ kpc) from the bar pattern speed. We find that NGC 4264 hosts a strong and large bar which extends out to its corotation radius ($\mathcal{R} \equiv R_{\rm cr}/R_{\rm bar} = 0.88 \pm 0.23$). This means that the bar is rotating as fast as it can like nearly all the other bars measured so far, even when the systematic error due to the uncertainty on the disc position angle is taken into account. The accurate measurement of the bar rotation rate allows us to infer that the formation of the bar of NGC 4264 was due to self-generated internal processes and not triggered by the ongoing interaction. *Based on V. Cuomo, E. M. Corsini, J. A. L. Aguerri et al. 2019, MNRAS, 488, 4972.*

Chapter 3 We aim to investigate the formation process of weak bars by measuring their properties in a sample of 29 nearby weakly barred galaxies, spanning a wide range of morphological types and luminosities. The sample galaxies were selected to each have an intermediate inclination, an intermediate bar between the disc minor and major axes, and undisturbed morphology and kinematics, to allow the direct measurement of the bar pattern speed. Combining our analysis with previous studies, we compared the properties of weak and strong bars. We measured the bar radii and strengths from the r-band images available in the SDSS and the bar pattern speeds and corotation radii from the stellar kinematics obtained by the CALIFA survey. We derived the bar rotation rates as the ratios between the corotation and bar radii. Thirteen out of 29 galaxies (45 per cent), which were morphologically classified as weakly barred from a visual inspection, do not actually host a bar component or their central elongated component is not in rigid rotation. We successfully derived the bar pattern speed in the other 16 objects. Two of them host an ultrafast bar. Using the bar strength to differentiate weak and strong bars, we found that the weakly-barred galaxies host shorter bars with smaller corotation radii than their strongly barred counterparts. Weak and strong bars have similar bar pattern speeds and rotation rates, which are all consistent with being fast. We did not observe any difference between the bulge prominence in weakly and strongly-barred galaxies, whereas nearly all the weak bars reside in the disc inner parts, contrary to strong bars. We excluded that the bar weakening is only related to the bulge prominence and that the formation of weak bars is triggered by the tidal interaction with a companion. Our observational results suggest that weak bars may be evolved systems exchanging less angular momentum with other galactic components than strong bars. *Based on V. Cuomo, J. A. L. Aguerri, E. M. Corsini et al. 2019, A&A, in press, arXiv:1909.01023.*

Chapter 4 We aim to investigate the relations between the properties of bars and their host galaxies in a sample of 100 nearby barred galaxies, spanning a wide range of morphological types and luminosities. The sample includes all the galaxies known to have a direct measurement of $\Omega_{\rm bar}$ based on long-slit or IFU spectroscopic data of stellar kinematics. For each galaxy we collected $R_{\rm bar}$, $S_{\rm bar}$, $\Omega_{\rm bar}$, $\mathcal{R}$ and $R_{\rm cr}$ for the bar and we considered the Hubble type and absolute SDSS r-band magnitude of the host galaxy. We also derived the bulge-to-total luminosity ratio for a subsample of 34 galaxies with an available photometric decomposition.

We limited our analysis to the galaxies with a relatively small relative error on the bar pattern speed ($\Delta\Omega_{\rm bar}/\Omega_{\rm bar} < 0.5$) and not hosting an ultrafast bar ($\mathcal{R} > 1$). The final sample consists of 75 objects with 33 SB0-SBa and 42 SBab-SBc galaxies. We confirmed earlier observational findings that longer bars rotate with a lower $\Omega_{\rm bar}$, shorter bars are weaker, fast bars rotate with higher $\Omega_{\rm bar}$ and have shorter corotation radii, and disc-dominated galaxies host weaker bars. In addition, we found that stronger bars rotate with a lower $\Omega_{\rm bar}$ as predicted for the interchange of angular momentum during bar evolution depending on galaxy properties. Moreover, we reported that brighter galaxies host longer bars, which rotate with a lower $\Omega_{\rm bar}$ and have a larger corotation. This result together with the fact that we observed stronger bars in bulge-dominated galaxies is in agreement with a scenario of downsizing in bar formation and co-evolution of bars and bulges if more massive galaxies formed earlier and had sufficient time to slow down, grow in length, and push outwards corotation. *Based on V. Cuomo, J. A. L. Aguerri, E. M. Corsini et al. 2019, A&A, in preparation.*

Chapter 5 In this chapter we report our conclusions and some future perspectives.

Chapter 2

Evidence of a fast bar in the weakly-interacting galaxy NGC 4264 with MUSE[§]

Abstract We present surface photometry and stellar kinematics of NGC 4264, a barred lenticular galaxy in the region of the Virgo Cluster undergoing a tidal interaction with one of its neighbours, NGC 4261. We measured the bar radius ($a_{\rm bar} = 3.2 \pm 0.5$ kpc) and strength ($S_{\rm bar} = 0.31 \pm 0.04$) of NGC 4264 from SDSS imaging, and its bar pattern speed ($\Omega_{\rm bar} = 71 \pm 4$ km s^{-1} kpc^{-1}) using the TW method with stellar-absorption integral-field spectroscopy performed with the MUSE at the VLT. We derived the circular velocity in the disc region ($V_{\rm circ} = 189 \pm 10$ km s^{-1}) by correcting the stellar streaming velocity for asymmetric drift and calculated the corotation radius ($R_{\rm cr} = 2.8 \pm 0.2$ kpc) from the bar pattern speed. We find that NGC 4264 hosts a strong and large bar which extends out to its corotation radius ($\mathcal{R} \equiv R_{\rm cr}/a_{\rm bar} = 0.88 \pm 0.23$). This means that the bar is rotating as fast as it can like nearly all the other bars measured so far, even when the systematic error due to the uncertainty on the disc position angle is taken into account. The accurate measurement of the bar rotation rate allows us to infer that the formation of the bar of NGC 4264 was due to self-generated internal processes and not triggered by the ongoing interaction.

2.1 Introduction

Early applications of the TW method based on long-slit spectroscopy were challenging in terms of both integration times and kinematical analysis, and therefore focused on early-type barred galaxies (see Corsini, 2011, for a review). Over a dozen galaxies were measured with a typical uncertainty of ~ 30 per cent, mostly due to errors in identifying the position of the galaxy centre and in measuring the galaxy systemic velocity, the low S/N ratio of the spectra, the limited number of slits and their misalignment with respect to the disc major

[§] *Based on V. Cuomo, E. M. Corsini, J. A. L. Aguerri et al. 2019, MNRAS, 488, 4972.*

axis. The advent of IFU spectroscopy with wide fields of view promises to overcome these problems and to lead to more efficient and precise TW measurements (but see Debattista & Williams, 2004, for a first application). Indeed, the centring errors in both the position of the galaxy centre and in measuring the galaxy systemic velocity are minimised by the unambiguous determination of a common reference frame for the distribution and velocity field of the stars, the S/N of the spectra can be increased by binning adjacent spaxels, and the number and orientation of the pseudo-slits can be optimised during the analysis.

Aguerri et al. (2015) measured $\Omega_{\rm bar}$ of 15 galaxies using the stellar velocity maps provided by the CALIFA IFU spectroscopic survey (Sánchez et al., 2012). More recently, Guo et al. (2019) obtained the bar pattern speed for another 51 galaxies[1] using the IFU spectroscopic data from the MaNGA project (Bundy et al., 2015). Neither of them found significant trends between $\mathcal{R}$ and morphological type, although the two samples cover the entire sequence of barred galaxies from SB0s to SBds. The fast bar solution can not be ruled out for any galaxy, in agreement with results from indirect measurements of bar pattern speeds. However, the typical uncertainty of the bar pattern speeds of the CALIFA and MaNGA galaxies is ~ 30 and ~ 50 per cent, respectively, because of the limited spatial sampling of the spectroscopic data which restricted the TW analysis to only three to five pseudo-slits.

In this Chapter we derive $\Omega_{\rm bar}$ of the lenticular galaxy NGC 4264 from IFU spectroscopy performed with MUSE at the VLT. With this pilot study we aim to show that IFU spectroscopic data with high spatial sampling are mandatory to substantially reduce the uncertainty on the bar pattern speeds measured with the TW method and properly compare the observed bar rotation rates with theoretical predictions and results of numerical simulations (see Debattista & Williams, 2004). We structure the Chapter as follows. We present the general properties of NGC 4264 in Sec. 2.2. We show the broad-band imaging in Sec. 2.3 and the IFU spectroscopy in Sec. 2.4. We derive the bar properties in Sec. 2.5 and discuss our findings in Sec. 2.6.

2.2 Global properties of NGC 4264

NGC 4264 is an early-type disc galaxy which was classified as SB0 by Nilson (1973), as SB0$^+$(rs) by de Vaucouleurs et al. (1991, hereafter RC3), and as SBa by Kim et al. (2014). It is characterised by an apparent magnitude $B_T = 13.70$ mag (RC3), which corresponds to a total corrected absolute magnitude $M^0_{B_{\rm T}} = -19.27$ mag, obtained adopting a distance $D = 39.2$ Mpc from the radial velocity with respect to the cosmic microwave background reference frame $V_{\rm CMB} = 2864 \pm 25$ km s^{-1} (Fixsen et al., 1996) and assuming the Hubble constant $H_0 = 73$ km s^{-1} Mpc^{-1}. The galaxy is located in the region of the Virgo Cluster and was classified as a possible member (Kim et al., 2014), however the lack of a solid distance estimate does not allow to confirm this hypothesis. It certainly belongs to the rich galaxy group around NGC 4261 (Garcia, 1993; Kourkchi & Tully, 2017). According to Schmitt (2001), NGC 4264 forms an interacting pair with the early-type galaxy NGC 4261 which lies

[1]The paper lists 53 objects but the galaxies 8274-6101 and 8603-12701 are duplications of 8256-6101 and 8588-3701, respectively.

at a projected distance of 3.5 arcmin corresponding to 30 kpc (Fig. 2.1, left-hand panel).

The apparent isophotal major and minor diameters measured at a surface brightness level of $\mu_B = 25$ mag arcsec^{-2} are $D_{25} \times d_{25} = 1.6$ arcmin $\times$ 1.3 arcmin (RC3). They correspond to a galaxy size of 15.3 kpc $\times$ 12.4 kpc.

The H_2 content of the galaxy was estimated by Young et al. (2011), through observations of the ^{12}CO(1-0) and ^{12}CO(2-1) emission lines. They found a total mass of the molecular hydrogen $\log(M_{H_2}/M_\odot) < 7.98$ within the central 22 arcsec (3.5 kpc) of the galaxy, in agreement with the typical value found for the other early-type galaxies analysed in their sample.

Cappellari et al. (2013a) constructed a JAM model to constrain the orbital structure of the stars and the DM content within the half-light radius R_e by matching the galaxy surface brightness and stellar kinematics available from the ATLAS^{3D} project (Cappellari et al., 2011). They found a stellar mass-to-light ratio $\log(M/L_r)_{stars} = 0.445$ and a DM fraction $f(DM) = 0.31$, obtained within a sphere of radius R_e in the SDSS r-band image, for the best-fitting JAM model with a Navarro-Frenk-White (NFW) halo and for their assumed distance (Cappellari et al., 2013b).

2.3 Broad-band imaging

2.3.1 Image acquisition and reduction

We retrieved the g- and i-band images of NGC 4264 from the Data Archive Server (DAS) of the Data Release 12 of the SDSS (SDSS-DR12, Alam et al. 2015). The images were already bias subtracted, flatfield-corrected, sky-subtracted, and flux-calibrated according to the associated calibration information stored in the DAS.

We trimmed the images selecting a field of view (FOV) of 800×800 pixel^2 (corresponding to 5.3×5.3 arcmin^2) centred on the galaxy (Fig. 2.1). To estimate the goodness of the SDSS sky subtraction, we fitted elliptical isophotes with the ELLIPSE task in IRAF[2] (Jedrzejewski, 1987) and measured the radial profile of the surface brightness at large distances from the galaxy centre. We masked foreground stars, nearby and background galaxies, residual cosmic rays, and bad pixels before fitting the isophotes. As a first step, we allowed the centre, ellipticity, and position angle of the ellipses to vary. Then, we adopted the centre of the inner ellipses ($R < 2$ arcsec, where R is the semi-major axis length of the fitted isophotes) and the ellipticity and position angle of the outer ones ($R > 180$ arcsec). The radial profile of the background surface brightness shows a remarkable gradient in both g- and i-band images, due to the residual light contribution from the bright nearby galaxy NGC 4261.

Since NGC 4261 is not fully covered by the FOV of the NGC 4264 images, we retrieved also the g- and i-band images of NGC 4261 from SDSS-DR12. Then we performed a photometric decomposition of NGC 4261 by using the Galaxy Surface Photometry 2-Dimensional Decomposition algorithm (GASP2D; Méndez-Abreu et al. 2008, 2014; de Lorenzo-Cáceres et al.

[2]Image Reduction and Analysis Facility is distributed by the National Optical Astronomy Observatories, which are operated by the Association of Universities for Research in Astronomy under cooperative agreement with the National Science Foundation.

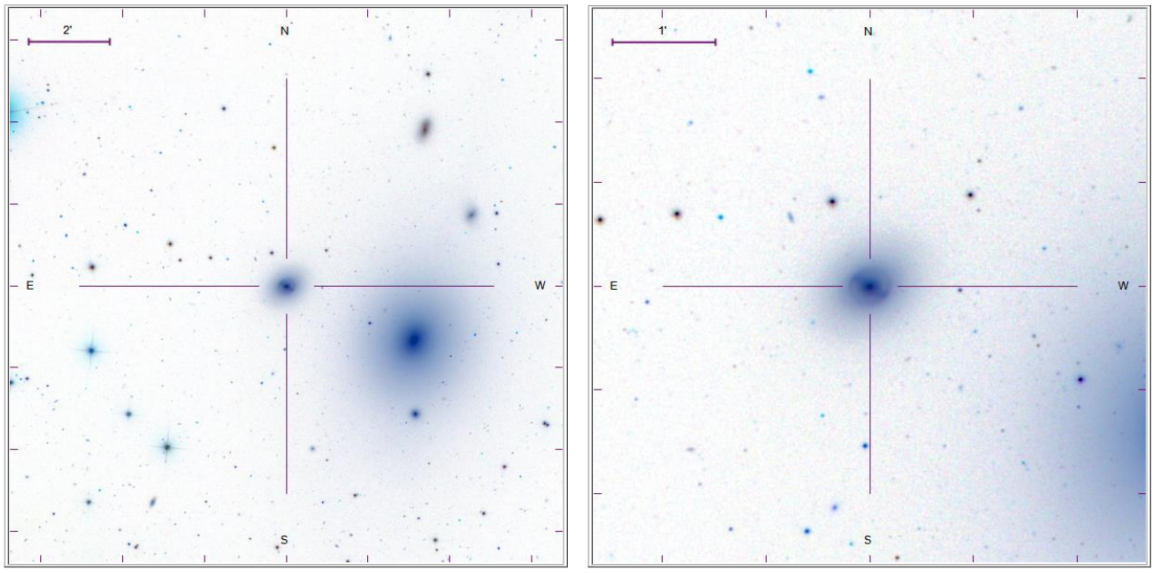

Figure 2.1: *Left panel*: SDSS i-band image of NGC 4264 and NGC 4261; *right panel*: trimmed image of NGC 4264. The size and orientation of the FOV are given for both panels, where a cross marks the centre of NGC 4264.

2019a) in IDL[3]. We modelled the surface brightness distribution of the galaxy with a Sérsic law following the prescriptions given in Sec. 2.3.3. The model image of NGC 4261 was convolved with a circular Moffat point spread function (PSF; Moffat, 1969) with the shape parameters measured directly from the field stars of the NGC 4264 image, and then it was subtracted from the image of NGC 4264. We conducted this analysis for both the g- and i-band images.

Finally, we repeated the ellipse fitting of the isophotes with constant centre, ellipticity, and position angle on the corrected images of NGC 4264. We found a constant surface brightness at $R \gtrsim 140$ arcsec, which we adopted as the residual sky level to be subtracted from the image. We measured the standard deviation of the image background after the residual sky subtraction in regions free of sources at the edges of the FOV (Fig. 2.1, right-hand panel) using the IRAF task IMEXAMINE. We found $\sigma_{\mathrm{sky},g} = 0.07$ and $\sigma_{\mathrm{sky},i} = 0.04$ mag arcsec^{-2}, while the sky surface brightness was $\mu_{\mathrm{sky},g} = 24.80$ and $\mu_{\mathrm{sky},i} = 23.69$ mag arcsec^{-2}.

2.3.2 Isophotal analysis

We performed an isophotal analysis of the sky-subtracted images of NGC 4264 in both SDSS g- and i-band images using ELLIPSE. We fitted the galaxy isophotes with ellipses, fixing the centre coordinates after checking they do not vary within their uncertainties. Figure 2.2 shows the resulting radial profiles of the azimuthally-averaged surface brightness μ, position angle PA, and ellipticity ϵ as well as the radial profile of the $\mu_g - \mu_i$ colour.

We measured similar radial profiles of PA and ϵ in both bands and no colour variation over the observed radial range ($\mu_g - \mu_i = 1.148 \pm 0.006$ mag arcsec^{-2}). Despite the colour profile was obtained as a difference between not identical ellipses, the radial profiles are however very

[3]Interactive Data Language is distributed by Harris Geospatial Solutions.

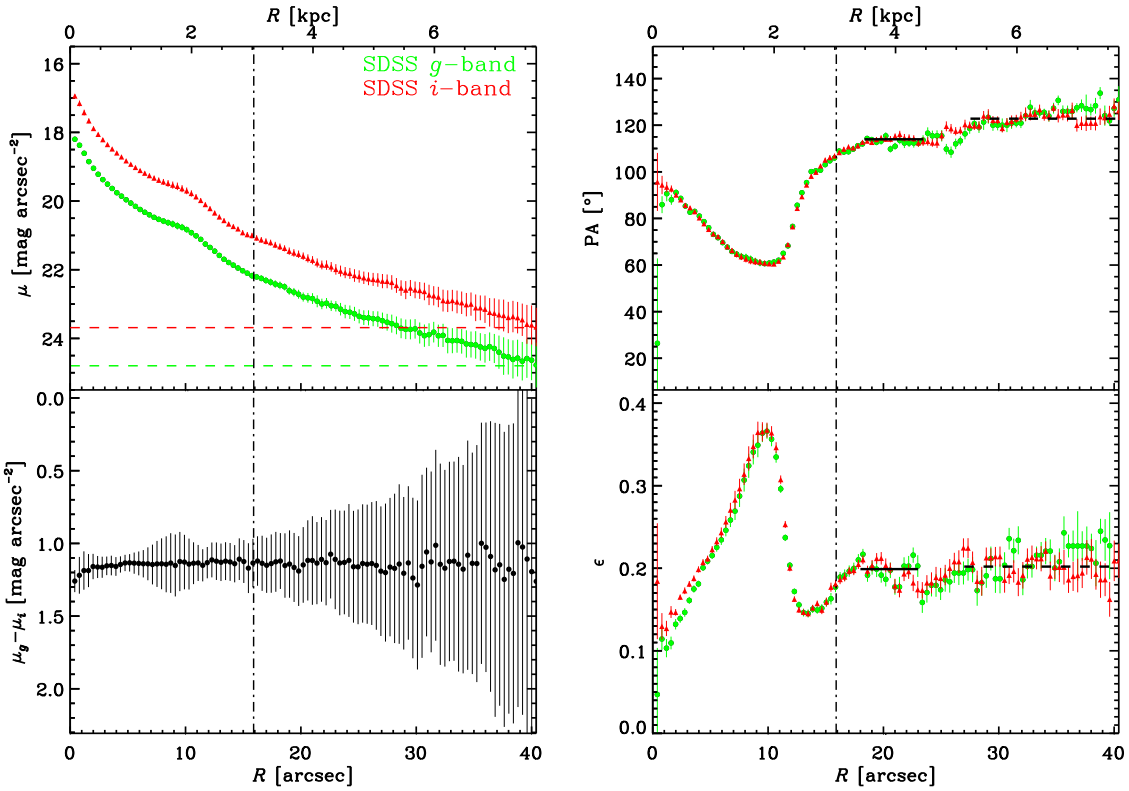

Figure 2.2: Isophotal parameters of NGC 4264 from the SDSS g-band (*green*) and i-band (*red*) images as a function of the semi-major axis distance. The radial profiles of surface brightness (*top-left panel*), $g - i$ colour index (*bottom-left panel*), position angle PA (*top-right panel*), and ellipticity ϵ (*bottom-right panel*) are shown. The measured surface brightnesses are not corrected for cosmological dimming, Galactic absorption, or K correction. The *horizontal dashed lines* in the *top-left panel* correspond to the sky level in each band. The *horizontal solid* and *dashed segments* in the *top* and *bottom-right panels* give the mean values of the PA and ϵ, respectively and mark the extension of the radial range which we adopted to calculate them. The *vertical dot-dashed lines* correspond to the bar radius.

similar, so the slight inconsistency of the two bands produces a colour profile which can be considered nevertheless satisfactory. The PA decreases from PA $\sim 95°$ to PA $\sim 60°$ in the inner 10 arcsec, where ϵ peaks to $\epsilon \sim 0.37$. The PA then steadily rises outwards to PA $\sim 110°$ at $R \sim 16$ arcsec, while ϵ falls to $\epsilon \sim 0.15$ at $R \sim 13$ arcsec and it increases to $\epsilon \sim 0.19$ at $R \sim 16$ arcsec. The PA shows a constant behaviour of PA $\sim 60°$ around $R \sim 9$ arcsec, corresponding to the region of the peak in ϵ.

The presence of a local maximum in the ϵ radial profile, which corresponds to a nearly constant PA, is a typical feature of barred galaxies (e.g., Wozniak et al., 1995; Aguerri et al., 2009) and is due to the shape and orientation of the stellar orbits of the bar (e.g., Contopoulos & Grosbol, 1989; Athanassoula, 1992). Further out, the PA of NGC 4264 rises to PA $\sim 120°$ at the farthest measured radius, while ϵ remains constant.

Table 2.1: Isophotal analysis of NGC 4264 before and after masking the side of the SDSS g-band image near NGC 4261.

NGC 4264 - full image			
Radial range [arcsec]	PA [°]	ϵ	i [°]
18 – 23	114.0 ± 1.2	0.199 ± 0.008	36.7 ± 0.7
27 – 41	122.8 ± 2.4	0.20 ± 0.02	37 ± 1
NGC 4264 - masked image			
18 – 23	113.2 ± 2.6	0.20 ± 0.01	36 ± 1
27 – 41	122.3 ± 6.1	0.20 ± 0.02	37 ± 2

We repeated the ellipse fitting of the galaxy isophotes after masking the half of the NGC 4264 image on the side of NGC 4261. We found the same radial profiles of PA and ϵ as those we measured on the unmasked image. We therefore double-checked that the subtraction of the modelled light contribution of NGC 4261 was performed well and we concluded that the isophotal twist measured in the outer regions of NGC 4264 is not a spurious effect due to residual surface brightness contributed by NGC 4261.

To quantify such an isophotal twist, we derived the mean PA of the galaxy isophotes in two different radial ranges corresponding to the inner and outer portion of the disc, respectively. We fixed the lower limit of the inner radial range to be just outside the bar-dominated region ($R = 18$ arcsec) and the upper limit of the outer range to be at the farthest observed radius ($R = 41$ arcsec). We defined the extension of the radial ranges by fitting the PA measurements with a straight line and considered all the radii where the line slope was consistent with being zero within the associated root mean square error. The two regions have the same ϵ ($\epsilon \sim 0.20$) and therefore the discs have the same inclination ($i = \arccos(1 - \epsilon) \sim 37°$ for an infinitesimally thin disc),they but are characterised by significantly different PAs (ΔPA $\sim$ 10°). The best-fitting ellipses are shown in Fig. 2.3, while results are reported in Table 2.1, together with the results obtained masking the half of the NGC 4264 image on the side of its companion.

Previous measurements of the PA and ϵ of NGC 4264 were obtained by Krajnović et al. (2011) by fitting the galaxy surface brightness distribution from the SDSS r-band image using all the available radial range and with no distinction between the inner and outer region of the disc. They found PA $= 119\overset{\circ}{.}8 \pm 5\overset{\circ}{.}5$, which is in between and consistent within the errors with our two estimates, and $\epsilon = 0.19 \pm 0.01$, which fully agrees with our findings.

Finally, to exclude that the behaviour of the PA is due to the presence of a warp or spiral arms in the disc of the galaxy, we analysed the residual images of NGC 4264. We ran ELLIPSE fixing the values of the centre and adopting the two PAs reported in Table 2.1 corresponding to the full image. Then we modelled the galaxy using the IRAF task BMODEL and subtracted it from the SDSS i-band image. No such structure is visible in the residual images (see e.g., Fig. 2.4 obtained with PA $= 114\overset{\circ}{.}0 \pm 1\overset{\circ}{.}2$).

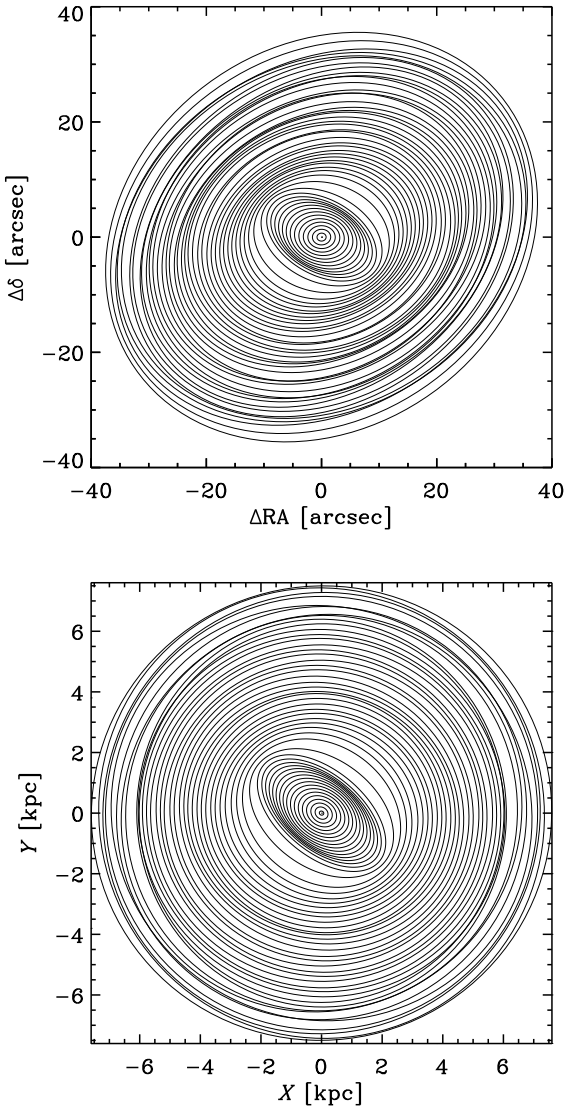

Figure 2.3: *Top panel*: best-fitting ellipses to the isophotes of the SDSS i-band image of NGC 4264. *Bottom panel*: best-fitting ellipses after deprojection to the inner disc plane ($i = 36.^\circ7$, PA $= 114.^\circ0$). The FOV of the original image is oriented with North up and East left. Only one in two ellipses is drawn for sake of clarity.

2.3.3 Photometric decomposition

We derived the structural parameters of NGC 4264 by applying the GASP2D algorithm to the sky-subtracted SDSS i-band image of the galaxy. We modelled the galaxy surface brightness in each image pixel to be the sum of the light contribution of the bulge, disc, and bar. We assumed that their isophotes are elliptical and centred on the galaxy centre (x_0, y_0), with constant values of $\mathrm{PA_{bulge}}$, $\mathrm{PA_{disc}}$, $\mathrm{PA_{bar}}$ and the axial ratios q_{bulge}, q_{disc}, and q_{bar}, respectively.

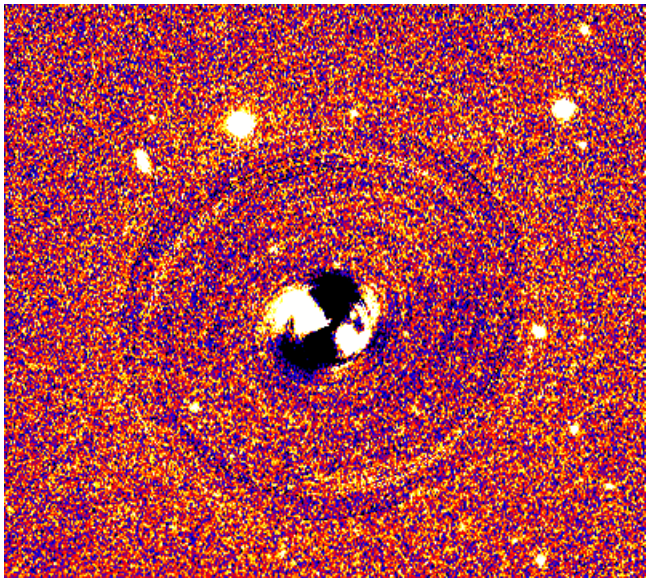

Figure 2.4: Residual image after subtracting the model image obtained with a fixed value of the PA ($114\overset{\circ}{.}0 \pm 1\overset{\circ}{.}2$) from the SDSS i-band image of NGC 4264. The FOV is 2.6×2.4 arcmin^2 with North up and East left.

We did not account for other luminous components, such as rings or spiral arms.

We modelled the bulge with a Sérsic law (Sérsic, 1968):

$$I_{\rm bulge}(x,y) = I_{\rm e} 10^{-b_n[(r/r_{\rm e})^{1/n}-1]}, \tag{2.1}$$

where (x, y) are the coordinates of each image pixel, $r_{\rm e}$ is the effective radius, $I_{\rm e}$ is the surface brightness at $r_{\rm e}$, n is the shape parameter of the surface brightness profile, and $b_n = 0.868n - 0.142$ is a normalisation coefficient (Caon et al., 1993). The distance r of each image pixel from the galaxy centre is

$$\begin{aligned} r(x,y) \;\; = \;\; & \big[(-\Delta x \sin {\rm PA}_{\rm bulge} + \Delta y \cos {\rm PA}_{\rm bulge})^2 + \\ & (\Delta x \cos {\rm PA}_{\rm bulge} - \Delta y \sin {\rm PA}_{\rm bulge})^2 / q^2_{\rm bulge}\big]^{1/2} \end{aligned} \tag{2.2}$$

where $\Delta x = x - x_0$ and $\Delta y = y - y_0$. The total luminosity of the bulge is

$$L_{\rm bulge} = \frac{2\pi n I_{\rm e} r_{\rm e}^2 e^{b_n}}{b_n^{2n}} q_{\rm bulge}\ \Gamma(2n). \tag{2.3}$$

We considered the disc to follow a double exponential law (Méndez-Abreu et al., 2017):

$$I_{\rm disc}(x,y) = \begin{cases} I_0 e^{-r/h_{\rm in}}, & \text{if } r \le r_{\rm break} \\ I_0 e^{-r_{\rm break}(h_{\rm out}-h_{\rm in})/h_{\rm out}} e^{-r/h_{\rm out}}, & \text{if } r > r_{\rm break} \end{cases}, \tag{2.4}$$

where I_0 is the central surface brightness, $r_{\rm break}$ is the break radius at which the slope of the

surface brightness profile changes, and $h_{\rm in}$ and $h_{\rm out}$ are the scalelengths of the inner and outer exponential profiles. The distance r of each image pixel from the galaxy centre is

$$\begin{aligned} r(x,y) &= \big[(-\Delta x \sin \mathrm{PA_{disc}} + \Delta y \cos \mathrm{PA_{disc}})^2 + \\ &\quad (\Delta x \cos \mathrm{PA_{disc}} - \Delta y \sin \mathrm{PA_{disc}})^2 / q_{\rm disc}^2\big]^{1/2}, \end{aligned} \tag{2.5}$$

and the total luminosity of the disc in the axisymmetric case is

$$L_{\rm disc} = \begin{cases} 2\pi I_0 q_{\rm disc} h_{\rm in}^2, & \text{if } r \le r_{\rm break} \\ 2\pi I_0 q_{\rm disc} e^{-r_{\rm break}(h_{\rm out}-h_{\rm in})/h_{\rm out}} h_{\rm out}^2, & \text{if } r > r_{\rm break} \end{cases}. \tag{2.6}$$

Finally, we parametrised the bar with a Ferrers law (Ferrers, 1877; Aguerri et al., 2009), as described in Sec. 1.1.

The best-fitting values of the structural parameters of the bulge, disc, and bar are returned by GASP2D by performing a χ^2 minimization. We weighted the surface brightness of the image pixels according to the variance of the total observed photon counts due to the contribution of both galaxy and sky, which we calculated by taking into account the photon noise, gain and read-out noise of the detector. We adopted the same mask image as that built for the isophotal analysis and excluded the masked pixels from the fit. We handled the seeing effects by convolving the model image with a circular Moffat PSF with the shape parameters (FWHM = 1.18 arcsec, $\beta = 2.99$) measured directly from the stars in the image. We hold $q_{\rm disc}$ fixed (0.798), because of the constant ϵ measured from the isophotal analysis, and $r_{\rm break} = 24.3$ arcsec (61 pixels; the end of the inner disc from a visual inspection of the surface brightness radial profile), to allow to find the remaining parameters. We adopted a double exponential law for the disc after checking that the residuals in the outer regions have a median value consistent with 0 mag arcsec^{-2}, whereas they systematically rise from 0 to 0.4 mag arcsec^{-2} if a single exponential is adopted.

We estimated the errors on the best-fitting structural parameters of NGC 4264 by analysing the images of a sample of mock galaxies generated by Méndez-Abreu et al. (2017) with Monte Carlo simulations and mimicking the instrumental setup of the available SDSS image, which allows to cover a large variety of possible morphologies (see Méndez-Abreu et al., 2008, 2014, 2017, for a discussion). They assumed their mock galaxies to be at a distance of 67 Mpc, the median value of their sample, and we checked our galaxy is in the same distance range. Moreover, we analysed the barred galaxies with total apparent magnitudes in the range $12 \le m_i \le 13$ mag to match the characteristics of NGC 4264. For the bulge ($I_{\rm e}$, $r_{\rm e}$, n), disc ($I_{0,\rm disc}$, $h_{\rm in}$, $h_{\rm out}$) and bar surface brightness parameters ($I_{0,\rm bar}$,$a_{\rm bar}$), we adopted the mean and standard deviation of the relative errors of the mock galaxies as the systematic and statistical errors of the observed galaxies, respectively. For $q_{\rm bulge}$, $q_{\rm bar}$, $\mathrm{PA_{bulge}}$, $\mathrm{PA_{disc}}$, and $\mathrm{PA_{bar}}$ we adopted the mean and standard deviation of the absolute errors of the mock galaxies as the systematic and statistical errors $\sigma_{\rm syst}$ and $\sigma_{\rm stat}$ of the observed galaxies, respectively. We computed the errors as $\sigma^2 = \sigma_{\rm stat}^2$, since the systematic errors are negligible compared to the statistical ones.

Figure 2.5 shows the SDSS i-band image, GASP2D best-fitting image, and residual image

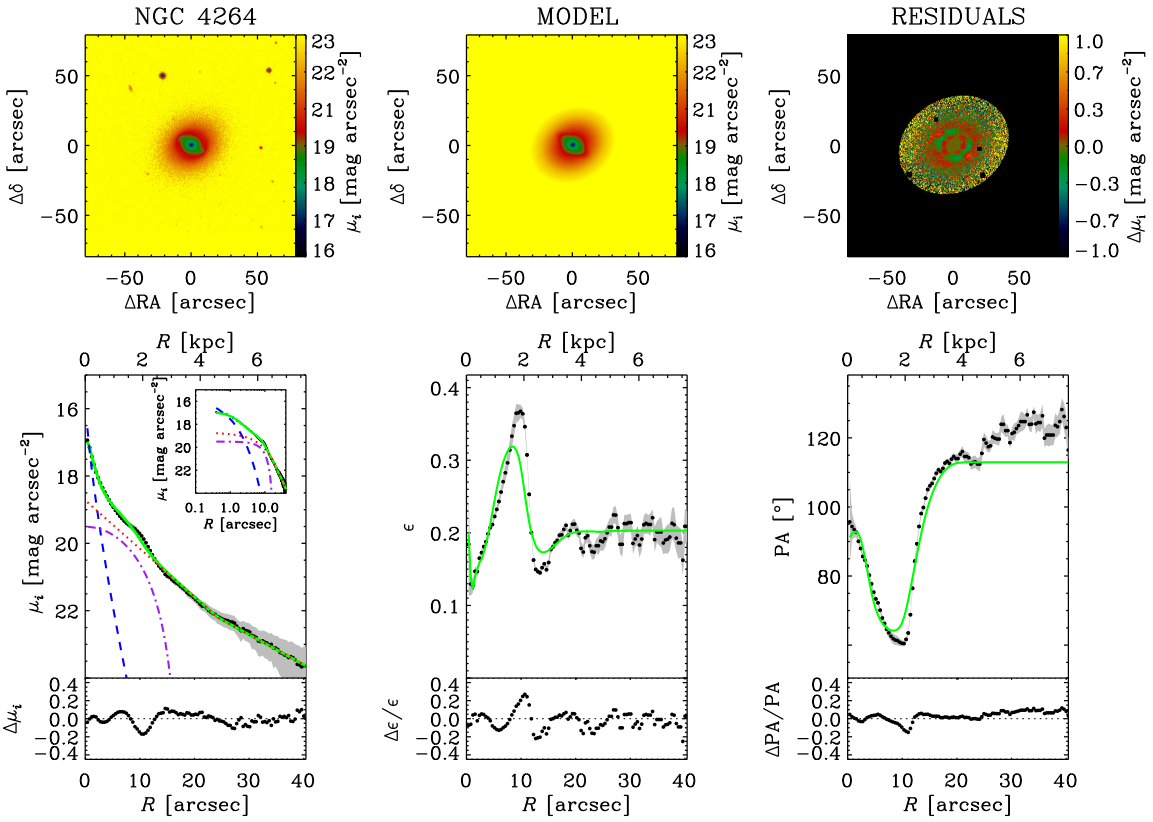

Figure 2.5: Two-dimensional photometric decomposition of the SDSS i-band image of NGC 4264, as obtained from GASP2D. *Top panels*: maps of the observed, modelled, and residual (observed−modelled) surface brightness distributions. The FOV is oriented with North up and East left. The black areas in the residual image correspond to pixels excluded from the fit. *Bottom panels*: radial profiles of surface brightness, PA, and ϵ from the isophotal analysis of the observed (*black dots*) and seeing-convolved (*green solid line*) modelled image and their corresponding difference. The surface brightness radial profiles of the best-fitting bulge (*blue dashed line*), bar (*violet dot-dashed line*), and disc (*red dotted line*) are also shown in both linear and logarithmic scale for the semi-major axis distance to the centre of the galaxy.

Table 2.2: Bulge, disc and bar structural parameters from the photometric decomposition of NGC 4264.

Bulge	
$\mu_{\rm e}$	18.23 ± 0.04 mag arcsec^{-2}
$r_{\rm e}$	1.53 ± 0.03 arcsec
n	1.38 ± 0.03
$q_{\rm bulge}$	0.77 ± 0.01
$\rm PA_{bulge}$	$96\overset{\circ}{.}7 \pm 0\overset{\circ}{.}9$
$L_{\rm bulge}/L_{\rm T}$	0.09
Disc	
μ_0	18.72 ± 0.01 mag arcsec^{-2}
$h_{\rm in}$	7.6 ± 0.1 arcsec
$h_{\rm out}$	12.2 ± 0.3 arcsec
$r_{\rm break}$	24.3 ± 0.4 arcsec
$q_{\rm disc}$	0.796 ± 0.002 arcsec
$\rm PA_{disc}$	$113\overset{\circ}{.}0 \pm 0\overset{\circ}{.}1$
$L_{\rm disc}/L_{\rm T}$	0.78
Bar	
$\mu_{\rm bar}$	19.51 ± 0.01 mag arcsec^{-2}
$a_{\rm bar}$	17.31 ± 0.05 arcsec
$q_{\rm bar}$	0.412 ± 0.001 arcsec
$\rm PA_{bar}$	$56\overset{\circ}{.}4 \pm 0\overset{\circ}{.}1$
$L_{\rm bar}/L_{\rm T}$	0.13

of NGC 4264. The values of the best-fitting structural parameters and corresponding errors are reported in Table 2.2.

NGC 4264 hosts a small and nearly exponential bulge and a large anti-truncated disc, which is characterised by an outer scalelength larger than the inner one. The bulge and disc contribute 9 and 78 per cent of the galaxy luminosity, respectively. GASP2D does not allow to fit separately the PA for the inner and outer regions of the disc. The best-fitting value of the disc PA ($\rm PA_{disc} = 113\overset{\circ}{.}0 \pm 0\overset{\circ}{.}1$) is consistent within the errors with the value we measured from the isophotal analysis for $18 < R < 23$ arcsec ($\rm PA = 114\overset{\circ}{.}0 \pm 1\overset{\circ}{.}2$). This is due to the fact that $\rm PA_{disc}$ is driven by the surface brightness distribution of the inner portion of the galaxy, since the image pixels are weighted according to their S/N ratio and GASP2D does not allow to fit different values of PA inside and outside the break radius in the case of a double-exponential disc. Although the bar never dominates the galaxy surface brightness, it remarkably contributes 13 per cent of the galaxy luminosity.

2.4 Integral-field spectroscopy

2.4.1 Spectra acquisition and reduction

The spectroscopic observations of NGC 4264 were carried out in service mode on 18 and 20 March 2015 (Prog. Id. 094.B-0241(A); P.I.: E.M. Corsini) with MUSE (Bacon et al., 2010) mounted on the Yepun Unit Telescope 4 of VLT at the Paranal Observatory (Chile) of the European Southern Observatory (ESO).

We configured MUSE in Wide-Field Mode and nominal filter. This set up ensured a FOV of 1×1 arcmin^2 with a 0.2×0.2 arcsec^2 spatial sampling and wavelength coverage of 4800–9300 Å with a spectral sampling of 1.25 Å pixel^{-1} and a nominal spectral resolution corresponding to FWHM= 2.71 Å at 4800 Å and 2.59 Å at 9300 Å.

We split the observations in three observing blocks (OBs) to map the entire galaxy along the photometric major axis for a field coverage of 2.0×1.7 arcmin^2. We organised each OB to perform four pointings. The first pointing was on the nucleus of the galaxy and the second one was a sky exposure on a blank sky region a few arcmins away from the galaxy nucleus. The third and fourth pointings were at an eastward and westward offset along the galaxy major axis at a distance of 20 arcsec from the galaxy nucleus, respectively. The exposure time of the on-target and on-sky exposures was 780 sec and 300 sec, respectively. In the second and third OB, the pointings were respectively rotated by 90° and 180° with respect to the first OB in order to average the spatial signatures of the 24 IFUs on the FOV. During both nights the seeing reached a mean value of FWHM $\sim$ 1 arcsec. Along with the target and sky observations, day-time (including bias, lamp flatfield, and arc lamp exposures) and twilight (including sky flatfield and spectro-photometric standard exposures) calibration exposures were taken following the standard calibration plan.

We performed the data reduction using the MUSE pipeline version 1.6.2 (Weilbacher et al., 2012) under the ESOREFLEX environment (Freudling et al., 2013). The steps included bias and overscan subtraction, lamp flatfielding to correct the pixel-to-pixel response variation of the detectors and illumination edge effects between the detectors, wavelength calibration, determination of the line spread function, sky flatfielding to correct the large-scale illumination variation of the detectors, sky subtraction, and absolute flux calibration with correction for atmospheric transmission and differential refraction. We combined the twilight flatfield exposures following the same observing pattern of the on-target and on-sky exposure, producing a master twilight datacube to determine the effective spectral resolution and its variation across the FOV. We found an instrumental full width at half maximum FWHM = 2.80 Å (instrumental velocity dispersion $\sigma_{\rm strum}$ = 69 km s^{-1}) with a negligible variation over the FOV and in the wavelength range between 4800 and 5600 Å which we analysed to measure the stellar kinematics (see also Sarzi et al., 2018).

We estimated the sky contribution by fitting the sky continuum and emission lines on the on-sky exposures. We subtracted the resulting sky model spectrum from each spaxel of the on-target and on-sky exposures. We aligned the sky-subtracted on-target exposures using the common bright sources in the FOV as reference, to produce a combined datacube of the galaxy. Even so the resulting sky-subtracted datacube was characterised by a residual

sky contamination, which we further cleaned using the Zurich Atmospheric Purge (ZAP) algorithm version 1.1 (Soto et al., 2016). We ran ZAP within the ESOREFLEX environment using a dedicated workflow distributed with the MUSE pipeline. ZAP evaluates the principal components of the sky residuals by analysing a datacube obtained by the combination of all the individual sky-subtracted on-sky exposures. Then ZAP calculates the eigenvalues of these principal components in each spaxel of the combined sky-subtracted datacube of the galaxy and subtracts from it the best-fitting model of the residual sky lines. Unfortunately, we were left with residuals from the sky-line subtraction in the wavelength range centred on the Ca II$\lambda\lambda 8498, 8542, 8662$ absorption-line triplet.

Figure 2.6 shows the image of NGC 4264 obtained by collapsing the resulting sky-cleaned datacube of the galaxy along the spectral direction.

2.4.2 Stellar kinematics and circular velocity

We measured the stellar and ionized-gas kinematics of NGC 4264 from the sky-cleaned datacube of the galaxy using the Penalized Pixel-Fitting (PPXF; Cappellari & Emsellem 2004) and the Gas and Absorption Line Fitting (GANDALF; Sarzi et al. 2006) IDL algorithms, which we adapted to deal with MUSE datacubes.

We spatially binned the datacube spaxels to increase the S/N ratio of each spectrum and ensure a reliable extraction of the relevant kinematic parameters. We adopted the adaptive spatial binning algorithm by Cappellari & Copin (2003) based on a Voronoi tessellation to obtain a target $S/N = 40$ for each spatial bin, where the signal and noise are obtained in each spaxel using the spectral range between 4800 and 5600 Å and calculating the median of the flux in the wavelength range and the square root of the variance given by the pipeline, respectively. We selected this wavelength range to match the band of the SDSS image used in the application of the TW method (see Sec. 2.5.3).

The spaxels mapping the central regions of the galaxy remained unbinned since their S/N largely surpassed this limit. The resulting spectra are characterised by a maximum $S/N \sim 80$ in the innermost spaxels corresponding to the galaxy centre and a minimum $S/N \sim 20$ in the outermost spatial bins of the galaxy disc. We rebinned each spectrum along the dispersion direction to a logarithmic scale.

For each spatial bin, we convolved a linear combination of 229 stellar spectra available in the ELODIE library ($R = 10000$, $\sigma_{\rm instr} = 13$ km s^{-1}; Prugniel & Soubiran 2001) with a line-of-sight velocity distribution (LOSVD) modelled as a truncated Gauss-Hermite series (Gerhard, 1993; van der Marel & Franx, 1993).

We selected the stellar spectra to fully cover the parameter space of the effective temperature ($T_{\rm eff}$, from 3000 to 60000 K), surface gravity ($\log g$, from -0.3 to $+5.9$ dex), and metallicity ([Fe/H], from -3.2 to $+1.4$ dex) of the ELODIE library and we broadened the spectra to match the MUSE instrumental resolution. After rebinning the stellar spectra to a logarithmic scale along the dispersion direction, we dereshifted them to rest frame and cropped their wavelength range to match the redshifted frame of the galaxy spectra. Moreover, we added a low-order multiplicative Legendre polynomial (degree = 6) to correct for the different shape of the continuum of the spectra of the galaxy and optimal template due

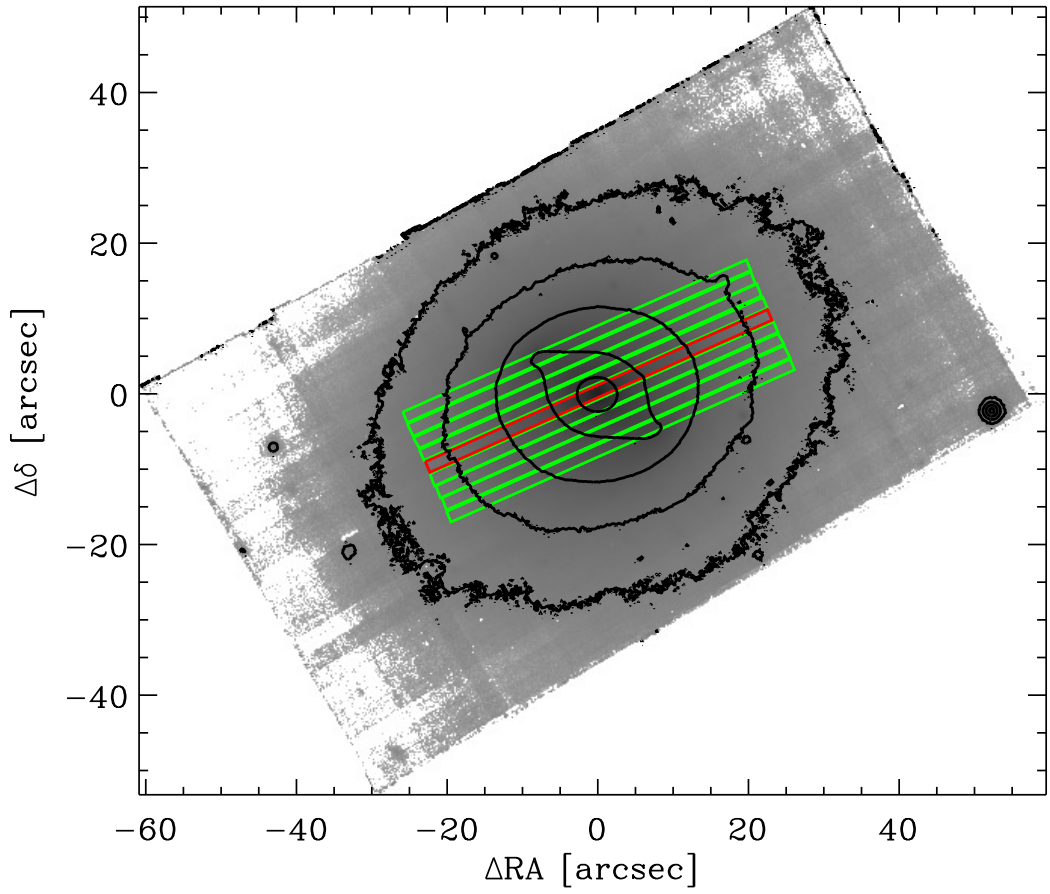

Figure 2.6: Reconstructed image of NGC 4264 obtained by collapsing the MUSE datacube between 4800 and 5600 Å. A few representative isophotes are plotted to show the orientation of the bar and disc components. The FOV is oriented with North up and East left. The *red* and *green rectangles* correspond to the central and offset pseudo-slits adopted to derive the bar pattern speed.

to reddening and large-scale residuals of flat-fielding and sky subtraction. We excluded from the fitting procedure the wavelength ranges with a spurious signal coming from imperfect subtraction of cosmic rays and bright sky emission lines.

The rest-frame galaxy spectra extracted from the central spaxel and from a spatial bin in the disc region are displayed with their best-fitting models in Fig. 2.7 as an example.

By measuring the LOSVD moments in all the available spatial bins in the wavelength range running from 4800 to 5600 Å and centred on the Mg I$\lambda\lambda$5167, 5173, 5184 absorption-

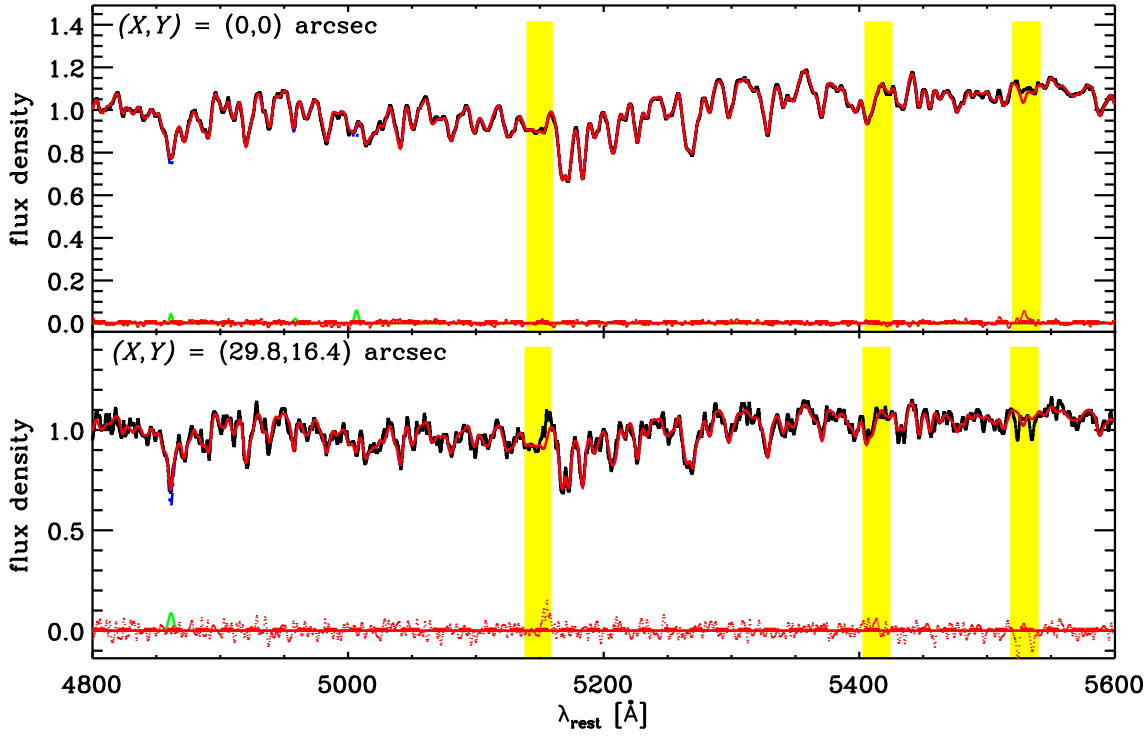

Figure 2.7: *Top panel*: GANDALF fits to rest-frame MUSE spectra (*black lines*) in the very centre of NGC 4264. *Bottom panel*: GANDALF fits in the disc region. The coordinates of the centre of the spatial bin where the spectra are extracted are given. The spectra are characterised by a $S/N \sim 80$ in the centre and $S/N \sim 30$ in the disc region. The best-fitting model (*red line*) is the sum of the spectra of the ionised-gas (*green line*) and stellar component (*blue line*). The latter is obtained by convolving the spectra of the ELODIE stellar library with the best-fitting LOSVD and multiplying them by the best-fitting Legendre polynomials. To allow a more direct comparison, both observed and model spectra are normalised and rescaled. Regions masked and not considered in the fits are highlighted (*yellow*). The residuals (*red dots*) are obtained by subtracting the model from the spectrum and the root mean square of the residuals are shown (*dashed line*).

line triplet, we produced the mean velocity v and velocity dispersion σ maps shown in Fig. 2.9. We assumed the statistical errors on the stellar kinematic parameters to be the formal errors of the PPXF best fit after rescaling the minimum χ^2 to achieve $\chi^2_{\rm min} = N_{\rm dof} = N_{\rm d} - N_{\rm fp}$, with $N_{\rm dof}$, $N_{\rm d}$, and $N_{\rm fp}$ the number of the degrees of freedom, data points, and fitting parameters, respectively (Press et al., 1992). Errors on v and σ range from 0.5 to 5 km s^{-1}. In addition, we simultaneously fitted with Gaussian functions the ionized-gas emission lines present in the selected wavelength range. The [O III]$\lambda\lambda$4959, 5007, [N I]$\lambda\lambda$5198, 5200 emission-line doublets and the H$\beta\lambda$4861 were barely detected in the spectra. Indeed, they have $S/N \gtrsim 3$, where we estimated the residual noise as the standard deviation of the difference between the galaxy and best-fitting stellar spectrum. The ionized-gas emission lines were considered too weak to

obtain a reliable TW measurement based on ionised-gas data.

In central regions the non-axisymmetric velocity field with an S-shaped zero-velocity isocontour is indicative of the presence of the bar. At larger radii, the regular and axisymmetric velocity field is dictated by the disc component. The velocity rises to $v \sim 130$ km s^{-1} within $R \sim 16$ arcsec along the major axis and remains almost constant further out. The central velocity dispersion is $\sigma \sim 90$ km s^{-1}. It steeply rises to $\sigma \sim 110$ km s^{-1} and it decreases to $\sigma \sim 60$ km s^{-1} in the outermost region. It shows a narrow dip at $\sigma \sim 45$ km s^{-1} at $R \sim 20$ arcsec along the major axis. This correspond to a ring located just outside the bar region. The central σ-drop is typical of barred galaxies (Wozniak & Champavert, 2006). We performed a kinemetric analysis of the velocity field using the KINEMETRY IDL algorithm (Krajnović et al., 2006) out to 25 arcsec from the centre, finding a good agreement of PA and ϵ with the photometric results (Fig. 2.8). The large bin sizes and low S/Ns prevented us from extending our analysis to the outer disc. Our findings are consistent within the errors with both the systemic velocity and the LOS heliocentric velocities obtained in the inner 0.4×0.7 arcmin^2 by Cappellari et al. (2011) and Krajnović et al. (2011), respectively.

We derived the circular velocity $V_{\rm circ}$ from the LOS stellar velocity and the velocity dispersion in the inner disc using the asymmetric drift equation (Binney & Tremaine, 2008). Following the prescription of Debattista et al. (2002) and Aguerri et al. (2003), presented in Sec. 1.3.4, we selected the spatial bins within an elliptical annulus with semi-major axis between $a = 18$ and 23 arcsec and $\epsilon = 0.20$ to obtain

$$v_{\rm stars} = \sqrt{V_{\rm circ}^2 + \sigma_R^2 \left[1 - \frac{\sigma_\theta^2}{\sigma_R^2} - R\left(\frac{1}{h_{\rm in}} + \frac{2}{a}\right)\right]} \cos\theta \sin i \tag{2.7}$$

$$\sigma_{\rm stars} = \sigma_R \sqrt{\sin^2 i \left[\sin^2\theta + \frac{\sigma_\theta^2}{\sigma_R^2}\cos^2\theta\right] + \frac{\sigma_{0,z}^2}{\sigma_{0,R}^2}\cos^2 i}, \tag{2.8}$$

where (r, ϕ) and (R, θ) are the polar coordinates defined on the sky plane and on the galactic plane with respect to the LON, respectively. We adopted $h_{\rm in} = 7.6 \pm 0.1$ arcsec and $i = 36\overset{\circ}{.}7 \pm 0\overset{\circ}{.}7$ for the scalelength of the inner disc from the photometric decomposition and inclination from the isophotal analysis, respectively. The three components of the velocity dispersion are assumed to have exponential radial profiles with the same scalelength a but different central values $\sigma_{0,R}$, $\sigma_{0,\theta}$, and $\sigma_{0,z}$, respectively, while the circular velocity is parametrised with a power law $V_{\rm circ} = V_0 R^\alpha$. Moreover, we assumed the epicyclic approximation ($\sigma_\theta/\sigma_R = \sqrt{0.5(1+\alpha)}$), constant circular velocity ($\alpha = 0$), and $\sigma_z/\sigma_R = 0.85$ (typical value for SB0–SB0a galaxies; Aguerri et al. 2015). First of all, we transformed the 2D kinematic maps measured from the MUSE datacube into 1D kinematic radial profiles, by projecting the kinematic data along the disc major axis, given i, PA, and ϕ. Then, we performed a set of 100 Monte Carlo simulations by varying the values of $h_{\rm in}$, i, and σ_z/σ_R within their errors and recovering $V_{\rm circ}$ from a Levenberg-Marquardt least-squares fit to the data in the disc region with the IDL procedure MPCURVEFIT. We adopted the mean estimate of the circular velocity and corresponding standard deviation as the best-fitting $V_{\rm circ}$ value and associated error, respectively. We found $V_{\rm circ} = 189 \pm 10$ km s^{-1}. This estimate is in agreement within the errors with the value

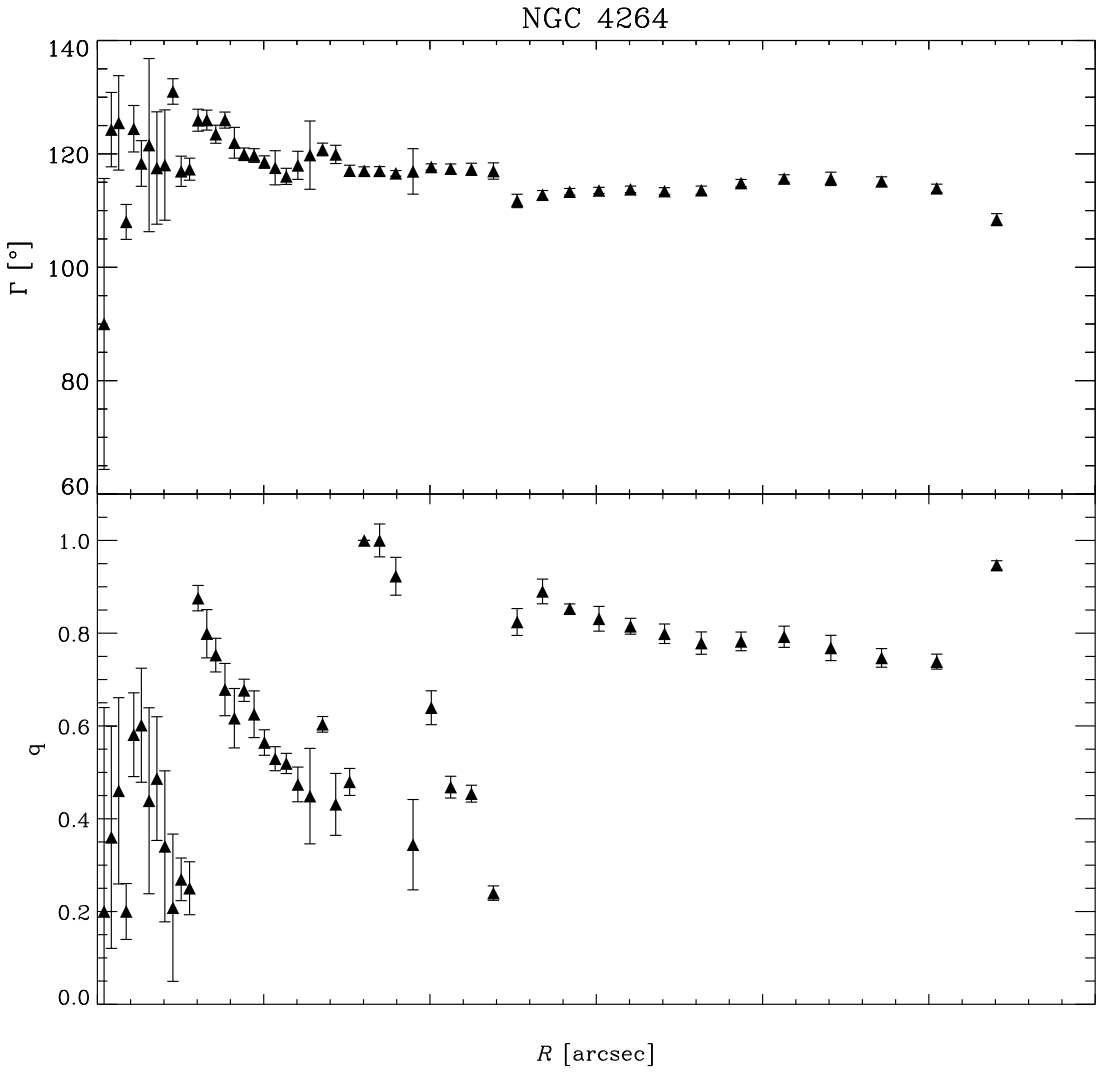

Figure 2.8: Radial profile of the kinematic PA (*top panel*) and flattening (*bottom panel*), obtained with the KINEMETRY analysis of the kinematic maps of NGC 4264.

$V_{\rm circ} = 190.6$ km s^{-1} obtained by Cappellari et al. (2013a) by fitting the stellar kinematics of Krajnović et al. (2011) with a mass-follows-light axisymmetric dynamical model.

The best-fitting velocity and velocity dispersion maps of inner disc kinematics are shown in Fig. 2.9.

2.5 Characterisation of the bar

We derived three observational parameters to fully characterise the bar of NGC 4264. The bar radius $a_{\rm bar}$ is indicative of the radial extension of the stellar orbits supporting the bar (Contopoulos, 1981). The bar strength $S_{\rm bar}$ parametrises the bar prominence and it is an

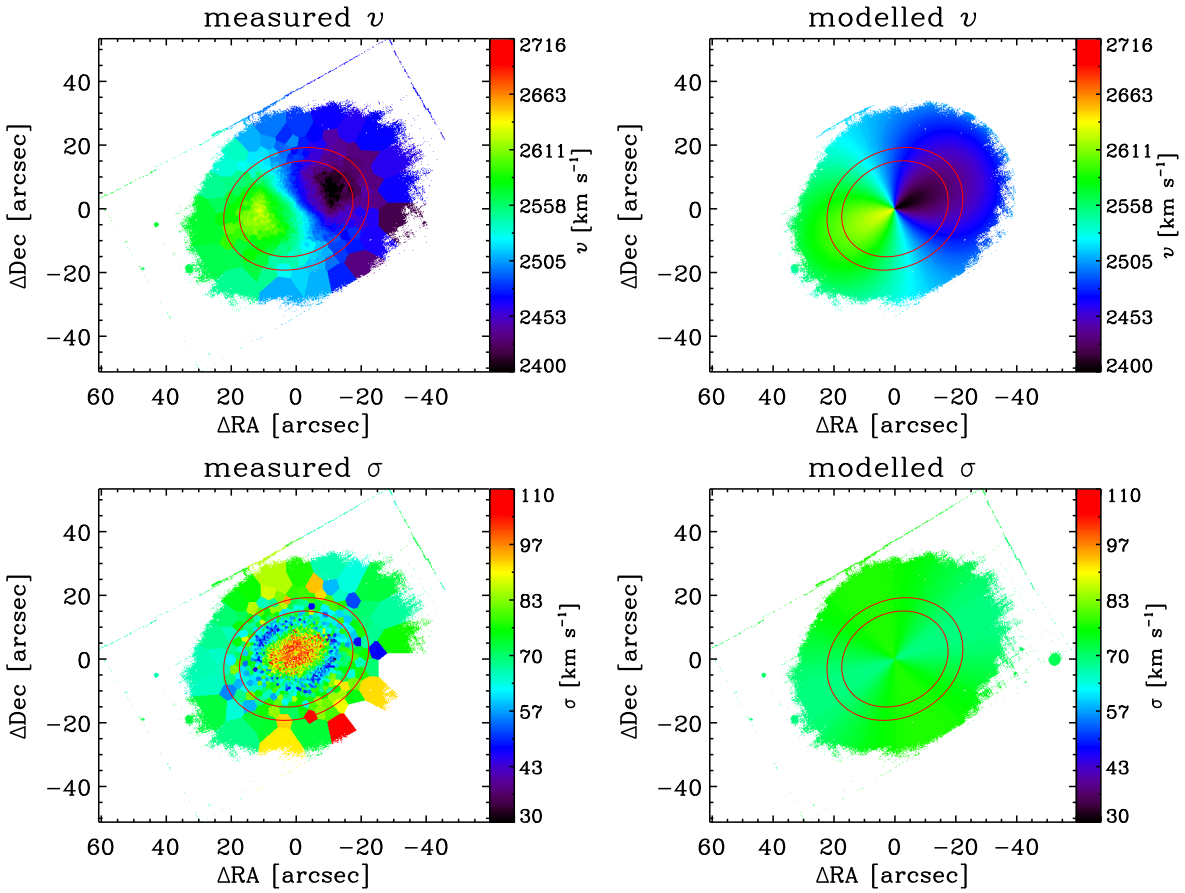

Figure 2.9: *Left panels*: stellar kinematic maps of the mean velocity v and velocity dispersion σ of the LOVSD for NGC 4264 derived from the $S/N = 40$ Voronoi binned MUSE data. *Right panels*: stellar kinematic maps of the best-fitting dynamical model based on asymmetric drift. The FOV is oriented with North up and East left. The region of the inner disc considered for modelling are marked (*red ellipses*).

estimate of the non-axisymmetric forces produced by the bar potential (Buta & Block, 2001a). The bar pattern speed $\Omega_{\rm bar}$ is the angular velocity of the bar (Binney & Tremaine, 2008). The ratio between $\Omega_{\rm bar}$ and $V_{\rm circ}$ defines the corotation radius $R_{\rm cr}$ of the bar. This latter, divided by the $a_{\rm bar}$, gives the bar rotation rate $\mathcal{R}$.

2.5.1 Bar radius

Since bars do not present sharp edges and are often associated with other components (like rings or spiral arms), which may affect the bar boundary identification, it is not easy to determine $a_{\rm bar}$ (Aguerri et al., 2009). Several methods have been developed to derive it, but each of them suffers from some limitations. The most largely used methods are presented in Sec. 1.1 (see Corsini, 2011, for a review). To overcome the problems related to choice of a single measurement method, we derived $R_{\rm bar}$ with three different independent methods, as done for example by Corsini et al. (2003), Aguerri et al. (2015) and Guo et al. (2019): the bar/interbar

intensity ratio (e.g., Aguerri et al., 2009), the PA of the deprojected ellipses which best fit the galaxy isophotes (see e.g., Aguerri et al., 2003, Sec. 2.3.2), and the photometric decomposition of the surface brightness distribution (e.g., Méndez-Abreu et al., 2017, Sec. 2.3.3).

First, we performed a Fourier analysis of the azimuthal luminosity profile (Aguerri et al., 2000), described in Sec. 1.3. The deprojected image is obtained using the values of $\mathrm{PA_{disc}}$ and i related to the inner part of the disc and recovered in Sec. 2.3.2.

Through this analysis the bar radius can be recovered from the luminosity contrasts between the bar and interbar intensity as a function of radial distance. The bar region is where the bar/interbar intensity ratio $I_{\mathrm{bar}}/I_{\mathrm{ibar}} > 0.5 \times [\max(I_{\mathrm{bar}}/I_{\mathrm{ibar}}) - \min(I_{\mathrm{bar}}/I_{\mathrm{ibar}})] + \min(I_{\mathrm{bar}}/I_{\mathrm{ibar}})$ and the bar radius corresponds to the FWHM of the curve given by $I_{\mathrm{bar}}/I_{\mathrm{ibar}}$ as a function of radius (Aguerri et al., 2000, Fig. 2.10). Our estimate of the bar radius is $R_{\mathrm{bar}} = 13.4^{+0.2}_{-0.3}$ arcsec.

A second method to recover the bar radius consists in the analysis of the PA of the deprojected isophotal ellipses (Debattista et al., 2002), as presented in Sec. 1.3. We obtained the radial profiles of ϵ and PA of the deprojected SDSS i-band image using ELLIPSE and considering a fixed value for the centre of the galaxy (Fig. 2.3, bottom panel). We adopted as bar radius the position where the PA changes by a value of 10° from the PA of the ellipse with the maximum ϵ value (Fig. 2.10). A difference of 10° is a reasonable choice because changing this value between 5° and 15° results in bar radius estimates compatible within 1σ. The final value is $R_{\mathrm{bar}} = 17 \pm 3$ arcsec.

Finally, we obtained a third estimate of the bar radius with the photometric decomposition method presented in Sec. 1.3, and discussed for this particular case in Sec. 2.3.3 (Fig. 2.5). We found $R_{\mathrm{bar}} = 17.31 \pm 0.05$ arcsec.

We adopted the mean value from the three measurements and the largest deviation from the mean as bar radius and corresponding error, respectively. This gives $R_{\mathrm{bar}} = 15.9 \pm 2.6$ arcsec. We reported our bar radius measurements in Table 2.3.

2.5.2 Bar strength

In order to estimate the bar strength of NGC 4264, we applied three different methods discussed in Sec. 1.3.

The Fourier analysis allowed us to evaluate S_{bar} (Aguerri et al., 2000), defined as $S_{\mathrm{bar}} = (1/R_{\mathrm{bar}}) \int_0^{R_{\mathrm{bar}}} (I_2/I_0) \mathrm{d}r$ and gave $S_{\mathrm{bar}} = 0.31^{+0.06}_{-0.09}$.

A strictly related definition of bar strength is based on the maximum of the ratio between the amplitudes of the $m = 2$ and $m = 0$ Fourier components (Athanassoula & Misiriotis, 2002; Guo et al., 2019), which resulted in $S_{\mathrm{bar}} = 0.35^{+0.02}_{-0.01}$.

An alternative definition for S_{bar} is based on the axial ratio of the bar (Abraham & Merrifield, 2000), for which we obtained $S_{\mathrm{bar}} = 0.27 \pm 0.01$.

We adopted the mean value from the three measurements and the largest deviation from the mean as bar strength and corresponding error, respectively. This gives $S_{\mathrm{bar}} = 0.31 \pm 0.04$. We reported our bar strength measurements in Table 2.3.

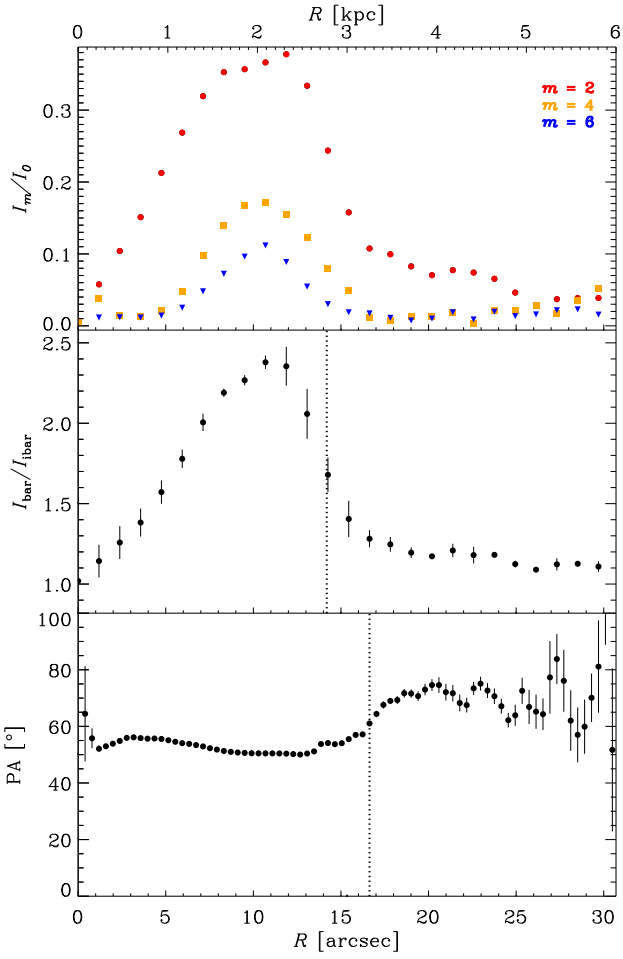

Figure 2.10: Bar radius of NGC 4264 from the analysis of the SDSS i-band image obtained with different methods: relative amplitude I_m/I_0 of the first even Fourier components $m = 2, 4, 6$ (*top panel*) to get the bar/interbar intensity ratio (*middle panel*), and PA of the deprojected best-fitting ellipses (*bottom panel*). The values of the bar radius obtained with each method are shown (*vertical dotted lines*).

2.5.3 Bar pattern speed

NGC 4264 nicely satisfies all the requirements of the model-independent TW method, discussed in Sec. 1.3.3, because it has an intermediate inclination, its bar is elongated at an intermediate PA between the disc major and minor axes and the disc shows no evidence of spiral arms or patchy dust.

We derived the bar pattern speed $\Omega_{\rm bar}$ with the TW method, as given by Eq. 1.30. Thanks to the IFU technique, the pseudo-slits were defined *a posteriori*, from the reconstructed image of NGC 4264. This allowed us to define *a posteriori* a reference frame centred on the galaxy centre.

We defined 9 adjacent pseudo-slits crossing the bar (Fig. 2.6). Each slit has a width of 9

Table 2.3: Bar radius and bar strength of NGC 4264.

$R_{\rm bar}$	
Bar/interbar intensity ratio	$13.4^{+0.2}_{-0.3}$ arcsec
PA of the deprojected isophotal ellipses	17 ± 3 arcsec
Surface brightness decomposition	17.31 ± 0.05 arcsec
$\langle R_{\rm bar} \rangle$	15.9 ± 2.6 arcsec
$S_{\rm bar}$	
Fourier analysis	$0.31^{+0.06}_{-0.09}$
Maximum in I_2/I_0 ratio	$0.35^{+0.02}_{-0.01}$
Maximum in bar axial ratio	0.27 ± 0.01
$\langle S_{\rm bar} \rangle$	0.31 ± 0.04

pixels (1.8 arcsec) to deal with seeing smearing effects, a half length of 125 pixels (25 arcsec) to cover the extension of the inner disc and a PA = 114.°0 corresponding to the PA of the inner disc, to get a physical solution, as described in Sec. 2.5.4.

To measure the photometric integrals of NGC 4264, we analysed the MUSE reconstructed image we obtained by summing the MUSE datacube along the spectral direction over the same wavelength range as adopted to measure the stellar kinematics. For each pseudo-slit, we calculated

$$\langle X \rangle = \frac{\sum_{(x,y)} F(x,y) \mathrm{dist}(x,y)}{\sum_{(x,y)} F(x,y)}, \tag{2.9}$$

where (x, y) are the single pixels in each pseudo-slit, $F(x, y)$ is the flux measured in each pixel in the collapsed image and $\mathrm{dist}(x, y)$ is the distance of each pixel with respect to the line crossing the centre of the pseudo-slit.

By measuring the values of $\langle X \rangle$ as a function of the pseudo-slit length from 10 to 45 arcsec, we found they do not converge and discovered that the reconstructed image was affected by a residual contribution of surface brightness due to the nearby galaxy NGC 4261. The sky subtraction of the MUSE data was performed using a dedicated sky datacube, but the choice of the corresponding pointings did not actually take into account for light contamination due to NGC 4261.

Therefore, we decided to estimate the photometric integrals from the SDSS g-band image of NGC 4264, which was obtained in a wavelength range close to that we are interested in ($\lambda_{\rm eff} = 4640.42$ Å, $\Delta\lambda = 1766.72$ Å; Gunn et al. 1998) and from which we carefully subtracted the surface brightness contribution of NGC 4261 as explained in Sec. 2.3.1.

We modelled the PSF of both the SDSS g-band (FWHM $\sim$ 1.5 arcsec) and MUSE reconstructed image (FWHM $\sim$ 1 arcsec) by fitting with a circular Moffat function several stars in the FOV. We deconvolved the SDSS g-band image with the Richardson-Lucy method

(Richardson, 1972; Lucy, 1974) by applying the IRAF task LUCY. We evaluated the relative increase of the surface brightness in the pixel corresponding to the galaxy centre and adopted a 5 per cent change in surface brightness as stop condition for the number of iterations. Finally, we convolved the deconvolved SDSS image with the PSF of the MUSE reconstructed image and rebinned the resulting SDSS image to the MUSE pixel scale. We extracted the photometric integrals from the convolved and resampled SDSS image in the pseudo-slits we defined on the MUSE reconstructed image. We estimated the errors on $\langle X \rangle$ with a Monte Carlo simulation by generating 100 mock images of the galaxy. For this, we processed the convolved and resampled SDSS image using the IRAF task BOXCAR. Then, we added to each image pixel the photon noise due to the contribution of both the galaxy and sky background and the read-out noise of the detector to mimic the actual image of NGC 4264. We measured the photometric integrals in the mock images and adopted the root mean square of the distribution of measured values as the error for the photometric integral in each pseudo-slit. We checked the convergence of the SDSS photometric integrals as a function of the pseudo-slit length from 10 to 75 arcsec and we found they converge for a length of around 25 arcsec.

To obtain the kinematic integrals, we measured the luminosity-weighted LOS velocity $\langle V \rangle$ from the spectra in the wavelength range between 4800 and 5600 Å, after collapsing each pseudo-slit along the spatial directions and applying the same method as described for the stellar kinematics in Sec. 2.4.2. It should be noticed that this is equivalent to using an explicit luminosity-weight because the spaxels with higher signal give higher contribution in the collapsed spectrum and consequently in the $V_{\rm LOS}$ determination of each pseudo-slit. This corresponds to measuring

$$\langle V \rangle = \sum_{(x,y)} V_{\rm LOS} F(x,y) \tag{2.10}$$

We adopted the formal errors provided by PPXF as errors in the kinematics integrals, following the same prescriptions described in Sec. 2.4.2.

We checked the convergence of the kinematic integrals by measuring their values as a function of the length along the pseudo-slits from 10 to 45 arcsec and we found they converge for a length of around 25 arcsec. The residual background contributed by NGC 4261 does not affect the kinematic integrals which converge in the inner disc region.

We derived $\Omega_{\rm bar}$ of NGC 4264 by fitting a straight-line to the photometric and kinematic integrals using the IDL algorithm FITEXY (Press et al., 1992), taking into account errors on both $\langle X \rangle$ and $\langle V \rangle$ values (Fig. 2.11). The slope of the best-fitting line is $\Omega_{\rm bar} \sin i$ from which we obtained our reference value of $\Omega_{\rm bar} = 13.6 \pm 0.7$ km s^{-1} arcsec^{-1}, which translates to 71 ± 4 km s^{-1} kpc^{-1}.

Although the TW method to derive $\Omega_{\rm bar}$ does not need any modelling, it requires careful measurements to obtain credible values of the photometric and kinematic integrals. To reduce measurement uncertainties associated with the definition of irregularly-shaped pseudo-slits, we always used perfectly rectangular horizontal pseudo-slits after recasting the MUSE datacube, as suggested and tested by Zou et al. (2019). Then, we performed a number of tests to scrutinise the different sources of uncertainties on $\Omega_{\rm bar}$ in order to check the reliability of our

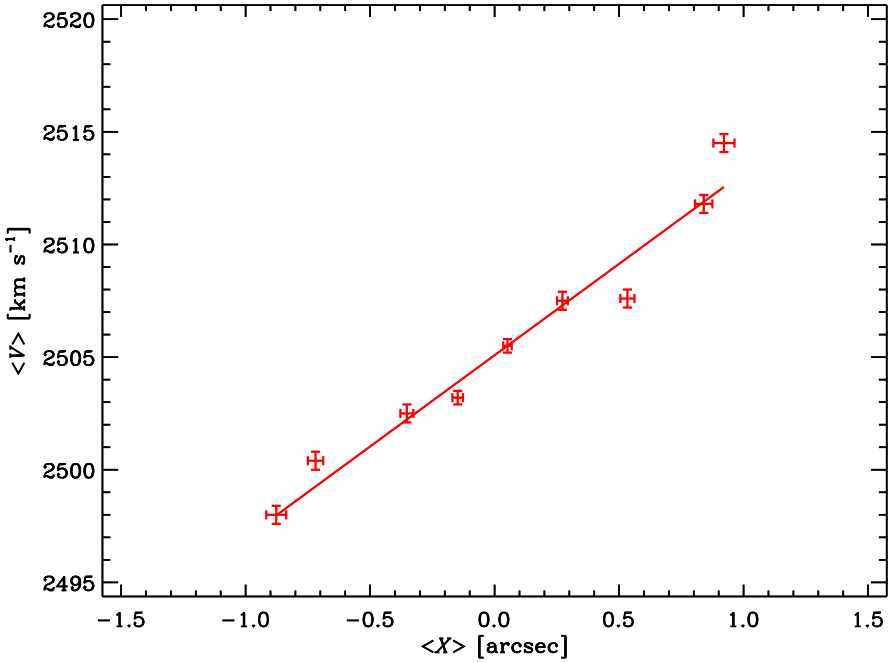

Figure 2.11: Pattern speed of the bar in NGC 4264. The MUSE kinematic integrals $\langle V \rangle$ are plotted as a function of the SDSS photometric integrals $\langle X \rangle$. The best-fitting straight line has a slope $\Omega_{\rm bar} \sin i = 8.1 \pm 0.3$ km s^{-1} arcsec^{-1}.

reference value. We considered narrower (5 pixels = 1.0 arcsec) and wider (15 pixels = 3.0 arcsec) pseudo-slits to halve and double the number of photometric and kinematic integrals to be fitted (test 1). We adopted different PAs for the pseudo-slits ($\mathrm{PA_{in}} - \sigma_{\mathrm{PA_{in}}} = 112.^{\circ}7$, $\mathrm{PA_{in}} + \sigma_{\mathrm{PA_{in}}} = 115.^{\circ}2$) to account for the uncertainty on the PA of the inner disc (test 2). We measured the kinematic integrals on a larger wavelength range (4800 − 5740 Å) to verify the kinematic integrals are not affected by the spectral range. This modified spectral interval was selected in order to avoid regions affected by emission or sky residuals and to use a spectral range still similar to the one adopted for the photometric integrals (test 3). We considered only even and odd pseudo-slits to deal with fully independent data and minimise the impact of spatial correlations on the photometric and kinematic integrals (test 4). The results of these tests are presented in Fig. 2.12 and collected together with the corresponding 1σ uncertainties in Table 2.4.

In addition, we adopted the photometric integrals measured on the reconstructed MUSE image to address the amount of light contamination due to NGC 4261 (test 5, Fig. 2.13 and Table 2.4). All the resulting values of $\Omega_{\rm bar}$ given in Table 2.4 are consistent within the errors with the adopted reference value, except for the case of test 2. As expected (see Corsini, 2011, for a discussion), the misalignment between the pseudo-slits and disc PA is the main source of uncertainty on $\Omega_{\rm bar}$ and it translates into a systematic error which depends on the bar orientation and disc inclination (Debattista, 2003). For NGC 4264, a PA error of about 1° translates into a systematic relative error $\Delta\Omega_{\rm bar}/\Omega_{\rm bar} \simeq 0.2$ in agreement with previous findings by Debattista & Williams (2004).

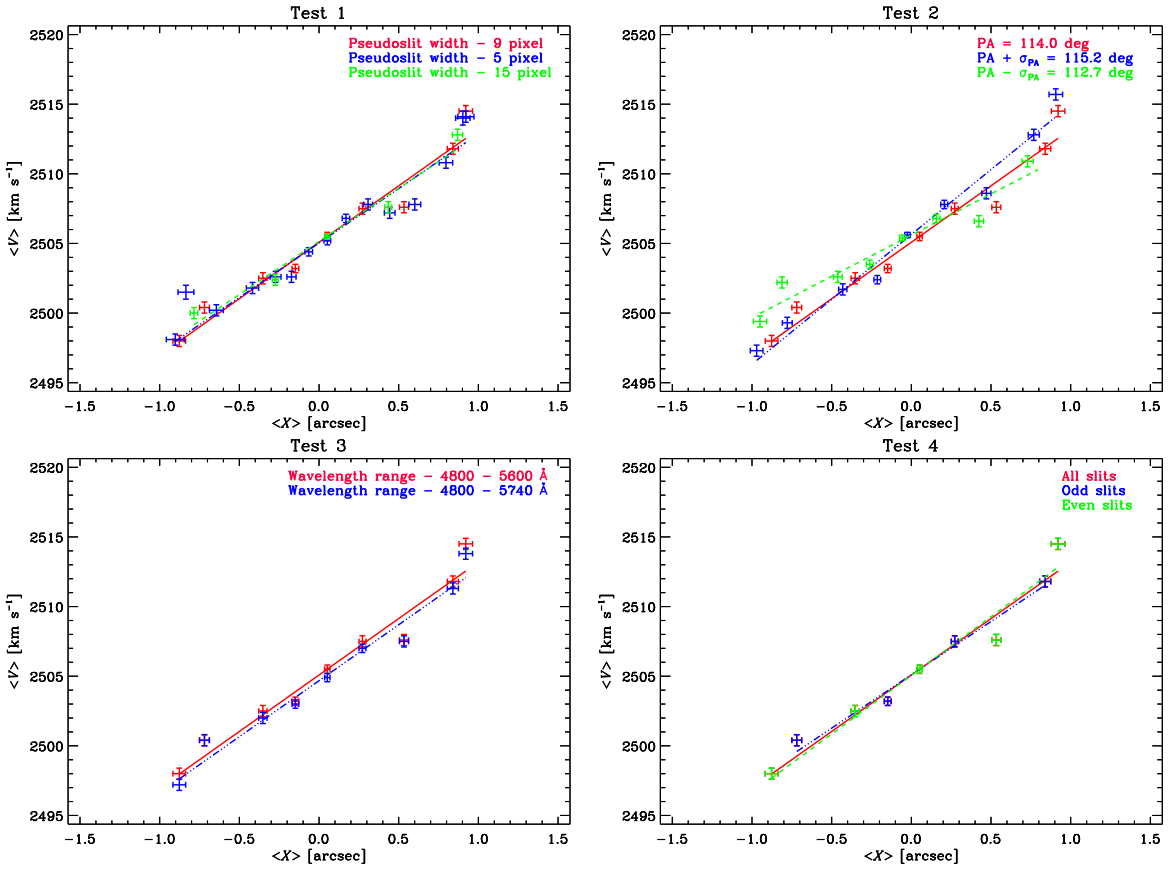

Figure 2.12: Pattern speed of the bar in NGC 4264 as in Fig. 2.11, but for the different tests we performed to assess how the slope of the best-fitting straight line changes as a function of the pseudo-slit width (*top left panel*), pseudo-slit PA (*top right panel*), wavelength range (*bottom left panel*), and fitted pseudo-slits (*bottom right panel*).

Table 2.4: Bar pattern speed and bar rotation rate of NGC 4264.

Parameters	$\Omega_{\rm bar} \pm 1\sigma$ [km s^{-1} arcsec^{-1}]	$\mathcal{R} \pm 1\sigma$
Reference value		
pseudo-slit width: 9 pixel (1.8 arcsec)		
disc PA: 114.°0	13.6 ± 0.7	0.88 ± 0.23
spectral range: 4800 –5600 Å		
Test 1 - different pseudo-slit width		
pseudo-slit width: 5 pixel (1.0 arcsec)	13.1 ± 0.6	0.91 ± 0.24
pseudo-slit width: 15 pixel (3.0 arcsec)	12.8 ± 0.8	0.93 ± 0.26
Test 2 - different pseudo-slit PA		
disc PA: 112.°7	15.6 ± 0.7	0.77 ± 0.20
disc PA: 115.°2	9.9 ± 0.6	1.20 ± 0.34
Test 3 - different spectral range		
spectral range: 4800–5740 Å	13.4 ± 0.7	0.87 ± 0.23
Test 4 - even or odd pseudo-slits		
odd pseudo-slits	12.8 ± 0.9	0.93 ± 0.26
even pseudo-slits	14.1 ± 0.8	0.85 ± 0.23
MUSE photometric integrals		
MUSE $\langle X \rangle$	13.8 ± 0.6	0.86 ± 0.22
Outer disc PA		
PA=122.°8	30 ± 1	0.40 ± 0.10

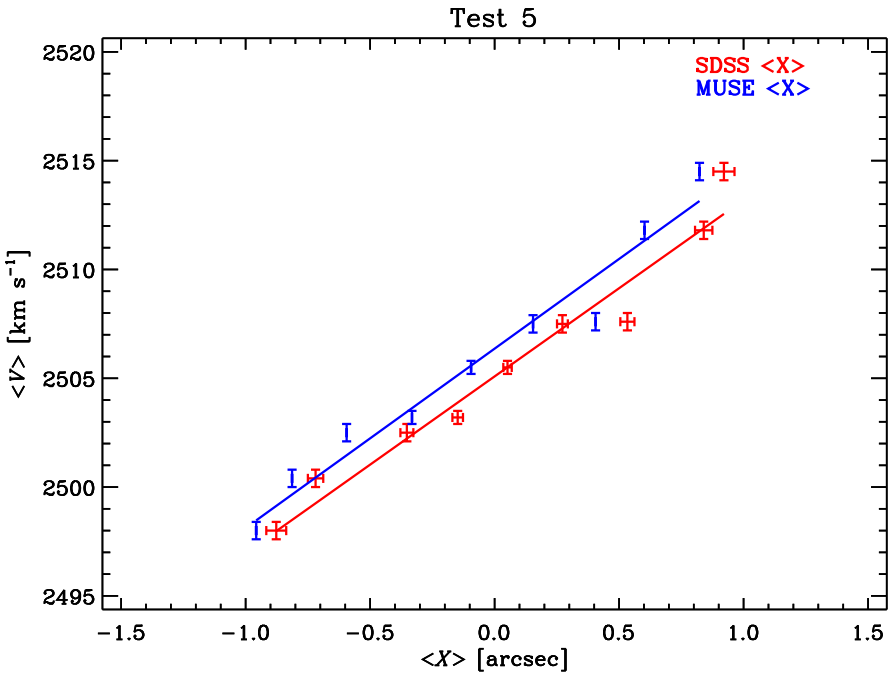

Figure 2.13: Pattern speed of the bar of NGC 4264 as in Fig.2.11, but from the photometric integrals measured in the SDSS image (*red*) and MUSE reconstructed image (*blue*). The best-fitting straight line to the MUSE photometric integrals has slope $\Omega_{\rm bar} = 8.2 \pm 0.2$ km s^{-1} arcsec^{-1}.

Thus, the right identification of the disc PA is crucial for a safe application of the TW (see Zou et al., 2019, for a discussion). NGC 4264 hosts an upbending disc with a twist of the external isophotes (ΔPA $\sim 10°$) moving from the inner to outer regions ($R > 27$ arcsec). We also applied the TW method adopting the PA of the outer disc (PA $= 122\overset{\circ}{.}8$) and extracting the kinematic integrals from 45-arcsec long pseudo-lits to cover the extension of the outer disc. We found $\Omega_{\rm bar} = 30.1 \pm 1.4$ km s^{-1} arcsec^{-1} corresponding to 158 ± 7 km s^{-1} kpc^{-1}. However, this results in an unphysical solution for $\mathcal{R}$ as discussed in Sec. 2.5.4. We were able to recognise this when applying the TW method thanks to the combination of deep SDSS imaging and excellent MUSE IFU spectroscopy in terms of FOV, spatial sampling, and S/N.

2.5.4 Bar rotation rate

We calculated the length of the corotation radius of NGC 4264 ($R_{\rm cr} = V_{\rm circ}/\Omega_{\rm bar} = 14.0 \pm 0.9$ arcsec) from the circular velocity and bar pattern speed estimated from the asymmetric drift equation and the TW method, respectively.

Finally, we derived the ratio of the length of the corotation radius to the bar semi-major axis, which is the bar rotation rate $\mathcal{R} = R_{\rm cr}/R_{\rm bar} = 0.88 \pm 0.23$. This value is consistent within the errors with the estimates of the bar rotation rates we obtained from the various tests assessing the reliability of $\Omega_{\rm bar}$ (Table 2.4). The PA uncertainty translates into a maximal systematic relative error $\Delta\mathcal{R}/\mathcal{R} = 0.38$. Therefore, we concluded that the bar of NGC 4264

is consistent with being rapidly rotating.

On the contrary, if we adopt PA_{out} of the outer disc (as estimated from the isophotal analysis) to derive the bar pattern speed, the corresponding bar rotation rate $\mathcal{R} = 0.40 \pm 0.10$ falls into the regime of the bars extending out of the corotation radius which is unphysical (Contopoulos, 1981). This is due to the fact that the PA of the outer disc is not representative of the region of the disc where the bar lives, but rather is a distortion due to the ongoing interaction with NGC 4261.

2.6 Discussion and conclusions

We measured the broad-band surface photometry and two-dimensional stellar kinematics of NGC 4264, a barred lenticular galaxy at 39.2 Mpc in the region of the Virgo Cluster, to derive the pattern speed of its bar ($\Omega_{bar} = 13.6 \pm 0.7$ km s^{-1} arcsec^{-1}, corresponding to 71 ± 4 km s^{-1} kpc^{-1}) and the ratio of the corotation radius to the bar radius ($\mathcal{R} = 0.88 \pm 0.23$). We showed that NGC 4264 hosts a strong ($S_{bar} = 0.31 \pm 0.04$) and large ($R_{bar} = 15.9 \pm 2.6$ arcsec, corresponding to 3.2 ± 0.5 kpc) bar, which nearly extends out to the corotation radius ($R_{cr} = 14.0 \pm 0.9$ arcsec, corresponding to 2.8 ± 0.2 kpc). This means the bar is rotating as fast as it can, like nearly all the other bars in lenticulars and spirals measured so far (Elmegreen, 1996; Rautiainen et al., 2008; Corsini, 2011; Aguerri et al., 2015; Guo et al., 2019).

The bar of NGC 4264 has properties typical of bars in lenticular galaxies. The radius and strength are consistent with the median values obtained for SB0 galaxies by Aguerri et al. (2009), who analysed the SDSS images of a volume-limited sample of about 2100 disc galaxies out to $z = 0.04$. They derived the bar semi-major axis as the radius at which the maximum in the bar ellipticity was reached or as the radius at which the PA changes by 5° with respect to the value corresponding to the maximum ellipticity (Wozniak et al., 1995) and estimated the bar strength from the maximum ellipticity (Abraham & Merrifield, 2000). The bar rotation rate is consistent within the errors with the mean value calculated by Aguerri et al. (2015) for 17 SB0–SB0/a galaxies for which Ω_{bar} was measured with the TW method.

We took advantage of the extended spectral range, fine spatial sampling, large FOV, and superb throughput of the MUSE IFU spectrograph in combination with wide-field SDSS imaging to deal with the sources of uncertainty in deriving Ω_{bar} and $\mathcal{R}$ of NGC 4264. We confidently constrained the position and LOS velocity of the galaxy centre, maximised the number and S/N of the spectra extracted from the pseudo-slits crossing the bar, carefully derived the orientation and inclination of the galaxy disc, accurately measured the bar radius, and recovered the circular velocity by modelling the stellar kinematics. As a result, the values of Ω_{bar} and $\mathcal{R}$ for the bar of NGC 4264 are amongst the best-constrained ones ever obtained with the TW method. Their statistical relative errors are as small as $\Delta\Omega_{bar}/\Omega_{bar} = 0.06$ and $\Delta\mathcal{R}/\mathcal{R} = 0.26$, respectively. The PA uncertainty translates into a maximal systematic error of 0.21 and 0.38 on Ω_{bar} and $\mathcal{R}$, respectively. Although a wrong assessment of the disc PA introduces a systematic error in the application of the TW method, it does not affect all the galaxy measurements in the same way. So when looking at a sample of galaxies, the misalignment between the pseudo-slits and disc PA will produce a scatter of the bar pattern

speeds and rotation rates rather than a systematic offset with respect to their actual values.

This is a remarkable result not only with respect to early TW measurements based on long-slit spectroscopy (see Corsini, 2011, for a list), but also with respect to those recently derived from IFU spectroscopy (Aguerri et al., 2015; Guo et al., 2019). The combined CALIFA and MaNGA sample counts 66 galaxies, of which 10 have $\mathcal{R} < 1$ at 95 per cent confidence level. After excluding these ultrafast bars, the relative error of $\Omega_{\rm bar}$ measured by averaging among the upper and lower 1σ statistical errors for the remaining 56 galaxies ranges from $\Delta\Omega_{\rm bar}/\Omega_{\rm bar} = 0.03$ o $\Delta\Omega_{\rm bar}/\Omega_{\rm bar} = 22$ with a median value of 0.32. Only 2 galaxies have error bars $\Delta\Omega_{\rm bar}/\Omega_{\rm bar} \lesssim 0.06$, i.e. smaller than those of the bar of NGC 4264. As far as $\mathcal{R}$ is concerned, the relative error is $0.19 < \Delta\mathcal{R}/\mathcal{R} < 1.5$ with a median value of 0.43. Only five galaxies in the combined CALIFA and MaNGA sample have $\Delta\mathcal{R}/\mathcal{R} \lesssim 0.26$, but none of them has $\Delta\Omega_{\rm bar}/\Omega_{\rm bar} \lesssim 0.06$. It should be noticed that as for NGC 4264 also the error budget of the CALIFA and MaNGA samples do not account for systematic errors due, for example, to distance determination and PA uncertainty.

The accuracy on the bar parameters of NGC 4264 is remarkably similar to that of NGC 7079 (Debattista & Williams, 2004), which has the best-constrained pattern speed ($\Delta\Omega_{\rm bar}/\Omega_{\rm bar} = 0.02$) and rotation rate ($\Delta\mathcal{R}/\mathcal{R} = 0.21$) ever measured for a bar using the TW method. It represents the first and only use of Fabry-Perot techniques for measuring the 2D stellar kinematics of a barred galaxy. However, handling this kind of data is generally more difficult with respect to the newly-developed packages for reducing, analysing, and visualising data from IFU spectrographs (see Mediavilla et al., 2011, and references therein), which are now routinely offered at 4m and 8m-class telescopes and which have become nearly standard tools for the systematic investigation of the structure and dynamics of nearby galaxies (e.g., Cappellari et al., 2011; Sánchez et al., 2012; Bundy et al., 2015; Sarzi et al., 2018).

Our analysis of the MUSE dataset of NGC 4264 represents a pilot study for further accurate MUSE measurements of $\Omega_{\rm bar}$ and $\mathcal{R}$ on a well-defined sample of barred galaxies covering different morphological types and luminosities. These would be of considerable interest to severely test the predictions of numerical simulations about the time evolution of bar radius and pattern speed as a function of gas content, luminous and DM distribution (Weinberg, 1985; Debattista & Sellwood, 2000; Athanassoula, 2003; Athanassoula et al., 2013; Martinez-Valpuesta et al., 2017; Algorry et al., 2017). Such a stringent comparison is still missing. For example, Guo et al. (2019) did not find any significant correlation between the bar pattern speed and galaxy properties, like the fraction of DM within the galaxy effective radius or the age and metallicity of the stellar populations inside the bar region. But their findings are severely limited by the large relative errors on $\mathcal{R}$ for the majority of their sample galaxies.

A small misalignment between the direction along which TW integrals are measured and the disc major axis may hamper the determination of $\Omega_{\rm bar}$ (Debattista, 2003). In this work, we showed that IFU spectroscopy alone can not successfully address this issue, but it has to be combined with accurate surface photometry to fine tune the extraction of the TW integrals. Indeed, we found that the bar of NGC 4264 appears to extend considerably beyond its corotation radius ($\mathcal{R} = 0.40 \pm 0.10$) if its pattern speed ($\Omega_{\rm bar} = 30.1 \pm 1.4$ km s^{-1} arcsec^{-1}) is mea-

sured by aligning the pseudo-slits with the major axis of the outermost disc (PA=122.°2±2.°4). This is unphysical for a self-consistent bar, and could be due to an incorrect measurement of either $R_{\rm bar}$ or $R_{\rm cr}$ or both. We measured $R_{\rm bar}$ from the SDSS i-band image of NGC 4264 with three different methods and they give results consistent within the errors. As a consequence, the problem is related to either $V_{\rm circ}$ or $\Omega_{\rm bar}$ or both. We estimated $V_{\rm circ}$ by correcting for asymmetric drift the LOS velocities and velocity dispersions measured from the MUSE spectra. Our value is in agreement within the errors with the one derived by Cappellari et al. (2013a) based on a mass-follows-light axisymmetric dynamical model of the stellar kinematics measured with the SAURON spectrograph (Bacon et al., 2001). This means that we can not trust the measurement of $\Omega_{\rm bar}$, which is very sensitive to the misalignment between the orientation of the TW measurement and the disc major axis (Debattista et al., 2002). We deduce that the PA and ϵ of the outermost isophotes of NGC 4264 are not indicative of the actual orientation and inclination of the disc where the bar lives. For this reason, we restricted our analysis of $\Omega_{\rm bar}$ and $\mathcal{R}$ to the inner disc.

Finally, the measurement of $\mathcal{R}$ of the bar of NGC 4264 allowed us to constrain its formation mechanism. We interpreted the twist of the outer isophotes ($R > 27$ arcsec) of NGC 4264, which are characterised by a rotation of the PA (ΔPA $\sim 10^{\circ}$) and no change of ϵ, as suggestive of a warp due to the ongoing interaction with NGC 4261. The limited number of spatial bins of the stellar velocity field at $R > 25$ arcsec prevented us from confirming this with a kinemetric analysis. However, NGC 4264 is at small projected distance from NGC 4261 (3.5 arcmin corresponding to 30 kpc) and it is seen through its stellar halo. The two galaxies are probably gravitationally bound, with the difference between their systemic velocities ($|\Delta V_{\rm sys,CMB}| = 306 \pm 50$ km s^{-1}; NED[4]) consistent with the velocity dispersion of the rich galaxy group they belong to ($\sigma_{\rm group} = 382$ km s^{-1}; Kourkchi & Tully, 2017).

The surface brightness radial profile of the disc is upbending in the outer regions ($R > 24$ arcsec). This feature is usually explained as the end result of mergers and interactions, which drive outwards migration or direct accretion of part of the stars and dynamically heat the outer region of the disc. An increase of the tangential-to-radial velocity dispersion ratio is expected (see Debattista et al., 2017, for a discussion). Unfortunately, we were not able to constrain the shape of the velocity ellipsoid in the disc region since the measured velocity dispersion was close to the instrumental velocity dispersion provided by our MUSE instrumental setup. The lack of an observed difference between upbending surface brightness radial profiles in barred and unbarred galaxies (Borlaff et al., 2014; Eliche-Moral et al., 2015) and the fact they are less common in barred galaxies, suggests that they are not likely to be formed by the action of the bar (Debattista et al., 2017).

We inspected the SDSS images as well as the residual image of the surface brightness model of NGC 4264 (Fig. 2.5), without finding any clear-cut evidence of tidal tails. Such an undisturbed morphology of NGC 4264, the fact that NGC 4261 is much more massive than NGC 4264 ($L_{\rm N4261}/L_{\rm N4264} = 6$) and their closeness suggest the interaction between the two galaxies is weak. In addition, NGC 4261 is a well studied LINER galaxy. But, Schmitt (2001) pointed out that the possible interaction with NGC 4264 is not a necessary condition

[4]The NASA/IPAC Extragalactic Database is available at `https://ned.ipac.caltech.edu/`

to trigger the nuclear activity of NGC 4261.

Martinez-Valpuesta et al. (2017) investigated with N-body numerical simulations the differences between bars resulting from disc instabilities induced by tidal interactions or self-generated internal processes. In agreement with previous findings (Noguchi, 1987; Salo, 1991; Miwa & Noguchi, 1998; Łokas et al., 2014), they found that bars formed through tidal interaction were born and stay slow ($\mathcal{R} > 1.4$) all along their evolution. The bar rotation rate is found to be $\mathcal{R} \simeq 1.4$ only at the end of an interaction occurred over a long timescale. Since the bar of NGC 4264 is fast, we conclude that its formation was not triggered either by the recent interaction with NGC 4261 nor by a previous interaction with an other galaxy in the region of the Virgo Cluster.

By analysing the MUSE dataset of NGC 4264, we showed that a fine spatial sampling is required to successfully overcome with IFU spectroscopy the problems of the application of the TW method to long-slit observations. This allows the optimal extraction of kinematic and photometric integrals from a large number of pseudo-slits crossing the bar parallel and leads to more efficient and accurate TW measurements. At the same time, only IFU spectroscopy allows to avoid the misalignment between the direction along which TW integrals are measured and the disc major axis which may hamper the determination of $\Omega_{\rm bar}$.

Chapter 3

Bar pattern speeds in CALIFA galaxies - The case of weakly barred galaxies[§]

Abstract About 35 per cent of nearby disc galaxies host a weak bar, for which different formation scenarios, including the weakening of a strong bar and tidal interaction with a companion, have been suggested. Measuring the bar pattern speeds of weakly barred galaxies is a key step to constrain their formation process, but such a systematic investigation is still missing. We aim to investigate the formation process of weak bars by measuring the properties of a sample of 29 weakly barred galaxies, spanning a wide range of morphologies and luminosities. The galaxies were selected to each have an intermediate inclination, a bar at an intermediate angle between the disc axes, and undisturbed morphology and kinematics, to allow the direct measurement of $\Omega_{\rm bar}$. Combining our analysis with previous studies, we compared the properties of weak and strong bars. We measured the bar radii and strengths from SDSS r-band images and the bar pattern speeds and corotation radii from the stellar kinematics obtained by the CALIFA survey. We derived each bar's rotation rate as the ratio between the corotation and bar radii. Thirteen out of 29 galaxies (45 per cent), which were classified as weakly barred from a visual inspection, do not actually host a bar because it was not identified with a Fourier analysis or their central elongated component is not in rigid rotation because the TW method did not provide a credible result for $\Omega_{\rm bar}$. We successfully derived the bar pattern speeds of the other 16 objects. Two of them host an ultrafast bar. Using $S_{\rm bar}$ to differentiate weak and strong bars, we found that weakly barred galaxies host shorter bars with smaller corotation radii than their strongly barred counterparts. Weak and strong bars have similar pattern speeds and rotation rates, which are all consistent with being fast. No difference of the bulge prominence was observed, whereas nearly all the weak bars reside in their disc's inner parts, contrary to strong bars. We thus exclude that bar weakening is only related to the bulge prominence and that the formation of weak bars is triggered by the tidal interaction with a companion. Our results suggest that weak bars may be evolved systems exchanging less angular momentum with other galactic components than strong bars.

[§] *Based on V. Cuomo, J. A. L. Aguerri, E. M. Corsini et al. 2019, A&A, in press, arXiv:1909.01023.*

3.1 Introduction

Since bars show a wide variety of properties in terms of size, luminosity, and shape, disc galaxies are divided into unbarred, weakly, and strongly barred galaxies.

Very little is known about the formation and evolution of weakly barred galaxies. A first pioneering effort to explain the formation of weak bars was done by Kormendy (1979), who found a large amount of lenses with the same size and stellar content of bars by analysing the properties of a sample of ~ 120 galaxies. Therefore, Kormendy (1979) concluded that lenses are the end result of the evolution of bars into nearly-axisymmetric structures. Since the fraction of barred galaxies hosting a lens is very high, since the majority of lenses are located in early-type galaxies with large central concentrations, the mechanism should be secular and possibly involve an interaction with the bulge. This is in conflict with the findings of Laurikainen et al. (2013), who analysed the near-infrared images of ~ 200 early-type galaxies and found that the radius of fully developed lenses is on average ~ 1.3 times larger than that of bars. Recently, Kruk et al. (2018) provided some evidence supporting the idea that bars dissolve into lenses. By analysing the images of ~ 3500 local galaxies from the SDSS (Alam et al., 2015), they found that unbarred discs are bluer than their barred counterparts while unbarred galaxies with a lens are similar to strongly barred galaxies, when considering the colours of discs and bulges, the galaxy masses, the Sérsic indices of the bulges and luminosity ratios. Weakly barred galaxies are much the same as unbarred galaxies since their discs are bluer and their bars are shorter than those in strongly barred galaxies (Abraham et al., 1999).

Debattista et al. (2006) claimed the effect of gas on bar amplitude depends on its physics. If the gas can cool, it rapidly becomes centrally concentrated and only weak bars can form.

Weak bars can also represent the end result of weak interactions. Martinez-Valpuesta et al. (2017) investigated, through numerical simulations, the formation of bars triggered or affected by fast interactions. These bars formed by interactions are slow throughout their lifetime. Low values of the bar pattern speed (corresponding to $\mathcal{R} \sim 2$) have been also found by Łokas (2018) in the late evolutionary stages of tidally-induced bars.

Therefore, measuring the bar pattern speed of a sample of weakly barred galaxies could constrain their formation process. Aguerri et al. (2015) measured the bar pattern speeds of 15 galaxies using the stellar velocity maps provided by the CALIFA survey (Sánchez et al., 2012), while Guo et al. (2019) obtained the bar pattern speeds of another 51 galaxies using the IFU spectroscopic data from the MaNGA survey (Bundy et al., 2015). But, neither Aguerri et al. (2015) nor Guo et al. (2019) included weakly barred galaxies in their samples. To date, the bar pattern speed was measured with the TW method in only one weakly barred galaxy, ESO 139-G0009, which turned out to host a fast bar (Aguerri et al., 2003). The bar pattern speed has been indirectly measured from the velocity field of the ionized/molecular gas in a number of weakly barred galaxies, suggesting that slow bars are hosted especially by late-type spirals, in spite of large uncertainties on $\mathcal{R}$ (Hirota et al., 2009; Font et al., 2017; Salak et al., 2019).

In this Chapter, we aim to investigate the formation of weak bars by measuring the bar radius, strength, and pattern speed with the TW method of a sample of weakly barred galaxies for which IFU spectroscopic data are available from the CALIFA survey. The Chapter

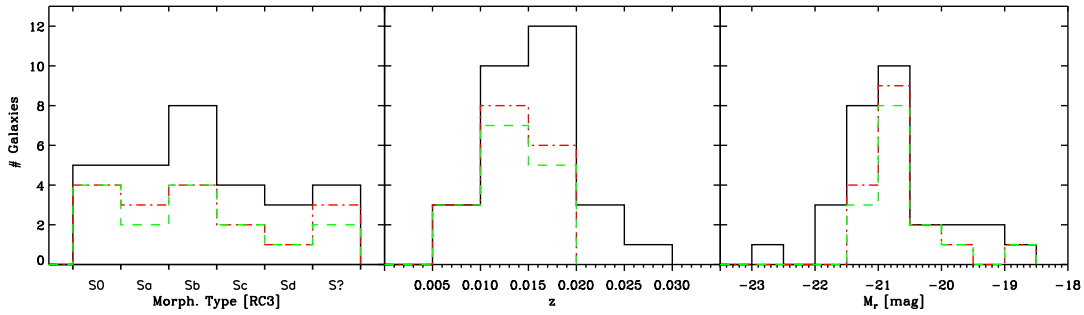

Figure 3.1: Distribution of the morphological types (*left panel*), redshifts (*middle panel*), and absolute SDSS r-band magnitudes (*right panel*) of our sample of 29 *bona fide* SAB galaxies (*black solid line*), the 16 SAB galaxies successfully analysed with the TW method (*red dot-dashed line*), and of the 14 SAB galaxies hosting a non-ultrafast bar (*green dashed line*).

is structured as follows. We present the galaxy sample in Sec. 3.2. We measure the bar properties of the sample galaxies in Sec. 3.3. We present our results in Sec. 3.4. We discuss our conclusions in Sec. 3.5. We adopt as cosmological parameters the following values for the matter density parameter $\Omega_{\rm m} = 0.286$, for the dark energy density parameter $\Omega_\Lambda = 0.714$, and for $H_0 = 69.3$ km s^{-1} Mpc^{-1} (Hinshaw et al., 2013).

3.2 Sample selection

The aim of this work is to analyse the bar properties of a large sample of galaxies with TW-measured $\Omega_{\rm bar}$ spanning a wide range of bar strengths. Several strongly barred galaxies have already been measured in the literature, but there is a lack of weak bar measurements. To fill this gap, we take galaxies from the CALIFA survey, which aimed to measure the properties of a statistically significant sample of nearby galaxies with IFU spectroscopy (Sánchez et al., 2012). The CALIFA Data Release 3 (DR3; Sánchez et al., 2016) includes ~ 700 galaxies from the SDSS Data Release 7 (SDSS-DR7; Abazajian et al., 2009), which are selected to have a major-axis diameter $45 < D_{25} < 80$ arcsec in the r-band and a redshift $0.005 < z < 0.03$. The galaxies were observed with the Potsdam Multi-Aperture Spectrophotometer (PMAS; Roth et al., 2005), an instrument developed at the Leibniz-Institute for Astrophysics Potsdam (AIP) and mounted at the 3.5-m telescope of the Calar Alto Observatory (Husemann et al., 2013; Walcher et al., 2014).

They were selected only according with their visibility from a larger 'mother sample' of galaxies which contains 939 objects with the same statistical properties. The CALIFA 'mother sample' is representative of galaxies over a luminosity range of $-23 < M_r < -19$ and over a stellar mass range between $10^{9.7} < M/M_\odot < 10^{11.4}$ and within these ranges, the diameter selection does not lead to any significant bias against – or in favour of – intrinsically large or small galaxies. Moreover, the estimated volume-corrected distribution functions in luminosities and sizes and show that these are statistically fully compatible with estimates

Table 3.1: Properties of the *bona fide* SAB galaxies.

Galaxy	Alt. Name	Morph. Type [RC3]	Morph. Type [CALIFA]	z	m_r [mag]	D [Mpc]	M_r [mag]	$D_{25} \times d_{25}$ [arcmin]	ΔPA [°]	i [°]	Rejection	$R_{\rm bar}$ [kpc]	$S_{\rm bar}$
(1)	(2)	(3)	(4)	(5)	(6)	(7)	(8)	(9)	(10)	(11)	(12)	(13)	(14)
IC 1199	PGC 57373	S?	SABb	0.016	14.33	69.5	−19.88	1.35×0.46	11.6	67.0 ± 0.5	TW	$7.2^{+3.8}_{-2.5}$	$0.37^{+0.03}_{-0.04}$
IC 1256	PGC 60203	Sb	SABb	0.016	13.60	67.7	−20.55	1.58×1.15	50.0	51.3 ± 0.7	TW	$2.71^{+0.22}_{-0.24}$	$0.21^{+0.01}_{-0.02}$
IC 1528	PGC 312	SB(r)b?	SABbc	0.013	12.92	49.9	−20.57	2.40×1.15	57.5	66.7 ± 0.8	...	$2.15^{+0.66}_{-0.71}$	$0.235^{+0.002}_{-0.016}$
IC 1683	PGC 5008	S?	SABb	0.016	13.37	66.2	−20.73	1.32×0.60	35.5	54.3 ± 0.9	...	$8.79^{+0.62}_{-0.65}$	$0.73^{+0.07}_{-0.08}$
IC 5309	PGC 71051	Sb	SABc	0.014	13.72	55.2	−19.99	1.35×0.60	10.5	60.0 ± 1.4	...	$1.98^{+0.89}_{-0.50}$	$0.205^{+0.006}_{-0.019}$
MCG-02-02-030	PGC 1841	(R)SB(r)a	SABb	0.012	12.74	45.9	−20.57	1.95×0.83	37.5	68.7 ± 0.5	...	$3.6^{+2.3}_{-1.2}$	$0.28^{+0.03}_{-0.03}$
NGC 192	PGC 2352	(R')SB(r)a:	SABab	0.014	12.39	54.7	−21.30	1.91×0.89	73.7	70.5 ± 0.5	...	$11.\ 0^{+1.8}_{-1.4}$	$0.83^{+0.09}_{-0.09}$
NGC 234	PGC 2600	SAB(rs)c	SABc	0.015	12.50	59.5	−21.37	1.62×1.62	20.0	29.4 ± 0.4	Fourier	...	...
NGC 364	PGC 3833	(R)SB(s)0:	EAB7	0.017	12.92	69.3	−21.28	1.41×1.26	57.8	44 ± 1	...	$3.17^{+0.62}_{-0.64}$	$0.46^{+0.01}_{-0.02}$
NGC 477	PGC 4915	SAB(s)c	SABbc	0.020	13.44	81.0	−21.10	2.19×1.17	35.3	52 ± 1	TW	$7.4^{+2.4}_{-1.3}$	$0.427^{+0.008}_{-0.004}$
NGC 551	PGC 5450	SBbc	SABbc	0.017	13.28	71.1	−20.98	1.82×0.79	28.0	64.7 ± 0.8	...	$3.9^{+2.0}_{-2.1}$	$0.30^{+0.07}_{-0.07}$
NGC 2410	PGC 21336	SBb?	SABb	0.016	12.57	69.8	−21.65	2.45×0.71	14.4	73.8 ± 0.7	TW	$5.77^{+3.37}_{-2.16}$	$0.55^{+0.05}_{-0.07}$
NGC 2449	PGC 21802	Sab	SABab	0.016	12.87	73.3	−21.40	1.35×0.65	59.2	69 ± 2	...	$4.59^{+0.75}_{-0.80}$	$0.60^{+0.04}_{-0.03}$
NGC 2553	PGC 23240	S?	SABab	0.016	13.04	71.5	−21.23	0.87×0.68	48.1	54.6 ± 0.9	...	$7.7^{+2.1}_{-1.8}$	$0.57^{+0.01}_{-0.01}$
NGC 2880	PGC 26939	SB0$^-$	EAB7	0.0051	11.57	24.1	−20.34	2.04×1.20	61.7	56.7 ± 0.2	...	$1.49^{+0.71}_{-0.42}$	$0.452^{+0.004}_{-0.006}$
NGC 3994	PGC 37616	S(r)c pec	SABbc	0.010	12.68	48.6	−20.75	1.05×0.59	80.0	63.0 ± 0.5	...	$1.77^{+0.56}_{-0.47}$	$0.38^{+0.01}_{-0.09}$
NGC 5056	PGC 46180	Scd:	SABc	0.019	13.13	84.3	−21.50	1.74×1.00	34.6	59.1 ± 0.8	TW	$2.25^{+0.18}_{-0.31}$	$0.40^{+0.05}_{-0.03}$
NGC 5971	PGC 55529	Sa	SABb	0.011	13.42	62.8	−20.57	1.58×0.56	23.8	69.0 ± 0.5	...	$7.3^{+6.1}_{-3.3}$	$0.504^{+0.009}_{-0.004}$
NGC 6278	PGC 59426	S0	SAB0/a	0.0090	12.20	40.9	−20.86	2.04×1.20	10.7	58.8 ± 0.3	...	$2.84^{+1.09}_{-0.17}$	$0.36^{+0.04}_{-0.04}$
NGC 6427	PGC 60758	S0$^-$:	SAB0	0.011	12.56	45.7	−20.74	1.58×0.63	44.1	68.1 ± 0.7	...	$1.9^{+1.7}_{-1.0}$	$0.63^{+0.02}_{-0.02}$
NGC 6978	PGC 65631	Sb	SABb	0.020	12.84	82.8	−21.75	1.48×0.69	10.0	68.5 ± 0.8	Fourier	...	...
NGC 7787	PGC 72930	(R')SB(rs)0/a:	SABab	0.022	13.91	93.0	−20.88	1.78×0.47	46.7	65 ± 1	Fourier	...	...
UGC 36	PGC 366	S(r)a:	SABab	0.021	13.27	85.6	−21.39	1.32×0.60	63.9	63.0 ± 0.8	TW	$6.8^{+1.4}_{-1.4}$	$0.43^{+0.04}_{-0.04}$
UGC 3944	PGC 21475	Scd:	SABbc	0.0083	13.80	58.3	−20.03	1.78×0.79	79.8	59.3 ± 0.5	...	$1.87^{+0.88}_{-0.63}$	$0.27^{+0.05}_{-0.02}$
UGC 7012	PGC 37976	Scd:	SABcd	0.010	14.06	49.7	−19.37	1.66×0.89	10.0	56.5 ± 0.8	Fourier	...	...
UGC 8231	PGC 45561	SB?	SABd	0.0083	14.18	37.8	−18.71	1.58×0.56	13.0	68.1 ± 0.5	...	$2.30^{+0.47}_{-0.70}$	$0.24^{+0.04}_{-0.04}$
UGC 9067	PGC 50621	Sab	SABbc	0.026	13.66	116.6	−21.67	1.38×0.68	14.0	63 ± 1	TW	$7.8^{+3.6}_{-2.0}$	$0.25^{+0.04}_{-0.06}$
UGC 10693	PGC 59560	E	EAB7	0.015	12.51	122.9	−22.89	1.82×1.23	10.0	49.8 ± 0.6	Fourier	...	...
UGC 10796	PGC 59997	SB(s)b	SABcd	0.010	13.91	43.8	−19.30	1.58×1.20	66.5	57 ± 1	Fourier	...	...

Notes: (1) Galaxy name. (2) Alternative name. (3) Morphological type from RC3. (4): Morphological type from Walcher et al. (2014). (5) Redshift from SDSS-DR14 (Abolfathi et al., 2018). (6) Apparent model total r-band magnitude from SDSS-DR14. (7) Distance from NED. (8) Absolute SDSS r-band magnitudes M_r obtained as described in Sec. 3.2. (9) Major and minor diameters of the isophote at a surface brightness level $\mu_B = 25$ mag arcsec^{-2} from RC3. (10) Difference between the PA of the bar and that of the disc major axis obtained either from the isophototal analysis of the r-band SDSS image or provided by Méndez-Abreu et al. (2017). (11) Galaxy inclination obtained from the disc ellipticity provided by Méndez-Abreu et al. (2017) and assuming an infinitesimally-thin disc. (12) Reason for the rejection of the galaxy, where Fourier signifies no evidence of a bar from the Fourier analysis of the r-band SDSS image and TW signifies unsuccessful application of the TW method to the CALIFA stellar velocity field. (13) Bar radius obtained as described in Sec. 3.3.4. (14) Bar strength obtained as described in Sec. 3.3.3.

from the full SDSS when accounting for large-scale structure (Walcher et al., 2014).

In this study, we considered the 265 CALIFA galaxies, which were morphologically classified as doubtful barred galaxies (Walcher et al., 2014). A visual identification of bars is not always obvious, and it is even more difficult in the case of weakly barred galaxies. The morphological classification performed by the CALIFA collaboration does not always match the RC3 classification (Table 3.1).

From the CALIFA SAB galaxies, we selected those for which the stellar kinematic maps were measured by Falcón-Barroso et al. (2017). These selection criteria allowed us to discard *a priori* the objects with disturbed kinematics. There remained 58 galaxies visually classified as SAB, for which we analysed the stellar kinematics obtained with a spectral resolution of $R = 1650$ (corresponding to $\sigma_{\rm strum} \sim 70$ km s^{-1} at 4500 Å) and a spatial resolution of 1 arcsec.

The TW method allows to measure $\Omega_{\rm bar}$ from Eq. 1.30. The use of IFU spectroscopic data allows measurements of $\langle X \rangle$ and $\langle V \rangle$ in several parallel pseudo-slits by collapsing their corresponding spectra along the spectral and spatial direction, respectively, and defining a reference frame centred on the galaxy centre. To this aim we followed the prescriptions of Aguerri et al. (2015).

To apply any further analysis on our sample, we need to have the structural parameters of the galaxies. To this aim, we selected the 37 sample galaxies whose SDSS r-band images were analysed by Méndez-Abreu et al. (2017). They performed isophotal analyses and photometric decompositions of the surface brightness distributions using the IRAF task ELLIPSE (Jedrzejewski, 1987) and GASP2D (Méndez-Abreu et al., 2008, 2014), respectively.

Moreover, to successfully apply the TW method, we rejected all the galaxies with a ΔPA $< 10^\circ$ between the bar major axis and the disc major/minor axis and kept objects with a disc inclination $25^\circ < i < 75^\circ$, as done in Aguerri et al. (2015). When the photometric decomposition did not include a bar component, we recovered the bar PA from the analysis of the ellipticity ϵ and PA radial profiles, as discussed in Sec. 3.3.1. At the end, our sample of *bona fide* SAB galaxies totals 29 objects, whose main properties are listed in Table 3.1. The distributions of their morphological types, redshifts, and absolute SDSS r-band magnitudes are plotted in Fig. 3.1. Since the distribution of morphologies, redshifts and absolute magnitudes reflect the properties of the mother sample of CALIFA, we can conclude there is no bias in our final selected sample with respect to the initial one.

In addition, the TW method works for a tracer satisfying the continuity equation and because of this it was initially applied to early-type disc galaxies, which do not show strong evidence of spiral arms or heavily-patchy dust distribution. Spiral arms may lead to a wrong determination of the disc PA and their light contribution may affect the photometric integrals of the bar. The presence of dust and/or star formation may cause a non-coincidence between the surface brightness and mass distribution of the galaxy, which results in a mismatch between photometric and kinematic measurements. These effects may be mitigated by computing the mass-weighted kinematic and photometric integrals (Gerssen & Debattista, 2007). However, Aguerri et al. (2015) compared the values of $\Omega_{\rm bar}$ derived for a number of spirals from both light- and mass-weighted TW integrals and found consistent results, even

in late-type galaxies, which are the most affected by this problem. This means that the TW method can be applied to barred spirals after checking the convergence of the TW integrals, which allows to control and limit contamination from other spurious features, such as foreground stars or bad pixels.

3.3 Properties of the weak bars

3.3.1 Disc inclination and position angle

The TW method is very sensitive to the misalignment between the orientation of the pseudo-slits and the disc major axis, and the calculation of $\Omega_{\rm bar}$ also requires knowing the disc inclination (Debattista, 2003).

To accurately constrain the disc's orientations, we decided to consider both the photometric decompositions and the isophotal analyses of the SDSS r-band images provided by Méndez-Abreu et al. (2017). For each object, we derived the disc inclination i and PA from the ellipticity ϵ and major-axis PA of the ellipses fitted to the outermost galaxy isophotes measured by Méndez-Abreu et al. (2017). We defined the disc radial range by fitting the PA measurements with a straight line and selecting all the radii where the linear slope was consistent with zero within the associated root mean square error. We adopted the mean PA and mean ϵ (and corresponding root mean square errors) as the disc geometric parameters (and their errors). Finally, we derived $i = \arccos(1-\epsilon)$ by assuming an infinitesimally thin disc.

The resulting PA values are not always consistent within the 3σ errors with those from the photometric decompositions by Méndez-Abreu et al. (2017). Although the mean difference of ΔPA is lower than $1\overset{\circ}{.}5$ in 80 per cent of the sample, for a few galaxies the difference is as large as $\Delta{\rm PA} \sim 7^\circ$. It has to be noted that the bar component was not always included in the photometric decomposition due to the weakly barred nature of these galaxies and this affects the resulting best-fitting parameters of the disc (see Méndez-Abreu et al., 2014, for a discussion). For each galaxy, we also defined a range for the disc PA which covers the values from the photometric decomposition and the isophotal analysis (and their errors), to explore role of the PA in the application of the TW method (see Sec. 3.3.6). The i values from the isophotal analyses are consistent with those from the photometric decompositions listed in Table 3.1, which we adopt here.

3.3.2 Bar detection

The visual identification of weakly barred galaxies is difficult (Nair & Abraham, 2010; Lee et al., 2019) and most of our *bona fide* SAB galaxies were actually listed in RC3 either as unbarred galaxies or their classification was uncertain (Table 3.1). For this reason, an accurate analysis of each galaxy's surface brightness distribution is a mandatory step to identify the presence of a genuine bar component.

The Fourier analysis of the light distribution has often been used to detect and characterise the different galactic components, especially bars, which correspond to bisymmetric depar-

tures from axisymmetry (Ohta et al., 1990; Athanassoula, 2003; Garcia-Gómez et al., 2017). Following Aguerri et al. (2000), we decomposed the deprojected azimuthal surface brightness profiles $I(r, \phi)$, adopting the geometric parameters of the discs derived by Méndez-Abreu et al. (2017) for the deprojection.

We know that the bar region is characterised by large values of the even Fourier components and in particular of the $m = 2$ Fourier component. The odd Fourier components are generally smaller than the even ones because they are associated with the presence of asymmetric components. The maximum amplitude of the $m = 2$ Fourier component is correlated with the bar strength and bars typically have $(I_2/I_0)_{\max} > 0.2$ (Aguerri et al., 2003). We expect that the phase angle ϕ_2 of the $m = 2$ Fourier component is constant within the bar region. We found that the Fourier components of six sample galaxies do not meet these criteria. Therefore, we concluded that these galaxies are more likely to be unbarred systems and we excluded them from the analysis (Table 3.1).

Figure 3.2 shows the Fourier analysis of the galaxy UGC 7012, which turned out not to host a proper bar according to these criteria, taken as an example. Figure 3.3 shows the Fourier analysis of MCG-02-02-030, which turned out to host a bar weak in term of bar strength (described in Sec. 3.3.3), taken as an example. Figure 3.4 shows the Fourier analysis of NGC 2880, which turned out to host a bar strong in term of bar strength, taken as an example.

3.3.3 Bar strength

We measured $S_{\rm bar} = (I_2/I_0)_{\max}$ for all the sample galaxies with a weak bar, as the maximum of the intensity ratio between the $m = 2$ and $m = 0$ Fourier components (Athanassoula & Misiriotis, 2002). The uncertainties associated with the measurement of the strength are obtained by performing a Fourier analysis using the two portions of the deprojected azimuthal surface brightness $I(r, \phi)$ with $0° < \phi < 180°$ and $180° < \phi < 360°$. The difference between these two measurements, with respect to the reference value obtained from the full surface brightness distribution, provided the upper and lower limits on the bar strength, typically smaller than 10 per cent. The resulting values of $S_{\rm bar}$ and their corresponding errors are reported in Table 3.1. We will define in Sec. 3.4 a quantitative criterion based on $S_{\rm bar}$ to distinguish between weak and strong bars.

3.3.4 Bar radius

For each of the 23 galaxies confirmed to host a weak bar, we measured $R_{\rm bar}$ from the analysis of the SDSS r-band image using three independent methods presented in Sec. 1.3, as done in Aguerri et al. (2015). We considered the bar/interbar intensity ratio obtained from the Fourier analysis, the location of the maximum in the ϵ radial profile, and the behaviour of the PA radial profile. We derived the radial profiles of ϵ and PA by fitting ellipses to the isophotes of the r-band image using ELLIPSE and considering a variable value for the centre of the galaxy (Méndez-Abreu et al., 2017).

First, we measured $R_{\rm bar}$ from the Fourier analysis by tracing the radial profile of the

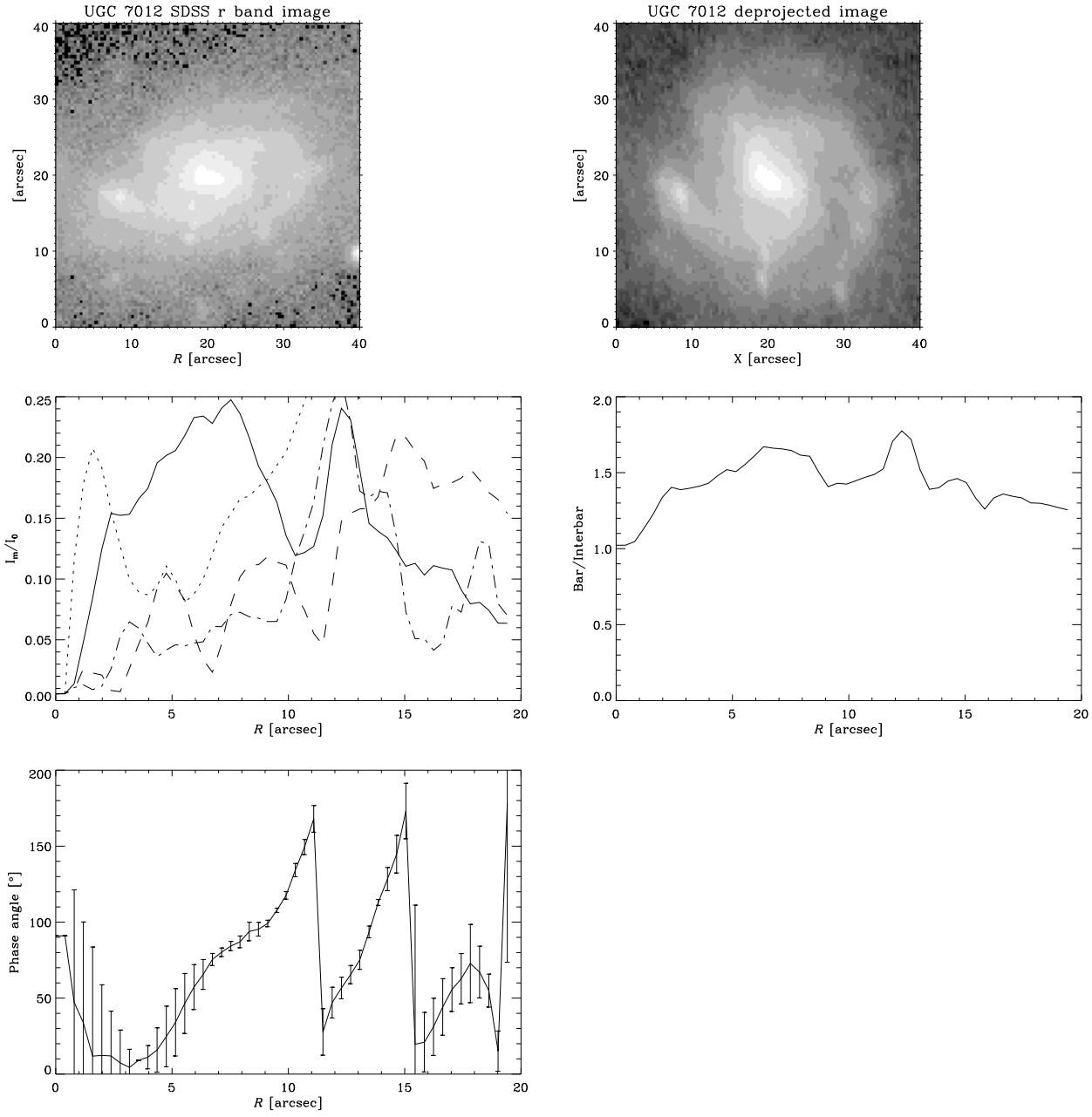

Figure 3.2: Fourier analysis of UGC 7012, which presented no evidence of a bar from this analysis and was excluded. *Top panels*: SDSS r-band image before and after deprojection. *Middle panels*: relative amplitudes I_m/I_0 of the first Fourier components $m = 1, 2, 3, 4$ (*dotted, solid, dashed,* and *dot-dashed lines*, respectively), and bar/interbar intensity ratio. *Bottom panel*: phase angle ϕ_2 of the $m = 2$ Fourier component.

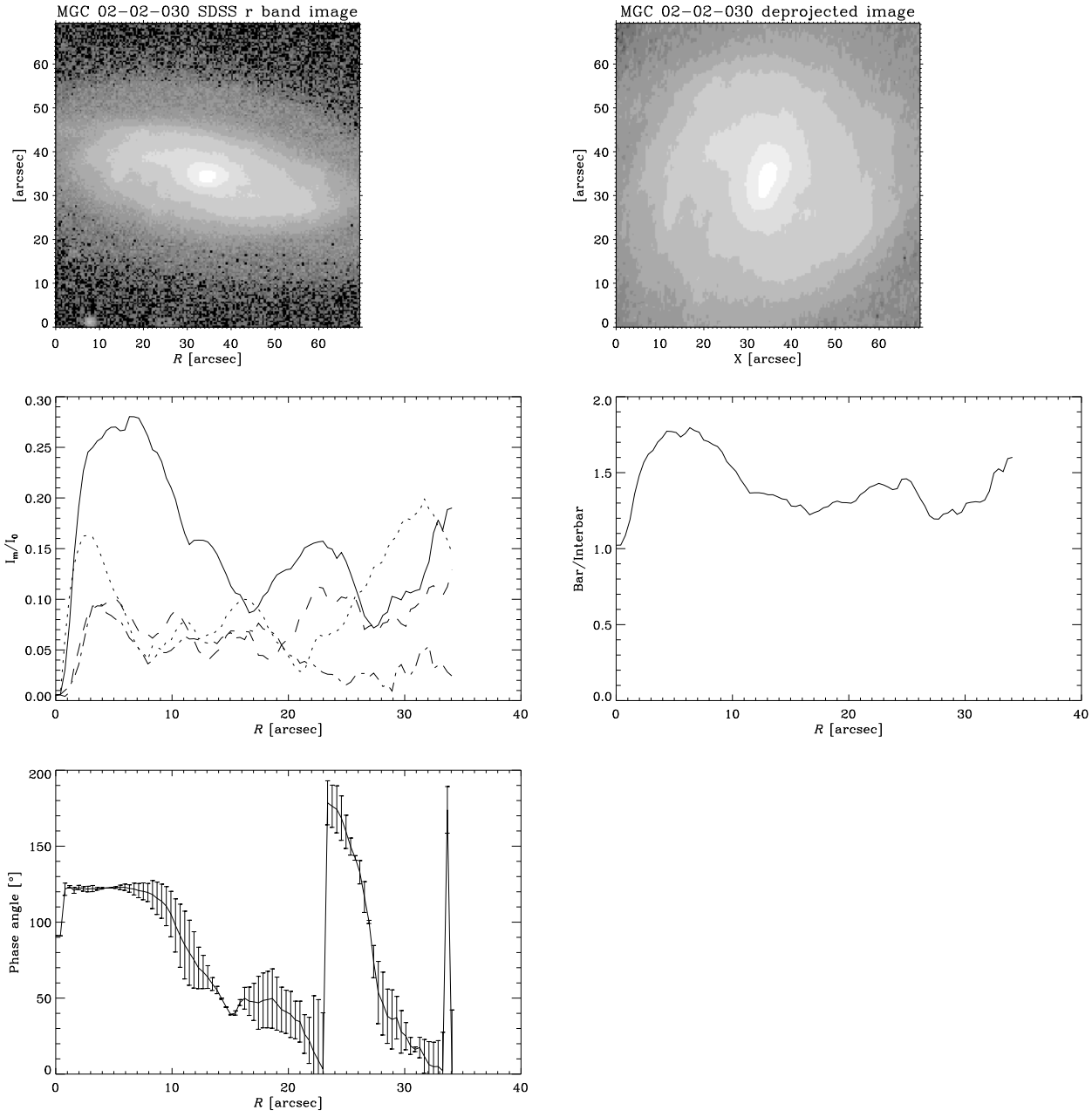

Figure 3.3: Fourier analysis of MCG-02-02-030, which hosts a weak bar in terms of strength. *Top panels*: SDSS r-band image before and after deprojection. *Middle panels*: relative amplitudes I_m/I_0 of the first Fourier components $m = 1, 2, 3, 4$ (*dotted, solid, dashed,* and *dot-dashed lines*, respectively), and bar/interbar intensity ratio. *Bottom panel*: phase angle ϕ_2 of the $m = 2$ Fourier component.

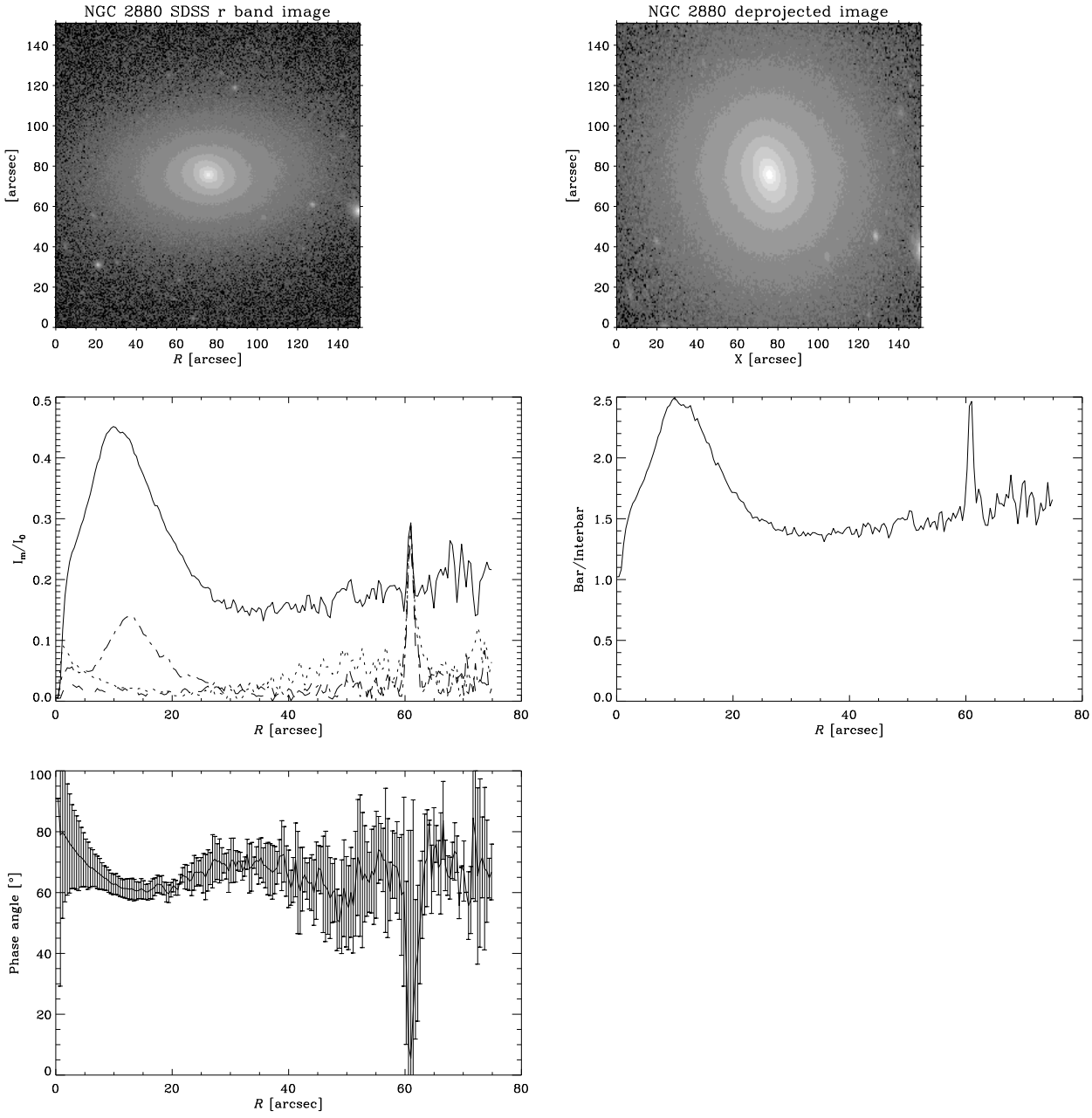

Figure 3.4: Fourier analysis of NGC 2880, which hosts a strong bar in terms of strength. *Top panels*: SDSS r-band image before and after deprojection. *Middle panels*: relative amplitudes I_m/I_0 of the first first Fourier components $m = 1, 2, 3, 4$ (*dotted, solid, dashed,* and *dot-dashed lines*, respectively), and bar/interbar intensity ratio. *Bottom panel*: phase angle ϕ_2 of the $m = 2$ Fourier component.

intensity contrast between the bar and interbar regions. We adopted the FWHM of the radial profile of $I_{\rm bar}/I_{\rm ibar}$ as the bar radius.

Then, we measured $R_{\rm bar}$ from the ϵ radial profile of the isophotal ellipses. The galaxy isophotes usually appear almost circular near the centre, while their ϵ increases up to a local maximum in the bar region and decreases outwards to a local minimum in the disc region. Following Wozniak & Pierce (1991), we adopted the position of the maximum ϵ as second estimate of $R_{\rm bar}$.

Finally, we obtained a third estimate of $R_{\rm bar}$ from the analysis of the radial profile of the PA of the isophotal ellipses. The galaxy isophotes show a constant PA in the bar and disc regions. Usually, the two values are different, being related to the orientation of the bar and LON, respectively. As in Aguerri et al. (2015), we adopted as $R_{\rm bar}$ the position where the PA changes by $\Delta{\rm PA} = 5^\circ$ from the PA of the ellipse with the maximum ϵ value.

We adopted for each galaxy the mean value of the three measurements as $R_{\rm bar}$, and the largest deviation from the mean of the highest and lowest estimates as pper and lower errors, respectively. This corresponds to a typical error ~ 30 per cent. The resulting values of $R_{\rm bar}$ and their errors are reported in Table 3.1.

3.3.5 Bar pattern speed

We applied the TW method as outlined in Eq. 1.30. For each galaxy, the pseudo-slits were defined *a posteriori* from the CALIFA reconstructed image (Fig. 3.5). We traced from three up to thirteen 1-arcsec wide pseudo-slits crossing the bar and oriented with the disc PA. A minimum separation of 1 arcsec between adjacent pseudo-slits was fixed to deal with independent data and minimise the impact of spatial correlations on the TW integrals. We adopted a half length of the pseudo-slits in the range of $(1-4)h$, where h is the exponential scalelength of the disc from the photometric decomposition of Méndez-Abreu et al. (2017). In all cases, we checked that the pseudo-slits extended out to the axisymmetric region of the disc defined from the photometric decomposition performed by Méndez-Abreu et al. (2017), by performing a stability test on the TW integrals.

We measured $\langle X \rangle$ in the CALIFA reconstructed image obtained by summing the CALIFA datacube along the spectral direction in a wavelength range between 4500 Å and 4650 Å and excluding intervals severely affected by bad pixels. This spectral range was selected because it does not include prominent emission lines. Errors on $\langle X \rangle$ in each slit were defined as the standard deviation of $\langle X \rangle$ measured varying the slit length within the range of the constant behaviour of each integrals. The errors typically range from 0.07 to 0.15 arcsec, similar to what was found in Aguerri et al. (2015). The convergence of the photometric integrals was checked by measuring them as a function of the coordinates of the galaxy centre and the pseudo-slit length.

We measured $\langle V \rangle$ by collapsing each pseudo-slit along the spatial direction and measuring the LOS velocity of the resulting spectrum in the wavelength range from 3400 to 4750 Å using the IDL algorithms PPXF (Cappellari & Emsellem, 2004) and GANDALF (Sarzi et al., 2006). Since the kinematic integrals are not affected by corrupted pixels at the ends of the spectral intervals, the entire CALIFA spectral range was adopted to recover them. This approach is

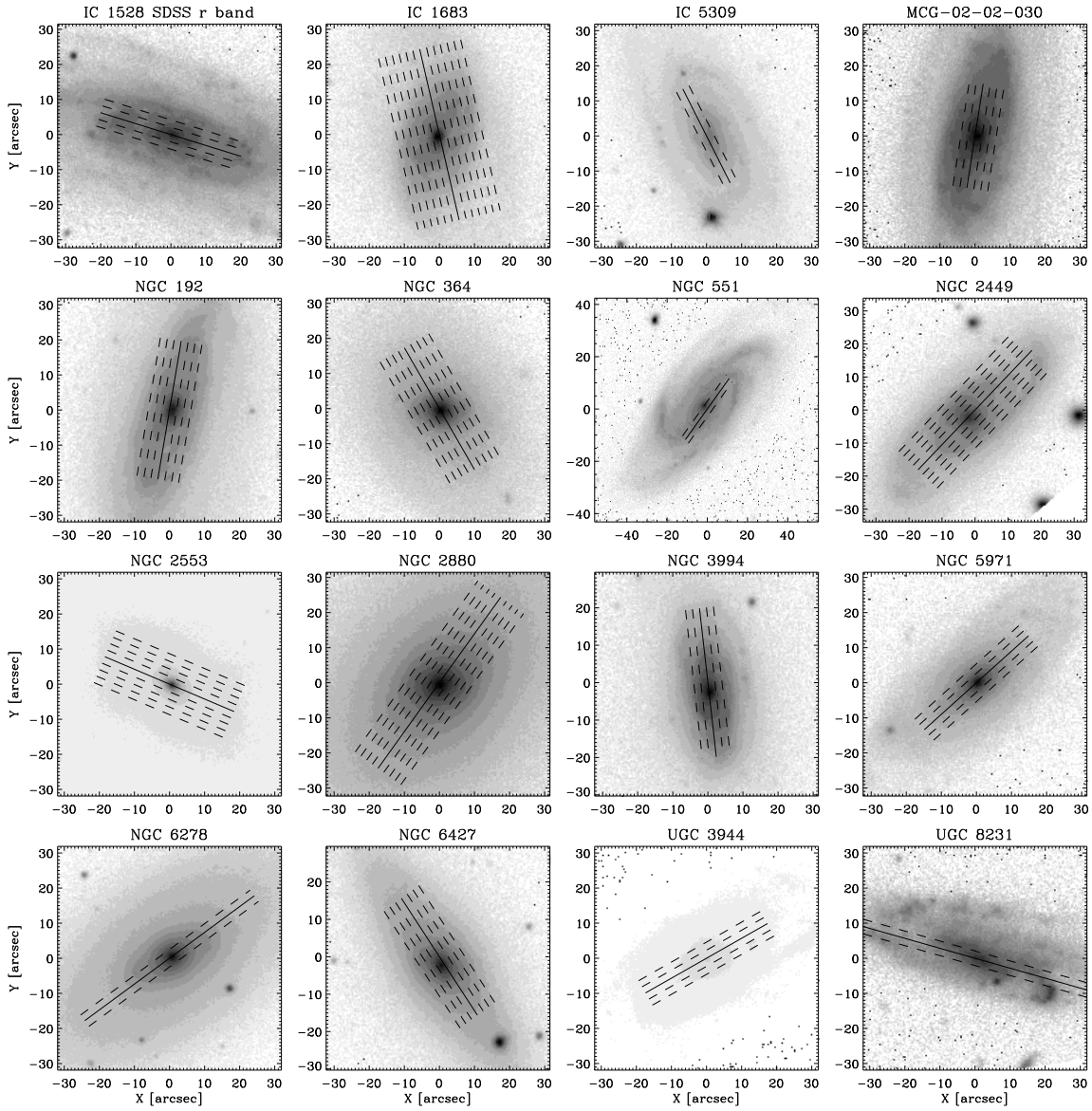

Figure 3.5: SDSS r-band images of the sample of 16 SAB galaxies successfully analysed with the TW method. The FOV is oriented with North up and East left. For each galaxy, the position and length of the pseudo-slits which are parallel to the disc major axis and cross the galaxy centre (*solid line*) or are offset with respect to it (*dashed lines*) are shown.

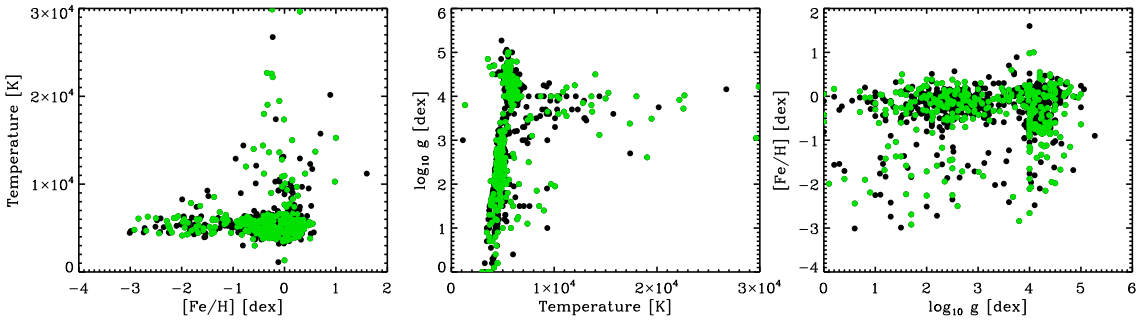

Figure 3.6: The distribution of parameters (effective temperature $T_{\rm eff}$, surface gravity $\log g$, and metallicity [Fe/H]) of the Indo-US stellar library (*black circles*; Valdes et al. 2004). The subsample adopted to recover the stellar kinematics of the sample galaxies is shown (*green circles*).

equivalent to using an explicit luminosity weighting because the spaxels with higher signals give higher contributions to the collapsed spectrum and consequently to the $\langle V \rangle$ determination of each pseudo-slit. We convolved a linear combination of ~ 330 stellar spectra available in the Indo-US library ($R \sim 4200$, $\sigma_{\rm strum} \sim 30$ km s^{-1}; Valdes et al. 2004; Beifiori et al. 2011) with a LOSVD modelled as a truncated Gauss-Hermite series (Gerhard, 1993; van der Marel & Franx, 1993) via a χ^2 minimization. A subsample of the ~ 1200 stellar spectra was selected to fully cover the parameter space of the effective temperature $T_{\rm eff}$ (from 1000 to 30000 K), surface gravity $\log g$ (from 0.0 to 6.0 dex) and metallicity [Fe/H] (from -3.0 to 1.0 dex), broadened to match the CALIFA instrumental resolution (Fig. 3.6). After rebinning the stellar spectra to a logarithmic scale along the dispersion direction, we redshifted them to the rest frame and cropped their wavelength range to match that of the redshifted frame of the galaxy spectra. Moreover, a low-order multiplicative Legendre polynomial was added to correct for the different shape of the continuum of the spectra of the galaxy and the optimal template, due to reddening and large-scale residuals of flat-fielding and sky subtraction. The statistical errors of the stellar kinematic parameters were assumed to be the formal errors of the PPXF best fit after rescaling the minimum χ^2 to achieve $\chi^2_{\rm min} = N_{\rm dof} = N_{\rm d} - N_{\rm fp}$, where $N_{\rm dof}$, $N_{\rm d}$, and $N_{\rm fp}$ the number of the degrees of freedom, data points, and fitting parameters, respectively (Press et al., 1992). Errors on $\langle V \rangle$ range from 1 to 15 km s^{-1}. The convergence of the kinematic integrals was checked by measuring them as a function of the coordinates of the galaxy centre and pseudo-slit length.

The value of $\Omega_{\rm bar} \sin i$ was obtained by fitting a straight line to the values of $\langle X \rangle$ and $\langle V \rangle$ using the IDL task FITEXY (Fig. 3.7).

We calculated the value of $\Omega_{\rm bar}$ for both the PAs obtained with the photometric decomposition and the isophotal analysis of each galaxy's surface brightness distribution, and adopting the corresponding values for i, as discussed in Sec. 3.3.6. As reference result, we adopted the value of $\Omega_{\rm bar}$ obtained using the PA and i defined from the radial profiles, as we already did in previous works (Aguerri et al. 2015; Chapter 2). At the end of this analysis, seven more galaxies were discarded (Table 3.1) because of large errors on $\langle V \rangle$ ($\Delta\langle V \rangle / \langle V \rangle > 0.5$, translating into $\Delta\Omega_{\rm bar}/\Omega_{\rm bar} \sim 1$), or because the presence of residual spectral features in the

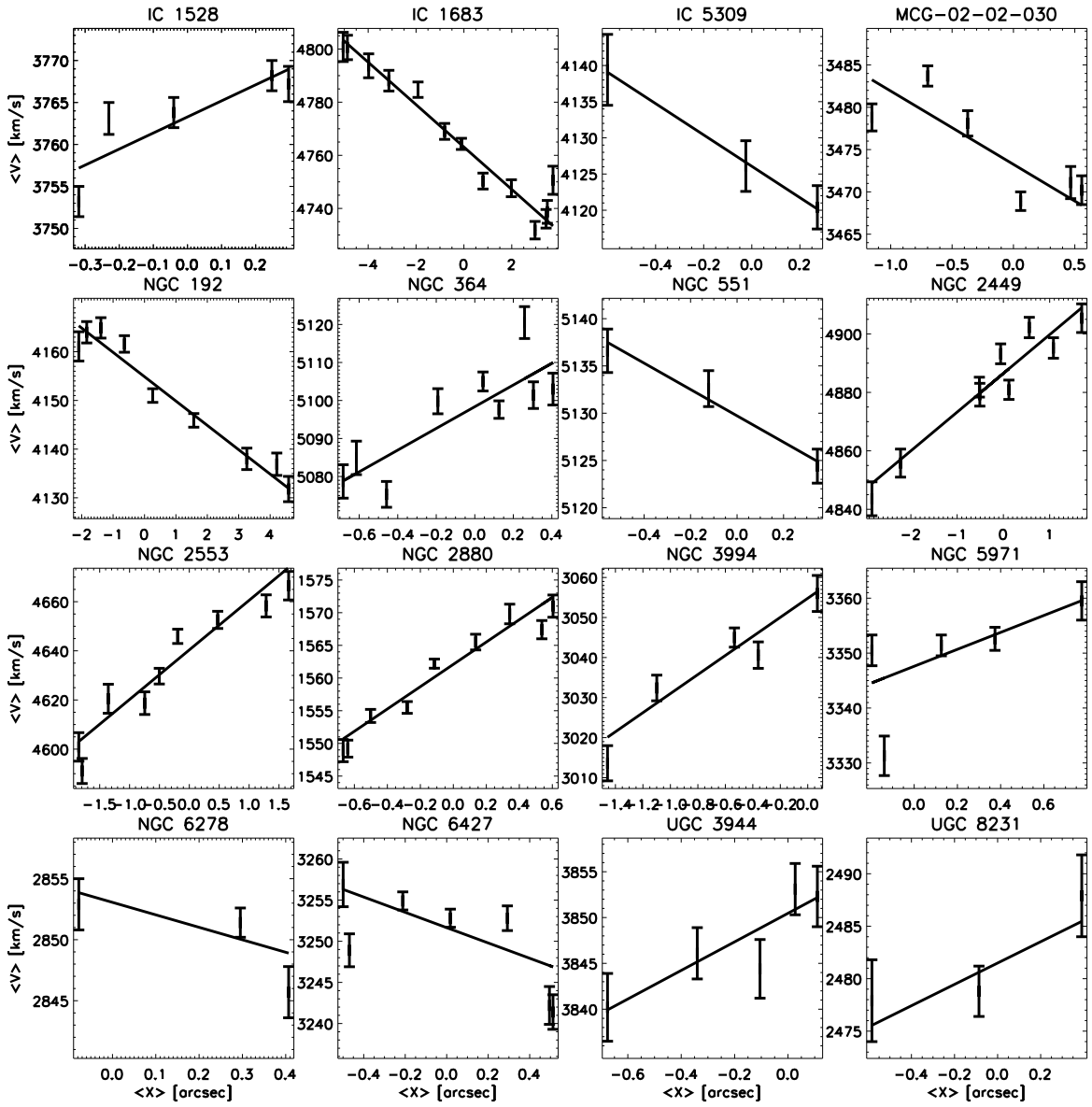

Figure 3.7: Bar pattern speeds of the 16 SAB galaxies shown in Fig. 3.5. For each galaxy, the kinematic integrals $\langle V \rangle$ are plotted as a function of the photometric integrals $\langle X \rangle$ and the best-fitting straight line, which has a slope equal to $\Omega_{\rm bar} \sin i$, is overplotted.

Table 3.2: Properties of the bar and disc of the SAB galaxies successfully analysed with the TW method.

Galaxy	PA_{TW}	Ω_{bar}	V_{circ}	R_{cr}	$\mathcal{R}$
	[°]	[km s^{-1} kpc^{-1}]	[km s^{-1}]	[kpc]	
(1)	(2)	(3)	(4)	(5)	(6)
IC 1528	72.7	87 ± 20	142 ± 14	1.63 ± 0.51	$0.76^{+0.14}_{-0.22}$
IC 1683	13.0	30.3 ± 5.1	191 ± 45	6.3 ± 2.7	$0.71^{+0.21}_{-0.21}$
IC 5309	26.7	91 ± 26	114 ± 25	1.3 ± 1.0	$0.63^{+0.36}_{-0.45}$
MCG-02-02-030	171.1	43.4 ± 6.5	210 ± 55	4.8 ± 2.2	$1.32^{+0.36}_{-0.53}$
NGC 192	170.4	20.9 ± 2.1	248.3 ± 6.6	11.9 ± 1.9	$1.08^{+0.10}_{-0.13}$
NGC 364	29.9	120 ± 31	317 ± 30	2.6 ± 1.1	$0.83^{+0.22}_{-0.26}$
NGC 551	137.0	45 ± 11	202 ± 43	4.5 ± 2.4	$1.17^{+0.39}_{-0.71}$
NGC 2449	136.4	40.7 ± 5.5	236.9 ± 2.6	5.84 ± 0.99	$1.27^{+0.11}_{-0.14}$
NGC 2553	67.0	68.1 ± 9.8	269 ± 34	3.95 ± 0.91	$0.515^{+0.077}_{-0.110}$
NGC 2880	144.6	190 ± 28	209 ± 15	1.09 ± 0.36	$0.74^{+0.15}_{0.19}$
NGC 3994	6.9	119 ± 27	226.4 ± 5.5	1.90 ± 0.67	$1.06^{+0.22}_{-0.31}$
NGC 5971	132.0	55 ± 15	226 ± 16	4.1 ± 2.0	$0.56^{+0.15}_{-0.32}$
NGC 6278	126.4	92 ± 28	279 ± 13	3.1 ± 1.1	$1.07^{+0.26}_{-0.25}$
NGC 6427	34.7	46 ± 10	245 ± 21	5.3 ± 3.6	$2.8^{+1.0}_{-1.8}$
UGC 3944	119.6	62 ± 22	148 ± 30	2 ± 12	$1.28^{+3.8}_{-5.7}$
UGC 8231	74.2	58 ± 31	136 ± 27	2.3 ± 5.3	$1.01^{+1.6}_{-2.0}$

Notes: (1) Galaxy name. (2) Adopted value of the position angle of the pseudo-slits for the TW analysis. (3) Bar pattern speed. (4) Disc circular velocity. (5) Bar corotation radius. (6) Bar rotation rate.

CALIFA datacube prevented the convergence of $\langle X \rangle$ and/or $\langle V \rangle$.

The SDSS r-band images of the remaining 16 galaxies, which represent our sample of SAB galaxies successfully analysed with the TW method, are shown in Fig. 3.5. This means that 45 per cent of the galaxies of the initial sample do not actually host a genuine bar component. The adopted values of PA and measurements of Ω_{bar} are reported in Table 3.2. Typical errors on Ω_{bar} are $\sim$ 25 per cent. The TW integrals and best-fitting straight lines are plotted in Fig. 3.7.

3.3.6 Bar pattern speeds obtained with different position angles

The correct location of the pseudo-slits is decisive to obtain a reliable value of Ω_{bar}. This needs the correct identification of the PA of the disc (Debattista, 2003). A large effort was performed in the literature to address this issue: the disc PA can be defined from the photometry, either by performing a photometric decomposition (e.g., Treuthardt et al., 2007) or by analysing the PA radial profile from isophotal fitting (e.g., Aguerri et al., 2015; Guo et al., 2019). Another possibility consists in deriving and using the PA obtained from the

kinematics (e.g., Krajnović et al., 2006), finding the angle that gives the lowest difference between the observed and symmetrised velocity map. This is defined as the kinematic disc PA. Guo et al. (2019) obtained $\Omega_{\rm bar}$ measurements using both the photometric and kinematic PA and did not find any dramatic difference.

To test the robustness of our choice, we applied the TW methods using three different PAs: the first two PAs are obtained from our photometric analysis as described in Sec. 3.3.1 and a third one is defined *a posteriori*, from the linear fit of the integrals in Eq. 1.30. To define the latter PA, we calculated the value of $\Omega_{\rm bar}$ for 10 different PAs in a range covering the two estimates from the photometric decomposition and the isophotal analysis of the galaxy surface brightness distribution, and adopting i from the photometric decomposition. For each of these PAs, we measured the TW integrals as outlined in Sec. 3.3.5 and calculated their Pearson linear-correlation coefficient r with the IDL task CORRELATE (Dunnett, 1979). When the correlation was good ($r > 0.8$), we adopted the value of $\Omega_{\rm bar}$ corresponding to the highest r as the reference value for the galaxy.

Figure 3.8 shows the estimates of $\Omega_{\rm bar}$ obtained using the two PAs from photometry, as a function of the difference in PA. The resulting values of $\Omega_{\rm bar}$, are in most of the cases compatible within 1σ of each other. Nevertheless, we have three cases where the $\Omega_{\rm bar}$ measurements are not consistent within the errors. The difference between the two PAs used to apply the TW method is between 2° and 7° and it explains the different results for $\Omega_{\rm bar}$.

Figure 3.9 shows the estimates of $\Omega_{\rm bar}$ obtained using the PA from the radial profile and the PA which maximises the linearity of the correlation between the integrals, as a function of the difference in PA. In this case, 75 per cent of the galaxies present a difference in PA larger than 3°, leading to non consistent results for $\Omega_{\rm bar}$ in most of the cases.

At the end of the TW analysis, we adopted the PA from the radial profile. In this case, we discarded seven galaxies because these objects were not successfully analysed with the TW method. Moreover, 9 per cent of the resulting sample turned to host an ultrafast bar. Concerning the PA from the photometric decomposition, nine galaxies have to be discarded. So this PA represents the worst choice in term of efficiency. In fact, analysing the PA radial profiles when the pattern speeds are not consistent, we found that the photometric decomposition is not able to actually describe the PA of the disc. Moreover, the PA obtained from the best correlation brought us to discard six more galaxies because of the low value of the Pearson coefficient ($r < 0.8$ indicating a poor linear correlation between $\langle X \rangle$ and $\langle V \rangle$), large errors on $\langle V \rangle (\Delta \langle V \rangle / \langle V \rangle > 0.5$, which translates to $\Delta\Omega_{\rm bar}/\Omega_{\rm bar} \sim 1$), and non convergence of $\langle X \rangle$ and/or $\langle V \rangle$ due to residual spectral features in the CALIFA datacubes. With our choice, the number of discarded galaxies is only six. This gives evidence that this approach is selecting the best results from the application of the TW method, but not that it necessarily provides the right estimation of $\Omega_{\rm bar}$. In fact, $\sim$ 30 per cent of the galaxies turned out to host ultrafast bars, due to the wrong choice of PA. Debattista (2003) also showed that the PA which maximises the correlation between the integrals is not necessarily the correct one.

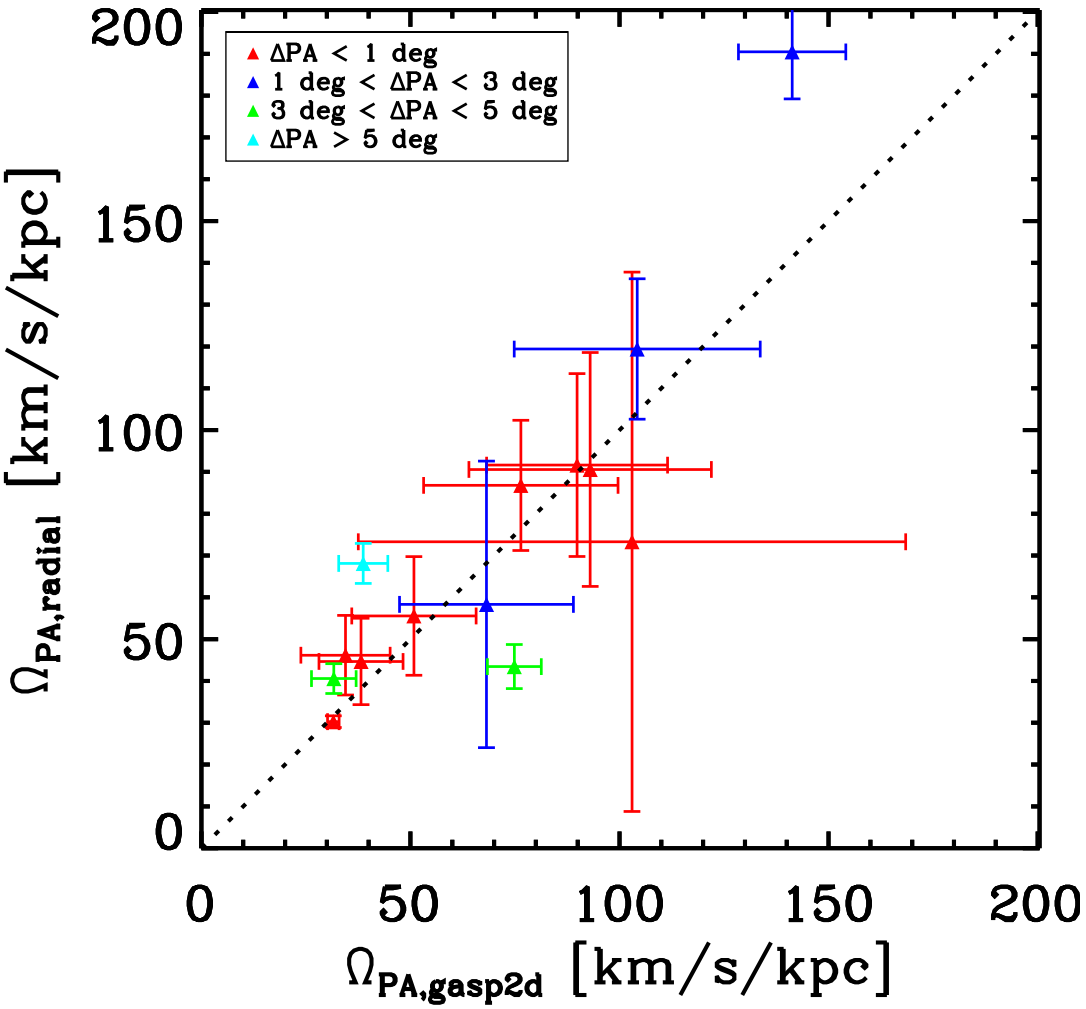

Figure 3.8: Comparison of the $\Omega_{\rm bar}$ measured with the PA derived from the radial profile and from the photometric decomposition. The difference in PA between the two adopted methods is color coded: eight galaxies have ΔPA $< 1^\circ$ (*red*), three galaxies have $1^\circ < \Delta$PA $< 3^\circ$ (*blue*), two galaxies have $3^\circ < \Delta$PA $< 5^\circ$ (*green*), and only one galaxy has ΔPA $> 5^\circ$ (*cyan*). The 1:1 relation is shown (*black dotted line*).

3.3.7 Corotation radius and bar rotation rate

Although the TW method does not need any modelling to derive $\Omega_{\rm bar}$, we need some assumptions to derive the circular velocity $V_{\rm circ}$ and consequently $R_{\rm cr}$ and $\mathcal{R}$.

We obtained $V_{\rm circ}$ from the maps of stellar LOS velocity and velocity dispersion in the disc region provided by Falcón-Barroso et al. (2017), using the asymmetric drift equation (Binney & Tremaine, 2008) and following the prescriptions of Debattista et al. (2002) and Aguerri et al. (2003), presented in Sec. 1.3.4. In particular, we assumed an exponential radial profile with the same scalelength for the radial, azimuthal, and vertical components of the

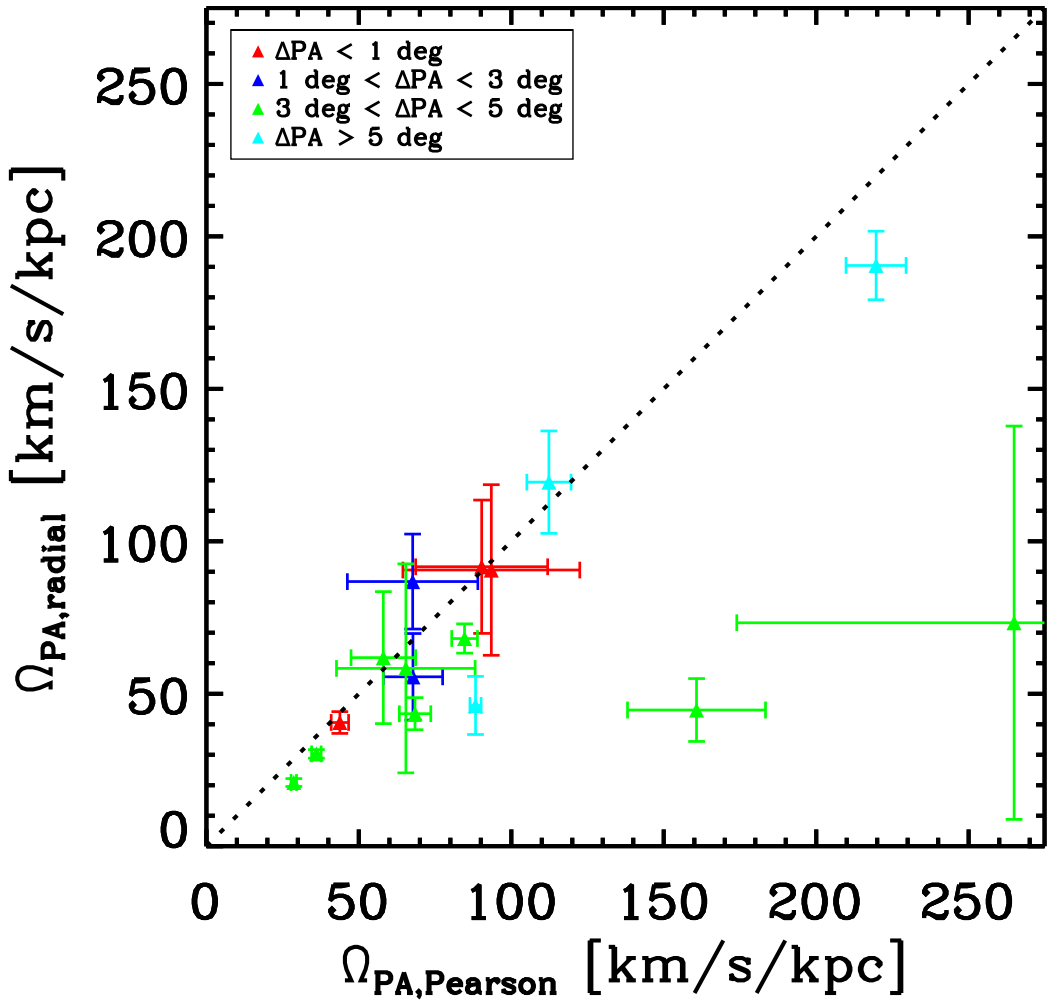

Figure 3.9: Comparison of the $\Omega_{\rm bar}$ measured with the PA derived from the r Pearson correlation parameter and from the radial profile. The difference in PA between the two adopted methods is color coded: three galaxies have ΔPA $< 1^\circ$ (*red*), two galaxies have $1^\circ < \Delta$PA $< 3^\circ$ (*blue*), eight galaxies have $3^\circ < \Delta$PA $< 5^\circ$ (*green*), and three galaxy have ΔPA $> 5^\circ$ (*cyan*). The 1:1 relation is shown (*black dotted line*).

velocity dispersion $(\sigma_R, \sigma_\phi, \sigma_z)$, the epicyclic approximation and a constant $V_{\rm circ}$ (resulting in $\sigma_\phi/\sigma_R = 1/\sqrt{2}$), and a value of σ_z/σ_R depending on the morphological type (Gerssen & Shapiro Griffin, 2012; Aguerri et al., 2015).

We checked the reliability of our circular velocities by performing a comparison with the $V_{\rm circ}$ values predicted by the Tully-Fisher relation of Reyes et al. (2011) and with those obtained by Leung et al. (2018) with different dynamical models than ours. Although our results are consistent within the 3σ scatter of the relation between circular velocity and absolute SDSS r-band magnitude calculated by Reyes et al. (2011) for a sample of $\sim$ 200

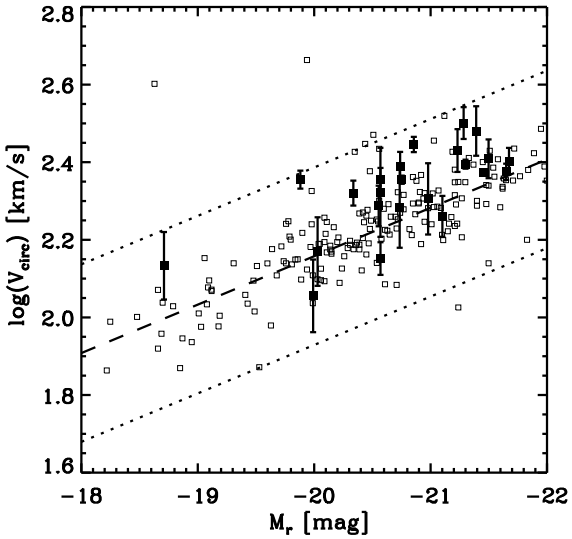

Figure 3.10: Circular velocity as a function of absolute SDSS r-band magnitude of the SAB galaxies successfully analysed with the TW method (*filled squares*) and the galaxy sample of Reyes et al. (2011) (*open squares*). The best-fitting relation (*dashed line*) of Reyes et al. (2011) and the region of 3σ deviation (*dotted lines*) in $\log(V_{\rm circ})$ are given.

nearby SDSS galaxies (Fig. 3.10), our circular velocities are higher on average. However, Reyes et al. (2011) obtained $V_{\rm circ}$ from the rotation curve of the ionized gas, without taking into account for its velocity dispersion. Usually, the ionized gas velocity dispersion in spirals can be as large as $\sim$ 50 km $^{-1}$ in the disc region (Pizzella et al., 2004). Negletting disc contribution biases down the derived value of $V_{\rm circ}$ (Bertola et al., 1995; Cinzano et al., 1999; Corsini et al., 1999; Ho, 2009). Eight galaxies in our sample are common with the subsample of $\sim$ 50 CALIFA galaxies studied by Leung et al. (2018). Our values of $V_{\rm circ}$ are in agreement within the errors.

We calculated $R_{\rm cr} = V_{\rm circ}/\Omega_{\rm bar}$ from the asymmetric-drift-corrected circular velocities and the TW bar pattern speeds, and we derived the ratio between the corotation and bar radius $\mathcal{R} = R_{\rm cr}/R_{\rm bar}$. The values of $V_{\rm circ}$, $R_{\rm cr}$ and $\mathcal{R}$ are reported in Table 3.2.

3.4 Results

3.4.1 Weak bar properties

Our initial sample of *bona fide* SAB galaxies included 29 objects (Table 3.1). They were selected from the CALIFA survey to satisfy the requirements of the TW method. The visual identification of SAB galaxies is difficult (e.g. Nair & Abraham, 2010; Lee et al., 2019) and most of the sample galaxies were actually listed in RC3 either as unbarred galaxies or they could not be more accurately classified as barred or unbarred systems. First, we analysed their surface brightness distributions using SDSS r-band images and CALIFA stellar kine-

matic maps, to check they do not show any morphological or kinematic peculiarity related to interactions or mergers. Then, we considered only galaxies with an intermediate inclination and with a bar with an intermediate orientation with respect to the major and minor axes of the disc. All of these criteria are required by the TW method, but they should favor the choice of objects with a bar component standing out in both the photometric and spectroscopic data. Despite these stringent selection criteria, we discarded six galaxies after performing a Fourier analysis of their surface brightness distributions, because they turned out not to host a clear bar component (Table 3.1). The $m = 2$ Fourier components did not show an amplitude peak with a constant phase angle typical of barred galaxies, while the large odd components were indicative of the presence of non-axisymmetric structures other than an elongated bisymmetric component.

We measured the bar radius and strength of the remaining 23 galaxies and derived their mean strength. We then rejected seven more galaxies because we were not able to measure their $\Omega_{\rm bar}$ with the TW method, due to either a poor correlation between the integrals, large errors, or the non-convergence of the integrals measured from the CALIFA stellar kinematics. This means that 45 per cent of the galaxies of the initial sample do not actually host a genuine bar component. We ended up with 16 confirmed SAB galaxies, which we successfully analysed with the TW method (Table 3.2).

3.4.2 Ultrafast bars

Two galaxies with a TW-measured $\Omega_{\rm bar}$ (13 per cent) host an ultrafast bar having $\mathcal{R} < 1$ at 95 per cent confidence level (Table 3.2). This regime for $\mathcal{R}$ corresponds to bars extending beyond $R_{\rm cr}$, which are expected to rapidly dissolve.

Aguerri et al. (2015) explored possible explanations for measuring $\mathcal{R} < 1$ with the TW method, which include obtaining the wrong estimate of $R_{\rm bar}$ and/or $R_{\rm cr}$, the application to objects which do not meet all the TW requirements, or the presence of multiple pattern speeds associated with the main bar, spiral arms, and for a nuclear bar. To address these issues, we obtained $R_{\rm bar}$ with three different and independent methods. In some cases, these estimates are quite different from each other, but this is reflected in the adopted upper and lower errors on $R_{\rm bar}$ which are defined as the largest differences between the mean value and the three measurements. On the other hand, $R_{\rm cr}$ depends on both $V_{\rm circ}$ and $\Omega_{\rm bar}$. The circular velocity was obtained using the asymmetric drift correction and the resulting values are consistent with the predictions of the Tully-Fisher relation (Reyes et al., 2011) and previous measurements based on different dynamical models (Leung et al., 2018). In Chapter 2, we showed that $\mathcal{R} < 1$ could be the result of a wrong estimate of the disc PA when the PA radial profile does not present a constant trend in the disc region. This is the reason why we checked the constancy of the profiles and finally used the PA from the radial profiles to recover $\Omega_{\rm bar}$. A slope change with radius of the straight-line fit between $\langle X \rangle$ and $\langle V \rangle$ is interpreted as due to components rotating with a different pattern speed with respect to the main bar (Corsini et al., 2003; Maciejewski, 2006; Meidt et al., 2009). This change is observed in IC 1683, NGC 2553, and NGC 6427 (Fig. 3.7), although not all of them host an ultrafast bar (Table 3.2).

We ran a Kolmogorov-Smirnov (KS) test with the IDL procedure KSTWO to verify if there

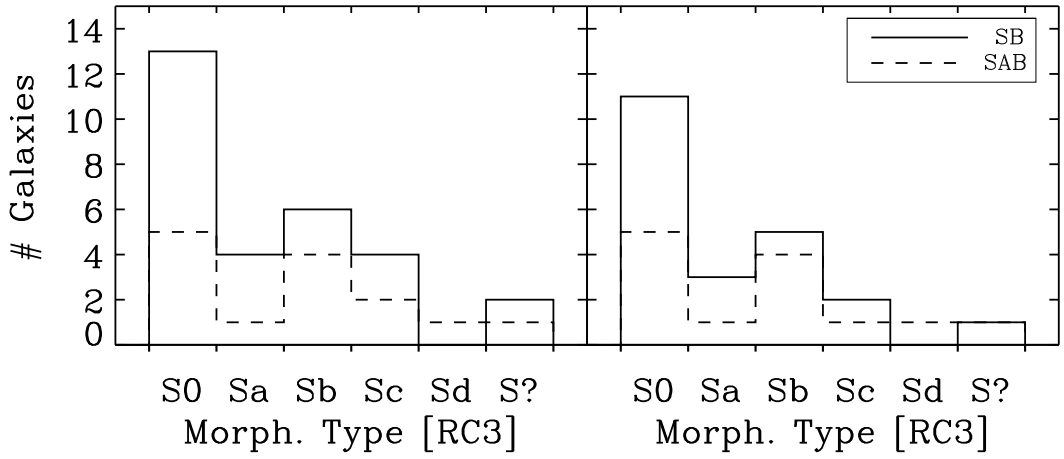

Figure 3.11: Distributions of the morphological types of the SB (*solid line*) and SAB (*dashed line*) galaxies including (*left panel*) and excluding (*right panel*) the ultrafast bars.

are statistical differences between the distributions of morphological types, redshifts, and absolute SDSS r-band magnitudes of the initial sample of 29 *bona fide* SAB galaxies, the sample of 16 SAB galaxies successfully analysed with the TW method, and the sample of 14 SAB galaxies without an ultrafast bar (Fig. 3.1). Since we found no significant difference at a very high confidence level (> 95 per cent) between the properties of the three samples, we decided to not consider further the ultrafast bars.

3.4.3 Bar properties in weakly and strongly barred galaxies

Our goal is to compare the bar properties of a sample of SB and SAB galaxies with TW-measured $\Omega_{\rm bar}$ as well as the properties of their host galaxies. To perform a valid comparison, the different bar properties have to be derived using similar methodologies. To this aim, we added ESO-139-G0009 (Aguerri et al., 2003) to our sample of SAB galaxies without an ultrafast bar and as a comparison sample of SB galaxies, we collected 17 (Debattista & Williams 2004; Aguerri et al. 2015; Chapter 2) and 15 (Merrifield & Kuijken, 1995; Gerssen et al., 1999, 2003; Debattista et al., 2002; Aguerri et al., 2003; Corsini et al., 2003, 2007; Treuthardt et al., 2007) galaxies with $\Omega_{\rm bar}$ measured with the TW method using stellar kinematics obtained with IFU and long-slit spectroscopy, respectively. Only three out of 32 SB galaxies host an ultrafast bar (9 per cent). In Fig. 3.11, we show the distributions of morphological types of the SAB and SB galaxies including or excluding the ultrafast bars. The remarkably large number of SB0 galaxies is an effect of the selection bias due to the application of the TW method to early-type disc galaxies with a low dust and gas content (see Corsini, 2011, for a review).

We also investigated the distributions of absolute SDSS r-band magnitudes and the bar properties of SAB and SB galaxies without an ultrafast bar, respectively. For each parameter, we performed a KS test to look for statistically significant differences between the two samples. We found that the bars in SAB galaxies are similar to those of SB for all the explored

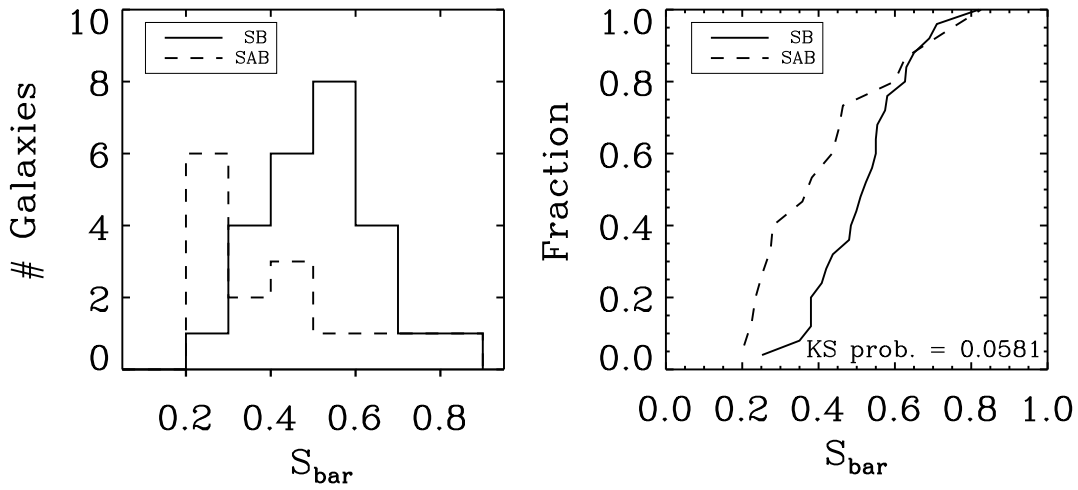

Figure 3.12: *Left panel*: distribution of the bar strengths of the SB (*solid line*) and SAB (*dashed line*) galaxies excluding the ultrafast bars. *Right panel*: cumulative distributions of SB (*solid line*) and SAB (*dashed line*) galaxies without an ultrafast bar as a function of bar strength.

parameters, in particular the two samples have similar bar strengths, when the visual classification is adopted (Figs. 3.12 and 3.13). This is due to the fact that visually-classified SAB galaxies are contaminated by strong bars while comparing the strength of the bars. In fact, the mean bar strength of the SAB galaxies is $\langle S_{\rm bar,SAB} \rangle = 0.42 \pm 0.18$, which is consistent within 1σ error with the mean bar strength of the SB galaxies $\langle S_{\rm bar,SB} \rangle = 0.52 \pm 0.13$. In fact, visually-classified SB galaxies may host weak bars in term of strength and the peak in the SAB bar strength at $S_{\rm bar,SAB} = 0.25$ corresponds to genuine weak bars (Fig. 3.12). This point towards the fact that a visual separation between weak and strong bars does not correspond to classifying the galaxies according to the bar strength.

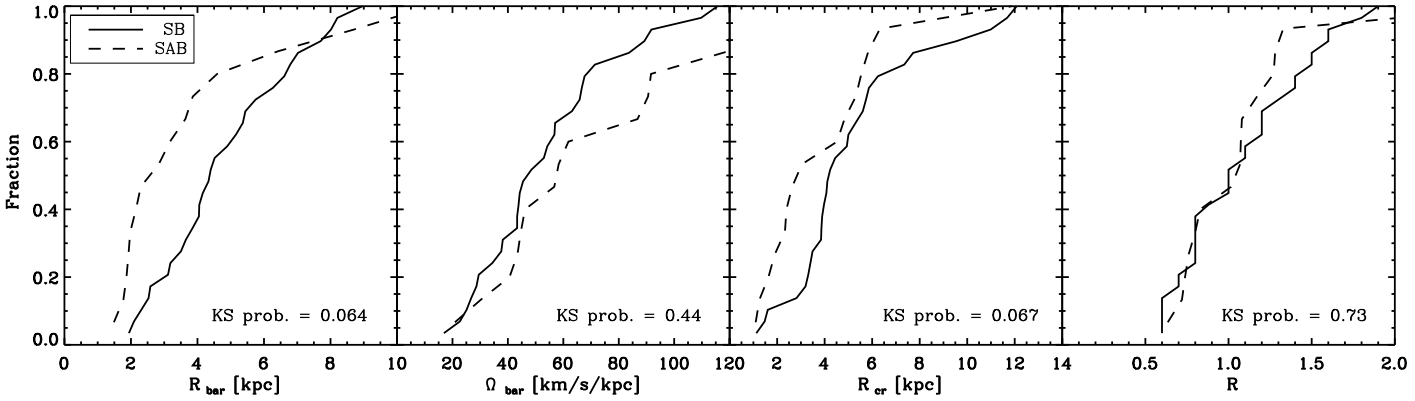

Figure 3.13: Cumulative distributions of visually-classified SB (*solid line*) and SAB (*dashed line*) galaxies without an ultrafast bar as a function of bar radius, bar pattern speed, corotation radius, and bar rotation rate, respectively. The significance level of the KS test is given in each panel.

Since a unique quantitative distinction between strong and weak bars is not found (Athanassoula, 2003; Athanassoula et al., 2013; Vera et al., 2016; Kruk et al., 2018), we decided to split our full sample of 46 galaxies using a quantitative criterion based on the bar strength, if available. The chosen limiting value is $S_{\rm bar} = 0.4$, which corresponds to including 50 per cent of visually-classified SAB galaxies in the new quantitatively-defined SAB sample and to having enough objects in the SB and SAB samples to perform some significant statistics. Speaking about strong and weak bars, from now on we refer to those quantitatively-defined SB and SAB galaxies, because their definitions are based on the bar strength.

We investigated the distributions of bar properties and absolute SDSS r-band magnitudes of the quantitatively-defined 13 SAB and 27 SB galaxies classified through the bar strength and without an ultrafast bar (Figs. 3.14 and 3.15). For each parameter, we performed a KS test to look for statistically significant differences between the two samples. We confirmed that the bars of SAB galaxies are weaker that those of SB galaxies, although their hosts have the same luminosity distribution. In addition, we found at a very high confidence level (> 99 per cent) that weak bars are shorter and have smaller $R_{\rm cr}$ than their strong bar counterparts. On the other hand, SAB and SB galaxies display similar distributions of $\Omega_{\rm bar}$ and $\mathcal{R}$. We repeated this analysis using the results obtained with the PA from the photometric decomposition and obtained similar results. The relations between bar and galaxy properties are investigated in the following section.

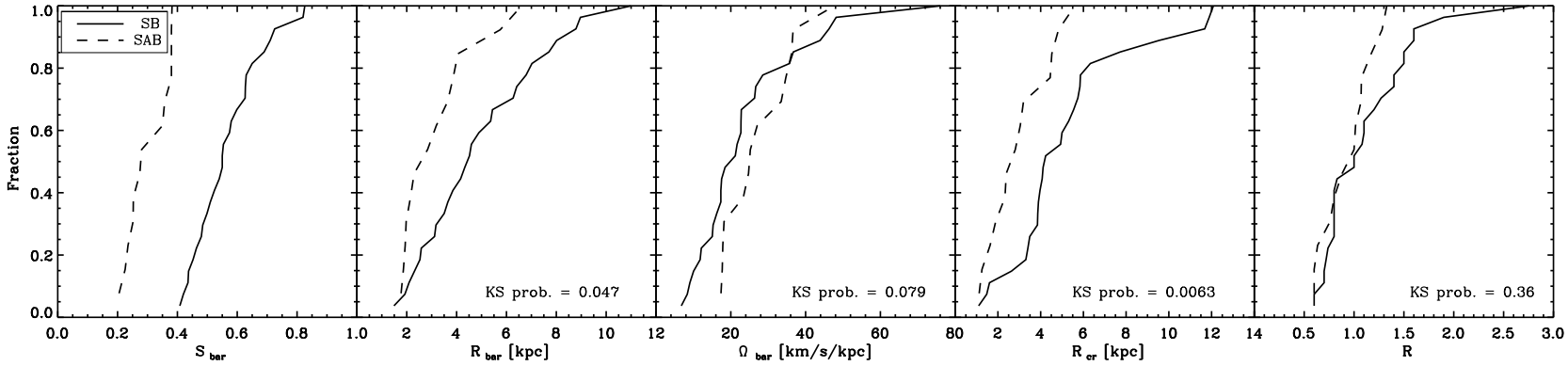

Figure 3.14: Cumulative distributions of SB (*solid line*) and SAB (*dashed line*) galaxies without an ultrafast bar as a function of bar strength, bar radius, bar pattern speed, corotation radius, and bar rotation rate, respectively. The significance level of the KS test is given in each panel.

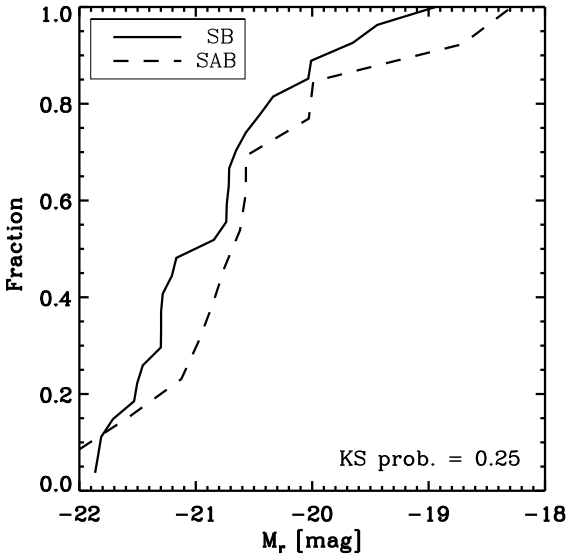

Figure 3.15: Cumulative distributions of SB (*solid line*) and SAB (*dashed line*) galaxies without an ultrafast bar as a function of absolute SDSS r-band magnitude. The significance level of the KS test is given.

3.4.4 Bulge and disc properties in weakly and strongly barred galaxies

We also analysed the relations between the bar parameters and the bulge and disc properties of the SAB and SB galaxies. We recovered the bulge-to-total luminosity ratio B/T, bulge Sérsic index n and effective radius $r_{\rm e}$, and the scalelength h of the disc from Méndez-Abreu et al. (2017) for the CALIFA galaxies and from the quoted papers for the other galaxies.

We performed a KS test on the bulge properties and found that SB and SAB galaxies present at a high significance level the same distributions of n and $r_{\rm e}$ of the bulges, but different distributions of B/T (Fig. 3.16). Moreover, two SAB galaxies turned out to be bulgeless, and the result of the KS tests on the bulge properties remain the same even when discarding these two objects. This analysis suggests that the bulges of SAB and SB galaxies present similar properties but a different contribution to the total light of their host galaxies, giving a larger contribution in SB galaxies.

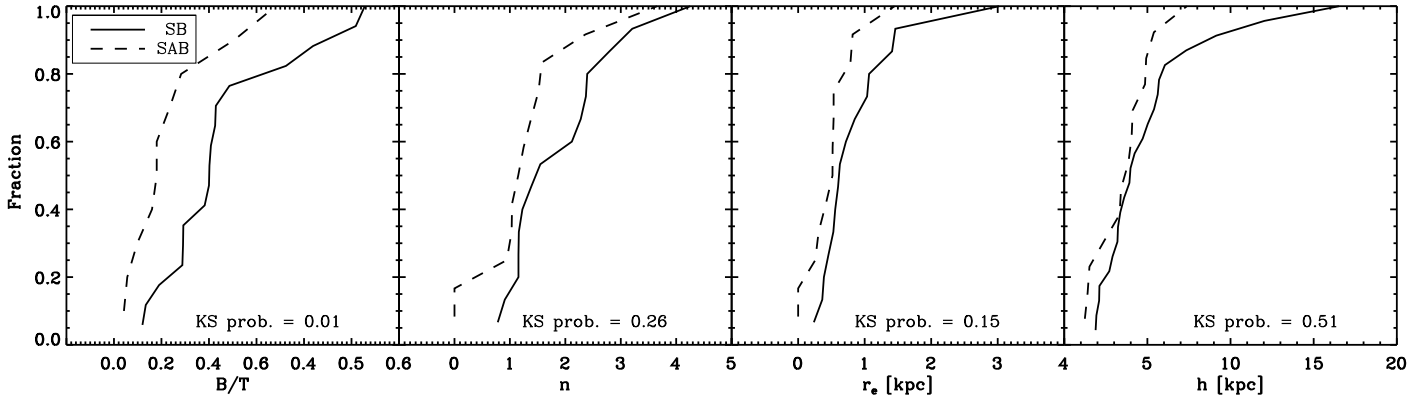

Figure 3.16: Cumulative distributions of SB (*solid line*) and SAB (*dashed line*) galaxies as a function of bulge-to-total luminosity, bulge Sérsic index, and bulge effective radius; cumulative distributions of SB and SAB galaxies without an ultrafast bar as a function of disc scalelength, respectively. The significance level of the KS test is given in each panel.

The discs of SAB and SB galaxies are also similar to each other (Fig. 3.16). To investigate the disc regions hosting weak and strong bars, we measured the ratios between $R_{\rm cr}$ and h and between $R_{\rm bar}$ and h for the SAB and SB galaxies (Fig. 3.17). Most of the bars and corotation radii of both galaxy samples are confined within or are close to their disc scalelength, since the $R_{\rm cr}/h$ and $R_{\rm bar}/h$ typically range from 1 to 1.5. In particular, for SAB galaxies both $R_{\rm bar}/h$ and $R_{\rm cr}/h$ are smaller than 1.5 (except for one outlier, whose $S_{\rm bar}$ lies near the limiting value adopted to split the sample), while 30 per cent of SB galaxies are characterised by $R_{\rm cr}/h$ and $R_{\rm bar}/h$ larger than 1.5. The ratio of $R_{\rm cr}/h$ and $R_{\rm bar}/h$ corresponds to $\mathcal{R}$, which ranges from 1 to 1.4, corresponding to the fast bar regime.

3.5 Discussion and conclusions

In this work, we obtained the bar properties of a sample of 29 *bona fide* SAB galaxies by analysing their r-band images available from the SDSS survey and stellar kinematic maps obtained from the CALIFA survey (Table 3.1). The galaxies were selected to have an intermediate inclination and a bar elongated in between the minor and major axes of the disc and to be morphologically and kinematically undisturbed. The sample galaxies have morphological types ranging from S0 to Scd, with redshifts between 0.005 and 0.3 and absolute SDSS r-band total magnitudes from -18.5 to -23.0 mag.

We derived the bar radii $R_{\rm bar}$ in the deprojected images of the galaxies by measuring the bar/interbar intensity ratios obtained from Fourier analyses of the surface brightness distributions, the locations of the maxima in the ϵ radial profile and the behaviours of the PA radial profiles of the ellipses fitting the galaxy isophotes. At the same time, we measured the bar strengths $S_{\rm bar}$ from the Fourier analyses. Despite the stringent criteria we adopted for the selection, we discarded six galaxies because they turned out not to host a clear bar component. The $m = 2$ Fourier component did not show an amplitude peak with a constant phase angle typical of barred galaxies, while the large odd components revealed the presence of non-axisymmetric structures other than a bar.

We applied the TW method to obtain the bar pattern speeds $\Omega_{\rm bar}$ from the CALIFA datacubes. This study represents the third effort to apply the TW method to a large sample of galaxies using IFU spectroscopy, and the first one including SAB galaxies. To this aim, we measured the luminosity-weighted mean positions and LOS velocities of the stars across the bars in several pseudo-slits parallel to the disc major axes. We rejected seven more galaxies because of their poor correlations, or the large errors, or the non-convergence of the TW integrals. This means that 13 galaxies of the sample (45 per cent), which were morphologically classified as weakly barred galaxies from a visual inspection, do not actually host a genuine bar component or the central elongated structure is not in rigid rotation. For the remaining 16 SAB galaxies, we derived the corotation radii $R_{\rm cr}$ from the circular velocities obtained by applying asymmetric drift corrections to the stellar kinematics and the bar rotation rates $\mathcal{R}$ as the ratios between $R_{\rm cr}$ and $R_{\rm bar}$. All the measured SAB bars are consistent with being fast within their errors ($1 < \mathcal{R} < 1.4$), except for two of them which are ultrafast ($\mathcal{R} < 1$) at 95 per cent confidence level (Table 3.2) and were not considered further. Although several

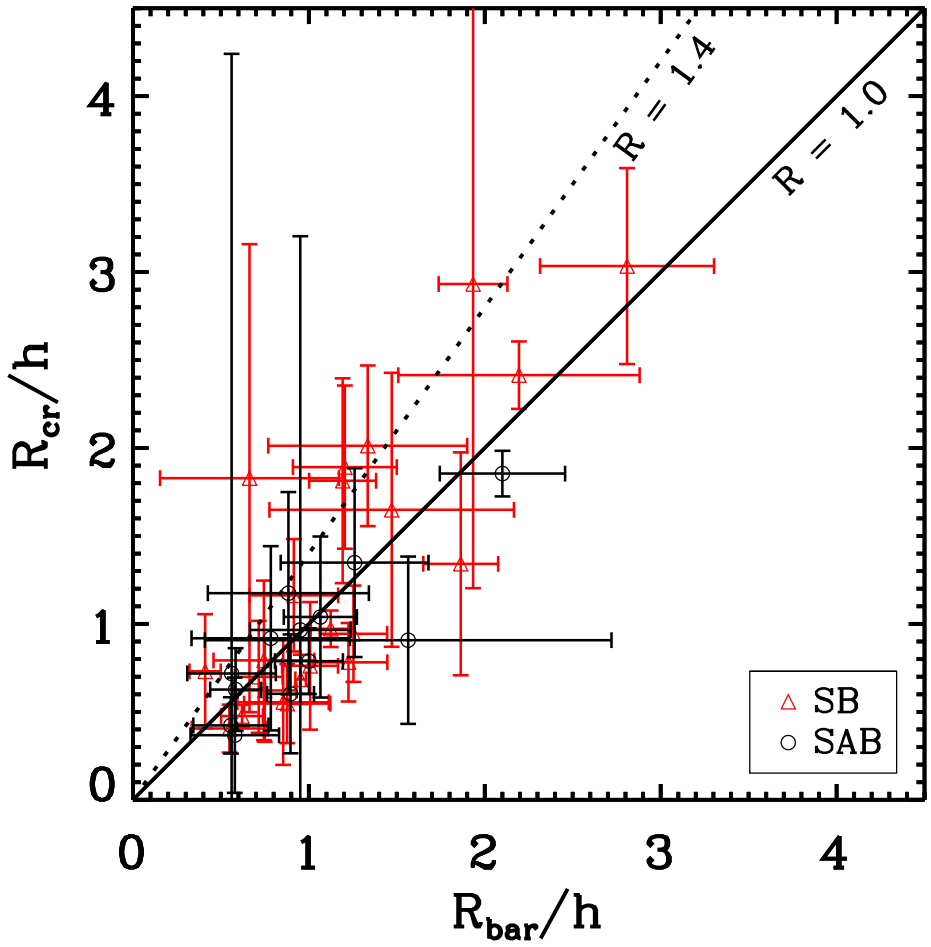

Figure 3.17: Ratio between the corotation radius and the disc scalelength as a function of the ratio between the bar radius and the disc scalelength for SB (*red triangles*) and SAB (*black circles*) galaxies without an ultrafast bar. The locations of $\mathcal{R} = 1.0$ and 1.4 are marked (*solid* and *dashed lines*, respectively).

ultrafast bars have been found with the TW method using IFU spectroscopic data (Aguerri et al., 2015; Guo et al., 2019), their dynamics is not yet fully explained and requires a deeper analysis both from an observational and theoretical point of view.

We built a comparison sample of SB galaxies with TW-based $\Omega_{\rm bar}$ from the literature (Corsini, 2011; Aguerri et al., 2015) and from Chapter 2 (Fig. 3.11). We split the entire sample of 46 barred galaxies (visually-classified SB + SAB) analysed with the TW method so far according to the strength (if available) of the bar and excluding the ultrafast bars. The value $S_{\rm bar} = 0.4$ was adopted to provide a quantitative definition of SAB and SB galaxies, and the final sample includes 13 quantitatively-defined SAB and 27 quantitatively-defined SB galaxies. The SAB galaxies host weaker and shorter bars with smaller corotation radii than the bars of SB galaxies. In the end, both SAB and SB galaxies have similarly large pattern speeds and bar rotation rates and therefore host fast bars (Fig. 3.14). After checking that the two samples do have similar absolute SDSS r-band total magnitudes, we excluded that this result is due to a bias in the distribution of their luminosities (Fig. 3.15). Since SAB galaxies, similarly to SB galaxies, host fast bars, we can exclude that their formation was tidally triggered by a past interaction with a companion. The numerical simulations by Martinez-Valpuesta et al. (2017) and Łokas (2018) show that tidally-induced bars suffer a steady weakening across their evolution but their rotation rate is always in the slow regime, except if the end evolutionary phase of an interaction occurred over a long timescale, where the bar rotation rate is found to be $\mathcal{R} \simeq 1.4$. Our SAB sample includes many early-type disc galaxies (Fig. 3.12), which were found to host fast bars in earlier studies (e.g., Rautiainen et al., 2008; Font et al., 2017). However, we did not find a significant correlation between $\mathcal{R}$ and morphological type because of the small number statistics.

Since one of the most promising and often advocated causes of bar weakening is the presence of a CMC, we investigated the relation between the presence of a weak/strong bars and the bulge properties of the host galaxy. We did not find any significant difference in the Seŕsic index n and effective radius $r_{\rm e}$ of the bulges of SAB and SB galaxies. Instead we found a lower B/T ratio in SAB galaxies. Moreover, we found two bulgeless SAB galaxies. A similar result was found by Abraham & Merrifield (2000), who showed that SAB galaxies are less concentrated that their SB counterparts. Therefore, we conclude that the presence of a prominent bulge does not necessarily imply a bar weakening. Moreover, we clearly found that $\Omega_{\rm bar}$ of weak and strong bars is similar, as previously suggested by measurements with other methods (Font et al., 2017). This allowed us to discard the dissolution scenarios, which always predict an increase in $\Omega_{\rm bar}$ while the bar is losing strength and dissolving, regardless of different causes of dissolution, such as the presence of a CMC, the shape of the DM halo, or gas accretion (Athanassoula, 2003; Bournaud et al., 2005; Athanassoula, 2005). Laurikainen et al. (2013) suggested that bulges in early-type SB galaxies are built by bars, while those in SAB galaxies are possibly the end result a several accretion events that occurred before the bar formation, prescribing different values for the Sérsic index n. In our sample this formation mechanism is not supported because we observe the same distribution of n in SB and SAB galaxies. We can not further investigate the bulge type in SB and SAB galaxies, because the Sérsic index n does not provide a clear separation between classical and pseudobulges and

a variety of spectroscopic and photometric diagnostics including the bulge intrinsic shape is needed (Costantin et al., 2017, 2018; Méndez-Abreu et al., 2018a).

We explored the relation between the presence of a weak/strong bar and the disc scale-length of the host galaxy. We found that weak bars are all hosted in the inner parts of their discs, because most SAB galaxies have both $R_{\rm bar}/h$ and $R_{\rm cr}/h$ smaller than 1.0 and in all SAB galaxies these ratios are smaller than 1.5, except for one outlier. We observed a larger spread of $R_{\rm bar}/h$ and $R_{\rm cr}/h$ in SB galaxies, with a clear tail to values larger than 1.5 (Fig. 3.17).

A generalised picture for bar formation and evolution may be summarised as follows. A bar in the early stage of evolution extends out to its corotation ($\mathcal{R} \sim 1$) and presents a high value of $\Omega_{\rm bar}$. Then, both $R_{\rm bar}$ and $R_{\rm cr}$ increase as a consequence of the angular momentum exchange between the bar and other galactic components, while $\Omega_{\rm bar}$ decreases. At some point during the evolution, corotation reaches a disc region where the stellar density is too low to further feed the bar. From this moment, $R_{\rm cr}$ increases more than $R_{\rm bar}$ and the rotation rate is expected to enter the slow regime ($\mathcal{R} > 1.4$) (Debattista et al., 2006; Athanassoula et al., 2013).

In this scenario, SAB galaxies with small $R_{\rm bar}/h$ and $R_{\rm cr}/h$ could be young bars, while SB galaxies with large $R_{\rm bar}/h$ and $R_{\rm cr}/h$ could be old bars. However, SB and SAB galaxies present similar value of $\Omega_{\rm bar}$ and none of the bars analysed in this work or in previous TW-based works are unambiguously located in the slow regime. Moreover, we are very unlikely to catch a bar in its early phase of evolution because the bar formation phase is very short. This evidence suggests that SAB galaxies are dynamically evolved systems which did not exchange as much angular momentum as the SB galaxies, so their bars have not grown, while the paucity of slow bars remains unexplained. To confirm this scenario, further observations, dynamical modelling, and numerical simulations focused on SAB galaxies are required because it is known that the exchange of angular momentum between the bar and other components depends on several parameters (including the DM central concentration, Debattista & Sellwood e.g. 2000; initial gas fraction and halo triaxiality, Athanassoula et al. e.g. 2013; disc thickness, Klypin et al. e.g. 2009; and stellar mass distribution) and/or weak interactions are not always clearly visible in the velocity fields, (e.g. Salak et al., 2019).

Chapter 4

Relations among structural parameters in barred galaxies with a direct measurement of bar pattern speed[§]

Abstract We aim to investigate the relations between the properties of bars and their host galaxies in a sample of 100 nearby barred galaxies, spanning a wide range of morphological types and luminosities. The sample includes all the galaxies known to have a direct measurement of $\Omega_{\rm bar}$ based on long-slit or IFU spectroscopic data of stellar kinematics. For each galaxy, we collected $R_{\rm bar}$, $S_{\rm bar}$, $\Omega_{\rm bar}$, $R_{\rm cr}$, and $\mathcal{R}$ for the bar and we considered the Hubble type and absolute SDSS r-band magnitude of the host galaxy. We also derived the bulge-to-total luminosity ratio for a subsample of 34 galaxies with an available photometric decomposition. We limited our analysis to the galaxies with a relatively small relative error on the bar pattern speed ($\Delta\Omega_{\rm bar}/\Omega_{\rm bar} < 0.5$) and not hosting an ultrafast bar ($\mathcal{R} > 1$). The final sample consists of 75 objects, with 33 SB0-SBa and 42 SBab-SBc galaxies. We confirmed earlier observational findings that longer bars rotate with a lower $\Omega_{\rm bar}$, shorter bars are weaker, fast bars rotate with higher $\Omega_{\rm bar}$ and have shorter corotation radii, and disc-dominated galaxies host weaker bars. In addition, we found that stronger bars rotate with a lower $\Omega_{\rm bar}$ as predicted for the interchange of angular momentum during bar evolution depending on galaxy properties. Moreover, we report that brighter galaxies host longer bars, which rotate with a lower $\Omega_{\rm bar}$ and have a larger corotation. This result, together with the fact that we observe stronger bars in bulge-dominated galaxies, is in agreement with a scenario of downsizing in bar formation and co-evolution of bars and bulges, if more massive galaxies formed earlier and had sufficient time to slow down, grow in length, and push corotation outwards.

[§] *Based on V. Cuomo, J. A. L. Aguerri, E. M. Corsini et al. 2019, A&A, in preparation.*

4.1 Introduction

Bars are a common feature in the local Universe across a wide range of galaxy morphologies (Aguerri et al., 2009; Buta et al., 2015), luminosities (Méndez-Abreu et al., 2010; Erwin, 2018), and environments (Méndez-Abreu et al., 2012; Lin et al., 2014). The photometric, kinematic, and dynamical properties of bars depend on their formation mechanisms and evolutionary processes including the interchange of angular momentum with the other galaxy components (Athanassoula, 2003; Villa-Vargas et al., 2010; Athanassoula et al., 2013).

According to their overall shape, bars can have either a classical morphology characterised by a smooth light distribution, or an ansae-type morphology with a light concentration at each end (Laurikainen et al., 2007; Martinez-Valpuesta et al., 2007). Bars can be roughly divided into flat and exponential based on their surface brightness radial profile. A flat bar has a flatter profile than the surrounding disc, whereas the profile of an exponential bar is more similar to that of the disc (Elmegreen & Elmegreen, 1985; Elmegreen et al., 1996). In addition, flat bars are more typical of early-type (ETBGs) rather than late-type barred galaxies (LTBGs) and they can display isophotal twists (Elmegreen, 1996).

The relations between the properties of bars and their host galaxies have been widely explored. Early findings include the results by Elmegreen & Elmegreen (1985), who found that bars in ETBGs are longer than those in LTBGs, and by Athanassoula & Martinet (1980), who observed that galaxies with smaller bulges have also shorter bars. Kruk et al. (2018) confirmed these findings using the GalaxyZoo project (Lintott et al., 2008). In fact, they observed that low-mass, disc-dominated galaxies have bars with an almost exponential light profile, while high-mass galaxies characterised by the presence of a prominent bulge have bars with a flat light profile. Moreover, bars in ETBGs seem to be on average stronger than those in LTBGs (Lee et al., 2019). Díaz-García et al. (2016) studied the shapes of bars. In lenticular galaxies, especially in low-mass objects ($M_*/M_\odot < 10^9$), bars are oval-shaped, while in early- and intermediate-type spirals (SB0/a-SBc) bars are intrinsically narrower than in later types. However, the shape of bars among ETBGs can be rounded by the presence of a bulge and/or barlens. Concerning the strength of bars, ETBGs (especially when more massive, $M_*/M_\odot > 10^9$) host stronger bars, which are characterised by more discy inner isophotes as well. Their results agree with a scenario whereby LTBGs move in the Hubble sequence towards earlier-types, while bars trap particles from the disc and become narrower and stronger (Kormendy, 2013). Kim et al. (2016) investigated the relations between the properties of bars and those of the inner parts of their host discs based on Spitzer data. They found that among massive galaxies ($M_*/M_\odot > 10^{10}$), longer bars reside in more flattened inner discs (i.e., discs with larger inner scalelengths and lower central surface brightnesses) than shorter bars. Moreover, such bars are often associated with a light deficit in the disc surrounding them. This deficit turns out to be more pronounced with longer bars and/or in galaxies with a higher Bar/T, this among all the explored masses ($10^9 < M_*/M_\odot < 10^{11}$). Consolandi (2016) found that massive spiral galaxies harbour a red and dead bar, and these bar properties are sharpened according with increasing mass. Aguerri (1999) found that the star formation activity is enhanced when the galaxy host a strong bar. Erwin (2005) confirmed that bars in ETBGs are larger than bars in LTBGs, but this is true also for relative sizes

($R_{\rm bar}$ relative to the radius of the isophote with 25 mag arcsec^{-2} in B-band R_{25} or to the disc scalelength h). Moreover, ETBGs present a strong correlation between $R_{\rm bar}$ and disc size, but this correlation disappears in LTBGs. Strong and weak bars in ETBGs differ primarily in ellipticity, while they present very similar sizes. However, strong bars in LTBGs are on average twice the size of weak bars. Menéndez-Delmestre et al. (2007) found a decrease in the mean bar ellipticity from ETBGs to LTBGs, so $S_{\rm bar}$ seems to decrease with the galaxy Hubble type.

The structural and dynamical evolution of a barred galaxy are driven by $\Omega_{\rm bar}$. This is the angular speed of the bar and determines how far from the galaxy centre the bar affects the orbits of stars and gas. Stellar dynamics sets an upper limit to $\Omega_{\rm bar}$, when the bar radius $R_{\rm bar}$ reaches the corotation radius $R_{\rm cr}$(where $\Omega_{\rm bar}$ equals the circular frequency), and the bar rotates as fast as it can. On the other hand, there is no lower limit for $\Omega_{\rm bar}$ since the bar can be much shorter than $R_{\rm cr}$, rotating slower than in the previous case. The bar rotation rate $\mathcal{R} \equiv R_{\rm cr}/R_{\rm bar}$ makes it possible to distinguish between 'fast' and 'slow bars' when $1 \leq \mathcal{R} \leq 1.4$ and $\mathcal{R} > 1.4$, respectively. The limiting value 1.4 was set by numerical simulations (Athanassoula, 1992; Debattista & Sellwood, 2000) and it does not imply any specific range for $\Omega_{\rm bar}$. The case of $\mathcal{R} < 1$ corresponds to a non-stable regime for stellar orbits leading to bar dissolution. Nevertheless, some example of these 'ultrafast' bars have been observed (Buta & Zhang, 2009; Aguerri et al., 2015; Guo et al., 2019).

A lot of effort has been devoted to determine $\Omega_{\rm bar}$ and/or $\mathcal{R}$ in a large number of galaxies, to understand how they are related to the properties of the bar or other galaxy components. Rautiainen et al. (2008) derived $R_{\rm cr}$ as the physical upper limit of $\Omega_{\rm bar}$ for 38 barred galaxies, by comparing their observed morphologies with those predicted by a set of dynamically-motivated numerical simulations. They found some weak correlations between $\mathcal{R}$ and galaxy morphology, with ETBGs hosting fast bars and LTBGs showing either fast or slow bars. Slow bars roughly tend to be shorter and weaker, with no clear trend with either galaxy luminosity or colour. Rautiainen et al. (2008) pointed out that their findings depend strongly on the adopted modelling and leave room for the possibility that the derived pattern speed in many galaxies is that of the spiral structure rather than the bar's one. Font et al. (2017) analysed a sample of 68 spirals with $R_{\rm cr}$ obtained from the phase-reversals of the streaming motions. The value of $\mathcal{R}$ increases from SBa to SBb galaxies, then it remains constant out to SBd galaxies and drops for SBm galaxies. Two third of the sample galaxies turned out to host a fast bar. The longest bars rotate with a lower $\Omega_{\rm bar}$ and are found only in the more massive galaxies ($M_*/M_\odot > 3.2 \times 10^{10}$), whereas the shortest bars are hosted in intermediate- and low-mass galaxies. Bars in intermediate-mass galaxies ($3.2 \times 10^9 < M_*/M_\odot \leq 3.2 \times 10^{10}$) can rotate both slowly and fast, while bars in low-mass galaxies ($M_*/M_\odot < 3.2 \times 10^9$) rotates only slowly. Moreover, more massive galaxies host both strong and weak bars, while less massive galaxies only host weak bars. Font et al. (2017) concluded that evolved barred galaxies should have large stellar masses and slow-rotating long bars. This is consistent with both scenarios of bar formation, as the result of either internal processes or tidal interactions.

However, the $\Omega_{\rm bar}$ values measured by Rautiainen et al. (2008) and Font et al. (2017) require some modelling, contrary to the TW method. The TW method's early applications to

long-slit spectroscopic data of a single or few galaxies prevented inferring any firm conclusion about the relations between $\Omega_{\rm bar}$ (and $\mathcal{R}$) and galaxy properties.

Very recently, the TW method has been applied to IFU spectroscopic data of a larger number of galaxies. Aguerri et al. (2015) investigated 15 strongly barred galaxies of the CALIFA survey (Sánchez et al., 2012). They combined their results with previous measurements based on the TW method (see Corsini, 2011, for a review), collecting a sample of 32 galaxies. For all these galaxies, $1.0 < \mathcal{R} < 1.4$ and does not depend on Hubble type. Aguerri et al. (2015) concluded that both ETBGs and LTBGs are consistent with hosting fast bars but they could not infer any other relations due to their small statistics. Guo et al. (2019) performed a similar analysis on a sample of 51 galaxies from the MaNGA survey (Bundy et al., 2015). They found that larger bars are stronger, but they were not able to observe any trend between $\mathcal{R}$ and stellar age, metallicity, strength of the bar or DM fraction within the galaxy effective radius. Guo et al. (2019) argued this is due to the various factors involved in the slowdown process and angular momentum exchange. However, it should be noticed that the large uncertainties of their measurements could have heavily affected their conclusions. Finally, in Chapter 3 we analysed 16 weakly barred CALIFA galaxies and found that weak bars have shorter $R_{\rm bar}$ and $R_{\rm cr}$ but similar $\Omega_{\rm bar}$ and $\mathcal{R}$ than strong bars. The fact that weak bars are fast excludes that their formation was triggered by tidal interactions.

In this Chapter we aim to revisit the full sample of galaxies with TW-measured $\Omega_{\rm bar}$. This will allow us to collect for the first time a statistically significant sample of galaxies spanning a wide range of $R_{\rm bar}$, $S_{\rm bar}$, and $\Omega_{\rm bar}$ with consistent direct measurements of $\Omega_{\rm bar}$, to infer possible relations between the properties of bars and their host galaxies. The Chapter is structured as follows. We present the galaxy sample in Sec. 4.2. We collect the bar properties of the sample galaxies in Sec. 4.3. We present and discuss our results in Sec. 4.4 and 4.5, respectively. We summarise our conclusions in Sec. 4.6.

4.2 The sample

We collected a sample of 100 galaxies with a direct measurement of $\Omega_{\rm bar}$ based on stellar kinematics available in the literature. Either long-slit or IFU spectroscopy was used to obtain the mean position and mean LOS velocity of the stars across the bar needed to apply the TW method. All the sample galaxies were analysed in a consistent way and are divided into three subsamples according to their source:

1. 18 galaxies (literature subsample; see Table 4.1) are taken from sparse papers (Merrifield & Kuijken, 1995; Gerssen et al., 1999, 2003; Debattista et al., 2002; Aguerri et al., 2003; Corsini et al., 2003, 2007; Debattista & Williams, 2004; Treuthardt et al., 2007) and from Chapter 2, applying the TW method to a single or a few objects observed with different telescopes and instruments (see Corsini, 2011, for an almost complete review). Although the Hubble types of this subsample runs from SB0 to SBbc, the majority of the galaxies (~ 85 per cent) are classified as SB0 or SBa. This reflects a selection bias of the early applications of the TW method, when ETBGs were preferred because they are easier to analyse. The redshifts are $z < 0.025$, with ~ 70 per cent of the subsample

galaxies having $z < 0.01$. The absolute SDSS r-band magnitudes are well distributed between -18.0 and -22.0 mag.

2. 31 galaxies (CALIFA subsample; see Table 4.2) are taken from the CALIFA survey and include 15 strongly barred galaxies and 16 weakly barred galaxies analysed by Aguerri et al. (2015) and Chapter 3, respectively. The CALIFA survey (Sánchez et al., 2012; Walcher et al., 2014) targeted ~ 600 galaxies selected from the SDSS-DR7 (Abazajian et al., 2009) according to their angular isophotal diameter ($D_{25} \sim 45 - 80$ arcsec) and redshift ($z \sim 0.005 - 0.03$). The galaxies of the CALIFA subsample have Hubble types from SB0 to SBd, redshifts $0.005 < z < 0.03$ with most of them (~ 85 per cent) in the range $0.01 < z < 0.02$, and absolute SDSS r-band magnitudes between -19.5 and -22.5 mag.

3. 51 galaxies (MaNGA subsample; see Table 4.3) are taken from the MaNGA survey and were measured by Guo et al. (2019). The MaNGA survey (Drory et al., 2015; Yan et al., 2016; Wake et al., 2017) aims to investigate ~ 10000 nearby galaxies from the SDSS Main Galaxy Legacy Area (Abazajian et al., 2009). The galaxies were selected to have redshifts $0.02 < z < 0.1$ and color-based stellar masses $M_*/M_\odot > 10^9$. The original 53 galaxies of Guo et al. (2019) turned out to be 51 because two objects are repeated. The galaxies of the TW subsample have Hubble types from SB0 to SBc, although most of them (~ 70 per cent) are characterised by a late-type morphology. Their redshift range reflects the mother sample distribution ($0.02 < z < 0.08$) and the galaxies of the most populated bin (~ 55 per cent) have $0.025 < z < 0.04$. The absolute SDSS r-band magnitudes are distributed between -19.5 mag and -23.0 mag.

For each sample galaxy, we adopted the morphological classification and redshift of its corresponding paper. If the galaxy redshift was not immediately available, we took the value given by NED. We calculated the absolute SDSS r-band magnitude M_r either from the apparent model r-band magnitude m_r provided by the SDSS DR14 or using the apparent magnitude in a different band, converted into m_r using the prescriptions of Fukugita et al. (1996). To this aim, we considered the galaxy distance from NED as obtained from the radial velocity with respect to the cosmic microwave background reference frame, and adopting as cosmological parameters $\Omega_{\rm m} = 0.286$, $\Omega_\Lambda = 0.714$, and $H_0 = 69.3$ km s^{-1} Mpc^{-1} (Hinshaw et al., 2013).

Figure 4.1 shows the distributions of the Hubble types, redshifts, and absolute SDSS r-band magnitudes of the three subsamples, together with the total distributions of the entire sample. The literature subsample is made mostly of ETBGs, whereas the CALIFA and MaNGA subsamples contain more LTBGs. The redshifts are smaller for the literature and CALIFA subsamples than the MaNGA ones. More than 90 per cent of the sample galaxies are brighter than $M_r = -20.0$ mag. Although the three subsamples show similar distributions of M_r, it is clear that the brighter galaxies mainly come from the MaNGA subsample and the fainter ones from the literature subsample.

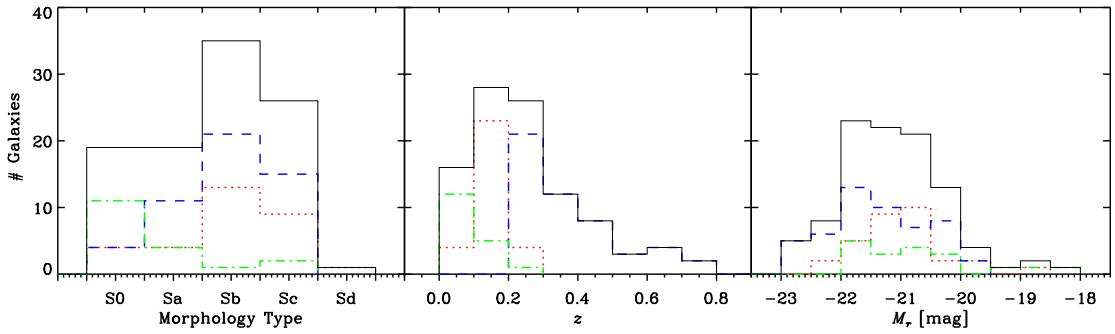

Figure 4.1: Distributions of Hubble types, redshifts z, and absolute SDSS r-band magnitudes M_r of the full sample of 100 galaxies (*black solid line*), literature subsample (*green dot-dashed line*), CALIFA subsample (*red dotted line*), and MaNGA subsample (*blue dashed line*).

4.3 Determination of the bar parameters

A bar is completely described by its $R_{\rm bar}$, $S_{\rm bar}$ and $\Omega_{\rm bar}$. The radius and strength of the bar are structural parameters and can be recovered from the analysis of optical and/or near-infrared images, while the pattern speed of the bar is a dynamical parameter and its determination requires a kinematic analysis.

4.3.1 Bar radius and strength

The value of $R_{\rm bar}$ is a measure of the extension of the stellar orbits supporting the bar. It is quite difficult to be derived because a bar does not present sharp edges and is often associated with other components (like rings or spiral arms) which may affect the identification of its boundary. To overcome these limitations, several methods have been used to constrain $R_{\rm bar}$. Here, we briefly review the measuring techniques adopted for the sample galaxies.

A first class of methods to measure $R_{\rm bar}$ is based on the direct analysis of galaxy images. A rough estimate is obtained by the visual inspection of the images (Merrifield & Kuijken, 1995; Treuthardt et al., 2007) or by identifying the slope change of the surface brightness profile along the bar major axis (Gerssen et al., 1999). Two more refined techniques require the study of the radial profile of ϵ and PA of the ellipses which best fit the galaxy isophotes, respectively. The galaxy isophotes show a peak of ϵ and a constant PA in the bar region, and constant PA in the disc region too. The value $R_{\rm bar}$ is identified as the position of the maximum in the ϵ profile (Aguerri et al. 2015; Guo et al. 2019; Chapter 3) or as the position where the PA changes by $\Delta{\rm PA} = 5^\circ$ from the PA of the ellipse corresponding to the maximum in ϵ (Aguerri et al. 2015; Guo et al. 2019; Chapter 3). A second class of methods is based on the Fourier analysis of the images, which consists in the decomposition of the deprojected azimuthal luminosity profile of the galaxy into a Fourier series (Aguerri et al., 2000). Through this analysis, $R_{\rm bar}$ can be recovered from the luminosity contrasts between the bar and interbar intensity as a function of radial distance (Debattista et al. 2002; Aguerri et al. 2003, 2015; Gerssen et al. 2003; Debattista & Williams 2004; Corsini et al. 2007; Guo

et al. 2019; Chapter 2 and 3) or studying the phase angle of the Fourier mode $m = 2$ (Aguerri et al., 2003; Gerssen et al., 2003; Corsini et al., 2003, 2007; Debattista & Williams, 2004). Analysing the PA of the deprojected isophotal ellipses, $R_{\rm bar}$ is the position where the PA changes by a value of 10° from the PA of the ellipse with the maximum ϵ value (Debattista et al. 2002; Aguerri et al. 2003; Corsini et al. 2003, 2007; Chapter 2). Finally, it is possible to perform a photometric decomposition of the surface brightness distribution of the galaxy (Aguerri et al. 2003; Corsini et al. 2003, 2007; Gerssen et al. 2003; Chapter 2), which however depends on the adopted parametric laws for the different galaxy components. The choice of a single measurement method is usually limited by its own weaknesses, so usually more than one method is adopted to recover $R_{\rm bar}$, which is then given by the combined results from the different applied methodologies (Aguerri et al. 2003, 2015; Guo et al. 2019; Chapters 2 and 3). We collected the values of $R_{\rm bar}$ provided by previous works for each galaxy in the sample.

The value of $S_{\rm bar}$ describes the contribution of the bar to the galaxy potential and measures the non-axisymmetric forces produced by the bar. A variety of methods have been developed to constrain $S_{\rm bar}$ and here, we briefly review those adopted for the sample galaxies. A first method is based on the ϵ of the bar, which can be obtained from the isophotal radial profile or from a photometric decomposition (Chapter 2). A related approach consists in measuring the Q_t parameter (Treuthardt et al., 2007). Finally, the $S_{\rm bar}$ can be recovered in various ways from a Fourier analysis, both from the peak of the ratio between the amplitudes of the $m = 2$ and $m = 0$ Fourier components (Guo et al. 2019; Chapter 2), or from the integral of the ratio between the $m = 2$ and $m = 0$ Fourier components divided by $R_{\rm bar}$ (Chapter 2). Since these different methods are connected to different bar properties, their results can considerably differ, even for the same object.

The strengths of the bars were not always measured in previous works; this is especially true for the literature and CALIFA subsamples. To have consistent measurements of $S_{\rm bar}$, we thus adopted the peak of the ratio between the amplitudes of the $m = 2$ and $m = 0$ Fourier components, and derived $S_{\rm bar}$ for all the galaxies for which it was not already available and for which we have photometric data to perform the Fourier analysis. The values of $R_{\rm bar}$ and $S_{\rm bar}$ for all the sample galaxies are listed in Tables 4.1, 4.2, and 4.3.

4.3.2 Bar pattern speed and corotation radius

There are several methods to recover $\Omega_{\rm bar}$ (see Chapter 1 for a discussion), but the only model-independent one is that based on the TW equation,

$$\langle X \rangle \, \Omega_{\rm bar} \sin i = \langle V \rangle, \tag{4.1}$$

where i is the disc inclination and

$$\langle X \rangle = \frac{\int X \Sigma dX}{\int \Sigma dX}, \;\; \langle V \rangle = \frac{\int V_{\rm los} \Sigma dX}{\int \Sigma dX} \tag{4.2}$$

are the photometric $\langle X \rangle$ and kinematic $\langle V \rangle$ integrals, defined as the luminosity-weighted average of position and LOS velocity $V_{\rm los}$, respectively, measured along directions parallel to

the disc major axis, and applied to a tracer population satisfying the continuity equation. In practice, the integrals are calculated along several apertures, one centred on the galaxy centre and the others with an offset, but all aligned with the disc major axis. The slope of the straight line defined by the measured values of $\langle X \rangle$ versus $\langle V \rangle$ gives $\Omega_{\rm bar} \sin i$. In IFU spectroscopy, $\langle X \rangle$ and $\langle V \rangle$ are derived by collapsing the datacube along the wavelength and the spatial directions of each pseudo-slit, respectively, and this corresponds to using a luminosity weight in the integrals (Chapter 2). As an alternative, the kinematic integrals can be directly obtained from the stellar velocity field using either a map of the surface brightness (Aguerri et al., 2015; Guo et al., 2019) or stellar mass (Aguerri et al., 2015) as a weight in the integrals definition.

The most critical parameter for the TW method is the correct definition of the PA of the disc, along which to locate the pseudo-slits (Debattista 2003; Zou et al. 2019; Chapter 2). Usually, it can be defined from a careful analysis of the surface photometry of the galaxy. Isophotal analysis, photometric decomposition, and kinemetry have been shown to give consistent results (Aguerri et al. 2015; Guo et al. 2019; Chapter 3).

To have consistent values of $\Omega_{\rm bar}$ for all the sample galaxies, we selected for our analysis the TW measurements adopting the photometric PA of the galaxy major axis, when more than one PA estimate was available (e.g., Guo et al. 2019; Chapter 3), and the luminosity weight in the integrals.

The value of $R_{\rm cr}$ is the radius where the gravitational and centrifugal forces cancel out in the rest frame of the bar and it is given by the ratio between $V_{\rm circ}$ and $\Omega_{\rm bar}$. A simple and basic approach consists in using the maximum of the (cold) gaseous rotational velocity as approximation for $V_{\rm circ}$ (Treuthardt et al., 2007). Another straightforward and more solid estimate consists in the application of the asymmetric drift correction to the observed stellar streaming velocities (Merrifield & Kuijken 1995; Debattista et al. 2002; Aguerri et al. 2003, 2015; Corsini et al. 2003, 2007; Gerssen et al. 2003; Debattista & Williams 2004; Chapter 2 and 3). A full dynamical model built from the kinematics and surface brightness of the stellar component represents a more sophisticated approach (Gerssen et al., 1999; Guo et al., 2019). The values of $\Omega_{\rm bar}$, $R_{\rm cr}$, and the resulting $\mathcal{R}$ for all the sample galaxies are listed in Tables 4.1, 4.2, and 4.3.

4.3.3 Selection bias and ultrafast bars

The successful application of the TW method requires the disc to have an intermediate i and the bar to be located at an intermediate PA with respect to the disc major and minor axes. In fact, when the galaxy is too inclined, it is difficult to identify the bar and its PA and consequently to place the apertures. On the other hand, a low value of i corresponds to low LOS velocities and large errors on the velocities. Concerning the bar, it can not be located too parallel to the disc axes. Given the difference ΔPA between bar PA and disc major axis PA, if the bar is almost aligned to the disc major axis (PA = 0°), it is difficult to define a sufficient number of apertures. The other extreme case, when the bar is closed to the disc minor axis (PA = 90°), leads to low values of the photometric integrals. These extreme situations make it hard to apply the TW method, and to take under control the source of

errors, which translate into large uncertainties in the measured parameters (Debattista, 2003; Corsini, 2011; Zou et al., 2019). For these reasons, all the sample galaxies have an inclination $30° \lesssim i \lesssim 70°$ and a PA difference between bar and disc major axis $10° \lesssim |\Delta\mathrm{PA}| \lesssim 80°$.

The disc inclination and the position of the bar with respect to the disc axes may also affect the correct estimation of $R_{\rm bar}$ (Debattista, 2003; Corsini, 2011).

Figures 4.2 and 4.3 show the relative errors on $\Omega_{\rm bar}$, $R_{\rm bar}$, and $R_{\rm cr}$ for the sample galaxies as a function of the disc i and bar ΔPA, respectively. Despite the large uncertainties of some values, we did not observe any significant trend and we excluded any selection bias on the galaxy sample. There is also no evident bias for the ultrafast bars. Indeed, 12 galaxies (12 per cent) of the sample host a bar with $\mathcal{R} < 1.0$ at 95 per cent confidence level. All of them are found in LTBGs. At the moment, we do not yet know whether ultrafast bars are either an artifact of the TW method or actually a new class of objects that overrule the predictions of theory and numerical simulations about the extension of the bar (see also Aguerri et al. 2015 and Guo et al. 2019, for a discussion). This issue requires further investigation which is beyond our aims, and we decided to discard the 12 ultrafast bars from the rest of the analysis.

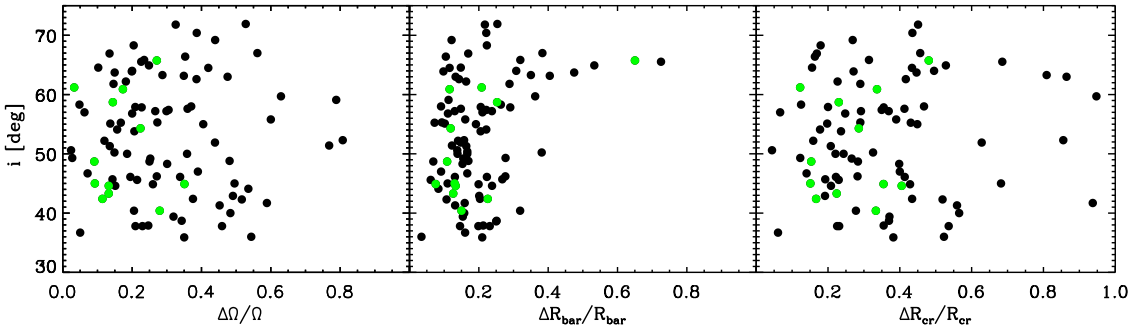

Figure 4.2: Relative errors of the bar pattern speed $\Delta\Omega_{\rm bar}/\Omega_{\rm bar}$, bar radius $\Delta R_{\rm bar}/R_{\rm bar}$, and corotation radius $\Delta R_{\rm cr}/R_{\rm cr}$ as a function of the disc inclination i. Ultrafast bars are highlighted (*green points*). Galaxies with relative errors larger than 100 per cent are not shown.

Table 4.1: Properties of the 18 galaxies of the literature subsample.

Galaxy	Morph. Type	z	M_r [mag]	$R_{\rm bar}$ [kpc]	$S_{\rm bar}$ [kpc]	$\Omega_{\rm bar}$ [km s^{-1} kpc^{-1}]	$R_{\rm cr}$ [kpc]	$\mathcal{R}$	B/T	Ref.	Final sample
(1)	(2)	(3)	(4)	(5)	(6)	(7)	(8)	(9)	(10)	(11)	(12)
ESO 139-G09	SAB0^0(rs)	0.018	-21.21	$6.4^{+2.4}_{-1.1}$	0.44	57 ± 15	$5.5^{+2.0}_{-1.2}$	$0.8^{+0.3}_{-0.2}$	...	1	yes
ESO 281-G31	SB0^0(rs)	0.018	-21.22	4.04 ± 0.37	...	29 ± 11	$7.4^{+4.4}_{-1.5}$	$1.8^{+1.1}_{-0.4}$	...	2	yes
IC 874	SB0^0(rs)	0.0078	-20.57	$3.65^{+0.94}_{-0.90}$	0.57	38 ± 13	$4.9^{+2.4}_{-1.2}$	$1.4^{+0.7}_{-0.4}$	...	1	yes
NGC 271	(R')SBab(rs)	0.014	-21.81	7.70 ± 0.27	0.63	29 ± 16	$11.7^{+8.0}_{-4.2}$	$1.5^{+1}_{-0.5}$	...	2	no
NGC 936	SB0$^+$(rs)	0.0048	-20.71	4.16	0.55	57 ± 13	$5.7^{+1.2}_{-1.2}$	$1.4^{+0.5}_{-0.4}$	...	3	yes
NGC 1023	SB0$^-$(rs)	0.0021	-20.01	$2.09^{+0.15}_{-0.29}$	0.48	89 ± 31	$1.61^{+0.18}_{-0.34}$	$0.8^{+0.5}_{-0.3}$	...	4	yes
NGC 1308	SB0/a(r)	0.021	-21.71	$5.36^{+0.78}_{-1.47}$	0.50	92 ± 32	$3.9^{+1.9}_{-1.0}$	$0.8^{+0.4}_{-0.2}$	...	1	yes
NGC 1358	SAB0/a(r)	0.013	-21.09	5.16 ± 0.81	...	34 ± 17	$6.2^{+5.2}_{-1.9}$	$1.2^{+1.0}_{-0.4}$	...	2	no
NGC 1440	(R')SB0^0	0.0053	-18.94	$2.53^{+0.63}_{-0.54}$	0.44	71 ± 16	$3.97^{+1.11}_{-0.73}$	$1.6^{+0.5}_{-0.3}$	...	1	yes
NGC 2523	SBbc(r)	0.012	-21.88	8.21	...	27 ± 6	10.988	$1.3^{+0.7}_{-0.5}$	0.07	5	yes
NGC 2950	(R)SB0^0(r)	0.0044	-20.72	3.50 ± 0.21	0.55	110 ± 24	$3.30^{+0.89}_{-0.63}$	$1.0^{+0.3}_{-0.2}$	...	6	yes
NGC 3412	SB00(s)	0.0028	-20.45	2.58 ± 0.24	0.41	53 ± 14	$3.90^{+1.44}_{-0.82}$	$1.5^{+0.6}_{-0.3}$	...	1	yes
NGC 3992	SBbc(rs)	0.0035	-19.44	4.9 ± 1.0	0.52	66.7 ± 4.2	3.86 ± 0.26	$0.8^{+0.2}_{-0.2}$	...	2	yes
NGC 4245	SB0/a	0.0030	-20.03	3.11	0.48	57 ± 23	3.490	$1.1^{+1.1}_{-0.4}$	0.2	5	yes
NGC 4264	SB0	0.0084	-20.62	3.19 ± 0.51	$0.35^{+0.02}_{-0.01}$	67.7 ± 3.4	2.81 ± 0.17	$0.88^{+0.2}_{-0.2}$	0.09	7	yes
NGC 4431	dSB0/a	0.0031	-18.27	1.94 ± 0.13	0.25	84 ± 21	$1.12^{+0.38}_{-0.26}$	$0.6^{+1.2}_{-0.4}$	...	8	yes
NGC 4596	SB0$^+$(r)	0.0063	-21.84	7.02	0.63	25.0 ± 6.3	$7.7^{+2.0}_{-1.6}$	$1.1^{+0.7}_{-0.3}$	0.42	9	yes
NGC 7079	SB0^0(s)	0.0090	-21.55	4.40 ± 0.61	...	48.5 ± 1.2	$5.30^{+0.24}_{-0.23}$	$1.2^{+0.3}_{-0.2}$	...	10	yes

Notes: (1) Galaxy name. (2) Hubble type from Corsini (2011), except for NGC 4264 (Chapter 2). (3) Redshift from NED. (4) Absolute SDSS r-band magnitude obtained as described in Sec. 3.2. (5) Bar radius obtained as described in Sec. 4.3.1. (6) Bar strength obtained as described in Sec. 4.3.1. (7) Bar pattern speed obtained as described in Sec. 4.3.2. (8) Bar corotation radius obtained as described in Sec. 4.3.2. (9) Bar rotation rate obtained as described in Sec. 4.3.2. (10) Bulge-to-total luminosity ratio provided by the corresponding literature, when available. (11) Reference paper for the direct measurement of the bar pattern speed: 1 = Aguerri et al. (2003); 2 = Gerssen et al. (2003); 3 = Merrifield & Kuijken (1995); 4 = Debattista et al. (2002); 5 = Treuthardt et al. (2007); 6 = Corsini et al. (2003); 7 = Chapter 2; 8 = Corsini et al. (2007); 9 = Gerssen et al. (1999); 10 = Debattista & Williams (2004). (12) Inclusion in the final analysed sample.

Table 4.2: Properties of the 31 galaxies of the CALIFA subsample.

Galaxy	Morph. Type	z	M_r [mag]	$R_{\rm bar}$ [kpc]	$S_{\rm bar}$ [kpc]	$\Omega_{\rm bar}$ [km s^{-1} kpc^{-1}]	$R_{\rm cr}$ [kpc]	$\mathcal{R}$	B/T	Final sample
(1)	(2)	(3)	(4)	(5)	(6)	(7)	(8)	(9)	(10)	(11)
IC 1528	SABbc	0.013	-20.57	$2.15^{+0.66}_{-0.71}$	$0.235^{+0.002}_{-0.016}$	87 ± 20	1.63 ± 0.51	$0.8^{+0.1}_{-0.2}$	0.021	yes
IC 1683	SABb	0.016	-20.73	$8.79^{+0.62}_{-0.65}$	$0.73^{+0.07}_{-0.08}$	30.3 ± 5.1	6.3 ± 2.7	0.7 ± 0.2	0.14	yes
IC 5309	SABc	0.014	-19.99	$1.98^{+0.89}_{-0.50}$	$0.205^{+0.006}_{-0.019}$	91 ± 26	1.3 ± 1.0	$0.6^{+0.4}_{-0.5}$	0.14	yes
MCG-02-02-030	SABb	0.012	-20.57	$3.6^{+2.3}_{-1.2}$	$0.28^{+0.03}_{-0.03}$	43.4 ± 6.5	4.8 ± 2.2	$1.3^{+0.4}_{-0.5}$	0.080	yes
NGC 36	SBb	0.020	-21.86	$8.0^{+2.0}_{-1.8}$	0.55	44 ± 13	$5.0^{+2.1}_{-1.5}$	$0.6^{+0.3}_{-0.2}$	0.24	yes
NGC 192	SABab	0.014	-21.30	$11.\ 0^{+1.8}_{-1.4}$	$0.83^{+0.09}_{-0.09}$	20.9 ± 2.1	11.9 ± 1.9	$1.1^{+0.1}_{-0.1}$	0.15	yes
NGC 364	EAB7	0.017	-21.28	$3.17^{+0.62}_{-0.64}$	$0.46^{+0.01}_{-0.02}$	120 ± 31	2.63 ± 1.13	$0.8^{+0.2}_{-0.3}$	0.20	yes
NGC 551	SABbc	0.017	-20.98	$3.9^{+2.0}_{-2.1}$	$0.30^{+0.07}_{-0.07}$	45 ± 11	4.52 ± 2.39	$1.2^{+0.4}_{-0.7}$	0.028	yes
NGC 1645	SB0/a	0.016	-21.53	$5.44^{+0.82}_{-0.44}$	0.69	66 ± 28	$4.1^{+2.3}_{-1.3}$	$0.8^{+0.4}_{-0.2}$	0.15	yes
NGC 2449	SABab	0.016	-21.40	$4.59^{+0.75}_{-0.80}$	$0.60^{+0.04}_{-0.03}$	40.7 ± 5.5	5.84 ± 0.99	$1.3^{+0.1}_{-0.1}$	0.21	yes
NGC 2553	SABab	0.016	-21.23	$7.7^{+2.1}_{-1.8}$	$0.57^{+0.01}_{-0.01}$	68.1 ± 9.8	3.95 ± 0.91	$0.52^{+0.08}_{-0.11}$	0.24	no
NGC 2880	EAB7	0.0051	-20.34	$1.49^{+0.71}_{-0.42}$	$0.452^{+0.004}_{-0.006}$	209 ± 15	1.09 ± 0.36	$0.7^{+0.2}_{0.2}$	0.51	yes
NGC 3300	SB0/a	0.010	-21.17	$3.853^{+0.65}_{-0.36}$	0.54	38 ± 10	$5.9^{+2.0}_{-1.5}$	$1.6_{+0.5-0.4}$	0.095	yes
NGC 3994	SABbc	0.010	-20.75	$1.77^{+0.56}_{-0.47}$	$0.38^{+0.01}_{-0.09}$	119 ± 27	1.90 ± 0.67	$1.1^{+0.2}_{-0.3}$	0.12	yes
NGC 5205	SBbc	0.0059	-19.65	$2.31^{+0.37}_{-0.27}$	0.42	116 ± 21	$1.48^{+0.39}_{-0.33}$	$0.7^{+0.2}_{-0.1}$	0.059	yes
NGC 5378	SBb	0.010	-20.84	$6.27^{+0.97}_{-1.52}$	0.58	43 ± 20	$4.1^{+2.7}_{-1.7}$	$0.6^{+0.4}_{-0.2}$	0.21	yes
NGC 5406	SBb	0.018	-22.25	$7.95^{+0.41}_{-0.79}$	0.53	61 ± 21	$4.1^{+1.8}_{-1.1}$	$0.5^{+0.2}_{-0.1}$	0.12	no
NGC 5947	SBbc	0.020	-21.28	$4.56^{+0.54}_{-0.67}$	0.50	76 ± 10	$2.43^{1.00}_{-0.96}$	$0.5^{+0.2}_{-0.2}$	0.13	no
NGC 5971	SABb	0.011	-20.57	$7.3^{+6.1}_{-3.3}$	$0.504^{+0.009}_{-0.004}$	55 ± 15	4.1 ± 2.0	$0.6^{+0.2}_{-0.3}$	0.67	no
NGC 6278	SAB0/a	0.0090	-20.86	$2.84^{+1.09}_{-0.17}$	$0.36^{+0.04}_{-0.04}$	92 ± 28	3.1 ± 1.1	1.1 ± 0.3	0.34	yes
NGC 6427	SAB0	0.011	-20.74	$1.9^{+1.7}_{-1.0}$	$0.63^{+0.02}_{-0.02}$	46 ± 10	5.3 ± 3.6	$2.8^{+1.0}_{-1.8}$	0.36	yes
NGC 6497	SBab	0.011	-21.72	$6.26^{+0.90}_{-0.55}$	0.61	100 ± 17	$2.3^{+0.90}_{-0.68}$	$0.3^{+0.1}_{-0.1}$	0.26	no
NGC 6941	SBb	0.021	-21.57	$6.61^{+0.54}_{-0.87}$	0.38	44 ± 23	$4.4^{+3.1}_{-1.5}$	$0.6^{+0.5}_{-0.2}$	0.089	no
NGC 6945	SB0	0.013	-21.12	$4.06^{+0.66}_{-0.66}$	0.38	63.1 ± 8.5	$3.20^{+0.71}_{-0.61}$	$0.8^{+0.2}_{-0.1}$	0.25	yes
NGC 7321	SBbc	0.024	-22.06	$5.75^{+0.81}_{-0.95}$	0.35	45 ± 14	$5.6^{+2.6}_{-1.9}$	$1.0^{+0.4}_{-0.3}$	0.049	yes
NGC 7563	SBa	0.014	-21.30	$6.79^{+0.75}_{-1.44}$	0.82	17 ± 10	$12.1^{+5.2}_{-4.2}$	$1.9^{+1.7}_{-0.7}$	0.53	no
NGC 7591	SBbc	0.017	-21.50	$4.33^{+0.80}_{-0.48}$	0.65	43 ± 16	$4.2^{+2.1}_{-1.4}$	$1.0^{+0.5}_{-0.3}$	0.19	yes
UGC 3253	SBb	0.014	-20.65	$4.52^{+0.37}_{-0.63}$	0.51	54 ± 11	$3.40_{+0.92-0.77}$	$0.7^{+0.2}_{-0.2}$	0.067	yes
UGC 3944	SABbc	0.0083	-20.03	$1.87^{+0.88}_{-0.63}$	$0.27^{+0.05}_{-0.02}$	62 ± 22	2 ± 12	1^{+4}_{-6}	0.0	yes
UGC 8231	SABd	0.0083	-18.71	$2.30^{+0.47}_{-0.70}$	$0.24^{+0.04}_{-0.04}$	58 ± 31	2.3 ± 5.3	1^{+2}_{-2}	0.0	no
UGC 12185	SBb	0.022	-21.30	$9.0^{+3.6}_{-1.9}$	0.71	23 ± 4.5	$9.5^{+5.4}_{-4.0}$	$1.2^{+0.6}_{-0.5}$	0.20	yes

Notes: (1) Galaxy name. (2) Hubble type from CALIFA. (3) Redshift from SDSS-DR14 (Abolfathi et al., 2018). (4) Absolute SDSS r-band magnitude obtained as described in Sec. 3.2. (5) Bar radius obtained as described in Sec. 4.3.1. (6) Bar strength obtained as described in Sec. 4.3.1. (7) Bar pattern speed obtained as described in Sec. 4.3.2. (8) Bar corotation radius obtained as described in Sec. 4.3.2. (9) Bar rotation rate obtained as described in Sec. 4.3.2. (10) Bulge-to-total light contribution provided by Méndez-Abreu et al. (2017). (11) Inclusion in the final analysed sample.

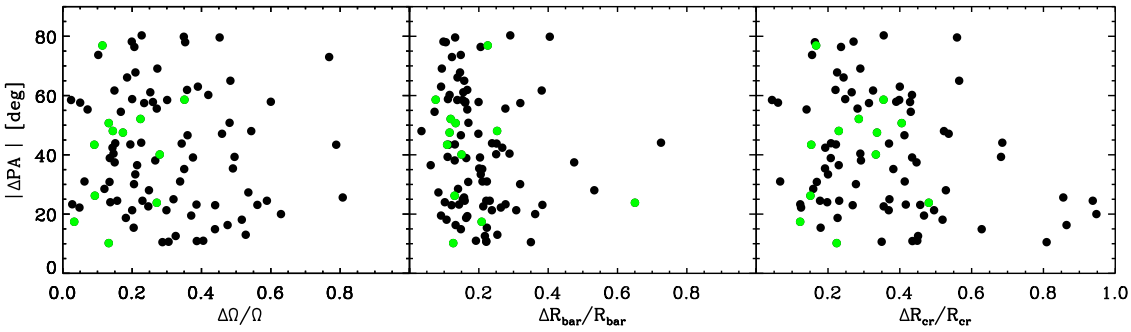

Figure 4.3: Relative errors of the bar pattern speed $\Delta\Omega_{\rm bar}/\Omega_{\rm bar}$, bar radius $\Delta R_{\rm bar}/R_{\rm bar}$, and corotation radius $\Delta R_{\rm cr}/R_{\rm cr}$ as a function of the bar orientation with respect to the disc major and minor axes ΔPA, given as the absolute value of the difference in PA between the PA of the bar and that of the major axis. Ultrafast bars are highlighted (*green points*). Galaxies with relative errors larger than 100 per cent are not shown.

Table 4.3: Properties of the 51 galaxies of the MaNGA subsample.

Galaxy	Morph. Type	z	M_r [mag]	$R_{\rm bar}$ [kpc]	$S_{\rm bar}$ [kpc]	$\Omega_{\rm bar}$ [km s^{-1} kpc^{-1}]	$R_{\rm cr}$ [kpc]	$\mathcal{R}$	Final sample
(1)	(2)	(3)	(4)	(5)	(6)	(7)	(8)	(9)	(10)
7495-12704	SBbc	0.029	−21.40	$4.70^{+0.69}_{-0.63}$	0.37	30.3 ± 3.6	$6.7^{+1.1}_{-1.0}$	1.4 ± 0.3	yes
7962-12703	SBab	0.048	−22.33	$16.1^{+3.7}_{-3.0}$	0.65	27.83 ± 0.91	$9.4^{+1.2}_{-1.1}$	$0.6^{+0.2}_{-0.1}$	no
7990-3704	SB0	0.029	−20.15	$2.37^{+0.30}_{-0.43}$	0.29	80 ± 25	$1.9^{+0.91}_{-0.49}$	$0.8^{+0.4}_{-0.3}$	yes
7990-9101	SBc	0.028	−19.77	$4.03^{+0.64}_{-1.11}$	0.37	15.5 ± 5.0	$7.7^{+4.9}_{-2.0}$	$2.2^{+1.3}_{-0.8}$	yes
7992-6104	SBc	0.027	−20.31	$5.11^{+0.91}_{-0.79}$	0.80	27.1 ± 1.9	$4.7^{+0.68}_{-0.62}$	$0.9^{+0.2}_{-0.2}$	yes
8082-6102	SB0	0.024	−21.46	$3.81^{+0.50}_{-0.50}$	0.59	51 ± 23	$4.7^{+3.8}_{-1.4}$	$1.3^{+1.0}_{-0.4}$	yes
8083-6102	SBa	0.037	−21.62	$5.3^{+1.1}_{-1.2}$	0.63	12.4 ± 4.8	$23.3^{+14.5}_{-5.7}$	5^{+3}_{-2}	yes
8083-12704	SBbc	0.023	−21.03	$3.09^{+0.47}_{-0.52}$	0.27	85 ± 50	$1.13^{+0.60}_{-0.52}$	$0.4^{+0.5}_{-0.2}$	no
8133-3701	SBb	0.044	−20.10	$3.88^{+0.83}_{-1.02}$	0.48	41.8 ± 6.3	$3.33^{+0.74}_{-0.65}$	$0.9^{+0.4}_{-0.2}$	yes
8134-6102	SB0a	0.032	−21.40	$8.0^{+1.9}_{-1.4}$	0.74	23.0 ± 4.7	$12.37^{+3.5}_{-2.3}$	$1.6^{+0.6}_{-0.4}$	yes
8137-9102	SBb	0.031	−21.07	$7.65^{+0.67}_{-1.26}$	0.62	33.1 ± 4.4	$3.86^{+0.93}_{-0.80}$	$0.5^{+0.2}_{-0.1}$	no
8140-12701	SBa	0.029	−20.61	$5.87^{+0.98}_{-0.73}$	0.68	39.5 ± 8.3	$4.34^{+1.04}_{-0.92}$	$0.7^{+0.2}_{-0.2}$	yes
8140-12703	SBb	0.032	−21.87	$7.3^{+1.4}_{-1.4}$	0.37	28 ± 11	$7.3^{+4.8}_{-1.8}$	$1.1^{+0.7}_{-0.4}$	yes
8243-6103	SB0	0.032	−21.65	$4.77^{+0.40}_{-0.67}$	0.70	21 ± 17	$14.1^{+27.9}_{-6.1}$	3^{+6}_{-2}	no
8244-3703	SB0	0.048	−21.03	$4.30^{+0.41}_{-0.72}$	0.38	73 ± 14	$2.8^{+0.72}_{-0.51}$	$0.7^{+0.2}_{-0.2}$	yes
8247-3701	SB0a	0.025	−20.59	$2.53^{+0.38}_{-0.70}$	0.40	22.1 ± 5.5	$5.4^{+2.1}_{-1.7}$	$2.3^{+1.2}_{-0.8}$	yes
8249-6101	SBc	0.027	−20.27	$7.42^{+0.69}_{-0.92}$	1.13	30.5 ± 2.8	$4.31^{+0.69}_{-0.63}$	$0.6^{+0.1}_{-0.1}$	no
8254-9101	SBa	0.025	−21.78	$6.91^{+0.55}_{-0.60}$	0.51	49 ± 26	$6.41^{+12.8}_{-2.3}$	$1.0^{+0.8}_{-0.4}$	no
8256-6101	SBa	0.025	−20.79	$5.02^{+0.75}_{-0.48}$	0.64	36 ± 28	$5.3^{+11.1}_{-2.2}$	$1.1^{+2.1}_{-0.5}$	no
8257-3703	SBb	0.025	−20.34	$4.0^{+1.1}_{-1.0}$	0.76	50.1 ± 2.4	3.87 ± 0.48	$1.0^{+0.3}_{-0.2}$	yes
8257-6101	SBc	0.029	−20.86	$2.57^{+0.25}_{-0.31}$	0.20	48 ± 24	$3.4^{+3.4}_{-1.3}$	$1.4^{+1.3}_{-0.6}$	yes
8312-12702	SBc	0.032	−21.24	$6.6^{+1.2}_{-1.4}$	0.63	35 ± 17	$4.07^{+0.88}_{-0.68}$	$0.6^{+0.2}_{-0.1}$	yes
8312-12704	SBb	0.030	−21.00	$7.0^{+1.4}_{-1.8}$	0.60	14.4 ± 4.9	$8.7^{+4.9}_{-2.3}$	$1.3^{+0.8}_{-0.4}$	yes
8313-9101	SBb	0.039	−21.87	$4.4^{+0.73}_{-1.46}$	0.24	0.8 ± 4.5	22^{+60}_{-13}	6^{+14}_{-4}	no
8317-12704	SBa	0.054	−22.68	$11.9^{+1.2}_{-1.7}$	0.71	12.2 ± 5.4	$27.7^{+8.9}_{-6.0}$	$2.4^{+0.8}_{-0.6}$	yes
8318-12703	SBb	0.039	−22.21	$6.5^{+1.8}_{-2.0}$	0.44	28.7 ± 4.2	$8.4^{+3.1}_{-1.8}$	$1.4^{+0.7}_{-0.4}$	yes
8320-6101	SBb	0.027	−20.37	$3.80^{+0.81}_{-0.46}$	0.43	27.2 ± 9.8	$6.9^{+1.7}_{-1.4}$	$1.8^{+0.5}_{-0.4}$	yes
8326-3704	SBa	0.027	−20.25	$4.07^{+0.51}_{-0.85}$	0.45	15 ± 17	$6.6^{+16.3}_{-4.5}$	2^{+4}_{-1}	no
8326-6102	SBb	0.070	−22.06	$8.00^{+0.89}_{-1.48}$	0.56	19.0 ± 8.3	$12.2^{+10.4}_{-4.9}$	$1.6^{+1.4}_{-0.7}$	yes
8330-12703	SBbc	0.027	−20.67	$5.80^{+0.70}_{-0.81}$	0.31	44.9 ± 4.1	$3.07^{+0.52}_{-0.41}$	$0.5^{+0.1}_{-0.1}$	no
8335-12701	SBb	0.063	−21.66	$12.1^{+4.8}_{-4.4}$	0.60	7.9 ± 4.5	29^{+16}_{-10}	3^{+2}_{-1}	no

8439-6102	SBab	0.034	−21.64	$5.359^{+1.448}_{-1.521}$	0.53	53.6 ± 1.5	$3.84^{+0.44}_{-0.51}$	$0.7^{+0.3}_{-0.2}$	yes
8439-12702	SBa	0.027	−21.57	$6.2^{+0.64}_{-0.64}$	0.46	30.8 ± 4.2	$7.7^{+1.8}_{-1.3}$	$1.3^{+0.3}_{-0.2}$	yes
8440-12704	SBb	0.027	−21.12	$3.3^{+0.70}_{-0.64}$	0.43	35.9 ± 7.5	$5.8^{+1.2}_{-1.1}$	$1.8^{+0.6}_{-0.5}$	yes
8447-6101	SBb	0.075	−22.89	$14.7^{+1.1}_{-1.8}$	0.30	37.6 ± 7.5	$9.4^{+2.9}_{-2.2}$	0.7 ± 0.2	yes
8452-3704	SBc	0.025	−19.97	$2.2^{+0.92}_{-0.65}$	0.21	76 ± 48	$2.06^{+3.03}_{-0.87}$	$1.1^{+1.4}_{-0.6}$	no
8452-12703	SBb	0.061	−22.83	$9.2^{+1.9}_{-3.0}$	0.38	42.2 ± 6.0	$5.05^{+1.04}_{-0.91}$	$0.6^{+0.3}_{-0.2}$	yes
8481-12701	SBa	0.067	−21.91	$8.2^{+1.1}_{-1.4}$	0.65	40 ± 10	$6.6^{+2.3}_{-1.3}$	$0.9^{+0.3}_{-0.2}$	yes
8482-9102	SBb	0.058	−21.59	$6.84^{+0.73}_{-1.22}$	0.41	15.3 ± 5.9	$14.7^{+8.7}_{-3.5}$	$2.3^{+1.3}_{-0.7}$	yes
8482-12703	SBbc	0.050	−22.21	$6.2^{+1.1}_{-1.4}$	0.41	42 ± 16	$4.0^{+2.3}_{-1.1}$	$0.7^{+0.4}_{-0.2}$	yes
8482-12705	SBb	0.042	−22.06	$8.24^{+0.88}_{-1.32}$	0.32	12.9 ± 6.1	$18.4^{+25.5}_{-6.3}$	2^{+3}_{-1}	yes
8486-6101	SBc	0.060	−21.57	$5.8^{+1.6}_{-2.1}$	0.59	18.8 ± 3.9	$10.0^{+3.5}_{-2.1}$	$1.8^{+1.1}_{-0.6}$	yes
8548-6102	SBc	0.048	−20.83	$7.0^{+1.6}_{-1.5}$	0.98	35.2 ± 5.5	$4.52^{+0.91}_{-0.71}$	0.7 ± 0.2	yes
8548-6104	SBc	0.048	−20.47	$4.94^{+0.71}_{-0.91}$	0.49	23.4 ± 4.3	$7.6^{+1.9}_{-1.5}$	$1.6^{+0.5}_{-0.4}$	yes
8549-12702	SBb	0.043	−22.03	$5.42^{+0.83}_{-0.46}$	0.49	76 ± 17	$3.21^{+1.01}_{-0.83}$	$0.6^{+0.2}_{-0.2}$	no
8588-3701	SBb	0.13	−22.88	$13.7^{+1.9}_{-2.2}$	0.46	45 ± 13	$5.7^{+2.5}_{-1.4}$	$0.4^{+0.2}_{-0.1}$	no
8601-12705	SBc	0.030	−21.21	$4.07^{+1.0}_{-0.82}$	0.40	23.5 ± 4.8	7.3 ± 1.31	$1.8^{+0.6}_{-0.4}$	yes
8603-12703	SBa	0.030	−21.04	$7.65^{+0.60}_{-0.82}$	0.30	25.2 ± 9.3	$5.8^{+3.5}_{-1.9}$	$0.8^{+0.5}_{-0.3}$	yes
8604-12703	SBab	0.031	−21.67	$6.59^{+0.83}_{-1.41}$	0.50	16.4 ± 7.9	$13.6^{+26.1}_{-4.5}$	2^{+4}_{-1}	yes
8612-6104	SBb	0.036	−21.83	$6.1^{+1.6}_{-1.1}$	0.56	104 ± 12	1.8 ± 0.30	$0.29^{+0.09}_{-0.07}$	no
8612-12702	SBc	0.063	−22.60	$7.1^{+1.2}_{-1.1}$	0.30	41 ± 33	$5.03^{+6.4}_{-2.3}$	$0.7^{+0.9}_{-0.4}$	no

Notes: (1) Galaxy name. (2) Hubble type from MaNGA. (3) Redshift from MaNGA. (4) Absolute SDSS r-band magnitude obtained as described in Sec. 3.2. (5) Bar radius obtained as described in Sec. 4.3.1. (6) Bar strength obtained as described in Sec. 4.3.1. (7) Bar pattern speed obtained as described in Sec. 4.3.2. (8) Bar corotation radius obtained as described in Sec. 4.3.2. (9) Bar rotation rate obtained as described in Sec. 4.3.2. (10) Inclusion in the final analysed sample.

4.4 Results

The mean relative errors on the bar parameters for the sample galaxies listed in Tables 4.1, 4.2 and 4.3 are $\langle \Delta\Omega_{\rm bar}/\Omega_{\rm bar} \rangle = 0.36^{+0.59}_{-0.36}$, $\langle \Delta R_{\rm bar}/R_{\rm bar} \rangle = 0.20 \pm 0.11$, and $\langle \Delta S_{\rm bar}/S_{\rm bar} \rangle = 0.09 \pm 0.07$, leading to $\langle \Delta R_{\rm cr}/R_{\rm cr} \rangle = 0.47^{+0.57}_{-0.47}$ and $\langle \Delta\mathcal{R}/\mathcal{R} \rangle = 0.5 \pm 0.4$. In a number of galaxies, the uncertainties on $\Omega_{\rm bar}$, $R_{\rm cr}$, and $\mathcal{R}$ are larger than 100 per cent.

We decided to consider only galaxies with $\langle \Delta\Omega_{\rm bar}/\Omega_{\rm bar} \rangle < 0.5$ and not hosting an ultrafast bar. The final sample consists of 75 objects with 33 ETBGs (SB0-SBa) and 42 LTBGs (SBab-SBc). They have mean relative errors of $\langle \Delta\Omega_{\rm bar}/\Omega_{\rm bar} \rangle = 0.26 \pm 0.12$, $\langle \Delta R_{\rm bar}/R_{\rm bar} \rangle = 0.20 \pm 0.11$, and $\langle \Delta S_{\rm bar}/S_{\rm bar} \rangle = 0.09 \pm 0.07$, leading to $\langle \Delta R_{\rm cr}/R_{\rm cr} \rangle = 0.40^{+0.56}_{-0.40}$ and $\langle \Delta\mathcal{R}/\mathcal{R} \rangle = 0.4 \pm 0.4$. For a subsample of 27 galaxies we derived the bulge-to-total luminosity ratio B/T from the available photometric decompositions (Tables 4.1 and 4.2).

We investigated all the possible relations between the available parameters of the bars ($R_{\rm bar}$, $S_{\rm bar}$, $\Omega_{\rm bar}$, $R_{\rm cr}$, and $\mathcal{R}$) and their host galaxies (Hubble type, M_r and B/T) using the IDL task R_CORRELATE, which computes the Spearman rank correlation r of two populations and the corresponding two-sided significance p of its deviation from zero. In the case of correlation between the populations, it also allows to estimate the number of standard deviations σ by which the sum-squared differences of the ranks deviates from its null-hypothesis (Press et al., 1992). The resulting correlation parameters are given in Table 4.4.

We observed

- very strong correlations ($|r| \geq 0.7$ and/or $p < 0.01$) between $\Omega_{\rm bar}$ and $R_{\rm bar}$ (longer bars rotate with lower $\Omega_{\rm bar}$), between $R_{\rm bar}$ and $R_{\rm cr}$ (longer bars have larger corotations), between $\Omega_{\rm bar}$ and $R_{\rm cr}$ (bars with larger corotations rotate with lower $\Omega_{\rm bar}$), and between M_r and $R_{\rm bar}$ (fainter galaxies host shorter bars);

- strong correlations ($0.4 \leq |r| < 0.7$ and/or $0.01 \leq p < 0.05$) between M_r and $\Omega_{\rm bar}$ or $R_{\rm cr}$ (fainter galaxies host bars which rotate with higher $\Omega_{\rm bar}$ and have smaller corotations), between $R_{\rm bar}$ and $S_{\rm bar}$ (shorter bars are weaker), between $\mathcal{R}$ and $\Omega_{\rm bar}$ or $R_{\rm cr}$ (fast bars rotate with higher $\Omega_{\rm bar}$ and have larger corotations), and between B/T and $S_{\rm bar}$ (disc-dominated galaxies host weaker bars);

- weak correlations ($0.2 \leq |r| < 0.4$ and/or $0.05 \leq p < 0.1$) between $\Omega_{\rm bar}$ and Hubble type (ETBG bars rotate with higher $\Omega_{\rm bar}$), between $\Omega_{\rm bar}$ and $S_{\rm bar}$ (weaker bars rotate both slowly and fast in terms of $\Omega_{\rm bar}$, while stronger bars rotate only fast), and between $R_{\rm cr}$ and $S_{\rm bar}$ (weaker bars have smaller corotations);

- no correlation ($|r| < 0.2$ and/or $p \geq 0.1$) between Hubble type and M_r, $R_{\rm bar}$, $S_{\rm bar}$, $R_{\rm cr}$ or $\mathcal{R}$, between $\mathcal{R}$ and $R_{\rm bar}$, $S_{\rm bar}$, or M_r, and between B/T and $\Omega_{\rm bar}$, $R_{\rm bar}$, $R_{\rm cr}$ or $\mathcal{R}$.

Splitting the final sample between ETBGs and LTBGs, the correlations remain mostly unchanged (Table 4.4). For ETBGs, the correlations $\Omega_{\rm bar}$-$R_{\rm bar}$, $R_{\rm bar}$-$S_{\rm bar}$, and $R_{\rm cr}$-$S_{\rm bar}$ become strong. In addition, we found a strong correlation between M_r and $S_{\rm bar}$ (brighter galaxies host stronger bars), while a weak correlation $\mathcal{R}$-$S_{\rm bar}$ appears. For LTBGs, the correlation $S_{\rm bar}$-M_r disappears, while a weak correlation $\mathcal{R}$-$S_{\rm bar}$ appears.

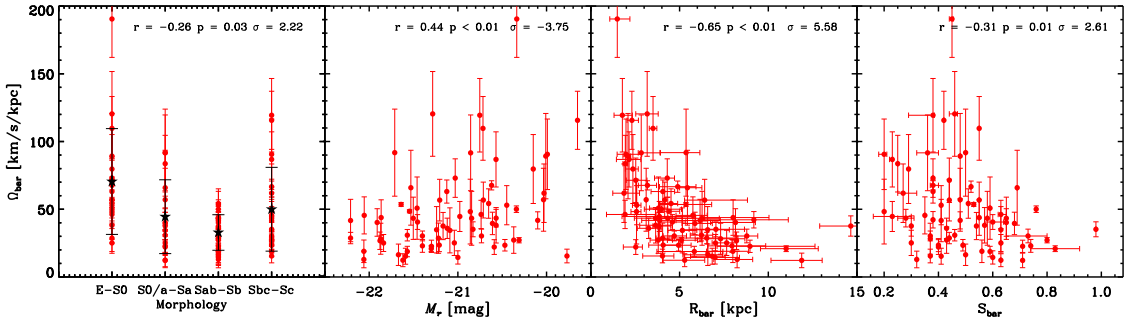

Figure 4.4: Relations between the bar pattern speed $\Omega_{\rm bar}$ and the Hubble type, absolute SDSS r-band magnitude M_r, bar radius $R_{\rm bar}$, and bar strength $S_{\rm bar}$ for the selected sample of 75 galaxies. The Spearman rank correlation r, two-sided significance p, and number of σ from the null-hypothesis are given in each panel. The mean value of $\Omega_{\rm bar}$ for each bin of Hubble type is shown (*black stars*).

The mean values of the bar parameters of the final sample are $\langle\Omega_{\rm bar}\rangle = 49 \pm 31$ km s^{-1} kpc^{-1}, $\langle R_{\rm bar}\rangle = 5.2 \pm 2.5$ kpc, $\langle S_{\rm bar}\rangle = 0.5 \pm 0.2$, $\langle r_{\rm cr}\rangle = 6.2 \pm 4.6$ kpc, and $\langle\mathcal{R}\rangle = 1.3 \pm 0.7$. We obtained $\langle\Omega_{\rm bar}\rangle = 59 \pm 36$ km s^{-1} kpc^{-1}, $\langle R_{\rm bar}\rangle = 4.5 \pm 2.3$ kpc, $\langle S_{\rm bar}\rangle = 0.5 \pm 0.1$, $\langle r_{\rm cr}\rangle = 5.9 \pm 5.6$ kpc, and $\langle\mathcal{R}\rangle = 1.3 \pm 0.9$ for ETBGs, and $\langle\Omega_{\rm bar}\rangle = 41 \pm 25$ km s^{-1} kpc^{-1}, $\langle R_{\rm bar}\rangle = 5.7 \pm 2.7$ kpc, $\langle S_{\rm bar}\rangle = 0.5 \pm 0.2$, $\langle r_{\rm cr}\rangle = 6.4 \pm 3.8$ kpc, and $\langle\mathcal{R}\rangle = 1.2 \pm 0.5$ for LTBGs.

Figures 4.4 and 4.5 show the correlations found between $\Omega_{\rm bar}$ and Hubble type, M_r, $R_{\rm bar}$, or $S_{\rm bar}$ before and after splitting the final sample between ETBGs and LTBGs, respectively. Figures 4.6 and 4.7 show the correlations found between $R_{\rm bar}$ and M_r, $S_{\rm bar}$, or $R_{\rm cr}$ before and after splitting the final sample between ETBGs and LTBGs, respectively. Figure 4.8 shows the correlation between B/T and $S_{\rm bar}$ for the subsample of 26 galaxies with an available photometric decomposition.

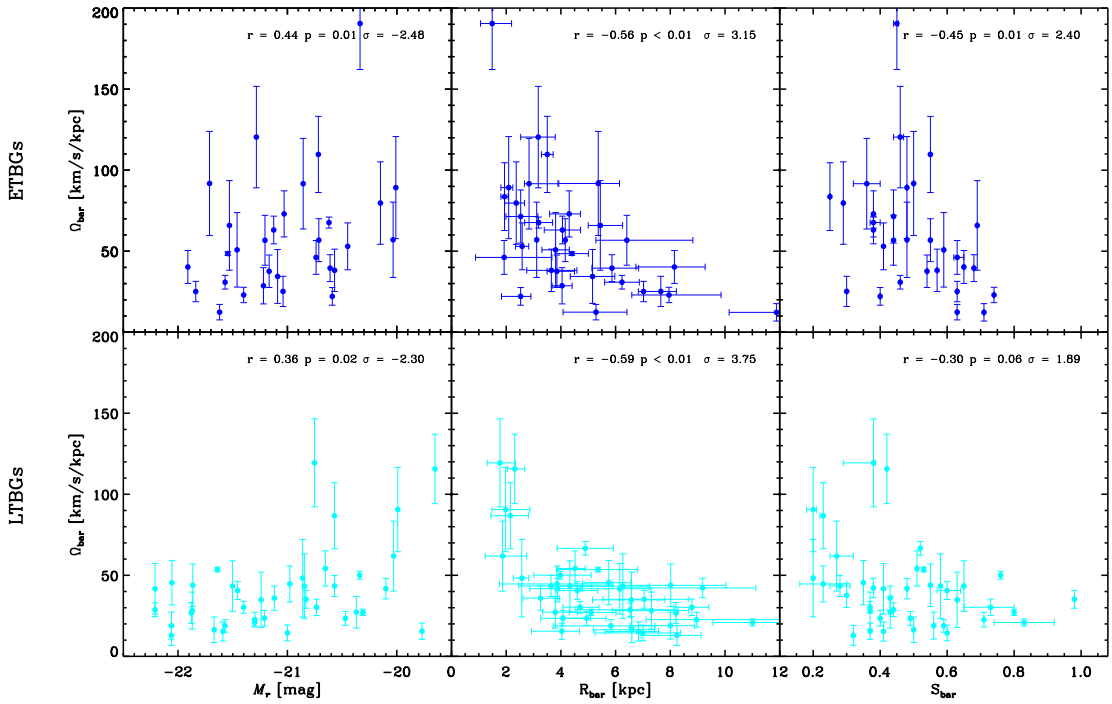

Figure 4.5: *Top panels:* relations between the bar pattern speed $\Omega_{\rm bar}$ and the absolute SDSS r-band magnitude M_r, bar radius $R_{\rm bar}$, and bar strength $S_{\rm bar}$ for the subsample of 33 ETBGs. *Bottom panels:* same as above but for the subsample of 42 LTBGs. The Spearman rank correlation r, the two-sided significance p, and number of σ from the null-hypothesis are given in each panel.

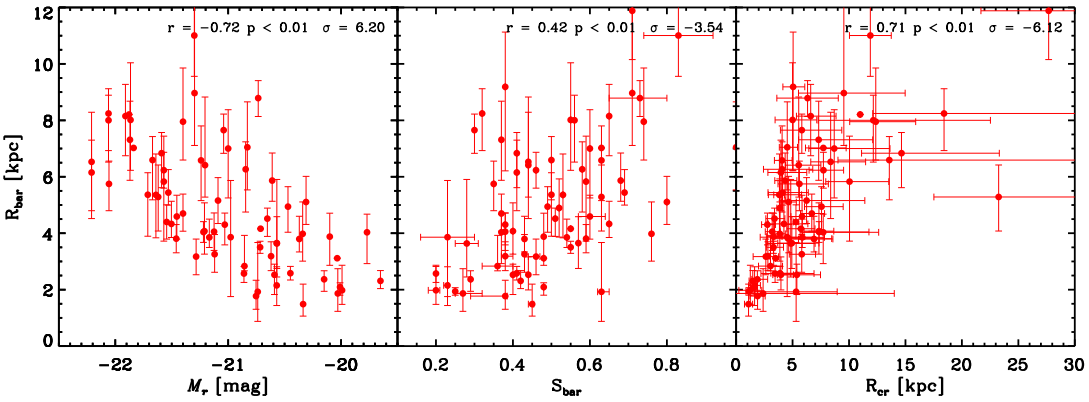

Figure 4.6: Relations between the bar radius $R_{\rm bar}$ and the absolute SDSS r-band magnitude M_r, bar strength $S_{\rm bar}$, and corotation radius $R_{\rm cr}$ for the selected sample of 75 galaxies. The Spearman rank correlation r, two-sided significance p, and number of σ from the null-hypothesis are given in each panel.

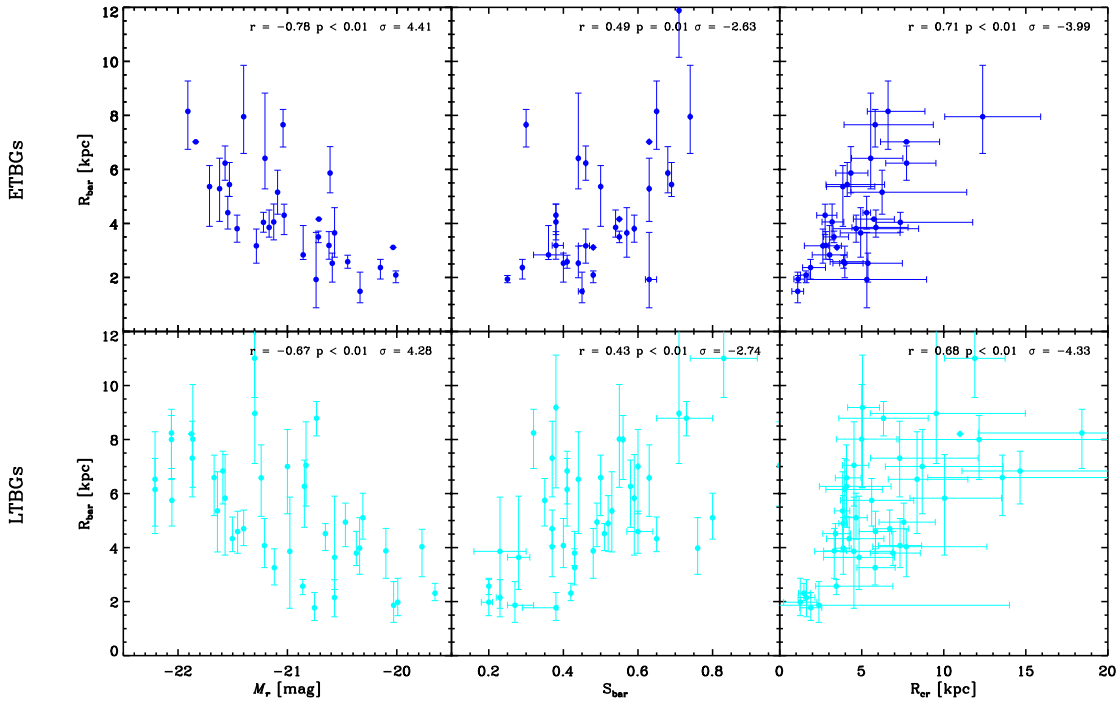

Figure 4.7: *Top panels:* relations between the bar radius $R_{\rm bar}$ and the absolute SDSS r-band magnitude M_r, bar strength $S_{\rm bar}$, and corotation radius $R_{\rm cr}$ for the subsample of 33 ETBGs. *Bottom panels:* same as above but for the subsample of 42 LTBGs. The Spearman rank correlation r, two-sided significance p, and number of σ from the null-hypothesis are given in each panel.

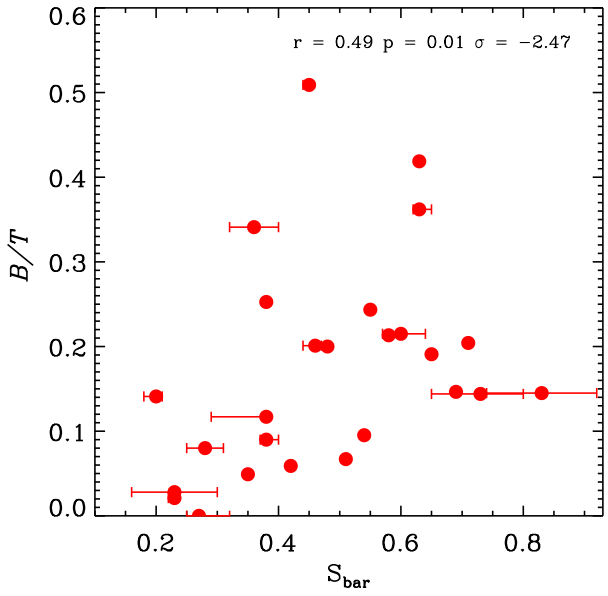

Figure 4.8: Relation between the bulge-to-total luminosity ratio B/T and the bar strength $S_{\rm bar}$ for the subsample of 26 galaxies with a photometric decomposition. The Spearman rank correlation r, the two-sided significance p, and number of σ from the null-hypothesis are given in each panel.

Table 4.4: Spearman parameters of the explored correlations within the properties of the galaxies.

Correlation	Selected sample				ETBGs				LTBGs			
	N	r	p-value	σ	N	r	p-value	σ	N	r	p-value	σ
(1)	(2)	(3)	(4)	(5)	(2)	(3)	(4)	(5)	(2)	(3)	(4)	(5)
(Hubble Type-$\Omega_{\rm bar}$)	75	-0.3	0.03	2.2	...	...	...	...	...	...	...	...
(Hubble Type-$R_{\rm bar}$)	75	0.2	0.1	-1.5	...	...	...	...	...	...	...	...
(Hubble Type-$R_{\rm cr}$)	75	0.1	0.4	-0.9	...	...	...	...	...	...	...	...
(Hubble Type-$\mathcal{R}$)	75	-0.06	0.6	0.5	...	...	...	...	...	...	...	...
(Hubble Type-$S_{\rm bar}$)	71	-0.1	0.3	1.2	...	...	...	...	...	...	...	...
(Hubble Type-M_r)	75	-0.05	0.7	0.4	...	...	...	...	...	...	...	...
($\Omega_{\rm bar}$-$R_{\rm bar}$)	75	-0.7	< 0.01	5.6	33	-0.6	< 0.01	3.2	42	-0.6	< 0.01	3.8
($\Omega_{\rm bar}$-$R_{\rm cr}$)	75	-0.9	< 0.01	7.8	33	-0.9	< 0.01	5.1	42	-0.9	< 0.01	5.8
($\Omega_{\rm bar}$-$\mathcal{R}$)	75	-0.6	< 0.01	4.8	33	-0.6	< 0.01	3.4	42	-0.6	< 0.01	4.0
($\Omega_{\rm bar}$-$S_{\rm bar}$)	71	-0.3	< 0.01	2.6	30	-0.5	0.01	2.4	41	-0.3	0.06	1.9
($\Omega_{\rm bar}$-M_r)	75	0.4	< 0.01	-3.7	33	0.4	0.01	-2.5	42	0.4	0.02	-2.3
($R_{\rm bar}$-$R_{\rm cr}$)	75	0.7	< 0.01	-6.1	33	0.7	< 0.01	-4.0	42	0.7	< 0.01	-4.3
($R_{\rm bar}$-$\mathcal{R}$)	75	-0.05	0.7	0.46	33	-0.005	1	0.028	42	-0.1	0.5	0.65
($R_{\rm bar}$-$S_{\rm bar}$)	71	0.4	< 0.01	-3.5	30	0.5	< 0.01	-2.6	41	0.4	< 0.01	-2.7
($R_{\rm bar}$-M_r)	75	-0.7	< 0.01	6.2	33	-0.8	< 0.01	4.4	42	-0.7	< 0.01	4.3
($R_{\rm cr}$-$\mathcal{R}$)	75	0.6	< 0.01	-5.2	33	0.6	< 0.01	-3.6	42	0.6	< 0.01	-4.0
($R_{\rm cr}$-$S_{\rm bar}$)	71	0.3	< 0.01	-2.8	30	0.6	< 0.01	-3.2	41	0.2	0.2	-1.2
($R_{\rm cr}$-M_r)	75	-0.6	< 0.001	5.1	33	-0.6	< 0.01	3.6	42	-0.6	< 0.01	3.6
($\mathcal{R}$-$S_{\rm bar}$)	71	-0.05	0.7	-0.39	30	0.4	0.03	-2.1	41	-0.2	0.3	1.1
($\mathcal{R}$-M_r)	75	-0.1	0.3	0.98	33	-0.2	0.3	1.1	42	-0.08	0.6	0.50
($S_{\rm bar}$-M_r)	71	-0.2	0.2	1.4	30	-0.5	< 0.01	2.8	41	0.003	1	-0.017
(B/T-$\Omega_{\rm bar}$)	27	-0.05	0.8	0.28	...	...	...	...	...	...	...	...
(B/T-$R_{\rm bar}$)	27	-0.1	0.6	0.52	...	...	...	...	...	...	...	...
(B/T-$S_{\rm bar}$)	26	0.5	0.01	-2.5	...	...	...	...	...	...	...	...
(B/T-$R_{\rm cr}$)	27	0.1	0.5	-0.69	...	...	...	...	...	...	...	...
(B/T-$\mathcal{R}$)	27	-0.06	0.8	0.29	...	...	...	...	...	...	...	...

Notes: (1) Correlated parameters. (2) Number of objects to explore the correlation. (3) Spearman rank correlation r parameter. (4) Two-sided significant p-value of the correlation. (5) Number of standard deviation σ from null-hypothesis.

4.5 Discussion

4.5.1 Relations among the bar parameters

Some of the relations we reported among the bar parameters of TW-measured galaxies either confirm earlier observational findings or theoretical predictions ($\Omega_{\rm bar}$-$R_{\rm bar}$, $\Omega_{\rm bar}$-$S_{\rm bar}$, $\Omega_{\rm bar}$-M_r, $R_{\rm bar}$-$S_{\rm bar}$, $S_{\rm bar}$-$R_{\rm cr}$, $R_{\rm bar}$-M_r, Figs. 4.4 and 4.6) or are expected by definition ($\mathcal{R}$-$\Omega_{\rm bar}$, $\mathcal{R}$-$R_{\rm cr}$, $\Omega_{\rm bar}$-$R_{\rm cr}$). Others ($R_{\rm bar}$-$R_{\rm cr}$, Fig. 4.6) are related to fact that the galaxies analysed with the TW method resulted to host mainly fast bars. Some bar parameters are not correlated at all ($\mathcal{R}$-$R_{\rm bar}$, $\mathcal{R}$-$S_{\rm bar}$) because of the large scatter of their distribution. For example, the weak $\mathcal{R}$-$S_{\rm bar}$ relation found for ETBGs is found in the opposite sense for LTBGs giving no correlation in the final sample. Moreover, we did not find any relations between Hubble type and bar properties (Hubble type-$R_{\rm bar}$, Hubble type-$\Omega_{\rm bar}$, Hubble type-$S_{\rm bar}$, Hubble type-$R_{\rm cr}$, or Hubble type-$\mathcal{R}$), even if some of them were previously pointed out.

It was already known that longer bars are stronger (Erwin 2005; Kruk et al. 2018; Guo et al. 2019; Chapter 3), but we found that they are also rotating slower (Fig. 4.4). Such a $\Omega_{\rm bar}$-$S_{\rm bar}$ relation was theoretically predicted (Sellwood, 1981; Athanassoula, 2003; Villa-Vargas et al., 2010; Athanassoula et al., 2013) but never clearly observed. It can be explained in terms of bar evolution because of the interchange of different amount of angular momentum during bar evolution, which can vary according to different properties of the host galaxy as investigated by Athanassoula (2003). The observed trend shown in the right panel of Fig. 4.4 is somewhat similar to the time evolution of $\Omega_{\rm bar}$-$S_{\rm bar}$ reported in the left panels of Figs. 15, 16, and 17 by Athanassoula (2003). In their numerical simulations, the DM halo is initially non-rotating and surrounds an axisymmetric disc, then the time evolution of $S_{\rm bar}$ and $\Omega_{\rm bar}$ for two extreme cases of an initially cold and an initially hot disc are considered. In the first case, both $\Omega_{\rm bar}$ and $S_{\rm bar}$ change similarly and they are almost linearly correlated. In the second case, there are two distinct evolution phases: at the beginning $S_{\rm bar}$ hardly increases, while $\Omega_{\rm bar}$ strongly decreases, later on, $\Omega_{\rm bar}$ stops decreasing very abruptly, while $S_{\rm bar}$ starts to increase. The evolution of the initially hot/cold discs is quantitatively very different. Changing the initial value of disc coldness/hotness will produce an evolutionary path of $\Omega_{\rm bar}$-$S_{\rm bar}$ located in the region between those corresponding to the two extreme cases.

Our observational results are now in agreement with the predictions of these numerical simulations. Although we are not able to probe the time evolution of a single bar, we conclude that the measured values of $\Omega_{\rm bar}$ and $S_{\rm bar}$ shown in the right panel of Fig. 4.4 represent snapshots of bars in galaxies with different properties. The relation $\Omega_{\rm bar}$-$S_{\rm bar}$ was already explored in Chapter 3, where we did not find any difference between the distribution functions of $\Omega_{\rm bar}$ in strongly and weakly barred galaxies defined according to $S_{\rm bar}$. This was probably due to the limited number of the sample galaxies, and/or because weak bars are expected both to rotate fast and slowly, according to the other galaxy parameters.

Moreover, Athanassoula (2003) show in Figs. 16 and 17 the final snapshots of their simulations corresponding to $t \sim 10^8$ yr. The anti-correlation between $S_{\rm bar}$ and $\Omega_{\rm bar}$ is clear, despite the spread due to the different initial conditions of each run (their Fig. 16), which decreases when only the simulations of galaxies with/without bulge are considered (their

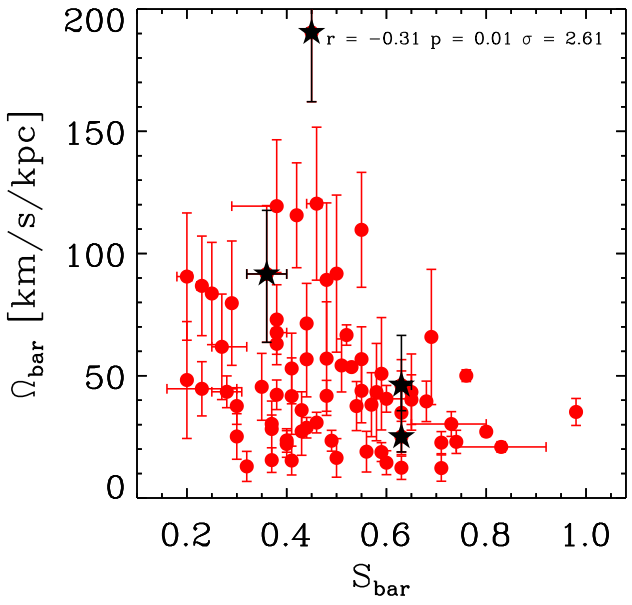

Figure 4.9: Relation between the bar pattern speed $\Omega_{\rm bar}$ and bar strength $S_{\rm bar}$ for the final sample of 75 galaxies. Galaxies with a bulge giving a strong contribution to the galaxy light ($B/T > 0.3$) are highlighted (*black stars*).

Fig. 17). These simulations are shifted in the $\Omega_{\rm bar}$-$S_{\rm bar}$ plane and such a displacement is particularly strong for simulations with large bulges. This is again in good agreement with our observations. Figure 4.9 shows the $\Omega_{\rm bar}$-$S_{\rm bar}$ relation highlighting those galaxies with a bulge contributing a large fraction of the total luminosity ($B/T > 0.3$). Despite the paucity of our data, we qualitatively observe the same displacement of the bulge-dominated galaxies as predicted by simulations.

4.5.2 Relations with the galaxy luminosity

We observed interesting relations between the bar parameters and galaxy luminosity. In particular, brighter galaxies host longer bars, which rotate slower and have larger corotations (Figs. 4.4 and 4.6). We verified that these strong correlations were not driven by fainter/brighter galaxies and/or by galaxies with very fast bars: only the correlation $\Omega_{\rm bar}$-M_r is driven by the selection criteria of the final sample because it disappears when considering all the original 100 galaxies. The relations survive even when we split the final sample between ETBGs and LTBGs (Fig. 4.5 and 4.7).

Sheth et al. (2008) studied the bar fraction over $0.2 < z < 0.84$ with a sample of more than 2000 luminous face-on spirals from the COSMOS survey. The presence of a bar strongly correlates with both the stellar mass and the bulge prominence. In fact, the bar fraction in very massive and luminous spirals ($M_*/M_\odot > 10^{10.9}$, $M_V < -23.5$ mag) is about constant out to $z \sim 0.84$, whereas for the low-mass blue spirals ($M_*/M_\odot < 10^{10.5}$, $M_V > -22.5$ mag) it significantly declines beyond $z = 0.3$. On the other hand, the bar fraction at low redshift is

roughly equal at all luminosities. The bar fraction at high redshift turned out to be slightly higher for bulge-dominated galaxies, suggesting a co-evolution of bars and bulges. At low redshift, this trend disappears and the bar fraction is roughly constant for all Hubble types, although only a few bulgeless galaxies are observed. Sheth et al. (2008) concluded that their results are a clue for a downsizing process in the formation of bars: the more massive and luminous galaxies have a higher bar fraction at higher redshift, which is close to the present-day value, whereas the less massive and luminous systems formed the majority of their bars at $z < 0.8$. The early presence of bars in massive galaxies suggests that these systems became dynamically cool and sufficiently massive to host a bar at earlier times. To the contrary, the less massive systems have a low bar fraction because they are either dynamically hot, or not rotationally supported, or have not accreted sufficient mass to form a bar at high redshift.

Our results support this scenario: we found in brighter galaxies smaller $\Omega_{\rm bar}$ values together with larger $R_{\rm bar}$ and $R_{\rm cr}$ values, which are a signature of bar evolution in agreement with the idea these bars may have formed earlier and had sufficient time to slow down, grow in length, and push outwards corotation. The fact that stronger bars are observed in bulge-dominated galaxies (Fig. 4.9) is a further indication of the co-evolution of bars and bulges.

Surprisingly, we found no correlation between Hubble type and M_r, despite it is well-known at least for giant galaxies. This could be due to the selection criteria adopted in MaNGA and CALIFA surveys.

4.6 Conclusions

We took into account all the barred galaxies available in the literature with a direct measurement of $\Omega_{\rm bar}$ obtained with the TW method from long-slit and IFU spectroscopic data of stellar kinematics. We recovered the galaxies from Corsini (2011), Aguerri et al. (2015), and Guo et al. (2019), as well as those from Chapters 2 and 3. The sample consists of 100 galaxies with an Hubble types ranging from SB0 to SBd, redshift $z < 0.08$, and absolute SDSS r-band magnitudes $-23 < M_r < -18$ mag. We collected for each sample galaxy the values of $R_{\rm bar}$, $S_{\rm bar}$, $\Omega_{\rm bar}$, $R_{\rm cr}$, and $\mathcal{R}$. To have consistent measurements of $S_{\rm bar}$, we derived it from a Fourier analysis following Athanassoula & Misiriotis (2002) for galaxies for which it was not already available in literature. We also derived the B/T ratio for a subsample of galaxies with an available photometric decomposition.

The successful application of the TW method requires the disc to have an intermediate i and the bar to be located at an intermediate PA with respect to the disc major and minor axes. We checked that these selection criteria do not systematically affect the uncertainties on $R_{\rm bar}$, $\Omega_{\rm bar}$, and $R_{\rm cr}$. Moreover, there is no bias for the 12 ($\sim$ 12 per cent) ultrafast bars ($\mathcal{R} < 1.0$) we found in the LTBGs of the sample. At the moment, we do not yet know whether ultrafast bars are an artifact of the TW method or a new class of objects that overrules the predictions of theory and numerical simulations about the extension of the bar (see also Aguerri et al. 2015 and Guo et al. 2019, for a discussion). This issue requires further investigation, which is beyond our aims. Therefore, we decided to consider only the 75 sample galaxies with a relatively small relative error on $\Omega_{\rm bar}$ ($\Delta\Omega_{\rm bar}/\Omega_{\rm bar} < 0.5$) and not hosting

an ultrafast bar ($\mathcal{R} > 1$). We investigated all the possible relations between the available bar parameters ($R_{\rm bar}$, $S_{\rm bar}$, $\Omega_{\rm bar}$, $R_{\rm cr}$, and $\mathcal{R}$) and galaxy properties (Hubble type, M_r, and B/T) and discussed their significance. Some of the relations we reported confirm earlier observational findings or theoretical predictions ($\Omega_{\rm bar}$-$R_{\rm bar}$, $\Omega_{\rm bar}$-$S_{\rm bar}$, $\Omega_{\rm bar}$-M_r, $R_{\rm bar}$-$S_{\rm bar}$, $S_{\rm bar}$-$R_{\rm cr}$, $R_{\rm bar}$-M_r, B/T-$S_{\rm bar}$) or are expected by definition ($\mathcal{R}$-$\Omega_{\rm bar}$, $\mathcal{R}$-$R_{\rm cr}$, $\Omega_{\rm bar}$-$R_{\rm cr}$). We verified that the stronger relations are not driven by fainter/brighter galaxies, galaxies with very fast bars, and ETBGs/LTBGs.

In particular, we found that stronger bars rotate slower. Such a $\Omega_{\rm bar}$-$S_{\rm bar}$ relation was theoretically predicted but never clearly observed. It can be explained in terms of bar evolution because of the interchange of different amounts of angular momentum during bar evolution depending on galaxy properties, as numerically investigated by Athanassoula (2003). We also reported that brighter galaxies host longer bars, which rotate slower and have a larger corotation. This observational finding, together with the fact that stronger bars are observed in bulge-dominated galaxies, is in agreement with a scenario of downsizing in bar formation and co-evolution of bars and bulges if more massive galaxies formed earlier and had sufficient time to slow down, grow in length, and push outwards corotation (Sheth et al., 2008).

Chapter 5

Conclusions and future perspectives

5.1 Conclusions

In this thesis we aimed to increase the sample of direct measurements of the bar pattern speed in strongly and weakly barred galaxies by applying the TW method to high-quality new and archival IFU spectroscopic data, and to explore the relations between the properties of bars and their host galaxies.

Here we summarise our main results.

5.1.1 *Chapter 2* - Evidence of a fast bar in the weakly-interacting galaxy NGC 4264 with MUSE

We took advantage of the extended spectral range, fine spatial sampling, large FOV, and superb throughput of the MUSE IFU spectrograph in combination with wide-field SDSS imaging to apply the TW method to NGC 4264, a barred lenticular galaxy at 39.2 Mpc in the region of the Virgo Cluster. We measured the broad-band surface photometry and 2D stellar kinematics of NGC 4264 to derive the pattern speed of its bar ($\Omega_{\rm bar} = 71 \pm 4$ km s^{-1} kpc^{-1}) and the ratio of the corotation radius to the bar radius ($\mathcal{R} = 0.88 \pm 0.23$). We showed that NGC 4264 hosts a strong ($S_{\rm bar} = 0.31 \pm 0.04$) and large ($R_{\rm bar} = 3.2 \pm 0.5$ kpc) bar which nearly extends out to its corotation radius ($R_{\rm cr} = 2.8 \pm 0.2$ kpc).

Concerning the properties of the galaxy, we conclude that:

- the bar of NGC 4264 has properties typical of bars in lenticular galaxies. Its radius and strength are consistent with the median values obtained for SB0 galaxies by Aguerri et al. (2009), while the bar rotation rate is consistent within the errors with the mean value calculated by Aguerri et al. (2015) for 17 SB0–SB0/a galaxies with TW-measured $\Omega_{\rm bar}$. The bar of NGC 4264 is rotating as fast as it can, like nearly all the other bars in lenticulars and spirals measured so far (Chapter 1);

- NGC 4264 is located at a small projected distance from NGC 4261 (3.5 arcmin, corresponding to 30 kpc) and it is seen through its stellar halo. The two galaxies are

probably gravitationally bound, with the difference between their systemic velocities ($|\Delta V_{\rm sys,CMB}| = 306 \pm 50$ km s^{-1}; NED) consistent with the velocity dispersion of the rich galaxy group they belong to ($\sigma_{\rm group} = 382$ km s^{-1}; Kourkchi & Tully 2017); the surface brightness radial profile of the disc of NGC 4264 is also upbending in the outer regions ($R > 24$ arcsec). This feature is usually explained as the end result of mergers and interactions, which drive outwards migration or direct accretion of part of the stars and dynamically heat the outer regions of the disc (Debattista et al., 2017). We interpreted the twist of the outer isophotes of NGC 4264, which are characterised by a rotation of the PA (ΔPA $\sim 10^{\circ}$) and no change of ϵ, as suggestive of a warp due to the ongoing interaction with NGC 4261. The fact that NGC 4261 is much more massive than NGC 4264 ($L_{\rm N4261}/L_{\rm N4264} = 6$), their closeness, together with the undisturbed morphology of NGC 4264, suggest the interaction between the two galaxies is weak;

- the measurement of $\mathcal{R}$ of the bar of NGC 4264 allowed us to constrain its formation mechanism. Martinez-Valpuesta et al. (2017) investigated with N-body numerical simulations the differences between bars resulting from disc instabilities induced by tidal interactions and self-generated internal processes, and they found that bars formed through tidal interactions were born and stay slow ($\mathcal{R} > 1.4$) all along their evolution. The bar rotation rate is found to be $\mathcal{R} \simeq 1.4$ only at the end of an interaction occurring over a long timescale. Since the bar of NGC 4264 is fast, we conclude that its formation was triggered neither by the recent interaction with NGC 4261 nor by a previous interaction with another galaxy in the region of the Virgo Cluster.

Concerning the application of the TW method, we conclude that:

- we confidently constrained the position and LOS velocity of the galaxy centre, maximised the number and S/N of the spectra extracted from the pseudo-slits crossing the bar, carefully derived the orientation and inclination of the galaxy disc, accurately measured the bar radius, and recovered the circular velocity curve by modelling the stellar kinematics to deal with the sources of uncertainty when applying the TW method;

- since a small misalignment between the direction along which TW integrals are measured and the disc major axis may hamper the determination of $\Omega_{\rm bar}$ (Debattista, 2003), we showed that IFU spectroscopy alone can not successfully address this issue: it has to be combined with accurate surface photometry to fine tune the extraction of the TW integrals. Indeed, we found that the bar of NGC 4264 appears to extend considerably beyond its corotation ($\mathcal{R} = 0.40 \pm 0.10$) if its pattern speed ($\Omega_{\rm bar} = 146 \pm 16$ km s^{-1} kpc^{-1}) is measured by aligning the pseudo-slits with the major axis of the outermost disc (PA=$122\overset{\circ}{.}2 \pm 2\overset{\circ}{.}4$). This is an unphysical result for a self-consistent bar. We deduced that the PA and ϵ of the outermost isophotes of NGC 4264 are not indicative of the actual orientation and inclination of the disc where the bar lives. For this reason, we restricted our analysis of $\Omega_{\rm bar}$ and $\mathcal{R}$ to the inner disc (PA = $114\overset{\circ}{.}0 \pm 1\overset{\circ}{.}2$);

- the values of $\Omega_{\rm bar}$ and $\mathcal{R}$ for the bar of NGC 4264 are amongst the best-constrained ones ever obtained with the TW method. The relative errors are as small as $\Delta\Omega_{\rm bar}/\Omega_{\rm bar} =$

0.06 and $\Delta\mathcal{R}/\mathcal{R} = 0.26$, respectively. This pilot study with MUSE represents a remarkable result not only with respect to early TW measurements based on long-slit spectroscopy (see Corsini, 2011, for a list) but also with respect to those recently derived from IFU spectroscopy (Aguerri et al., 2015; Guo et al., 2019).

The results of this Chapter were published in Cuomo et al. (2019b).

5.1.2 *Chapter 3* - Bar pattern speeds in CALIFA galaxies - The case of weakly barred galaxies

We obtained the bar properties of a sample of 29 *bona fide* SAB galaxies by analysing the r-band images available from the SDSS survey and stellar kinematic maps obtained from the CALIFA survey. The galaxies were selected to have an intermediate inclination, a bar elongated between the minor and major axes of the disc, and to be morphologically and kinematically undisturbed. The sample galaxies have morphological types ranging from S0 to Scd, with redshifts between 0.005 and 0.30 and absolute r-band total magnitudes from -18.5 to -23.0 mag.

We derived $R_{\rm bar}$ in the deprojected images of the galaxies by measuring the bar/interbar intensity ratios obtained from Fourier analyses of the surface brightness distributions, the location of the maxima in the ϵ radial profiles, and the behaviours of the PA radial profiles of the ellipses fitting the galaxy isophotes. At the same time, we measured $S_{\rm bar}$ from the Fourier analyses. Despite stringent criteria adopted for the selection, we discarded six galaxies because they turned out not to host a clear bar component. The $m = 2$ Fourier components did not show amplitude peaks with constant phase angles typical of barred galaxies, while the large odd components revealed the presence of non-axisymmetric structures other than a bar.

We applied the TW method to obtain $\Omega_{\rm bar}$ from the CALIFA datacubes. This study represents the third effort to apply the TW method to a large sample of galaxies based on IFU spectroscopy, after Aguerri et al. (2015) and Guo et al. (2019), and it is the first one including SAB galaxies. To this aim, for each galaxy we measured the luminosity-weighted mean position and LOS velocity of the stars across the bar in several pseudo-slits parallel to the disc major axis. We rejected seven more galaxies because of their poor correlations, the large errors, or the non-convergence of the TW integrals. This means that 13 galaxies of the sample (45 per cent), which were morphologically classified as weakly barred from a visual inspection, do not actually host a genuine bar component or the central elongated structure is not in rigid rotation. For the remaining 16 SAB galaxies, we derived $R_{\rm cr}$ from the circular velocities obtained by applying asymmetric drift corrections to the stellar kinematics, and $\mathcal{R}$ as the ratio between $R_{\rm cr}$ and $R_{\rm bar}$. All the measured SAB bars are consistent with being fast within the errors ($1 < \mathcal{R} < 1.4$), except for two of them which are ultrafast ($\mathcal{R} < 1$) at the 95 per cent confidence level and were not considered further.

We built a comparison sample of SB galaxies with TW-based $\Omega_{\rm bar}$ from the literature. We split the entire sample of 46 (visually-classified SB + SAB) galaxies analysed with the TW method so far according to the strength of the bar (if available) and excluding the ultrafast bars. A value of $S_{\rm bar} = 0.4$ was adopted to provide a quantitative definition of SAB and SB

galaxies, and the final sample includes 13 quantitatively-defined SAB and 27 quantitatively-defined SB galaxies. Our results can be summarised as follows:

- SAB galaxies host weaker and shorter bars with smaller corotation radii than the bars of SB galaxies. SAB and SB galaxies have similarly large pattern speeds and bar rotation rates. After checking that the two samples do have similar absolute total magnitudes, we excluded that this result is due to a bias in the distribution of their luminosities;

- SAB galaxies, similarly to SB galaxies, turned out to host fast bars. Slow bars are expected to be tidally triggered by a past interaction with a companion, so we can exclude this formation scenario;

- we investigated the relation between the presence of a weak/strong bar and the bulge properties of the host galaxy, since one of the most promising and often advocated cause of bar weakening is the presence of a CMC. We did not find any significant difference in the Seŕsic index n and effective radius $r_{\rm e}$ of the bulges of SAB and SB galaxies. Instead, we found a lower B/T ratio in SAB galaxies. Moreover, we found two bulgeless SAB galaxies. Therefore, we conclude that the presence of a prominent bulge does not necessarily imply bar weakening. Moreover, we clearly found that $\Omega_{\rm bar}$ of weak and strong bars are similar, as previously suggested by measurements with other methods (Font et al., 2017). This allowed us to discard the dissolution scenario for weak bars, which always predicts an increase in $\Omega_{\rm bar}$ while the bar is losing strength and dissolving, regardless of the cause of dissolution, such as the presence of a CMC, the shape of DM halo, or gas accretion (Athanassoula, 2003; Bournaud et al., 2005; Athanassoula, 2005). Laurikainen et al. (2013) suggested that bulges in early-type SB galaxies are built by bars, while those in SAB galaxies are possibly the end result of several accretion events that occurred before the bar formation, prescribing different values for the index n. In our sample this formation mechanism is not supported because we observe the same distribution of Sérsic index n in SB and SAB galaxies;

- we explored the relation between the presence of a weak/strong bar and the disc scale-length h of the host galaxy. We found that weak bars are all hosted in the inner parts of discs, because most SAB galaxies have both $R_{\rm bar}/h$ and $R_{\rm cr}/h$ smaller than 1.0 and in all SAB galaxies these ratios are smaller than 1.5, except for one outlier. We observed a larger spread of $R_{\rm bar}/h$ and $R_{\rm cr}/h$ for SB galaxies, with a clear tail to values larger than 1.5. SB and SAB galaxies have similar $\Omega_{\rm bar}$ and none of the bars analysed in this work or in previous TW-based works is unambiguously located in the slow regime. Moreover, we are very unlikely to catch a bar in its early phase of evolution, because the bar formation phase is very short. All evidence thus suggests that SAB galaxies are dynamically evolved systems, which did not exchange as much angular momentum as SB galaxies, and their bars have not grown, while the paucity of slow bars remains unexplained.

The results of this Chapter were presented in Cuomo et al. (2019a).

5.1.3 *Chapter 4* - Relations among structural parameters in barred galaxies with a direct measurement of bar pattern speed

We took into account all the barred galaxies available in the literature with a direct measurement of $\Omega_{\rm bar}$ obtained with the TW method using long-slit and IFU spectroscopic data of stellar kinematics. We recovered the galaxies from Corsini (2011), Aguerri et al. (2015), and Guo et al. (2019), as well as those from Chapters 2 and 3. The sample consists of 100 galaxies with Hubble types ranging from SB0 to SBd, redshifts $z < 0.08$, and absolute SDSS r-band magnitudes $-23 < M_r < -18$ mag. We collected for each sample galaxy the values of $R_{\rm bar}$, $S_{\rm bar}$, $\Omega_{\rm bar}$, $R_{\rm cr}$, and $\mathcal{R}$. To have consistent measurements of $S_{\rm bar}$for galaxies for which it is not already available in literature, we derived them from Fourier analyses following Athanassoula & Misiriotis (2002). We also derived the B/T ratios for a subsample of galaxies with an available photometric decomposition.

The successful application of the TW method requires the disc to have an intermediate i and the bar to be located at an intermediate PA with respect to the disc major and minor axes. We checked that these selection criteria do not systematically affect the uncertainties on $R_{\rm bar}$, $\Omega_{\rm bar}$, and $R_{\rm cr}$. Moreover, no bias was found for the 12 ($\sim$ 12 per cent) ultrafast bars ($\mathcal{R} < 1.0$), all belonging to the LTBGs of the sample. Since we do not yet know whether ultrafast bars are an artifact of the TW method or a new class of objects that overrules the predictions of theory and numerical simulations about the extension of the bar, we decided to consider only the 75 sample galaxies with a relatively small relative error on $\Omega_{\rm bar}$ ($\Delta\Omega_{\rm bar}/\Omega_{\rm bar} < 0.5$) and not hosting an ultrafast bar ($\mathcal{R} > 1$). We investigated all the possible relations between the available bar parameters ($R_{\rm bar}$, $S_{\rm bar}$, $\Omega_{\rm bar}$, $R_{\rm cr}$, and $\mathcal{R}$) and galaxy properties (Hubble type, M_r, and B/T) and discussed their significance.

We conclude that:

- some of the relations we reported confirm earlier observational findings or theoretical predictions ($\Omega_{\rm bar}$-$R_{\rm bar}$, $\Omega_{\rm bar}$-$S_{\rm bar}$, $\Omega_{\rm bar}$-M_r, $R_{\rm bar}$-$S_{\rm bar}$, $S_{\rm bar}$-$R_{\rm cr}$, $R_{\rm bar}$-M_r, B/T-$S_{\rm bar}$) or are expected by definition ($\mathcal{R}$-$\Omega_{\rm bar}$, $\mathcal{R}$-$R_{\rm cr}$, $\Omega_{\rm bar}$-$R_{\rm cr}$). We verified that the stronger relations are not driven by fainter/brighter galaxies, galaxies with very fast bars, or ETBGs/LTBGs;

- we found that stronger bars rotate slower. Such a $\Omega_{\rm bar}$-$S_{\rm bar}$ relation was theoretically predicted but never clearly observed. It can be explained in terms of bar evolution, because of the interchange of different amounts of angular momentum during bar evolution depending on galaxy properties, as numerically investigated by Athanassoula (2003);

- we also reported that brighter galaxies host longer bars, which rotate slower and have larger corotations. This observational finding, together with the fact that stronger bars are observed in bulge-dominated galaxies, is in agreement with a scenario of downsizing for bar formation and co-evolution of bars and bulges, if more massive galaxies formed earlier and had sufficient time to slow down, grow in length, and push outwards corotation (Sheth et al., 2008).

We aim to present the results of this Chapter in V. Cuomo, J. A. L. Aguerri, E. M. Corsini et al. 2019, A&A, in preparation.

5.2 Future perspectives

There are still open questions posed with respect to the TW method measurements: the relation between DM content and $\mathcal{R}$, the presence of many ultrafast bars despite the absence of a theoretical explanation, and the absence of slow bars.

Studying the nature of ultrafast bars and addressing the absence of slow bars will allow to exclude systematic errors in the TW method, and together with the results of dynamical modelling, to draw solid cosmological conclusions on DM content in the central regions of barred galaxies.

5.2.1 Comparison with dynamical modelling

The analysis of the MUSE dataset of NGC 4264 presented in Chapter 2 represents a pilot study for further accurate MUSE measurements of $\Omega_{\rm bar}$ and $\mathcal{R}$ on a well-defined sample of barred galaxies. This would be of considerable interest to severely test the predictions of numerical simulations about the time evolution of the bar radius and pattern speed as a function of gas content, luminous and DM distribution (Weinberg, 1985; Debattista & Sellwood, 2000; Athanassoula, 2003; Athanassoula et al., 2013; Martinez-Valpuesta et al., 2017; Algorry et al., 2017). However, this comparison requires to build solid dynamical models, to infer some information about the DM content, distribution and density in the bar regions of the analysed galaxies, and this is still a missing piece of information. Previous efforts in this direction were limited by large uncertainties on $\mathcal{R}$. As an example, Guo et al. (2019) built JAM dynamical models of their MaNGA galaxies, but no significant correlation was found between $\mathcal{R}$ and the fraction of DM within the galaxy effective radius obtained from the models.

All the galaxies with a direct measurement of $\Omega_{\rm bar}$, including those from this thesis, turned out to host fast bars, when neglecting measurements with large uncertainties. This result is compatible with the case of maximum discs, in which bars are embedded in DM halos with low central densities (Debattista & Sellwood, 2000). Again, this scenario could be confirmed through a comparison with dynamical modelling. Fast bars from TW measurements are found in all the explored morphological types. This was originally pointed out by Aguerri et al. (2015), and now confirmed with the wider sample studied in Chapter 4. However, this is slightly different from the results of indirect methods, which observed fast bars in ETBGs but both fast and slow bars in LTBGs (Rautiainen et al., 2008; Font et al., 2017). Figure 5.1 shows $\mathcal{R}$ obtained with both direct and indirect methods with respect to galaxy morphological type, including the results obtained in this thesis.

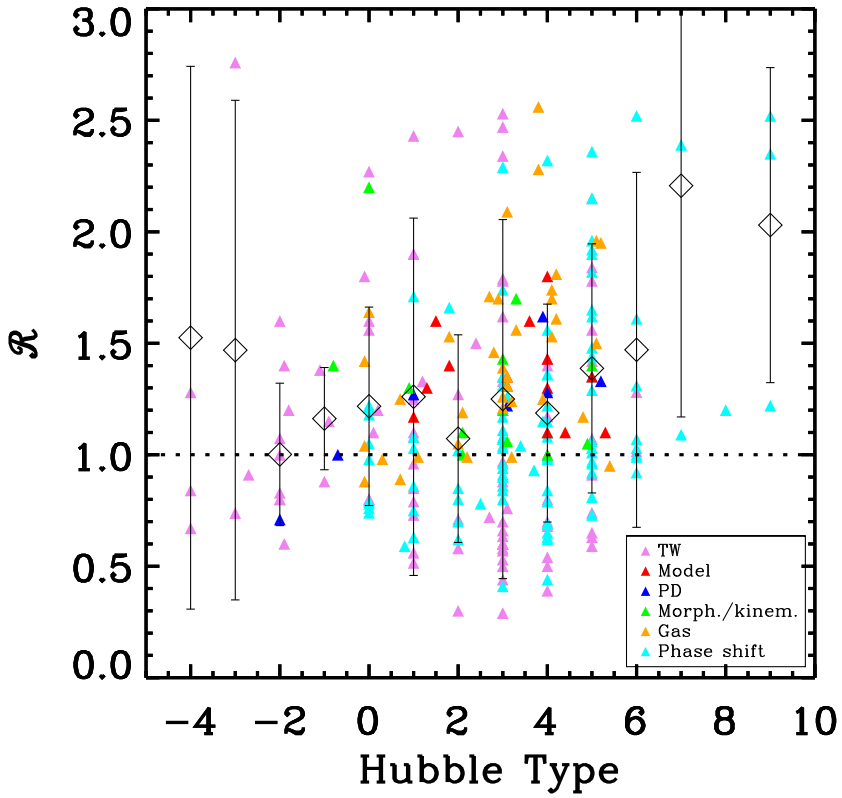

Figure 5.1: Bar rotation rate as a function of galaxy morphological type, obtained with different methods to measure the bar pattern speed. The mean value of the bar pattern speed and associated uncertainties for each bin in morphological type is shown (*black open squares*). Adapted from Rautiainen et al. (2008) by including the results of this thesis.

5.2.2 Ultrafast bars

When $\mathcal{R} < 1.0$, the x_1 family orbits enter a non-stability regime, the stellar orbits are elongated perpendicular to the bar major axis, and consequently the bar dissolves (Contopoulos, 1981). Despite theoretical predictions, ultrafast bars are observed at 95 per cent confident level in a non-negligible fraction of around 10 per cent of the TW measurements, so they require further investigations. They are hosted only in LTBGs (Chapter 4), which are the most difficult cases for the application of the TW method. Using N-body simulations, Zou et al. (2019) suggested false ultrafast bar measurements can occur when the angle between the bar and the assumed PA of the disc is overestimated, when the bar is too close to the disc minor axis, and/or if the FOV is too small for convergence of the integrals. One might therefore think ultrafast bars are due to the wrong application of the method, as suggested by the tests of the TW method based on numerical simulations, but this case was excluded by previous observational results (Aguerri et al. 2015; Guo et al. 2019; Chapter 3). No clear trend was observed with respect to the disc inclination and/or the orientation of the bar with respect to the major and minor axes of its host disc (Chapter 4). Moreover, a non-negligible fraction of ultrafast bars was also observed while applying other methods (Buta & Zhang, 2009). New studies are required to eventually exclude that these results are flawed because of an improper application of the TW method and/or to suggest if some information about the nature of ultrafast bars is still missing.

5.2.3 Slow bars

The paucity of slow bars, expected from an efficient exchange of angular momentum within the galaxy and/or triggered by tidal interaction, is again controversial. This can be explained with an erroneous and/or biased application of the TW method, or with a bias in the selection of the galaxies. To push the quest of slow bars, it could be interesting to define a new and promising sample. Barred galaxies having dark gaps between the inner and outer rings were first theoretically predicted (Schwarz, 1981; Kim et al., 2016) and now commonly observed in early-to-intermediate barred galaxies (Buta, 2017). Their morphology is explained by a large exchange of angular momentum within the galaxy, responsible to shift the bar in the slow regime. In addition, dwarf galaxies are commonly thought to host a massive and centrally-concentrated DM halos (Côté et al., 1991), which may cause the same effect on their bars. Measuring $\Omega_{\rm bar}$ from stellar dynamics in a sample barred galaxies having dark gaps between the inner and outer rings and/or of dwarf barred galaxies by means of IFU spectroscopy may help to constrain the inner mass distribution of DM and to draw solid dynamical and cosmological conclusions, but this will require robust dynamical models to have a complete view. Along these lines, we started the study of the dwarf galaxy NGC 4598, which is nicely suited for TW analysis because it has an intermediate disc i and the bar is located at intermediate angle between the disc major and minor axes (Fig. 5.2).

NGC 4598 is a small and faint dwarf barred galaxy located in the Virgo Cluster (Kim et al., 2014). It is a lenticular galaxy with an undisturbed morphology, classified as SB0 (RC3). Its apparent magnitude $B_T = 13.7$ mag corresponds to a total corrected absolute

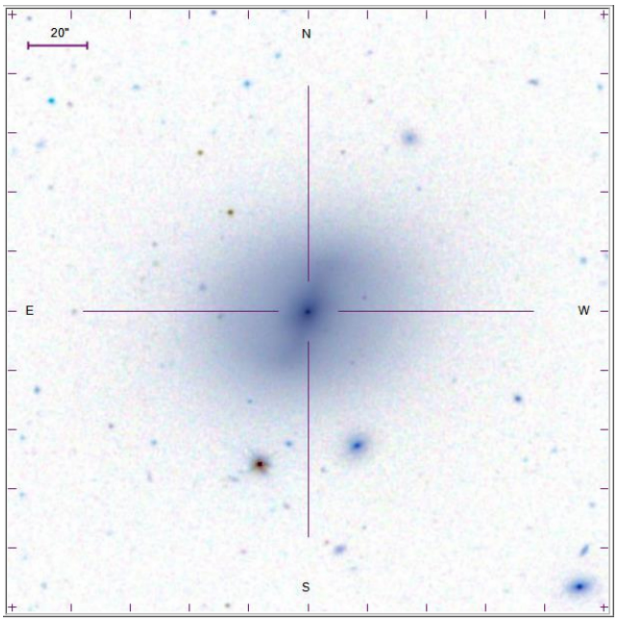

Figure 5.2: SDSS i-band image of NGC 4598. The size and orientation of the FOV are given, where a cross marks the centre of NGC 4598.

magnitude $M^0_{B,T} = -18.77$ mag, obtained assuming a distance $D = 31.2$ Mpc from the radial velocity with respect to the cosmic microwave background reference frame $V_{\rm CMB} = 2292 \pm 33$ km s^{-1} (Binggeli et al., 1985) and $H_0 = 73$ km s^{-1} Mpc^{-1} or $M^0_{B,T} = -17.73$ mag, obtained assuming a distance $D = 19.3$ Mpc for the Virgo Cluster (Fixsen et al., 1996). The galaxy has a small extension of 82.8 arcsec $\times$ 67.3 arcsec (RC3), measured at a surface brightness level of $\mu_B = 25$ mag arcsec^{-2}.

We performed an isophotal analysis of the galaxy using a SDSS i-band image, following the same approach described in Sec. 2.3.1: we trimmed the image to select the region of the galaxy, we subtracted the sky-residuals estimating the contribution of the sky at large distances from the galaxy centre, we performed the isophotal analysis on the sky-subtracted image with the ELLIPSE procedure, and we estimated the position angle (PA $= 108\overset{\circ}{.}66 \pm 3\overset{\circ}{.}17$) and inclination ($i = \arccos(1-\epsilon) = 37\overset{\circ}{.}16 \pm 1\overset{\circ}{.}99$) of the disc, necessary for the TW analysis.

IFU medium-resolution data were obtained in March 2008 using the PMAS (Roth et al., 2005) installed at the Calar Alto Observatory 3.5m Telescope in Spain. The instrument was used in PPAK off-axis fiber bundle mode, which is recommended for large FOV and low surface brightness objects, together with the V1200 grating. The selected setup covers the wavelength range $4800 - 5500$ Å, with an instrumental spectral resolution $\sigma_{\rm strum} \sim 70$ km s^{-1} and a FOV of ~ 60 arcsec $\times$ 60 arcsec.

The stellar kinematics of NGC 4598 was recovered from the PMAS-PPAK datacube of the galaxy using the PPXF code (Cappellari & Emsellem, 2004) and the Mg line triplet (Fig. 5.3, middle and right panels).

To recover $\Omega_{\rm bar}$, the photometric integrals can be measured as usual by summing up all the flux of each spectrum of the datacube in the available wavelength range,

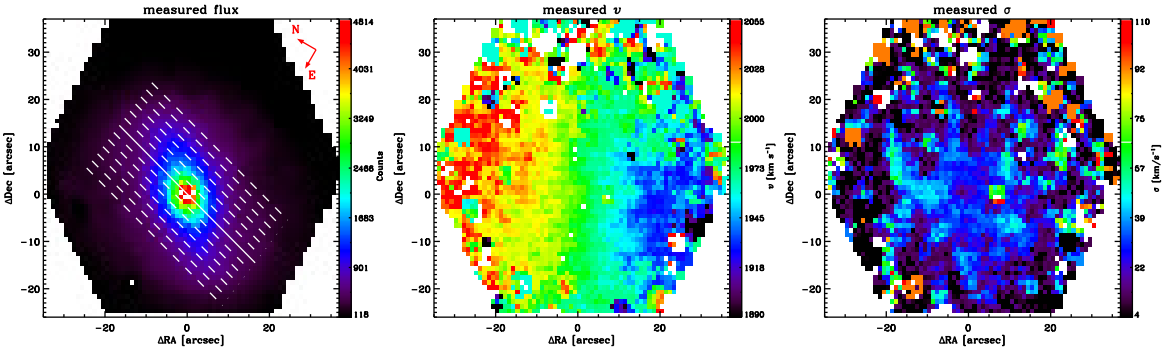

Figure 5.3: Surface brightness distribution obtained from the PMAS-PPAK data (*left panel*), measured velocity field (*middle panel*) and velocity dispersion (*right panel*) of the stars of NGC 4598. As an example, 13 pseudo-slits which can be defined to recover the bar pattern speed are shown (*white lines*). The orientation of the FOV is given and corresponds to the orientation used during the acquisition of the data.

$$\langle X \rangle = \frac{\sum_{(x,y)} \mathrm{dist}(x,y) F(x,y)}{\sum_{(x,y)} F(x,y)}, \tag{5.1}$$

where (x, y) are the single pixels in each pseudo-slit, $F(x, y)$ is the flux measured in each pixel in the collapsed image and $\mathrm{dist}(x, y)$ is the distance of each pixel with respect to the line crossing the centre of the pseudo-slit. The kinematic integrals can be directly obtained from the stellar velocity field using the surface brightness map as weight, by summing up all the luminosity-weighted velocities from the kinematic maps,

$$\langle V \rangle = \frac{\sum_{(x,y)} v_\star(x,y) F(x,y)}{\sum_{(x,y)} F(x,y)}, \tag{5.2}$$

where $v_\star$ is the velocity measured in each pixel belonging to each pseudo-slit. Aguerri et al. (2015) showed that using this approach to recover the kinematic integrals, instead of extracting the LOS velocity from each collapsed spectra, does not lead to any differences in the value of Ω_{bar}. We adopted 13 pseudo-slits with a width of 1 arcsec and a semi-major length of 22 arcsec. Fig. 5.3 shows the surface brightness and stellar kinematics of NGC 4598.

To recover $\Omega_{\mathrm{bar}} \sin i = 3.2^{+0.8}_{-1.0}$ km s^{-1} arcsec^{-1}, the resulting integrals were fitted with a linear relation. Figure 5.4 shows three different estimates of Ω_{bar}, which can be obtained varying the disc PA within the corresponding uncertainties, and are used to recover upper and lower errors on Ω_{bar}.

These preliminary results helped us to conclude that this galaxy and the available data are suitable to obtain a reliable TW measurement. In the future, we aim to complete the analysis on NGC 4598 and test the corresponding results with a dynamical model of the galaxy.

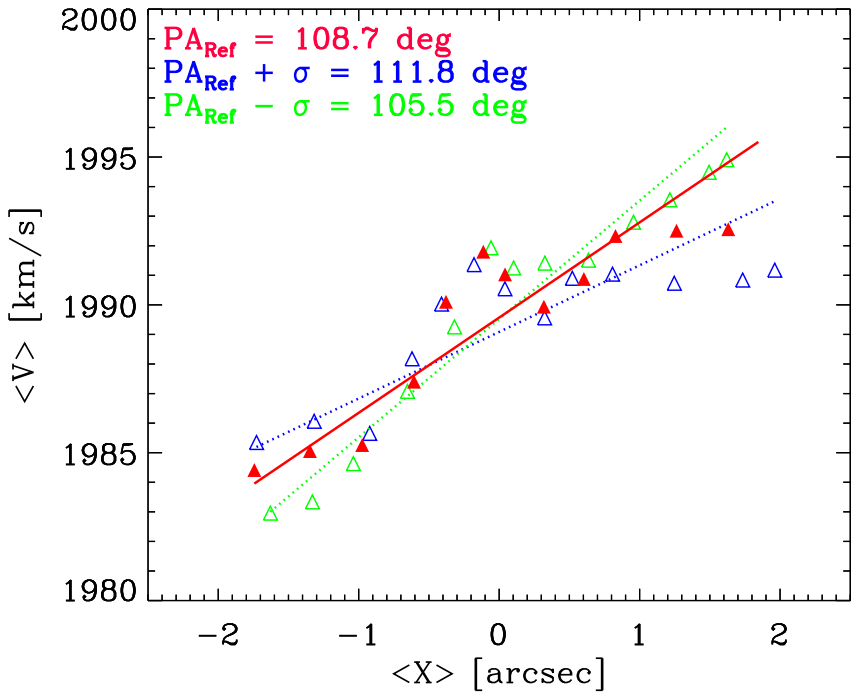

Figure 5.4: Three different pattern speeds of the bar in NGC 4598, obtained adopting three different PAs of the galaxy disc (the reference PA from the isophotal analysis PA_{Ref} and $PA_{Ref} \pm \sigma_{PA}$).

Ringraziamenti

A tutte le persone che mi hanno cambiato attraverso questo incantevole viaggio, vorrei dire grazie.

A mia mamma e mio papà, che sono sempre troppo orgogliosi di me.

All'energia potenziale, mie amiche di sempre e sorelle, Costanza, Emma, Beatrice, Marta e Camilla, perché da oggi in poi le cose possono solo andare meglio, e dovunque saremo il destino ci riporterà sempre a casa.

To the Canarian girls, che mi hanno mostrato la forza per sopravvivere da sola così lontano da casa. Ad Anastasia e Federica, le mie folli compagne di avventure, perché *in the worst case scenario* si può sopravvivere con hummus, pankace e aguacate, perché è impossibile dimenticare il tramonto a Punta Teno, o di aver guidato per le strade incredibili di El Hierro, o di aver dormito in una caverna o in una casa per le capre.

Al Prof. Corsini e ad Alfonso, che hanno creduto in me e mi hanno dato la possibilità di mettermi alla prova.

Ai miei amici astronomi, Annagrazia, Giada, Nicola, Giampaolo e Chiara, perché in un modo o nell'altro continueremo a incontrarci in giro per il mondo e avremo talmente tante cose da dirci che parleremo allo sfinimento.

A Ilaria e Michela, le mie sagge compagne di scientifiche avventure, (eccessive) bevute e mangiate.

A Luca, che avendo intimamente compreso che non è possibile fermare la mia giostra, ha deciso coraggiosamente di salirci.

Bibliography

Abazajian K. N., et al., 2009, ApJS, 182, 543

Abolfathi B., et al., 2018, ApJS, 235, 42

Abraham R. G., Merrifield M. R., 2000, AJ, 120, 2835

Abraham R. G., Merrifield M. R., Ellis R. S., Tanvir N. R., Brinchmann J., 1999, MNRAS, 308, 569

Abramowitz M., Stengun I., 1964, Handbook of Mathematical Functions. Dover Publications, New York USA

Aguerri J. A. L., 1999, A&A, 351, 43

Aguerri J. A. L., Muñoz-Tuñón C., Varela A. M., Prieto M., 2000, A&A, 361, 841

Aguerri J. A. L., Hunter J. H., Prieto M., Varela A. M., Gottesman S. T., Muñoz-Tuñón C., 2001, A&A, 373, 786

Aguerri J. A. L., Debattista V. P., Corsini E. M., 2003, MNRAS, 338, 465

Aguerri J. A. L., Elias-Rosa N., Corsini E. M., Muñoz-Tuñón C., 2005, A&A, 434, 109

Aguerri J. A. L., Méndez-Abreu J., Corsini E. M., 2009, A&A, 495, 491

Aguerri J. A. L., et al., 2015, A&A, 576, A102

Alam S., et al., 2015, ApJS, 219, 12

Algorry D. G., et al., 2017, MNRAS, 469, 1054

Athanassoula E., 1992, MNRAS, 259, 345

Athanassoula E., 2003, MNRAS, 341, 1179

Athanassoula E., 2005, MNRAS, 358, 1477

Athanassoula E., 2008, in Bureau M., Athanassoula E., Barbuy B., eds, IAU Symposium Vol. 245, Formation and Evolution of Galaxy Bulges. Cambridge University Press, UK, p. 93

Athanassoula E., 2014, MNRAS, 438, L81

Athanassoula E., Martinet L., 1980, A&A, 87, L10

Athanassoula E., Misiriotis A., 2002, MNRAS, 330, 35

Athanassoula E., Sellwood J. A., 1986, MNRAS, 221, 213

Athanassoula E., Morin S., Wozniak H., Puy D., Pierce M. J., Lombard J., Bosma A., 1990, MNRAS, 245, 130

Athanassoula E., Machado R. E. G., Rodionov S. A., 2013, MNRAS, 429, 1949

Aumer M., Schönrich R., 2015, MNRAS, 454, 3166

Bacon R., et al., 2001, MNRAS, 326, 23

Bacon R., et al., 2010, in McLean I. S., Ramsay S. K., Takami H., eds, Ground-based and Airborne Instrumentation for Astronomy III. Proc. SPIE. Vol. 7735. SPIE, Bellingham, WA, p. 773508

Banerjee A., Patra N. N., Chengalur J. N., Begum A., 2013, MNRAS, 434, 1257

Barazza F. D., Jogee S., Marinova I., 2008, ApJ, 675, 1194

Barnes J. E., Hernquist L. E., 1991, ApJ, 370, L65

Barway S., Wadadekar Y., Kembhavi A. K., 2011, MNRAS, 410, L18

Beckman J. E., Fathi K., Piñol N., Hernandez O., Carignan C., Pérez I., 2011, Mem. Soc. Astron. Ital. Suppl., 18, 35

Beifiori A., Maraston C., Thomas D., Johansson J., 2011, A&A, 531, A109

Benjamin R. A., et al., 2005, ApJ, 630, L149

Berentzen I., Heller C. H., Shlosman I., Fricke K. J., 1998, MNRAS, 300, 49

Bertola F., Cinzano P., Corsini E. M., Rix H.-W., Zeilinger W. W., 1995, ApJ, 448, L13

Binggeli B., Sandage A., Tammann G. A., 1985, AJ, 90, 1681

Binney J., Tremaine S., 2008, Galactic Dynamics: Second Edition. Princeton University Press, Princeton, NJ USA

Binney J., Gerhard O. E., Stark A. A., Bally J., Uchida K. I., 1991, MNRAS, 252, 210

Binney J., Gerhard O., Spergel D., 1997, MNRAS, 288, 365

Bland-Hawthorn J., Gerhard O., 2016, ARA&A, 54, 529

Borlaff A., et al., 2014, A&A, 570, A103

Bournaud F., Combes F., 2002, A&A, 392, 83

Bournaud F., Combes F., Semelin B., 2005, MNRAS, 364, L18

Bovy J., Leung H. W., Hunt J. A. S., Mackereth J. T., Garcia-Hernandez D. A., Roman-Lopes A., 2019, MNRAS, submitted (arXiv:1905.11404)

Bundy K., et al., 2015, ApJ, 798, 7

Bureau M., Freeman K. C., 1997, PASA, 14, 146

Bureau M., Freeman K. C., Pfitzner D. W., Meurer G. R., 1999, AJ, 118, 2158

Bureau M., Aronica G., Athanassoula E., Dettmar R. J., Bosma A., Freeman K. C., 2006, MNRAS, 370, 753

Bureau M., Aronica G., Athanassoula E., 2007, ASSP, 3, 181

Buta R., 1995, ApJS, 96, 39

Buta R. J., 2017, MNRAS, 470, 3819

Buta R., Block D. L., 2001a, ApJ, 550, 243

Buta R., Block D. L., 2001b, ApJ, 550, 243

Buta R. J., Zhang X., 2009, ApJS, 182, 559

Buta R., Ryder S. D., Madsen G. J., Wesson K., Crocker D. A., Combes F., 2001, AJ, 121, 225

Buta R., Laurikainen E., Salo H., Knapen J. H., Block D. L., 2007, in Combes F., Palouš J., eds, IAU Symposium Vol. 235, Galaxy Evolution across the Hubble Time. Cambridge University Press, UK, p. 81

Buta R. J., et al., 2015, ApJS, 217, 32

Cabrera-Lavers A., González-Fernández C., Garzón F., Hammersley P. L., López-Corredoira M., 2008, A&A, 491, 781

Cameron E., et al., 2010, MNRAS, 409, 346

Canzian B., 1998, ApJ, 502, 582

Caon N., Capaccioli M., D'Onofrio M., 1993, MNRAS, 265, 1013

Cappellari M., Copin Y., 2003, MNRAS, 342, 345

Cappellari M., Emsellem E., 2004, PASP, 116, 138

Cappellari M., et al., 2011, MNRAS, 413, 813

Cappellari M., et al., 2013a, MNRAS, 432, 1709

Cappellari M., et al., 2013b, MNRAS, 432, 1862

Chemin L., Hernandez O., 2009, A&A, 499, L25

Cinzano P., Rix H. W., Sarzi M., Corsini E. M., Zeilinger W. W., Bertola F., 1999, MNRAS, 307, 433

Clarke J. P., Wegg C., Gerhard O., Smith L. C., Lucas P. W., Wylie S. M., 2019, MNRAS, p. 2055

Combes F., 2008, in Funes J. G., Corsini E. M., eds, ASP Conf. Ser. Vol. 396, Formation and Evolution of Galaxy Disks. Astron. Soc. Pac., San Francisco, CA, p. 325

Combes F., 2011, Mem. Soc. Astron. Ital. Suppl., 18, 53

Combes F., Elmegreen B. G., 1993, A&A, 271, 391

Combes F., Sanders R. H., 1981, A&A, 96, 164

Combes F., Debbasch F., Friedli D., Pfenniger D., 1990, A&A, 233, 82

Compère P., López-Corredoira M., Garzón F., 2014, A&A, 571, A98

Consolandi G., 2016, A&A, 595, A67

Contopoulos G., 1981, A&A, 102, 265

Contopoulos G., Grosbol P., 1989, A&A Rev., 1, 261

Contopoulos G., Papayannopoulos T., 1980, A&A, 92, 33

Corsini E. M., 2011, Mem. Soc. Astron. Ital. Suppl., 18, 23

Corsini E. M., et al., 1999, A&A, 342, 671

Corsini E. M., Debattista V. P., Aguerri J. A. L., 2003, ApJ, 599, L29

Corsini E. M., Aguerri J. A. L., Debattista V. P., Pizzella A., Barazza F. D., Jerjen H., 2007, ApJ, 659, L121

Costantin L., Méndez-Abreu J., Corsini E. M., Morelli L., Aguerri J. A. L., Dalla Bontà E., Pizzella A., 2017, A&A, 601, A84

Costantin L., Méndez-Abreu J., Corsini E. M., Eliche-Moral M. C., Tapia T., Morelli L., Dalla Bontà E., Pizzella A., 2018, A&A, 609, A132

Côté S., Carignan C., Sancisi R., 1991, AJ, 102, 904

Cuomo V., Aguerri J. A. L., Corsini E. M., Debattista V. P., Méndez-Abreu J., Pizzella A., 2019a, A&A, in press, (arXiv:1909.0102)

Cuomo V., et al., 2019b, MNRAS, 488, 4972

D'Onghia E., Aguerri J. A. L., 2019, ApJ, submitted, (arXiv:1907.08484)

Debattista V. P., 2003, MNRAS, 342, 1194

Debattista V. P., Sellwood J. A., 1998, ApJ, 493, L5

Debattista V. P., Sellwood J. A., 2000, ApJ, 543, 704

Debattista V. P., Williams T. B., 2004, ApJ, 605, 714

Debattista V. P., Corsini E. M., Aguerri J. A. L., 2002, MNRAS, 332, 65

Debattista V. P., Mayer L., Carollo C. M., Moore B., Wadsley J., Quinn T., 2006, ApJ, 645, 209

Debattista V. P., Roškar R., Loebman S. R., 2017, in Knapen J. H., Lee J. C., Gil de Paz A., eds, Astrophysics and Space Science Library Vol. 434, Outskirts of Galaxies. Springer International Publishing, Cham, Switzerland, p. 77

Díaz-García S., Salo H., Laurikainen E., 2016, A&A, 596, A84

Drory N., et al., 2015, AJ, 149, 77

Du M., Shen J., Debattista V. P., 2015, ApJ, 804, 139

Dunnett C. W., 1979, Canadian Journal of Statistics, 7, 234

Eliche-Moral M. C., Borlaff A., Beckman J. E., Gutiérrez L., 2015, A&A, 580, A33

Elmegreen B., 1996, in Buta R., Crocker D. A., Elmegreen B. G., eds, ASP Conf. Ser. Vol. 91, Barred Galaxies. Astron. Soc. Pac., San Francisco, CA, p. 197

Elmegreen B. G., Elmegreen D. M., 1985, ApJ, 288, 438

Elmegreen B. G., Elmegreen D. M., Chromey F. R., Hasselbacher D. A., Bissell B. A., 1996, AJ, 111, 2233

Emsellem E., Arsenault R., 1997, A&A, 318, L39

England M. N., 1989, ApJ, 344, 669

England M. N., Gottesman S. T., Hunter J. H. J., 1990, ApJ, 348, 456

Englmaier P., Gerhard O., 1999, MNRAS, 304, 512

Englmaier P., Shlosman I., 2004, ApJ, 617, L115

Erwin P., 2004, A&A, 415, 941

Erwin P., 2005, MNRAS, 364, 283

Erwin P., 2011, Mem. Soc. Astron. Ital. Suppl., 18, 145

Erwin P., 2018, MNRAS, 474, 5372

Erwin P., Debattista V. P., 2016, ApJ, 825, L30

Erwin P., Debattista V. P., 2017, MNRAS, 468, 2058

Falcón-Barroso J., et al., 2017, A&A, 597, A48

Ferrers N. M., 1877, Quart. J. Pure and Appl. Math., 14, 1

Fixsen D. J., Cheng E. S., Gales J. M., Mather J. C., Shafer R. A., Wright E. L., 1996, ApJ, 473, 576

Font J., Beckman J. E., Epinat B., Fathi K., Gutiérrez L., Hernandez O., 2011, ApJ, 741, L14

Font J., Beckman J. E., Querejeta M., Epinat B., James P. A., Blasco-Herrera J., Erroz-Ferrer S., Pérez I., 2014, ApJS, 210, 2

Font J., et al., 2017, AJ, 835, 279

Fragkoudi F., et al., 2019, MNRAS, 488, 3324

Freeman K. C., 1966, MNRAS, 133, 47

Freudling W., Romaniello M., Bramich D. M., Ballester P., Forchi V., García-Dabló C. E., Moehler S., Neeser M. J., 2013, A&A, 559, A96

Friedli D., 1998, in Friedli D., Edmunds M., Robert C., Drissen L., eds, ASP Conf. Ser. Vol. 147, Abundance Profiles: Diagnostic Tools for Galaxy History. Astron. Soc. Pac., San Francisco, CA, p. 287

Friedli D., 1999, in Beckman J. E., Mahoney T. J., eds, ASP Conf. Ser. Vol. 187, The Evolution of Galaxies on Cosmological Timescales. Astron. Soc. Pac., San Francisco, CA, p. 88

Friedli D., Martinet L., 1993, A&A, 277, 27

Friedli D., Benz W., Kennicutt R., 1994, ApJ, 430, L105

Fukugita M., Ichikawa T., Gunn J. E., Doi M., Shimasaku K., Schneider D. P., 1996, AJ, 111, 1748

Garcia A. M., 1993, A&AS, 100, 47

Garcia-Gómez C., Athanassoula E., Barberà C., Bosma A., 2017, A&A, 601, A132

Gerhard O. E., 1993, MNRAS, 265, 213

Gerhard O., Martinez-Valpuesta I., 2012, ApJ, 744, L8

Gerssen J., Debattista V. P., 2007, MNRAS, 378, 189

Gerssen J., Shapiro Griffin K., 2012, MNRAS, 423, 2726

Gerssen J., Kuijken K., Merrifield M. R., 1999, MNRAS, 306, 926

Gerssen J., Kuijken K., Merrifield M. R., 2003, MNRAS, 345, 261

Griv E., Chiueh T., 1998, ApJ, 503, 186

Gunn J. E., et al., 1998, AJ, 116, 3040

Guo R., Mao S., Athanassoula E., Li H., Ge J., Long R. J., Merrifield M., Masters K., 2019, MNRAS, 482, 1733

Hammersley P. L., Garzón F., Mahoney T. J., López-Corredoira M., Torres M. A. P., 2000, MNRAS, 317, L45

Heller C. H., Shlosman I., 1996, ApJ, 471, 143

Hinshaw G., et al., 2013, ApJS, 208, 19

Hirota A., Kuno N., Sato N., Nakanishi H., Tosaki T., Matsui H., Habe A., Sorai K., 2009, PASJ, 61, 441

Ho L. C., 2009, ApJ, 699, 638

Hohl F., 1971, ApJ, 168, 343

Hubble E. P., 1926, ApJ, 64, 321

Husemann B., et al., 2013, A&A, 549, A87

Jedrzejewski R. I., 1987, MNRAS, 226, 747

Jeong H., Bureau M., Yi S. K., Krajnović D., Davies R. L., 2007, MNRAS, 376, 1021

Jogee S., et al., 2004, ApJ, 615, L105

Kim S., et al., 2014, ApJS, 215, 22

Kim T., Gadotti D. A., Athanassoula E., Bosma A., Sheth K., Lee M. G., 2016, MNRAS, 462, 3430

Klypin A., Valenzuela O., Colín P., Quinn T., 2009, MNRAS, 398, 1027

Knapen J. H., Shlosman I., Peletier R. F., 2000, ApJ, 529, 93

Kormendy J., 1979, ApJ, 227, 714

Kormendy J., 2013, Secular Evolution in Disk Galaxies. Cambridge University Press, Cambridge, UK

Kourkchi E., Tully R. B., 2017, ApJ, 843, 16

Krajnović D., Cappellari M., de Zeeuw P. T., Copin Y., 2006, MNRAS, 366, 787

Krajnović D., et al., 2011, MNRAS, 414, 2923

Kruk S. J., et al., 2018, MNRAS, 473, 4731

Kuijken K., Merrifield M. R., 1995, ApJ, 443, L13

Laine S., Kenney J. D. P., Yun M. S., Gottesman S. T., 1999, ApJ, 511, 709

Laurikainen E., Salo H., Buta R., 2005, MNRAS, 362, 1319

Laurikainen E., Salo H., Buta R., Knapen J. H., 2007, MNRAS, 381, 401

Laurikainen E., Salo H., Buta R., Knapen J. H., 2009, ApJ, 692, L34

Laurikainen E., Salo H., Athanassoula E., Bosma A., Buta R., Janz J., 2013, MNRAS, 430, 3489

Lee G.-H., Park C., Lee M. G., Choi Y.-Y., 2012, ApJ, 745, 125

Lee Y. H., Ann H. B., Park M.-G., 2019, ApJ, 872, 97

Leung G. Y. C., et al., 2018, MNRAS, 477, 254

Li Z.-Y., Ho L. C., Barth A. J., 2017, ApJ, 845, 87

Lin L.-H., Wang H.-H., Hsieh P.-Y., Taam R. E., Yang C.-C., Yen D. C. C., 2013, ApJ, 771, 8

Lin Y., Cervantes Sodi B., Li C., Wang L., Wang E., 2014, ApJ, 796, 98

Lindblad P. A. B., Kristen H., 1996, A&A, 313, 733

Lintott C. J., et al., 2008, MNRAS, 389, 1179

Little B., Carlberg R. G., 1991, MNRAS, 251, 227

Łokas E. L., 2018, ApJ, 857, 6

Łokas E. L., Athanassoula E., Debattista V. P., Valluri M., Pino A. d., Semczuk M., Gajda G., Kowalczyk K., 2014, MNRAS, 445, 1339

Lucy L. B., 1974, AJ, 79, 745

Lütticke R., Dettmar R. J., Pohlen M., 2000, A&AS, 145, 405

Maciejewski W., 2006, MNRAS, 371, 451

Marinova I., Jogee S., 2007, ApJ, 659, 1176

Martin P., 1995, AJ, 109, 2428

Martin P., Roy J.-R., 1994, ApJ, 424, 599

Martinet L., 1995, Fund. Cosmic Phys., 15, 341

Martinet L., Friedli D., 1997, A&A, 323, 363

Martinez-Valpuesta I., Shlosman I., Heller C., 2006, ApJ, 637, 214

Martinez-Valpuesta I., Knapen J. H., Buta R., 2007, AJ, 134, 1863

Martinez-Valpuesta I., Aguerri J., González-García C., 2016, Galaxies, 4, 7

Martinez-Valpuesta I., Aguerri J. A. L., González-García A. C., Dalla Vecchia C., Stringer M., 2017, MNRAS, 464, 1502

Masters K. L., et al., 2012, MNRAS, 424, 2180

Mediavilla E., Arribas S., Roth M., Cepa-Nogué J., Sánchez F., 2011, 3D Spectroscopy in Astronomy. Cambridge University Press, Cambridge, UK

Meidt S. E., Rand R. J., Merrifield M. R., 2009, ApJ, 702, 277

Melvin T., et al., 2014, MNRAS, 438, 2882

Méndez-Abreu J., Aguerri J. A. L., Corsini E. M., Simonneau E., 2008, A&A, 478, 353

Méndez-Abreu J., Sánchez-Janssen R., Aguerri J. A. L., 2010, ApJ, 711, L61

Méndez-Abreu J., Sánchez-Janssen R., Aguerri J. A. L., Corsini E. M., Zarattini S., 2012, ApJ, 761, L6

Méndez-Abreu J., Debattista V. P., Corsini E. M., Aguerri J. A. L., 2014, A&A, 572, A25

Méndez-Abreu J., et al., 2017, A&A, 598, A32

Méndez-Abreu J., et al., 2018a, MNRAS, 474, 1307

Méndez-Abreu J., Costantin L., Aguerri J. A. L., de Lorenzo-Cáceres A., Corsini E. M., 2018b, MNRAS, 479, 4172

Méndez-Abreu J., et al., 2019, MNRAS, 482, L118

Menéndez-Delmestre K., Sheth K., Schinnerer E., Jarrett T. H., Scoville N. Z., 2007, ApJ, 657, 790

Merrifield M. R., Kuijken K., 1995, MNRAS, 274, 933

Merrifield M. R., Rand R. J., Meidt S. E., 2006, MNRAS, 366, L17

Merritt D., Sellwood J. A., 1994, ApJ, 425, 551

Michel-Dansac L., Wozniak H., 2006, A&A, 452, 97

Miwa T., Noguchi M., 1998, ApJ, 499, 149

Moffat A. F. J., 1969, A&A, 3, 455

Moiseev A. V., 2011, Mem. Soc. Astron. Ital. Suppl., 18, 153

Monari G., Kawata D., Hunt J. A. S., Famaey B., 2017, MNRAS, 466, L113

Moore B., Ghigna S., Governato F., Lake G., Quinn T., Stadel J., 1998, in Zaritsky D., ed., ASP Conf. Ser. Vol. 136, Galactic Halos. Astron. Soc. Pac., San Francisco, CA, p. 426

Nair P. B., Abraham R. G., 2010, ApJ, 714, L260

Navarro J. F., Frenk C. S., White S. D. M., 1996, ApJ, 462, 563

Ness M., et al., 2013, MNRAS, 432, 2092

Nilson P., 1973, Uppsala general catalogue of galaxies. Royal Society of Science of Uppsala, Sweden

Noguchi M., 1987, MNRAS, 228, 635

Noguchi M., 1988, A&A, 203, 259

Noguchi M., 1996, ApJ, 469, 605

O'Neill J. K., Dubinski J., 2003, MNRAS, 346, 251

Odewahn S. C., 1996, in Buta R., Crocker D. A., Elmegreen B. G., eds, ASP Conf. Ser. Vol. 91, IAU Colloq. 157: Barred Galaxies. Astron. Soc. Pac., San Francisco, CA, p. 30

Ohta K., Hamabe M., Wakamatsu K.-I., 1990, ApJ, 357, 71

Olle M., Pfenniger D., 1998, A&A, 334, 829

Ostriker J. P., Peebles P. J. E., 1973, ApJ, 186, 467

Patra N. N., Jog C. J., 2019, MNRAS, 488, 4942

Pérez I., Sánchez-Blázquez P., 2011, A&A, 529, A64

Pérez I., Aguerri J. A. L., Méndez-Abreu J., 2012, A&A, 540, A103

Pfenniger D., Friedli D., 1991, A&A, 252, 75

Pfenniger D., Norman C., 1990, ApJ, 363, 391

Pizzella A., Corsini E. M., Vega Beltrán J. C., Bertola F., 2004, A&A, 424, 447

Portail M., Wegg C., Gerhard O., 2015, MNRAS, 450, L66

Portail M., Gerhard O., Wegg C., Ness M., 2017, MNRAS, 465, 1621

Press W. H., Teukolsky S. A., Vetterling W. T., Flannery B. P., 1992, Numerical Recipes in FORTRAN. The Art of Scientific Computing. Cambridge University Press, Cambridge, UK

Prieto M., Gottesman S. T., Aguerri J.-A. L., Varela A.-M., 1997, AJ, 114, 1413

Prieto M., Aguerri J. A. L., Varela A. M., Muñoz-Tuñón C., 2001, A&A, 367, 405

Prugniel P., Soubiran C., 2001, A&A, 369, 1048

Puerari I., Dottori H., 1997, ApJ, 476, L73

Quillen A. C., 1996, in Buta R., Crocker D. A., Elmegreen B. G., eds, Astronomical Society of the Pacific Conference Series Vol. 91, IAU Colloq. 157: Barred Galaxies. Cambridge University Press, UK, p. 390

Quillen A. C., Frogel J. A., Gonzalez R. A., 1994, ApJ, 437, 162

Raha N., Sellwood J. A., James R. A., Kahn F. D., 1991, Nature, 352, 411

Rand R. J., Wallin J. F., 2004, ApJ, 614, 142

Rautiainen P., Salo H., Laurikainen E., 2005, ApJ, 631, L129

Rautiainen P., Salo H., Laurikainen E., 2008, MNRAS, 388, 1803

Reyes R., Mandelbaum R., Gunn J. E., Pizagno J., Lackner C. N., 2011, MNRAS, 417, 2347

Richardson W. H., 1972, J. Opt. Soc. Am., 62, 55

Ridley M. G. L., Sormani M. C., Treß R. G., Magorrian J., Klessen R. S., 2017, MNRAS, 469, 2251

Rodríguez S., Padilla N. D., 2013, MNRAS, 434, 2153

Rodriguez-Fernandez N. J., Combes F., 2008, A&A, 489, 115

Roth M. M., et al., 2005, PASP, 117, 620

Roy J. R., Walsh J. R., 1997, MNRAS, 288, 715

Ryden B. S., 2004, ApJ, 601, 214

Ryden B. S., 2006, AJ, 641, 773

Salak D., et al., 2019, PASJ, p. 17

Salo H., 1991, A&A, 243, 118

Sánchez-Janssen R., Méndez-Abreu J., Aguerri J. A. L., 2010, MNRAS, 406, L65

Sánchez S. F., et al., 2012, A&A, 538, A8

Sánchez S. F., et al., 2016, A&A, 594, A36

Sarzi M., et al., 2006, MNRAS, 366, 1151

Sarzi M., et al., 2018, A&A, 616, A121

Schmitt H. R., 2001, AJ, 122, 2243

Schwarz M. P., 1981, ApJ, 247, 77

Seigar M. S., James P. A., 1998, MNRAS, 299, 672

Seigar M. S., Harrington A., Treuthardt P., 2018, MNRAS, 481, 5394

Sellwood J. A., 1981, A&A, 99, 362

Sellwood J. A., 2014, Reviews of Modern Physics, 86, 1

Sellwood J. A., Evans N. W., 2001, ApJ, 546, 176

Sérsic J. L., 1968, Atlas de Galaxias Australes. Observatorio Astronomico de Cordoba, Cordoba, Argentina

Sheth K., et al., 2008, ApJ, 675, 1141

Shlosman I., Frank J., Begelman M. C., 1989, Nature, 338, 45

Simmons B. D., et al., 2014, MNRAS, 445, 3466

Skrutskie M. F., et al., 2006, AJ, 131, 1163

Sormani M. C., Magorrian J., 2015, MNRAS, 446, 4186

Sormani M. C., Sobacchi E., Shore S. N., Treß R. G., Klessen R. S., 2017, MNRAS, 471, 2932

Sormani M. C., Treß R. G., Ridley M., Glover S. C. O., Klessen R. S., Binney J., Magorrian J., Smith R., 2018, MNRAS, 475, 2383

Soto K. T., Lilly S. J., Bacon R., Richard J., Conseil S., 2016, MNRAS, 458, 3210

Starkman N., Lelli F., McGaugh S., Schombert J., 2018, MNRAS, 480, 2292

Toomre A., 1981, in Fall S. M., Lynden-Bell D., eds, Structure and Evolution of Normal Galaxies. Proc. of the Advanced Study Institute. Cambridge University Press, Cambridge, UK, p. 111

Tremaine S., Weinberg M. D., 1984, ApJ, 282, L5

Treuthardt P., Buta R., Salo H., Laurikainen E., 2007, AJ, 134, 1195

Valdes F., Gupta R., Rose J. A., Singh H. P., Bell D. J., 2004, ApJS, 152, 251

Vásquez S., et al., 2013, A&A, 555, A91

Vera M., Alonso S., Coldwell G., 2016, A&A, 595, A63

Vila-Costas M. B., Edmunds M. G., 1992, MNRAS, 259, 121

Villa-Vargas J., Shlosman I., Heller C., 2010, ApJ, 719, 1470

Wada K., Koda J., 2004, MNRAS, 349, 270

Wake D. A., et al., 2017, AJ, 154, 86

Walcher C. J., et al., 2014, A&A, 569, A1

Wegg C., Gerhard O., 2013, MNRAS, 435, 1874

Wegg C., Gerhard O., Portail M., 2015, MNRAS, 450, 4050

Weilbacher P. M., Streicher O., Urrutia T., Jarno A., Pécontal-Rousset A., Bacon R., Böhm P., 2012, in Radziwill N. M., Chiozzi G., eds, Software and Cyberinfrastructure for Astronomy II. Proc. SPIE. Vol. 8451. SPIE, Bellingham, WA, p. 84510B

Weinberg M. D., 1985, MNRAS, 213, 451

Weiner B. J., Sellwood J. A., Williams T. B., 2001, ApJ, 546, 931

Whyte L. F., Abraham R. G., Merrifield M. R., Eskridge P. B., Frogel J. A., Pogge R. W., 2002, MNRAS, 336, 1281

Wozniak H., 2015, A&A, 575, A7

Wozniak H., Champavert N., 2006, MNRAS, 369, 853

Wozniak H., Pierce M. J., 1991, A&AS, 88, 325

Wozniak H., Friedli D., Martinet L., Martin P., Bratschi P., 1995, A&AS, 111, 115

Yan R., et al., 2016, AJ, 152, 197

Young L. M., et al., 2011, MNRAS, 414, 940

Zasov A. V., Saburova A. S., Khoperskov A. V., Khoperskov S. A., 2017, Physics Uspekhi, 60, 3

Zhang X., Buta R. J., 2007, AJ, 133, 2584

Zimmer P., Rand R. J., McGraw J. T., 2004, ApJ, 607, 285

Zou Y., Shen J., Bureau M., Li Z.-Y., 2019, ApJ, 884, 23

de Lorenzo-Cáceres A., Falcón-Barroso J., Vazdekis A., 2013, MNRAS, 431, 2397

de Lorenzo-Cáceres A., Méndez-Abreu J., Thorne B., Costantin L., 2019a, MNRAS, 484, 665

de Lorenzo-Cáceres A., et al., 2019b, MNRAS, 484, 5296

de Vaucouleurs G., 1959, Handbuch der Physik, 53, 275

de Vaucouleurs G., de Vaucouleurs A., Corwin Jr. H. G., Buta R. J., Paturel G., Fouqué P., 1991, Third Reference Catalogue of Bright Galaxies. Springer-Verlag, New York USA

van den Bergh S., 1976, ApJ, 206, 883

van der Marel R. P., Franx M., 1993, ApJ, 407, 525